REAL-TIME, LABEL FREE DETECTION AND TREATMENT OF HUMAN CANCER INFILTRATION USING OPTICAL PROPERTY MAPPING AND OTHER IMAGING MODALITIES

by
Carmen Kut

A dissertation submitted to Johns Hopkins University in conformity with the requirements for the degree of Doctor of Philosophy

Baltimore, Maryland

March 2016

ABSTRACT

This dissertation presents the use of optical coherence tomography (OCT), multi-photon fluorescence (MPF) and other imaging techniques in the detection of human brain cancer infiltration.

In the first part of this study, we demonstrate the use of OCT and MPF in obtaining optical, structural, molecular and functional information of human brain cancer versus non-cancer tissues. A systematic *ex vivo* study has been performed using OCT to obtain the optimal quantitative diagnostic threshold for distinguishing brain cancer versus non-cancer tissues; an independent study using the optimal diagnostic threshold is able to achieve excellent sensitivity and specificity in the detection of brain cancer versus non-cancer. In addition, an *in vivo* study has begun to evaluate the performance of OCT in detecting brain cancer in patients in the operating room, with excellent results. In the second part of the study, we demonstrate how MPF can be used to provide complementary information to OCT in the real-time detection of human brain cancer. While OCT is able to volumetrically scan the entire resection cavity in the brain, MPF can be used to zoom in and provide additional information to assist surgeons and pathologists with the diagnosis. Finally, this dissertation also discusses supporting work in the identification of other existing techniques in the diagnostic and treatment of human cancer infiltration. To summarize, the results of this dissertation have motivated the development and optimization of the OCT and MPF software and hardware to enable *in vivo* imaging and analyses of human cancer infiltration.

ACKNOWLEDGEMENTS

I would like to dedicate this dissertation to the following persons who have provided me immeasurable support and guidance, and have contributed one way or another towards making this thesis possible. Thank you so much for helping me along my journey in PhD!

First of all, I would like to express my sincere gratitude to **Professor Xingde Li**, who has nurtured and provided me with numerous advice, opportunities and support during my graduate training. I cannot thank him enough for believing in me, and for his genuine care and excitement in my progress. He challenges me every day to do my very best, and for that I cannot thank him enough. Professor Li inspires me every day with his intellectual rigor and firm dedication to research.

At the same time, I would like to thank **Professor Alfredo Quinones-Hinojosa**, who has impassioned me with his fierce commitment to fight brain cancer. I am deeply grateful to him for believing and advocating for this project in numerous ways. His mentorship has helped me to understand the clinical need, and to fully comprehend the intraoperative challenges we must overcome for this project. I cannot thank him enough for taking this project into the clinical studies.

I would also like to thank **Professor Elliot R. McVeigh**, who has given me the courage and freedom to venture out and develop my own research project. Thanks to him, I was able to chat with physicians and researchers in multiple departments, and to initiate my own research project in a multidisciplinary setting. I am inspired by the breadth of his knowledge, and am thankful to him for his constant encouragement and confidence in me.

Thank you to **Professor Fausto J. Rodriguez,** who has taught me about brain cancer pathologies. Thank you for reviewing the histological slides for this project and for your patience and mentorship throughout my PhD. Thank you to **Professor Xiaobu Ye**, who is instrumental to the biostatistical analyses of this project, and for your mentorship throughout my PhD. Thank you to **Professor Ishan Barman**, who has given me valuable advice in biostatistics and in the translational of a project from the lab bench to the clinic.

Thank you so much to **Professor Russell Taylor**, who has opened my eyes to the world of robotics and computational biology. I am indebted to you for giving me the courage and courage and passion to pursue a PhD degree! I cannot thank you enough for inspiring and equipping me to innovate with engineering solutions in my thesis project.

Thank you to **Professor Aleksander Popel,** who introduced me to the world of research. Thank you so much for taking me into your laboratory as an undergraduate freshman. Your continued support and encouragement means a lot to me.

Thank you to **Professor Theodore DeWeese**, who has mentored me for many years. Thank you for supporting me through ups and downs of my life, and for teaching me what it is like to be a great physician advocate for the patients. Thank you to **Ms Nicole Mills** - your friendship means a lot to me, and you continue to inspire me every day with your strength, beauty and positive outlook in life.

Thank you **Professor Andrea Cox and Ms Sharon Welling** – thank you for being like family to the MSTP students. I cannot imagine going through the program without your support and encouragements!

Thank you so much to **Dr. Yonggang Zhang and Ms. Haoming Zhou**, who have given me a taste of home during my time at Johns Hopkins. Thank you for teaching me so much, for always taking care of me, and for your love and support.

Thank you to my friends and many others who support me and keep me sane throughout PhD.

Thank you so much to **Jordan White** for his never-ending love and support.

Finally, thank you so much to **my parents, Raymond Kut and Winnie Wong (Kut)** for loving me and for always putting my academics and my happiness first. I am most indebted to you for all of sacrifices that you have made for me, and for all the love, support, and hugs throughout my life journey. I would like to dedicate this thesis to you. I know we don't always put it in words, but at least for this one time, I just wanted to say thank you, and that I love you very much.

TABLE OF CONTENTS

TABLE OF CONTENTS

CHAPTER 1: INTRODUCTION

SECTION 1: OVERVIEW

Glioma is the most common and aggressive adult primary brain cancer, with inevitable recurrence and limited survival times. Current literature has repeatedly and consistently shown that maximal safe resection of the brain cancer can lead to improved overall survival and delayed recurrence. While some intra-operative imaging tools are already available (including MRI, CT, ultrasound, and fluorescence), these modalities have limitations in the ability to provide quantitative, real-time and/or three-dimensional continuous guidance in the operating room with optimal resolution and contrast. This dissertation aims to explore the advantages and challenges of existing imaging techniques, and demonstrate the exciting potential of Optical Coherence Tomography (OCT) in distinguishing human brain cancer from non-cancer with excellent sensitivity and specificity. Furthermore, it will demonstrate a novel method to quantitatively analyze OCT data and to generate a color-coded optical property map for real-time, continuous guidance in brain cancer resections. At the time of this dissertation, this novel optical mapping method has been extensively studied using freshly resected, *ex vivo* human brain cancer tissues from 32 patients. In addition, the intra-operative feasibility of this study has been demonstrated not only in *in vivo* rodent models with patient-derived brain cancer xenografts, but also in a pilot study with 3 *in vivo* brain cancer patients in the operating room. Furthermore, later chapters of this dissertation will cover the use of a different optical imaging technique, multiphoton fluorescence (MPF), in detecting brain cancer margins, which will prove especially useful when used in conjunction with OCT. Finally, this dissertation will also explore the potential of the OCT/MPF technique in other clinical applications, and postulate a few possible future directions for this technology.

SECTION 2: NEED FOR MAXIMAL SAFE CANCER RESECTION

On the overall, it is estimated that nearly 700,000 people living in the United States suffer from some form of primary brain cancer; every year, approximately 78,000 new cases of primary brain tumors are diagnosed (Source: ABTA). Of these brain cancers, approximately 25,000 are primary malignant brain cancers, while the remaining 53,000 are non-malignant primary bran cancers. Glioma is a brain cancer type which arises from glial cells in the brain, which are used to "glue' or support neuronal structures in the brain.

In this study, we focus on gliomas, the most common malignant adult human brain cancer. In fact, gliomas alone accounts for approximately 80% of all primary malignant brain tumors all age. Of all the gliomas, glioblastoma (GBM, or grade IV glioma) is the most common one and accounts for around 55% of all glioma cases. In addition, astrocytomas (which include GBM) accounts for approximately 75% of all glioma cases. In terms of prognosis, GBM is the most aggressive with a median overall survival of 14 months. While lower-grade gliomas have slightly better prognosis, 50 to 75% of patients with low-grade glioma die from recurrence or progression to a malignant (i.e. higher grade) glioma (*1*).

Surgery is a critical component in the management and treatment of brain cancer. While glioma treatment often include a combination of surgery, radiation and chemotherapy, surgery remains the first-line therapy and the most common initial step for glioma treatment. Multiple studies have repeatedly shown the significant long-term benefits of safe maximum cancer resection, including improved overall survival and delayed cancer recurrence; as a result, maximal safe resection of the brain cancer is significant for high-grade glioma patients, but even more critical for low-grade glioma patients who can enjoy years of improved survival *(2-19)*.

Consequently, the clinical standard of care requires the surgeon to resect as much cancer as possible, while preserving critical neurological functions including motor, sensory and speech.

As recent studies have clearly shown, the surgical extent of resection (EOR) is critical in prolonging progression-free and overall survivals for high-grade glioma patients *(2-13)*. In 2011, Sanai *et al.* conducted a systematic study with 500 glioblastoma (i.e. GBM, or high-grade glioma) patients, and reported significantly improved survival for patients with at least 78% of the cancer resected; furthermore, Sanai's group found that for GBM patients who had a gross total resection (defined as patients who had all visible tumor removed as shown on post-operative MRI scans) had a 1.6-fold increase in survival when compared with patients with only a subtotal resection (defined as patients who had visible tumor remaining as shown on post-operative MRI scans) *(3)*. Similarly, Chaichana *et al.* in 2013 reported that a EOR threshold of at least 70% has been associated with an increase in both progression-free and overall survivals, and that every 5% increase in resection decreases the risk of death by 5.2% for glioblastoma (GBM) patients (*2*).

Similar conclusions can also be made for lower-grade glioma patients, i.e., that maximal EOR in low-grade glioma is significantly associated with improved survival and delayed recurrence *(14-19)*. In 1994, Berger *et al.* demonstrated that patients with a residual tumor volume of less than 10 cm^3 (as shown in post-operative MRI images) enjoy an increase in progression-free survival (at 50 months) when compared with patients with >10 cm^3 residual tumor volume (at 30 months) (*20*). In 2008, McGirt *et al.* reported that patients with gross total resection are associated with both increased overall survival and progression free survival (when compared with subtotal resection); finally, Smith *et al.* published in the same year and reported that a >90% EOR (vs. <90% EOR) is associated with >50% increase in overall survival at the 5-8 year time points (*16, 17*).

As a result, there is a clear clinical need to maximize safe resection in order to delay cancer recurrence, improve patient response to adjuvant therapies (e.g. chemotherapy and radiation treatments), and ultimately increase survival. In response to this clinical need, multiple imaging tools are being developed for use in the operating room. In the next chapter, we will give an overview of the present and future imaging modalities used in the operating room for brain cancer resections, and discuss the overall advantages and limitations of each existing modality.

SECTION 3: OVERVIEW OF EXISTING IMAGING TOOLS

It is very difficult to distinguish brain cancer from non-cancer in the operating room for even the most experienced surgeons, whether by the naked eye alone or with help from the surgical microscope. As a result, there is a clear need to develop an imaging technology which is effective and reliable while providing continuous, real-time and high-resolution surgical guidance.

Multiple imaging tools have been developed for surgical use in the operating room in response to this clinical need. These imaging tools include MRI, CT, ultrasound, surgical microscope and navigational platforms, as well as more recent and experimental technologies such 5-ALA fluorescence and Raman Spectroscopy. All of these imaging tools have important contributions and provides intra-operative information to the surgeons; however, each of these imaging tools has its respective advantages and limitations, and does not completely resolve the clinical challenge to provide continuous and real-time guidance for surgeons to achieve maximal safe cancer resections.

SECTION 4: MAGNETIC RESONANCE IMAGING (MRI)

Magnetic resonance imaging (MRI) is a routine imaging technique used to detect, diagnose and monitor brain cancers. Established as part of standard of care, MRI images are obtained prior to surgery for examination of critical anatomical details of the brain cancer and the surrounding normal brain. A surgical plan is then established based upon the information given by the MRI.

Furthermore, a pre-operative MRI is often used to orient and localize the brain cancer during surgery. Using a neurosurgical navigational platform, the skull of the patient (marked with several visible optical trackers) can be co-registered with the pre-operative MRI images to determine the approximate location of the brain cancer.

As a result, MRI is indispensable to brain cancer diagnoses and management due to its large field of view and imaging depth (which enable whole-brain imaging) and its ability to provide three-dimensional anatomical details (which enables pre-surgical planning). Despite its advantages, however, MRI has limited volumetric resolution at 3-26 mm^3, and suffers from poor biological specificity; in other words, it cannot directly determine the presence (or absence) of brain cancer. Rather, MRI detects abnormality by observing contrast-enhancement in its T_2 weighted signals, which occurs when there is an increase in water as a result of the breakdown of the blood-brain-barrier. Since a breakdown in the blood-brain-barrier can be caused by numerous disease conditions including cancer, inflammation and neurodegenerative diseases (*21*), MRI has poor specificity in the detection of brain cancer. In addition, since MRI acquisition is slow and generally takes one hour to complete, pre-operative MRI cannot provide real-time surgical feedback, and as a result, is sensitive to brain shift, brain motions and positional errors during surgery (*22*).

Intra-operative MRI, on the other hand, is less prone to brain shift and positional errors as it allows for repeated image acquisition during surgery. However, few hospitals can afford to purchase intra-operative MRI as it is very expensive and costs several million dollars per unit. Furthermore, intra-operative MRI takes approximately 50 minutes per scan, which translates into more operating room time, higher risks for the patient (who is subjected to more time under anesthesia), and more costs associated with the procedure. Continuous real-time intra-operative guidance with MRI remains not possible.

In summary, MRI is excellent for visualizing anatomic details surrounding the brain cancer mass, so that a surgical plan can be established prior to actual surgery. However, neither pre-operative nor intra-operative MRI can provide continuous, real-time guidance during surgery; thus other intra-operative imaging tools are necessary to assist the surgeon in making real-time decisions throughout the resection process.

SECTION 5: OTHER STANDARD IMAGING TOOLS IN THE OR

Other standard imaging tools in the operating room include computed tomography (CT), ultrasound (US) and the use of a FDA approved fluorescent dye, indocyanine green (ICG).

Computed tomography (CT) scanning is occasionally used in the clinic to detect brain cancer, but it is considerably less sensitive than MRI at imaging soft tissues in the brain (*23*). As a result, it is difficult to use CT alone to distinguish human brain tumor from non-tumor tissues.

Ultrasound (US) is a non-invasive, affordable imaging tool in the operating room. It is optimal for guiding needle placements in brain biopsy procedures (*23*), as US has a relatively large field of view and imaging depth, and can provide three-dimensional anatomical details in the brain. In addition, US is especially useful in the operating room because it can provide continuous, real-

time feedback to the neurosurgeon for the identification and preservation of viable blood vessels in the human brain, thus preventing excessive bleeding or stroke complications for the patients. Despite its advantages, however, ultrasound has limited resolution at approximately 150-250 μm, and does not have sufficient contrast to clearly identify the surgical margins between tumor and non-tumor (*24, 25*). Consequently, US remains limited in its use to identify brain tumor from non-tumor in the OR.

Finally, indocyanine green (ICG) is a FDA approved fluorescent dye which has been routinely used in the brain to detect peri-tumoral and intra-tumoral blood vessels (*26*). However ICG has poor specificity for tumoral vessel detection, as it routinely binds to plasma proteins from within the bloodstream.

In conclusion, while there are several imaging tools which are commonly used in the operating room for brain cancer treatment, these tools have not resolved the important clinical challenge in achieving maximal safe resection of brain tumor in the operating room.

SECTION 6: EXPERIMENTAL IMAGING TOOLS IN THE OR

This section introduces novel experimental imaging modalities which have not yet received FDA approval in the US, but have demonstrated great potential in pilot clinical studies.

One of the most popular and recent methods involves the use of an orally administered fluorescent dye, 5-aminolevulinic acid (5-ALA) (*27*). As the first compound in the heme biosynthetic pathway, 5-ALA eventually elicits the synthesis and accumulation of fluorescent porphyrins (i.e., protoporphyrin IX, or PPIX) in neoplastic tissues such as malignant gliomas (*4, 27*). As a result, 5-ALA is capable of detecting brain tumors; when illuminated under blue light, the PPIX in the glioma gives a visible red fluorescence. As a result, 5-ALA surgical guidance has

led to more complete brain tumor resection and prolonged survival as demonstrated in a phase III clinical trial (*4*). However, the 5-ALA uptake is not consistent throughout the brain tumor. In particular, the 5-ALA uptake varies at brain regions with lower metabolism, i.e., at the infiltrative cancer margins and for lower-grade gliomas (*4, 27*). As a result, 5-ALA enjoys excellent specificity (92-100%), but suffers from relatively lower sensitivity (47-84%) (*28*).

Raman spectroscopy is another relatively novel technology with promising pilot results in detecting tumor cells *in vivo* in mice and in humans. Raman spectroscopy is a technique used to identify vibrational, rotational and other low frequency modes; as a result, it can characterize tissues by observing the molecular fingerprint for tumor versus non-tumor. The intra-operative feasibility of this technology is first tested by a Canadian group in 2015 with 17 patients (*29*), and the results are promising for spot detection of brain cancer during surgical resection. Nevertheless, Raman spectroscopy is limited by a very narrow field of view at 0.00000025 mm^2 area to 1 mm^3 volume per spot. Furthermore, it has a slow scanning rate at 1 second per spot, and therefore cannot be used to scan the entire resection cavity within the surgical timeframe (*29, 30*).

CHAPTER 2:
OPTICAL COHERENCE TOMOGRAPHY

SECTION 1: OVERVIEW

Optical Coherence Tomography (OCT) is a non-invasive, label-free and cost-effective imaging technology, capable of real-time cross-sectional imaging of tissue anatomy at micron-scale resolution (*31-39*). This chapter describes the basic principles of OCT, and provides an overview of OCT's history in brain cancer and other clinical applications. Finally, this chapter compares the performance of OCT with that of other imaging modalities as shown in Chapter 1.

SECTION 2: WHAT IS OCT?

OCT is a label-free, real-time imaging technique used to obtain volumetric images of biological tissues at a resolution equivalent to a low-powered microscope (e.g., around two- to four-fold magnification). OCT can be envisioned as an optical analog of ultrasound B-mode imaging, since both techniques acquire cross-sectional images of the tissues by collecting "reflected" light or sound waves. Unlike ultrasound, however, OCT uses a near-infrared light source (instead of sound waves), and does not use any matching medium e.g. gels as used in ultrasound imaging. In addition, OCT is capable of non-contact imaging and generally acquires images at a couple of centimeters above the tissue surface, therefore reducing the risks of infection. Compared with ultrasound, OCT generally has 10-100x better resolution (at 1-15 μm) when compared to ultrasound (typically at about 150 μm), but at the expense of a poorer imaging depth (at 1-3 mm for OCT, versus 10-100 mm for ultrasound).

The principle of OCT lies upon the use of low-coherence interferometry. A typical OCT imaging setup involves a Michelson interferometer with a low-coherence, a broad bandwidth infrared light source (generated using a superluminescent diode or a femtosecond laser), and a beam splitter which splits the light to the reference and sample arms **(Figure 1)**. The biological tissue is placed at the sample arm for OCT imaging, while a mirror is placed at the reference arm; together, the reflected signals from both the reference and sample arms rejoin at the beamsplitter and are sent to the detector. The combination of signals from both arms gives rise to an interference pattern, but only if the optical pathlength difference (i.e. the difference in distances traveled by the reflected light from both arms) is less than one coherence length. In OCT, since a broad bandwidth light source is used, the interference occurs over a distance of micrometers.

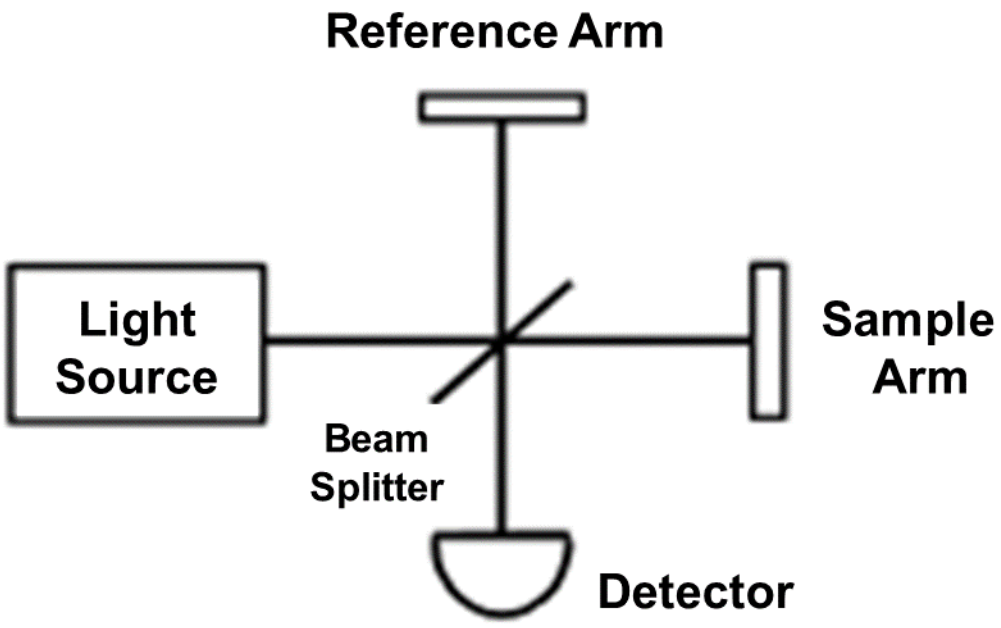

Figure 1. Basic Schematic of an OCT Imaging Setup

SECTION 3: DATA ACQUISITION AND SYSTEM SETUP

First, let us understand the basic principles in collecting spatially encoded information (in the x, y, and z directions) using optical coherence tomography.

Generally speaking, OCT collects data by acquiring A-lines (or axial scans, in the z direction) for each x-y coordinate in the tissue sample. At a given x-y position, the light incident on the sample is reflected back at different depths. The intensity versus depth forms an axial scan (A-scan). The depth-dependent reflectivity of the target tissue must be "recovered" using one of the following several mechanisms.

TIME-DOMAIN OCT

In time-domain OCT (TD-OCT), the mirror in the reference arm is mechanically shifted back and forth at a constant velocity. This results in depth-resolved information, where the optical pathlength at the reference arm (in the mirror) changes with different time points. As a result, interference signals at different time points can be matched to the OCT signal coming from a specific depth (or axial position) from within the biological tissue.

FREQUENCY-DOMAIN OCT

In frequency-domain OCT (FD-OCT), a spectrum of signals from different depths of the tissues are either sequentially or simultaneously acquired, and the OCT A-lines (or axial scans) are reconstructed using Fourier transform from the raw OCT data (*40*). Since this method does not involve any mechanical movement from the reference arm mirror, FD-OCT enjoys dramatically improved imaging speed and axial scan rate; in addition, it has superior detection sensitivity since

FD-OCT measures backreflected signal from all depths, and not piecewise along depths as is the case in time-domain OCT. As a result, FD-OCT is generally more suitable for *in vivo* clinical applications where real-time, continuous feedback is necessary for diagnostic and/or interventional purposes.

SPECTRAL-DOMAIN OCT

In spectral-domain OCT (SD-OCT), the diffraction grating disperses the light source into different optical frequencies (wavelengths), which are then refocused on the pixels of the line detector array. Since the position of the pixels on the detector can be mapped to the spatial frequency domain (i.e., K-space), a spectrum of interference signals can be generated without physically moving the reference arm mirror.

In swept-source OCT (SS-OCT), the light source emits different frequencies sequentially and at a very rapid speed. In other words, it encodes different optical frequencies temporally (as opposed to spatially as shown in SD-OCT). Consequently, the combination of the reference and sample arm signals will result in a beat frequency (i.e., in interference pattern between 2 signals with slightly different frequencies) which is proportional to the pathlength mismatch between the reference arm signal, and the sample arm signal generated each axial position (i.e. the depth or z coordinates). As a result, the A-line (or axial scan) can be generated by the Fourier transform of such a beat signal from the detector as in SD-OCT,

In summary, we have discussed the different OCT setups necessary to provide depth-encoded information (i.e. the A-lines or axial scans) in the z-coordinates. To resolve information in the x and y coordinates, the OCT imaging probe is usually equipped with some specific beam scanning mechanisms (e.g., two galvanometer-based scanning mirrors) which scans the beam to

various x and y coordinates. A single A-line is collected at each x and y coordinate visited. Consequently, the combination of all A-lines in the x and y directions form the basis for a volumetric OCT dataset.

SECTION 4: IMAGE RESOLUTION

In recent years, OCT has rapidly gained popularity as a clinical imaging tool in multiple applications including retinal imaging, intravascular imaging and breast cancer imaging. OCT functions as a form of "optical biopsy" as it provides label-free, high-speed and non-invasive imaging, all while achieving micron-scale resolution equivalent to the performance of a low-power microscope. In this section, we will briefly discuss how OCT achieves its image resolution in the axial and lateral directions.

First of all, OCT achieves its high axial resolution Δz (along the depth, or z direction) by using a broad spectral bandwidth $\Delta\lambda_{FWHM}$ for its infrared light source,

$$\Delta z = \frac{2\ln 2}{\pi} \times \frac{\lambda_c^2}{\Delta\lambda_{FWHM}}$$

where Δz is the axial resolution, $\Delta\lambda_{FWHM}$ is the spectral bandwidth of the light source, and λ_c is the central wavelength of the infrared light source.

Notably, the axial (Δz) and lateral (Δx) resolutions are decoupled from one another. In other words, the lateral resolution of the OCT imaging system is independent from its axial resolution, and is determined by the focusing power of the imaging probe in the sample arm,

$$\Delta x = \sqrt{\frac{2b\lambda_c}{\pi}}$$

where Δx is the lateral resolution, λ_c is the central wavelength of the infrared light source, and b is the confocal parameter which is defined as twice the Rayleigh range z_R of the Gaussian beam.

As a result, OCT is advantageous in that it allows for flexible OCT probe design; in other words, a carefully designed OCT imaging system can achieve its desired lateral resolution and confocal parameters without compromising its high axial resolution. In summary, the above two equations determine the image resolution for each two-dimensional OCT cross-sectional image (in the x and z directions). For OCT imaging of a three-dimensional volumetric tissue sample, the image resolution in the y direction (Δy) is further determined by the scanning rate of the galvanometer optical scanner; in other words, Δy is defined by the number of cross sectional images acquired over a 1 millimeter span in the y direction.

SECTION 5: CLINICAL APPLICATIONS FOR OCT

In this section, we will briefly describe the history of OCT in various clinical applications.

Since its introduction in the 1990s, OCT has evolved to become a powerful medical imaging technique with the unique ability to visualize the cross-sectional structures of human tissues non-invasively, at high speed, and with micron-level resolution (*41*). OCT was first used to detect the presence of retinal pathologies in the eye. Since then, multiple studies have been conducted to evaluate and validate the use of OCT in diagnosis or interventional procedures for multiple ophthalmic diseases such as glaucoma, macular edema, age-related macular degeneration, and chorioretinopathy (*42-46*). To this date, OCT is regarded as a new standard for clinical diagnosis and intervention of retinal diseases, and ophthalmology remains to be one of the most successful clinical applications of OCT.

In addition, OCT has also become extraordinarily successful in several other clinical fields, with FDA approval for imaging of the retina, artery, and esophagus. It is a promising tool for detection of atherosclerotic plaques in cardiology, as miniaturized OCT imaging catheters are capable of entering coronary blood vessels surrounding the heart, and of identifying the cholesterol-laden plaques which are prone to rupture and consequently result in myocardial infarctions (*41, 47, 48*). Furthermore, OCT is a powerful tool used in the detection of cancerous and pre-cancerous changes in the gastrointestinal tract. In particular, OCT is particularly well equipped to detect any structural changes which occur as a result of gastrointestinal lesions in the mucosal, submucosal and muscular layers. For example, OCT cross-sectional images were able to clearly identify the presence of sub-squamous Barrett's esophagus as well as the presence of dysplasia and adenocarcinoma in the human esophagus (*49, 50*). Finally, researchers are actively exploring the potential of OCT in numerous other clinical applications which include imaging of the respiratory, urinary, and reproductive systems (*51-57*).

Several studies have also begun to explore the potential in brain cancer detection, which is the central theme of this dissertation (*58-63*). For example, Boppart *et al.* performed the first OCT imaging of *ex vivo* human secondary brain cancer in 2008, where the research group has imaged a melanoma tumor mass which has been metastasized into the cerebral cortex of the patient (*58*). In 2005, Biheva *et al.* obtained the first cross-sectional OCT images of formalin fixed human brain cancer tissues such as meningioma and gangliogioma (*63*). In 2013, Assayag *et al.* performed the first *en face* OCT studies in human brain cancer specimens (*64*). Finally, Bohringer *et al.* conducted three pilot studies between 2006 and 2009 which resulted in the characterization of human primary brain cancers both *ex vivo* and *in vivo* using optical attenuation *(59, 60, 65)*.

Nevertheless, significant ongoing research is required to fully understand the potential of OCT in human brain cancer applications. As detailed in later chapters and as published (*66*), this dissertation builds upon previous studies and contributes by 1) conducting the first systematic study to compare cancer versus non-cancer brain tissues in a controlled environment using *ex vivo* human brain specimens with 32 patients and approximately 4,300 data points; 2) establishing the first diagnostic threshold for distinguishing brain cancer from non-cancer white matter by analyzing the optical attenuation of the brain tissue specimen; 3) performing the first sensitivity and specificity analysis for OCT detection of brain cancer; 4) establishing a high-resolution, color-coded optical property map which is generated in real-time and can provide direct visual cues for continuous surgical guidance; and 5) evaluating the intra-operative feasibility of our OCT and optical mapping technology by acquiring *in vivo* data in 3 human patients and also in rodent models implanted with patient-derived, infiltrative brain cancer.

SECTION 6: WHY OCT?

In summary, OCT is capable of providing high-resolution and continuous, quantitative feedback to the surgeons in real time. As a result, it attracts increasing interest in its application for brain cancer detection and resection. When compared with other imaging tools, OCT allows for deep penetration (compared to visible light or fluorescence imaging), label-free contrast, high-resolution imaging and a reasonable field of view (FOV). Most importantly, OCT is able to provide real-time, quantitative values for the optical attenuation of human brain tissues *in vivo*. As demonstrated in the data provided by this dissertation, OCT has a detection sensitivity and specificity which is superior to most existing imaging modalities (*66*). Finally, it is easy to use and provides non-contact imaging (i.e., imaging at a couple of several centimeters above the tissue surface) which minimizes infection risks for use in the operating room. **Table 1** summarizes the

performance of OCT when compared with other imaging modalities such as ultrasound, 5-ALA fluorescence, Raman spectroscopy, intra-operative MRI, and intraoperative CT.

Feature	OCT (this study)	Ultrasound	5-ALA fluorescence	Raman	iMRI	iCT
Resolution	0.004 mm^3	0.3 mm^3	0.001 mm^2	0.00000025 mm^2	3-20 mm^3	0.2 mm^3
FOV	8-16 mm^3	12,500 mm^3	75 – 2000 mm^2	0.1225 mm^3	Whole brain	Whole brain
Continuous guidance?	Yes	Yes	Yes	Yes	No	No
3D?	Yes	Yes	No	No	Yes	Yes
Numerical data?	Yes	No	Yes	Yes	No	No
Sensitivity (during and/or post-resection) (%)	92 - 100	26 – 87	47 (visual) 84 (spectrometry)	N/A (accuracy 99-100)	N/A	N/A
Specificity (during and/or post-resection) (%)	80 – 100	42 – 88	100 (visual) 92 (spectrometry)	N/A	N/A	N/A

Table 1. Comparison of different technologies in surgical guidance of brain cancer. Various technological advances have attempted to increase the surgeon's ability to identify cancer tissue, including ultrasound, 5-ALA fluorescence guided resections, Raman spectroscopy, intra-operative magnetic resonance imaging (iMRI), and intra-operative computed tomography (CT). These modalities, however, have different strengths and limitations in terms of resolution, field of view (FOV), sensitivity/specificity and the ability to provide quantitative and three-dimensional (3D) continuous imaging guidance. Optical coherence tomography (OCT) is a non-invasive, real-time, high-resolution and three-dimensional cross-sectional imaging technique that may be effective and practical at distinguishing brain cancer from non-cancer. **Table and table legends are originally from Kut *et al.*, Detection of human brain cancer infiltration ex vivo and in vivo using quantitative optical coherence tomography. Science translational medicine, 7(292), 292ra100-292ra100 (2015). Reprinted with permission from AAAS.**

SECTION 7: OVERVIEW OF OCT SYSTEM DESIGN

This chapter details the OCT system design (credited mainly to Dr. Jiefeng Xi, a former student in our group) and hardware specifications used to evaluate the feasibility of brain cancer detection in the operating room.

Several parameters should be considered in the design of an OCT imaging system which is designated for use in the operating room. First of all, to enable real-time continuous surgical guidance, the imaging system must be able to perform high-speed imaging over a relatively large tissue volume. This can be achieved by using a Fourier-domain OCT (FD-OCT) imaging system, which generally allows for higher speed imaging since no movement is required for the mirror in the reference arm. As noted in the earlier sections, there are two major types of FD-OCT imaging systems: the SD-OCT, and the SS-OCT. For this particular dissertation, a SS-OCT imaging system with at least 100 kHz is suggested for intra-operative applications.

Secondly, to ensure high-speed data acquisition, processing and display, a high speed digitizer with about a few hundred mega to 1 GigaSamples (GS) per second and a graphics processing unit (GPU) video card are also required to sustain the data stream >1 GigaByte (GB) per second. For example, for a 100 kHz SS-OCT system, 100,000 A0lines will be acquired per second. Each A-line consists of approximately 2,000 data points, which translates into 2 million data points per second, and a data rate at 400 MB per second (with 2 bytes per sample). In Chapter 3, we will also discuss the software and algorithmic related requirements for high-speed OCT imaging.

Thirdly, an infrared light source with a higher wavelength (for example, at 1300 nm instead of 800 nm) is desired as it can provide a greater imaging depth. Finally, the OCT handheld imaging

probe should be miniature (at a probe diameter of 4-26 mm, which is equivalent in size to the models for intra-operative ultrasound handheld probes), lightweight, and easy to operate. By choosing the right combination of imaging lenses and other probe parameters, it is possible to equip the OCT imaging probe with the desired specifications such as resolution, working distance, and the probe diameter and size. Further details of the OCT imaging system and handheld probe parameters can be located in the following sections.

SECTION 8: SWEPT-SOURCE OCT IMAGING SYSTEM

The results from this dissertation are primarily obtained from a home-built, swept-source OCT imaging system which is equipped with a Fourier-domain mode-locking (FDML) swept fiber laser [20, 55]. This swept fiber laser operates at a fundamental frequency of 40 kHz, but can reach a 220 kHz frequency after double buffering. Since the imaging speed of a SS-OCT system is determined by the wavelength swept rate of the laser source, a 40-220 kHz frequency means that the system is capable of imaging at a rate of 40,000 to 220,000 A-lines per second.

The swept fiber laser operates at a central wavelength of 1300 nm and at a 3dB spectral bandwidth of approximately 110-130 nm. The full bandwidth is at 150 nm, and on average, the laser source outputs over 50 mW power after amplification by a semiconductor optical amplifier (SOA) booster using the 220 kHz FDML configuration. Among the 50 mW output power, only about 15 mW will be delivered to the tissue sample through the OCT handheld imaging probe.

Using a high-speed data acquisition card (Alazar ATS9350 at 500 MegaSamples per second, 12-bit) and GPU-based signal processing, SS-OCT images can be acquired, processed, displayed and stored in real time at a speed of up to 220,000 A-lines per second, or up to 220 frames per second (fps) assuming that each frame consists of approximately 1,000 A-lines and approximately 2,000 pixels per A-line. This translates to a total of 1.2 to 2.4 seconds for the

scanning, processing and display of OCT cross-sectional data (and the optical property colormap) for an 8-16 mm^3 tissue sample (at 256 cross-sectional frames per volume) at the high-speed mode, (at around 110 – 220 frames per second). Such an imaging speed is ideal for surgical resection of the infiltrative brain cancer margins, as the usual volume resected by surgeons at a time is also about 16 mm^3 (*67*).

Figure 2 gives an overall description of the home-built swept-source OCT imaging system. In **Figure 2A**, a cabinet-sized, home-built SS-OCT imaging system was used to obtain imaging data for a systematic quantitative study involving *ex* vivo, freshly resected human brain tissues as well as *in vivo* murine model implanted with patient-derived, infiltrative brain cancer. In **Figure 2B**, a handheld imaging probe with a diameter of 12-mm and two galvanometer optical scanners (for lateral scanning in the x and y directions) was used to image the brain tissue samples. Finally, **Figure 2C** details the schematic of the SS-OCT system. First, an A-line trigger is sent from the swept fiber laser source directly to the high-speed data acquisition (DAQ) interface. Using a 95/5 optical fiber coupler, 5% of the FDML signal is tapped off from the frequency-swept laser and coupled into a Mach-Zehnder interferometer (MZI) to generate a calibration interference signal which adjusts for any asymmetry between the sample and reference arm lengths. The remaining 95% of the FDML signal is then delivered to the OCT interferometer, where a 70/30 optical fiber coupler splits and redirects the beams to sample arm and the reference arm, respectively. At the sample arm, the light beam passes through the handheld imaging probe to reach the biological tissue sample; while at the reference arm, the light beam passes through a collimator to reach the reference mirror. Any reflected or backscattered light from both arms are then directed through two fiber optic circulators and redirected to a 50/50 fiber coupler and recombined to form the OCT

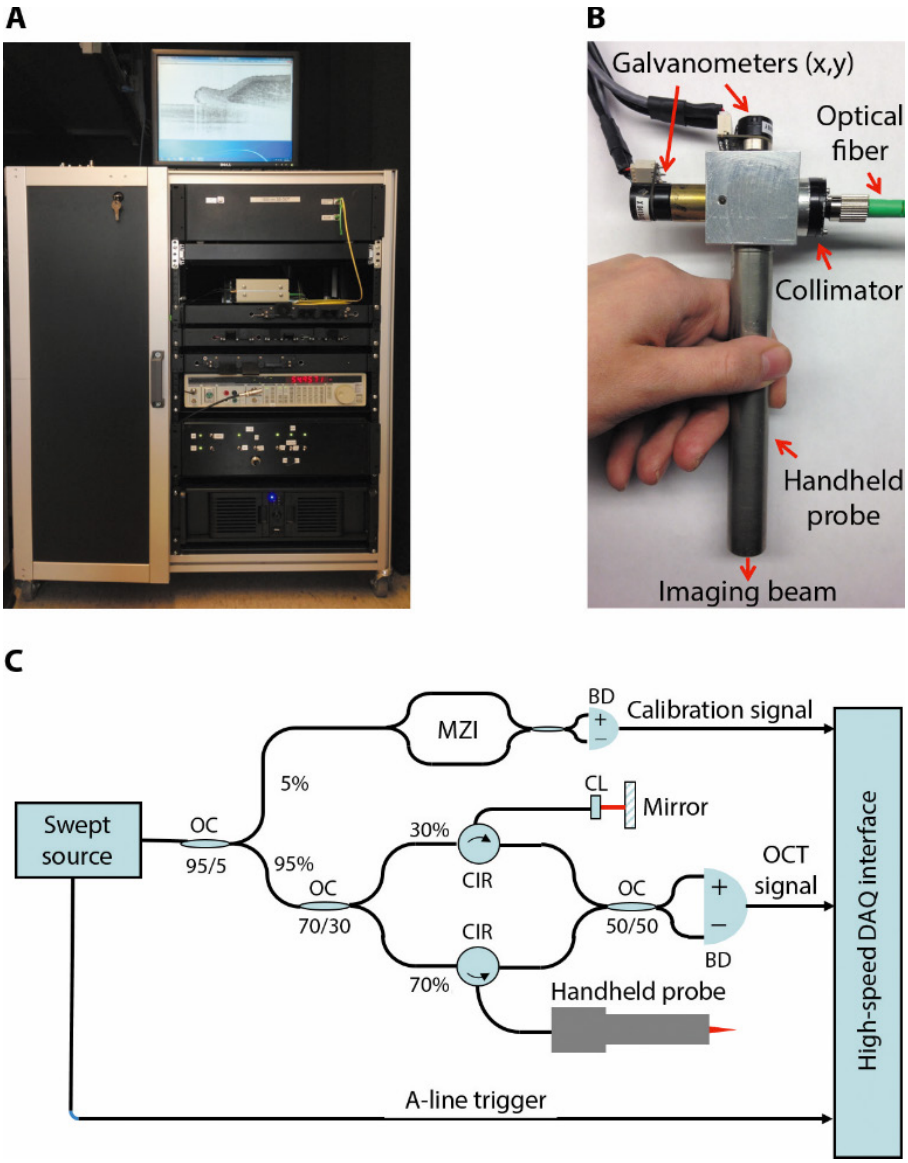

Figure 2. Swept-source optical coherence tomography (SS-OCT) system. OCT is a non-invasive, high-speed, high-resolution, cross-sectional imaging technique that may be effective at distinguishing cancer from non-cancer tissue. OCT measures reflected light (similar to B-mode ultrasound imaging). (**A**) A home-built SS-OCT system, which includes a 40-220 kHz Fourier Domain Mode Locking (FDML) swept fiber lase. (**B**) A 2D scanning handheld imaging probe were used for imaging all samples. (**C**) Schematic of the SS-OCT system. BD: balanced detector; CIR: circulator; CL: collimating lens; DAQ: data acquisition; MZI: Mach-Zehnder Interferometer; OC: optical coupler. **Figure and figure legends are originally from Kut *et al.*, Detection of human brain cancer infiltration ex vivo and in vivo using quantitative optical coherence tomography. Science translational medicine, 7(292), 292ra100-292ra100 (2015). Reprinted with permission from AAAS.**

interference signal. Notably, two circulators and a dual-balanced detector are installed in order to cancel out any excess laser noise. Finally, an OCT interferometric fringe signal is acquired by the high-speed data acquisition system and then delivered to the OCT imaging software for additional data processing and display.

In terms of imaging parameters, this SS-OCT imaging system achieves an axial resolution of approximately 6.4 μm in tissue, and a lateral resolution of approximately 15 μm in the x-y direction. Finally, the system is capable of imaging at a depth of 2.5 mm (in air) with a detection sensitivity of better than -125 dB (given an incident power in the sample arm of approximately 15 mW).

SECTION 9: ADDITIONAL SS-OCT SYSTEM FOR IN VIVO STUDY

At the beginning of this project and as described in the previous section, a cabinet-sized SS-OCT imaging system was used to obtain imaging data for the systematic quantitative study involving *ex* vivo, freshly resected human brain tissues as well as *in vivo* murine model implanted with patient-derived, infiltrative brain cancer. At the later stages of this project, however, a separate suitcase-sized SS-OCT system (aka system prototype B) was chosen instead for an overseas study in Guadalajara, Mexico, since this suitcase-sized system is more portable and better equipped for collection of *in vivo* human data from brain cancer patients in the operating room.

There is a fundamental design variation between the cabinet and suitcase sized imaging systems. For the cabinet-sized system, a calibration signal (from the Mach-Zehnder interferometer) is sent directly to the high-speed digitizer acquire the corresponding spatial frequency for each OCT data point versus time. For the suitcase-sized system, however, a K-clock generator is installed to convert the calibration signal into a digital clock signal which is uniformly distributed

in the frequency domain (i.e. K-space) to trigger OCT data digitization (*36*). This digital clock signal is then used to drives the high-speed digitizer. This reduces the need for numerical calibration algorithms (usually performed at the digitizer stage), and consequently, reduces the demand for digitization, data processing and storage speed.

For the most part, the suitcase-sized imaging system has similar operating parameters when compared with the cabinet-sized imaging in terms of axial resolution (about 6.25 μm in air), central wavelength (about 1310 nm), detection sensitivity (between than -120 dB), and average output power to the sample (about 15 mW). However, the suitcase-sized imaging system has a lower sweeping rate for its laser source (up to 100 kHz), but enjoys a better imaging depth (at 6 mm in air) when compared with the cabinet-sized system (with sweeping rate of up to 220 kHz and imaging depth of 2.5 mm in air).

SECTION 10: HANDHELD IMAGING PROBE DESIGN

A compact, handheld OCT imaging probe is used to acquire the data presented in this dissertation, and the probe is compatible with both SS-OCT imaging systems as described in the previous section. This imaging probe is small, lightweight and easy to use with a 12 mm tube diameter. The probe is forward-viewing and is equipped with two miniature galvanometer optical scanners (Cambridge Technologies ®) which is capable of scanning in the x and y directions.

The probe design involves the installment of four anti-reflection coated doublet lenses (lenses 1-4) housed in a stainless steel lens tube. First, an optical fiber directs the infrared light beam into the imaging tube. Then, the beam is collimated with an anti-reflection double-coated lens of a focal length f_1 = 11 mm (lens 1). At the next step, the beam is redirected by two galvanometer optical scanners into a stainless steel metal tube. Within the metal tube, the beam is refocused by 3 additional anti-reflection double-coated achromatic lenses with focal lengths f_2 =

25 (lens 2), f_3 = 35 (lens 3) and f_4 = 25 mm (lens 4). Furthermore, lens 2 and lens 3 are separated by a distance of 55 mm, and lens 3 and lens 4 are also separated by a distance of 55 mm. These parameters are chosen to balance the overall probe magnification (relevant to the lateral resolution), probe length, and working distance (relevant to ease of operation).

For example, the readers may recall from earlier sections that the lateral resolution is determined by the focusing power of the imaging probe in the sample arm. Based on the lens configuration provided, the overall probe magnification is given by $M = (f_2/f_1) * (f_4/f_3) = (25/11) * (25/35) = 1.6$. Considering that the mode-filed diameter of the single-mode fiber used in the OCT system is 9.2 μm, this will result in a lateral resolution of M * 9.2 μm = 14.9 μm. The probe length, on the other hand, is determined the length of stainless metal tube (55 mm + 55 mm = 110 mm = 11 cm, assuming that the lenses have negligible thickness) added to the length of the metal box used to house the two galvanometers. Finally, the working distance of the probe (i.e. the distance between the probe and the tissue surface) is determined by the focal length of lens 4, which is 2 centimeters for this particular handheld probe design. Depending on the user preference, these imaging parameters can be easily readjusted by replacing the lens configuration.

Notably, the galvanometer optical scanners are mirror-motor assemblies which are used to perform 2D (XY) scanning; in other words, it is used to move the focused beam laterally on the biological tissues in both X and Y directions. Generally speaking, a function generator (with square, ramp or sinusoidal input) is used to drive the rotatory behavior of the galvanometer mirrors and consequently redirect the beam onto a different X and Y coordinate on the biological tissue sample. Finally, an optical ray tracing simulation software such as Zemax is used to calculate the XY scanning range of the imaging probe. For this particular design, a lateral beam scanning range

of 2.5 mm can be conveniently achieved without beam vignetting (i.e. a reduction in the brightness and saturation at the image periphery), given the lens and probe configuration.

In addition, the handheld probe is easily detached. This is advantageous for two reasons: first of all, it allows users to easily change the internal lens configuration of the probe to achieve their desired imaging parameters such as lateral resolution, probe length, probe diameter and working distance; secondly, it allows for easy detachment and sterilization of the imaging probe for use in the operating room. For our particular design, the stainless tube of the handheld imaging probe is attached to the base of the galvanometers via precision threads and a locking setscrew. As a result, the tube (and the lenses inside) can be easily removed from the base for sterilization protocols.

There are two possible methods for sterilization of the imaging probe. First of all, the disassembled probe can undergo a cold sterilization method using ethylene oxide or hydrogen peroxide. Secondly, the probe can be simply wiped down with alcohol and then encased in a disposable, sterilized and FDA approved plastic sheath (which are routinely used for sterilization of the intra-operative ultrasound probes in standard neurosurgical procedures at Hopkins). Both sterilization methods are approved for routine use in the operating room.

Finally, it should be noted that the OCT infrared light source has a 1310 nm wavelength and therefore outside of the visible spectrum (i.e., invisible to the eye). In the laboratory setting, researchers use near infrared sensor cards to visualize the location of the beam on the biological tissue. In the surgical setting, however, this method is impractical and rarely practiced in the operating room. To address this issue, a green aiming beam is coupled into the handheld probe and co-registered with the near infrared OCT imaging beam. This enables the neurosurgeon to visualize the light beam and consequently pinpoint the exact location in the human brain for OCT to image. **Figure 3** demonstrates the effectiveness of the green aiming beam in *ex vivo* imaging of

freshly resected human brain cancer (*66*), *in vivo* imaging of a rodent model implanted with patient-derived brain cancer (*66*), and finally, *in vivo* imaging in a human high-grade brain cancer patient.

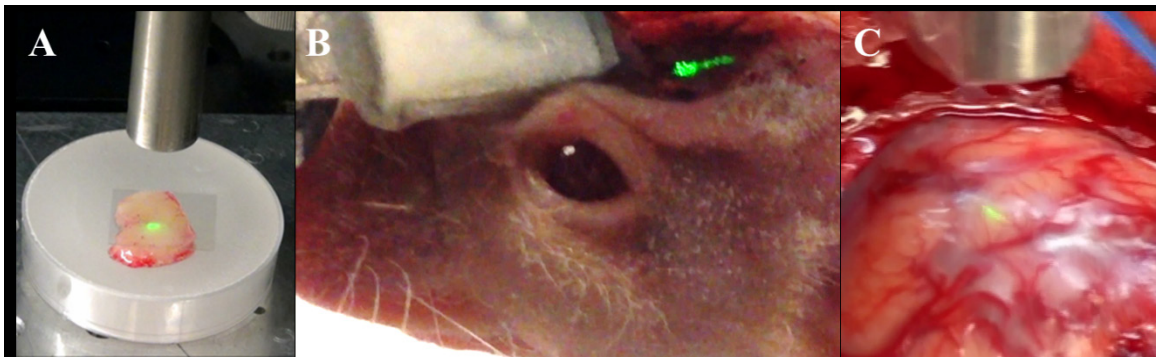

Figure 3. Green aiming beam for OCT imaging for (A) *ex vivo* in freshly resected human brain cancer tissue (high-grade glioma); **(B)** *in vivo* in a mouse with patient-derived high-grade brain cancer (GBM272) and **(C)** *in vivo* in a high grade brain cancer patient. The green aiming beam in the figures delineated the OCT field of view (FOV) at approximately 2 mm × 2 mm × 1.8 mm on the biological tissue sample (in the x, y, and z directions, respectively). **Figures 3A and 3B are adapted from Kut *et al.*, (2015). Detection of human brain cancer infiltration ex vivo and in vivo using quantitative optical coherence tomography. *Science translational medicine*, *7*(292), 292ra100-292ra100. Reprinted with permission from AAAS.**

CHAPTER 3:
OCT SOFTWARE AND ALGORITHMS

SECTION 1: OVERVIEW

This chapter details the OCT software and the algorithms implemented for brain cancer detection. More specifically, this chapter will discuss the overall layout of the home-built C++ OCT software program, and then focus on the particular theories and algorithms used to extra the optical properties from biological tissues for cancer margin detection.

SECTION 2: BASIC IMAGING SOFTWARE

In this dissertation, basic OCT data acquisition, processing and displayed are performed on a Windows® operating system using a C++ based software program which is developed in the laboratory over the years (http://bit.bme.jhu.edu).

The C++ software program includes a graphical user interface and can be used to perform the following functions: 1) it controls and synchronizes the hardware components such as the high-speed digitizer and galvanometer optical scanners; 2) it acquires, processes, displays and stores OCT data in real-time; and 3) it synchronizes the data flow between the central processing unit (CPU) and the graphics processing unit (GPU).

The overall workflow of the OCT software is described in the PhD dissertation by Jiefeng Xi, PhD in our group (the Biophotonics Imaging Technologies, or BIT, Laboratory), and is summarized as follows. Essentially, the program includes 5 major modules (#1 to #5). First, a data acquisition module (Module #1) is used to control the hardware components of the OCT imaging,

and to acquire raw OCT signals from the OCT imaging system. Then, the OCT raw data is first saved in the data storage module (Module #2). At the same, time, the raw OCT data is also sent to the data processing module (Module #3) where the raw OCT data undergoes Fourier transforms and basic image processing (such as image filtering, image calibration and contrast/brightness adjustments). In addition, more advanced processing algorithms (such as *en face* imaging, Doppler imaging, and attenuation mapping) are also performed in this module. The processed images are then displayed onto the computer screen using the image display module (Module #4). Finally, the core module (Module #5) synchronizes and manages the data flow among all the other existing modules (i.e. Module #1 to #4). The core module, in return, receives input from the graphical user interface (GUI) which is implemented to seek real-time user feedback in the specification of various imaging parameters during imaging.

While the core architecture of the data processing module is housed in the central processing unit (CPU), much of the data is actually directed into the graphics processing unit (GPU) to significantly reduce the computational time. In particular, GPU programming (also known as parallel programming) is particularly powerful for functions which require simple but repetitive operations for a large volume of data. As a result, GPU programming is highly beneficial for OCT imaging, since the average data size is large (at about 2 gigabytes with a total of about 512,000,000 A-lines collected for a 10 mm^3 tissue sample in approximately 1-2 seconds). Furthermore, most processing algorithms for OCT required simple operations. For example, some algorithms are applied individually to each of the A-lines within the dataset (e.g. summation functions to compute the *en face* map). Other algorithms are applied to a small subset of the A-lines at a time (e.g. averaging and fitting functions). Thanks to the GPU speedup and to the high-speed hardware components, the OCT imaging system is able to acquire, process, display and store data in real-

time at a rate of 40 – 220 frames per second (fps). At the high-speed mode (about 110 to 220 fps), the program is able to scan, process, and display both the OCT cross-sectional data and any additional processing results (e.g. *en face*, Doppler and attenuation) at a speed of 1.2 to 2.4 seconds for a 8 – 16 mm^3 tissue sample.

The following sections will now focus on the theory and algorithms behind the development of the optical attenuation mapping method.

SECTION 3: CALCULATION OF THE OPTICAL ATTENUATION COEFFICIENT USING A PHANTOM CALIBRATION METHOD

Once the OCT software acquires a raw imaging dataset, several basic processing steps are performed. First, the dataset is calibrated using the signal from the Mach-Zehnder interferometer. This can be achieved either by using a calibration algorithm to map all the data uniformly onto the K-space (e.g. by tracking the extrema values of the calibration signal), or alternatively, by implementing a uniform K-space sampling method (e.g. K-clock generator). Then, a fast Fourier transform (FFT) operation was performed on the calibrated data. Finally, the dataset is averaged laterally for speckle suppression (generally for every 300 – 500 A-lines, with a step size of 30 – 50 A-lines as described in **Figure 1**). The resultant OCT intensity signal profile can be described by the following equation (*68*):

$$I(z) = k\sqrt{\mu_{bs}}\, e^{-\mu_t z}\, h(z), \qquad (1)$$

where $I(z)$ is the OCT signal profile versus depth z (in mm), k is the system constant, μ_t and μ_{bs} are the optical attenuation and backscattering coefficients, respectively, and $h(z)$ is the geometric factor of the imaging beam (which has a Gaussian beam profile).

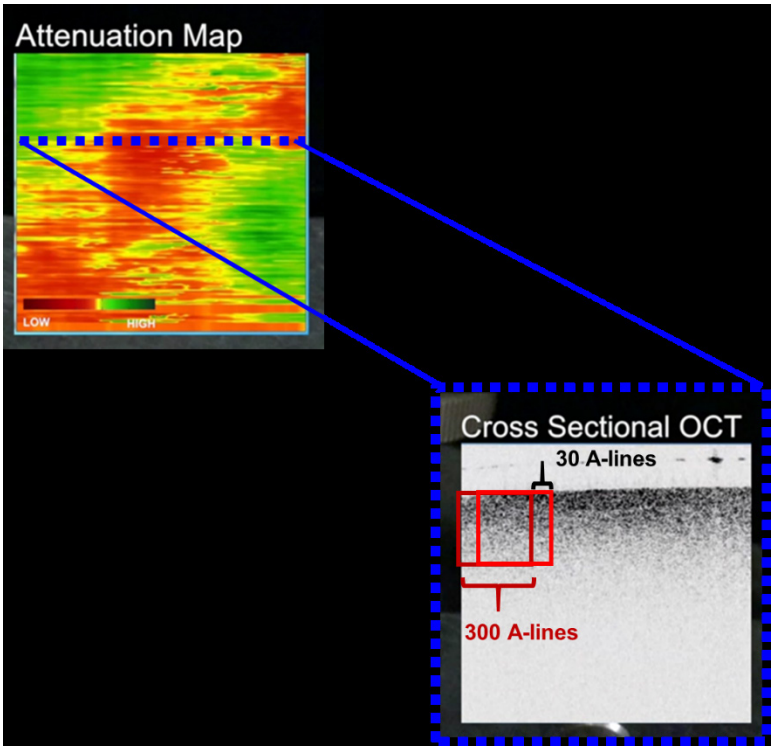

Figure 1. Averaging window for computation of optical attenuation properties. First of all, the attenuation map represents the attenuation values for a volumetric tissue sample with approximately 2000 A-lines in the x direction, 200 frames in the y-direction, and approximately 2000 pixels per A-line in the z-direction. Thus, each cross-sectional OCT frame (i.e., the dotted blue frame shown in the bottom right) contributes to a single horizontal line of attenuation data in the attenuation map (i.e., the dotted blue line on the attenuation map). To obtain the attenuation values for each pixels, we take the data from approximately 300 A-lines and average them laterally. Then, we fit the averaged intensity data to obtain an attenuation data, and shift the averaging window laterally by approximately 30 A-lines (i.e. moving from the magenta to the bright red rectangle). The fitting process is repeated, until we obtain approximately 50 attenuation data points for each cross sectional OCT frame. **Figure is modified from materials in Kut *et al.*, Detection of human brain cancer infiltration ex vivo and in vivo using quantitative optical coherence tomography. Science translational medicine, 7(292), 292ra100-292ra100 (2015). Reprinted with permission from AAAS.**

To extract the optical attenuation coefficient using **Equation (1)**, we need to solve the equation with 3 unknowns (k, μ_t and μ_{bs}) and a function $h(z)$. However, multi-parametric fitting is extremely difficult and often results in large errors in the estimation of the unknowns.

In order to overcome the challenges of multi-parametric fitting, a method (*68*) was introduced in 2013 which removes the influence of the depth-dependent effects of the beam profiles h(z). Furthermore, this method allows users to accurately assess the μ_t coefficient while removing the influence from the other two unknowns (k and μ_{bs}). This method is summarized as follows in the following paragraphs.

First of all, gelatin phantom is embedded with silicon dioxide (SiO_2) nanospheres with an average diameter of 180 ± 20 nm and a pre-specified concentration. Since the diameter of the nanospheres are significantly smaller than the wavelength (at 1310 nm), the Rayleigh theory can be used to estimate the optical attenuation coefficient (μ_t) of the silicon oxide phantom(*69*).

As an example, we estimate the following parameters for a silicon oxide phantom with 180 nm diameter nanospheres and a concentration of 50 mg/mL in the laboratory setting:

Averaged diameter of the nanospheres (2a) = 180 nm

Wavelength in vacuum (λ) = 1310 nm

Refractive index of the nanospheres (n_s) = 1.45 @ 1300 nm for SiO_2

Refractive index of the background (n_b) = 1.32 @ 1300 nm for H_2O

Specific weight of nanosphere (ρ_s) = 2.648 g/cm^3 for SiO_2

Concentration of nanospheres by weight (C) = 50 mg/mL = 50 mg/cm^3

Using these parameters, we can predict the propagation constant (k_p) in the background medium, relative refractive index (n_{rel}), polarizability (α), scattering cross section (σ), mass of sphere (m) and the number density of scatterers (N_s) by the following equations (*69*):

$$k_p = \frac{2\pi n_b}{\lambda} = 6.3311 * 10^6\ m^{-1}$$

$$n_{rel} = \frac{n_s}{n_b} = 1.0985$$

$$\alpha = a^3 * \frac{(n_{rel}^2 - 1)}{(n_{rel}^2 + 2)} = 4.6984 * 10^{-23}\, m^3$$

$$\sigma_s = 8\pi * k_p^4 * |\alpha|^2 * (\frac{1}{3}) = 2.9713 * 10^{-17}\, m^2$$

$$m = \rho_s * \frac{4}{3} * \pi * a^3 = 7.5364 * 10^{-15}\, gram$$

$$N_s = \frac{C}{m} = 6.6345 * 10^{18}\, m^{-3}$$

Finally, the attenuation coefficient (μ_t) is the sum of the absorption coefficient (μ_a) and the scattering coefficient (μ_s). Using the above parameters and estimating the absorption coefficient of water to be 0.135/mm, we can compute both the scattering and attenuation coefficients to be:

$$\mu_s = \sigma_s * N_s = 0.197\, mm^{-1}$$

$$\mu_t = \mu_s + \mu_a = 0.197\, mm^{-1} + 0.135\ mm^{-1} = 0.3\ mm^{-1}$$

As a result, we have computed the attenuation coefficient to be approximately 0.3 mm^{-1} for a silicon oxide phantom with an averaged diameter of 180 nm and a concentration of 50 mg/mL using the Rayleigh theory. Notably, the Rayleigh theory is only applicable if the diameter of nanospheres is significantly smaller than the laser source wavelength. Additional simulations using the Mie theory gives compatible estimates of the optical attenuation results as shown in the above example. Based on previous calibration studies, the attenuation coefficient of the silicon oxide nanospheres matched very well with both Rayleigh and Mie theory predictions (*18*).

As a result, the attenuation coefficient for the phantom can be accurately calculated using the aforementioned formulas and simulations. Recall from **Equation 1** that the OCT intensity signal can be characterized by $I(z) = k\sqrt{\mu_{bs}}\, e^{-\mu_t z}\, h(z)$. By normalizing the OCT signal from the tissue sample $I_b(z)$ with the one from the silicon oxide phantom $I_p(z)$, the attenuation coefficient

μ_{t_b} for each section from biological sample can be efficiently and accurately calculated by linear regression using the following equation:

$$\ln \frac{I_b(z)}{I_p(z)} = C + (\mu_{t\_p} - \mu_{t\_b}) * z, \qquad (2)$$

where $I_b(z)$ and $I_p(z)$ are the averaged OCT signal values of the biological tissue and phantom at a depth z (in mm), and C is a depth-independent constant. μ_{t_p} and μ_{t_b} are the attenuation coefficients of the phantom and biological tissue, respectively (*66, 68*).

To summarize, the phantom calibration method allows the user to accurately and expediently extract the attenuation coefficient without the need for multi-parametric fitting. Since the phantom construction and calibration steps can be performed prior to the imaging procedure, this method is ideal for *in vivo* intra-operative application which requires high-speed and often real-time computation of a tissue's optical attenuation properties.

SECTION 4: COMPARISON OF THE FOURIER DOMAIN, LOG-AND-LINEAR, AND EXPONENTIAL FITTING METHODS

As demonstrated in **Equation 1**, the optical attenuation coefficient is generally calculated by assuming a single scattering model, i.e. the exponential decay of light intensity in a homogeneous tissue sample along depth. Traditionally, the attenuation coefficient is obtained by using one the following two fitting methods: 1) an exponential fitting method (EF), which is very accurate but time-consuming as it involves an iterative computational step; and 2) a log-and-fitting method (LF) as shown in **Equation 2**, which first takes the natural log of the OCT signal profile and then performs linear fitting of the resulting dataset. This method is fast, but more prone to the effects of multi-scattering if the tissue is heterogeneous and/or highly scattering. As a result, a novel frequency domain (FD) method was developed to enable fast and robust characterization of the

attenuation coefficient, especially for *in vivo* clinical applications where the tissue surface is uneven and subject to motion artifacts (*70*).

After some algebra and Fourier transforms, the optical attenuation coefficient can be derived from **Equation 2** by comparing the amplitude of any two harmonic coefficients in the frequency domain. For example, the optical attenuation can be calculated by taking the ratio of the DC component with the first harmonic coefficient,

$$\beta = \frac{|F(\kappa=0)|}{\left|F(\kappa=\frac{2\pi}{N\cdot\Delta z})\right|} = \frac{\sqrt{\kappa^2+(\mu_{t,b}-\mu_{t,p})^2}}{(\mu_{t,b}-\mu_{t,p})} \quad (3)$$

where κ is the spatial frequency, *Δz* is the pixel size along depth, and *N* is the total number of data points (i.e. pixels) for each A-line. This FD method originated from the frequency domain method used to compute fluorescence lifetime in the microscopy field (*71*), and has been modified for the purposes of this dissertation. For discrete time sampling, the A-line data can be described (as opposed to *I(z)* when there is continuous time sampling). In this scenario, the amplitude of any harmonic coefficients (denoted by the order m) can be computed by the following

$$F(\kappa = m*\omega_0) = \left|\sum_{n=0}^{N-1} I(n\cdot\Delta z)\, e^{-i\kappa*n*\Delta z} by\, I(n\cdot\Delta z)\right| \quad (4)$$

where $\omega_0 = 2\pi/(N\cdot\Delta z)$ is the fundamental spatial frequency, and $n = 0\ to\ N-1$ denotes the sequential index for the A-line data by $I(n\cdot\Delta z)$ during discrete time sampling.

As a result, we can obtain the relative attenuation coefficient term, $\mu_{t,b} - \mu_{t,p}$ using **Equations 3 and 4**. Since the phantom attenuation coefficient $\mu_{t,p}$ is known, we are able to reliably and quickly extract $\mu_{t,b}$, the optical attenuation coefficient for biological tissues.

Additional studies have also been conducted to compare the performance of the frequency domain (FD) method versus the exponential fitting (EF) and log-and-linear fitting (LF) methods (*70*). In terms of speed, a benchmark test was performed using a dataset with approximately 524,000 A-lines (2048 Alines per frame x 256 frames). As shown in **Figure 2A**, the FD method and LF method have comparable

computational speeds, as both methods are able to process 524,000 A-lines in under 1 second using CPU-based Matlab programming (i.e., without GPU programming). Both FD and LF methods are significantly faster than the EF method, which takes approximately 22 times longer to process an idential dataset.

In terms of robustness, the FD method is found to be more robust against multi-scattering when compared with the LF and EF methods. While all the equations presented in this section have assumed a single scattering model, it is necessary to understand that multi-scattering occurs in real-life conditions. Generally speaking, the probability of multi-scattering increases when 1) the tissue is heterogeneous in nature; 2) when the tissue has a high attenuation coefficient; and 3) when the attenuation coefficient is computed using a larger fitting length (along the z-direction). As shown in **Figure 2B & C**, the fitting methods were compared against one another for their robustness against multi-scattering(*70*). A silicon oxide phantoms were used for this study. Three different regions of interests were selected based on their attenuation results (which are approximately 3 mm^{-1}, 5 mm^{-1}, and 7 mm^{-1}, respectively). When the region of interest has low attenuation (at 3 mm^{-1}), all three methods (FD, LF and EF) seemed to be equally robust against multi-scattering as the fitting length increases along the z-direction. When the region of interest has a medium attenation (at 5 mm^{-1}), the LF method becomes susceptible to the effects of multi-scattering and exhibited large fluctuations in its attenuation estimates as the fitting length increases. In contrast, the EF and FD method remains fairly robust against the multi-scattering effects as the fitting length increases. Finally, when the region of interest has a high attenuation (at 7 mm^{-1}), the LF method suffered a 35% reduction in its estimation of the the attenuation coefficient at a fitting length of 1200 data points. In comparison, the FD method experienced a 20% reduction in its estimation of the attenuation coefficient, while the EF method remains the most robust against multi-scattering effects.

Finally, we evaluated the robustness of the 3 methods when the tissue surface detection is inaccurate. As shown in **Figure 2B**, we displayed the averaged intensity signal I(z) for a region of interest with approximately 3 mm^{-1} attenuation when the tissue surface is detected accurately (i.e. the blue line) and again when the tissue surface detection is incorrectly detected (i.e. the magenta line as shown in the image). When the tissue surface detection is incorrect, **Figure 2D** demonstrated how both the EF and LF methods suffers by exhibiting large errors in their estimation of the attenuation coefficient. In fact, even negative attenuation coefficients were found with both the EF and EF methods when the surface detection is incorrect. In contrast, the FD method is

considerably more robust and produced attenuation coefficients which are much closer to its true value at 3 mm^{-1}. As a result, the FD method is desirable for *in vivo* and high-speed applications, where the experimental subject often undergoes complex motions as a result of respiratory motions heartbeat and other voluntary or involuntary bodily movements.

As a matter of fact, we predicted that the FD method will provide more reliable results when the tissue surface detection is inaccurate. Since our derivations assume a single scattering model, we can get the depth-dependent OCT signal with a single exponential decay by dividing the sample OCT signal $I_s(z)$ with the reference phantom OCT signal $I_r(z)$ in **Eq. (2)**:

$$\ln \frac{I_b(z)}{I_p(z)} = C + (\mu_{t\_p} - \mu_{t\_b}) * z,$$

where $C = \sqrt{\mu_{bs}^s / \mu_{bs}^r}$ is a constant, $\mu = \mu_{ext}^s - \mu_{ext}^r$ is the attenuation coefficient, and z is the depth. To derive μ, we can calculate the Fourier transform of **Eq. (4)**:

$$F(k) = \int_0^\infty C \cdot e^{-j.k.z-\mu \cdot z}\, dz = \frac{C}{j \cdot k + \mu} \qquad (5)$$

where κ is the frequency in space. The optical attenuation coefficient μ can be derived by comparing the DC component with the module of first harmonic coefficient, i.e.

$$\frac{|F(k=0)|}{\left|F(k=\frac{2\pi}{N \cdot \Delta z})\right|} = \frac{\sqrt{k^2+\mu^2}}{\mu} \qquad (6)$$

where Δz is the pixel size along depth and N is the total number of data points (i.e. pixels) per A-line. When the sample surface is not correctly detected, it equivalents to a spatial shift in z and the corresponding Fourier transform of **Eq. (4)** is:

$$F(k) = \int_{z_0}^\infty C \cdot e^{-j.k.z-\mu \cdot z}\, dz = \frac{C}{j \cdot k + \mu} e^{-(j \cdot k + \mu) \cdot z_0} \qquad (7)$$

To derive the optical attenuation coefficient μ by comparing the DC component with the module of first harmonic coefficient of **Eq. (7)**, we can reach the same result as **Eq. (6).** Thus, we find that in theory, FD method gives robust results even if surface detection is inaccurate.

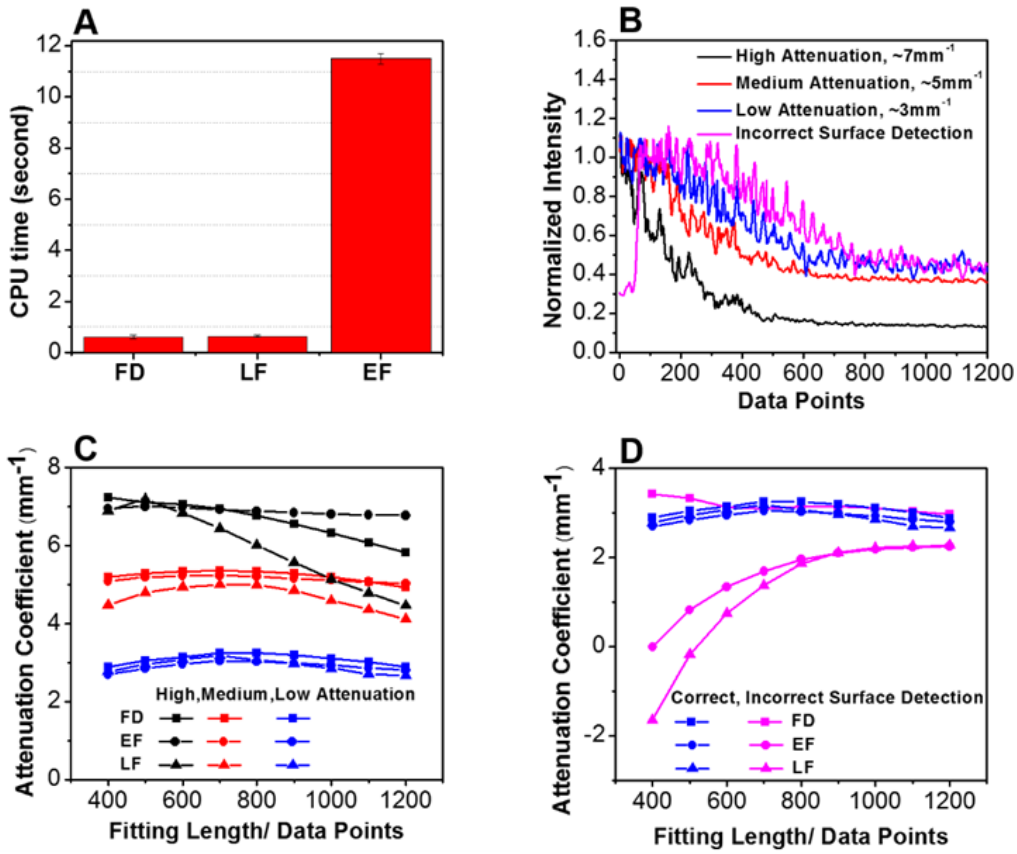

Figure 2. (A), CPU time required to process a dataset with approximately 2048 A-lines/frame * 256 frames using the Fourier domain (FD), linear fitting (LF), and exponential fitting (EF) methods. **(B)**, representative OCT averaged intensity signals I(z) with high (black line), medium (red line) and low (blue line) attenuation coefficients. Magenta line shows the same I(z) at low attenuation coefficient (blue line), but with incorrect tissue surface detection. **(C) and (D),** using the same averaged intensity signals as shown in (B), the attenuation coefficients were calculated using the FD (rectangles), EF (circles) and LF (triangles) methods as the fitting window length (i.e. the number of data points in the z direction) increases. **Figure and figure legends originally published by Wu Yuan, Carmen Kut, Wenxuan Liang & Xingde Li (2016). Ultrafast and robust characterization of OCT-based optical attenuations using a novel frequency-domain algorithm. Biomedical Optics Express (To be submitted).**

SECTION 5: ADDITIONAL ALGORITHMS FOR IN VIVO IMAGING

In order to reliably extract optical attenuation coefficients in *in vivo* surgical applications, there are several major challenges to overcome: 1) the uneven topology of the *in vivo* brain (as opposed to the flat surface of sectioned *ex vivo* tissues in the laboratory); 2) the presence of blood pooling on

top of the tissue surface during the resection procedure; 3) the presence of aliasing artifacts due to the limited imaging depth of the OCT imaging system; and finally, 4) the need for real-time and intuitive display of the optical attenuation data throughout the surgical resection procedure.

To overcome the uneven topology of the *in vivo* brain, a peak detection algorithm is implemented to automatically analyze the OCT signal profile and identify the tissue surface along the x-direction. Additionally, the algorithm also needs to be optimized for the identification between the blood and tissue layers during surgical resection. **Figure 3** illustrates how the peak detection algorithm overcomes the uneven topology and the presence of blood on the brain surface.

Furthermore, the uneven topology of the brain surface also led to the presence of aliasing artifacts, which were produced when the upper part of the brain surface moves outside of the OCT imaging depth (which is 1.8 mm in the cabinet-based FDML SS-OCT system, and 6 mm in the suitcase-sized K-clock SS-OCT system). When this occurs, the upper part of the brain surface will appear "folded" into the image after OCT signal processing (involving fast Fourier transform, or FFT). In those cases, the artifacts do not reflect the true optical property of the tissue and should be cropped out of the image. **Figure 4** provides an example of aliasing artifact in *in vivo* mice.

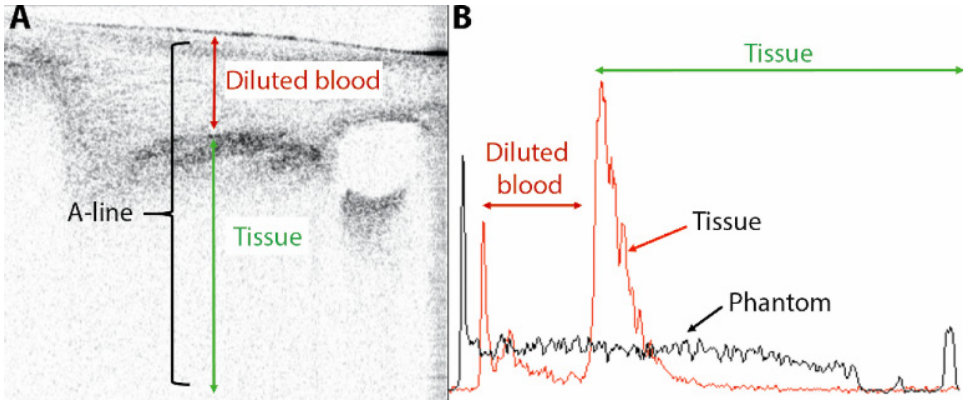

Figure 3. Automated peak detection algorithm to separate diluted blood from brain tissue signals. During surgical resection *in vivo,* we applied saline solution to dilute the blood pool accumulated within the resection cavity. (**A**) The resulting cross-sectional OCT image. (**B**) The corresponding OCT signal for an axial-line (A-line). In this study, an automated peak detection algorithm was implemented to distinguish between the diluted blood (red arrows) and the tissue signals (green arrows) along the same A-line. **Figure and figure legends are originally from Kut *et al.*, Detection of human brain cancer infiltration ex vivo and in vivo using quantitative optical coherence tomography. Science translational medicine, 7(292), 292ra100-292ra100 (2015). Reprinted with permission from AAAS.**

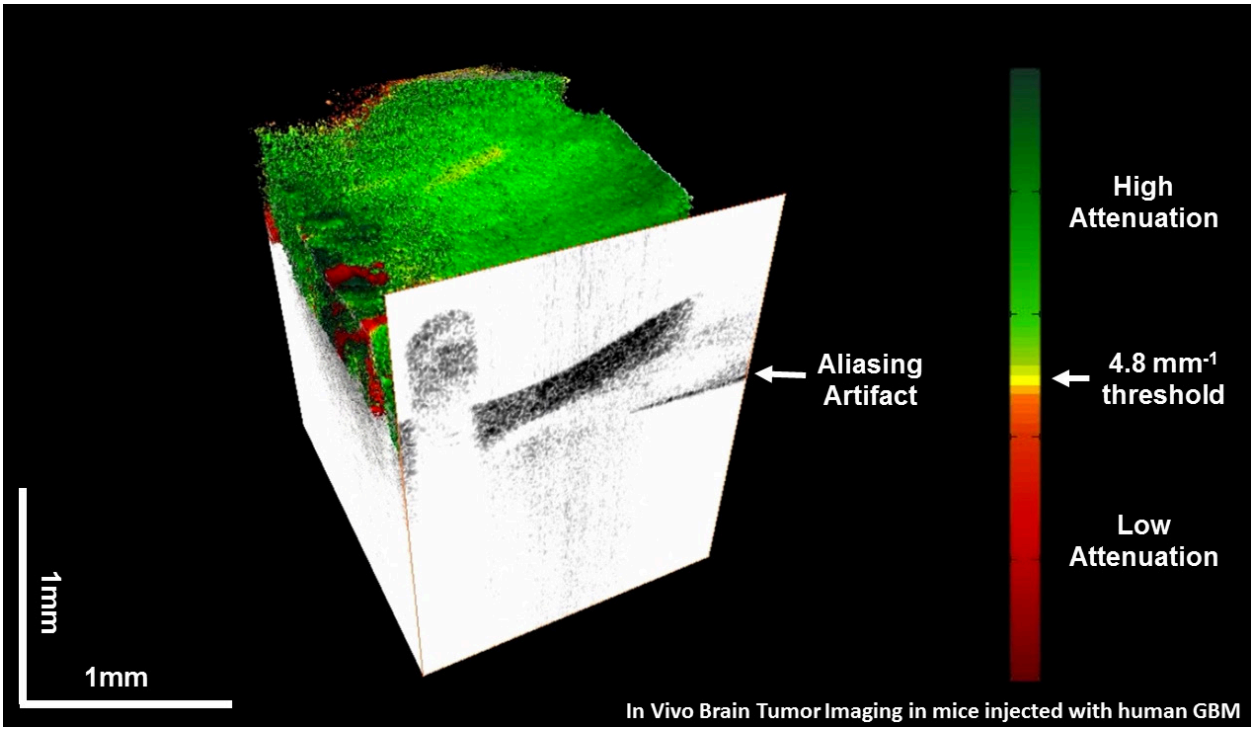

Figure 4. Aliasing Artifacts during *in vivo* imaging of brain tumor in mice. Aliasing artifacts are produced when the brain topology is so uneven such that the upper portion of the brain is "folded" back into the image since it is outside of the OCT imaging depth.

Finally, we need to provide a real-time and intuitive display of the optical attenuation data. Given the time and safety consideration in the operating room, it will be impossible for the surgeon it down and carefully study the numerical data for each image pixel before making his/her surgical decision. To combat this challenge, we have developed a novel optical property mapping method to provide real-time, color-coded and intuitive visual cues to the surgeons continuously throughout

the surgical resection procedure. Using this optical property mapping method, the cancer tissues will be displayed in red and the non-cancer white matter will be displayed in green. Infiltrative areas, on the other hand, will be displayed as yellow.

The optical mapping protocol is described as follows:

First, the OCT imaging system scans a three-dimensional brain region at a volume of approximately 8 mm^3 per scan. Over 524,000 A-lines are collected for each OCT dataset obtained (at 2048 A-lines per frame X 256 frames).

Secondly, the OCT signal profile is averaged laterally (in the x-direction) with a window of approximately 300 A-lines (i.e. ~0.3 mm in the spatial coordinates) and a step size of approximately 30 A-lines (i.e. ~0.03 mm in the spatial coordinates). Since the y resolution is defined by the number of cross-sectional frames obtained (i.e., 256 frames for a 2-mm span) and the z resolution is defined by the OCT imaging depth (i.e., 1.8 mm in tissue), the three-dimensional resolution of the optical mapping method is therefore 0.03 mm X 0.008 mm X 1.8 mm for the scanned volume (in the x, y and z dimensions, respectively).

Thirdly, the OCT data undergoes additional processing to combat the effects of brain motion, blood flow, and uneven tissue surfaces in *in vivo* applications. For example, thresholding and peak detection algorithms can be implemented to pinpoint the beginning depth of the tissue surface and to ignore the presence of blood pooling on top of the tissue surface. These algorithms are sequentially performed on the averaged OCT signal profiles (each representing approximately 300 A-lines of the OCT imaging data). After optimization, the beginning depth for each averaged OCT signal profile is recorded in terms of its pixel coordinates along the z direction.

Next, the phantom calibration technique is applied using a pre-recorded dataset obtained from a silicon oxide with known nanospheric diameter and concentration.

Then, fitting methods are applied to extract the attenuation coefficient from the averaged OCT signal profiles. Generally speaking, the fitting method is not applied to the entire length of the OCT signal profile (in the z direction). Rather, a fitting length (e.g. 400 to 800 pixels) is specified to minimize the computational time and also to reduce the effects of multi-scattering.

Finally, the program will output an *en face* attenuation matrix (with 52 x 256 pixels in the x and y directions). Each of the pixel values in this matrix represents the attenuation coefficient for the OCT signal profile located at the specific x and y coordinates. Using this matrix, a pseudo-colormap can be generated where cancer is coded in red, non-cancer white matter is coded in green, and infiltrative cancer margins are coded in yellow.

Figure 5 summarize the general protocol required to generate an optical property map for a volumetric OCT dataset. With GPU CUDA-based programming, it is possible to accomplish all of the above steps in approximately 1-2 seconds for the entire dataset.

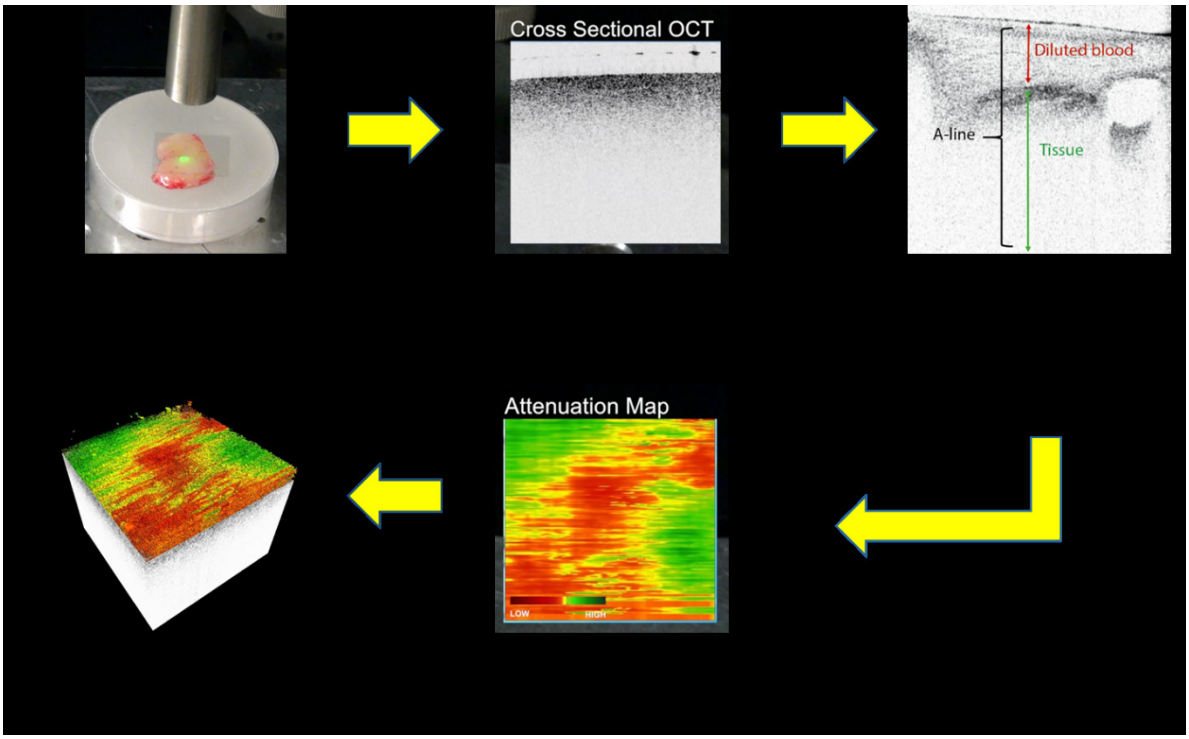

Figure 5. Protocol used to generate an optical property map for an *ex vivo*, freshly resected human brain cancer tissue. The OCT hardware is capable of acquiring up to 220,000 A-lines per second (after double buffering). Generally, up to 110 – 220 cross-sectional OCT frames are obtained per second from the three-dimensional tissue sample. Once a 3D dataset is obtained, data processing steps include phantom calibration and fitting, speckle suppression and blood and motion detection. If GPU-based CUDA programming is implemented, the C++ based software is capable of acquiring the *en face* attenuation map at a speed of 0.0025 seconds per frame, i.e. around 1.2 to 2.3 seconds per 8 – 16 mm^3 tissue block. **Figure is modified from materials in Kut *et al.*, Detection of human brain cancer infiltration ex vivo and in vivo using quantitative optical coherence tomography. Science translational medicine, 7(292), 292ra100-292ra100 (2015). Reprinted with permission from AAAS.**

SECTION 6: MATLAB CODE FOR OPTICAL PROPERTY MAPPING

For OCT software development, the MATLAB platform is generally used for debugging and code optimization before any new algorithms are introduced to the stable version in C++.

Figure 6 describes the overall workflow for the home-built MATLAB optical property mapping software. First, the software reads the raw OCT dataset and performs fast Fourier transform. If a FDML imaging system is used, the software will also need to perform an extra calibration step which maps all the data uniformly onto the K-space (i.e., by tracking the extrema values of the calibration signal captured by the Mach-Zehnder interferometer). Then, a core function is used to synchronize the data flow among different functions. First, the imaging parameters are specified prior to data processing. Then, different algorithms are implemented for tissue surface detection, removal of blood artifacts, phantom calibration and finally fitting and extraction of the optical attenuation coefficients. Finally, the processed dataset and the resultant attenuation matrix is returned to the core function, which performs the final step in the protocol: generating a pseudo-colormap for the attenuation matrix (known as the optical property map). The map is then graphically display in MATLAB. The imaging parameters, processed data, attenuation map and optical property maps are subsequently saved and stored in the Windows or OS based operating system.

The MATLAB software is generally used for debugging and code optimization for several reasons: (1) MATLAB has excellent documentation support and built-in functions for handling large data matrices and images; (2) MATLAB facilitates the debugging process by enabling the user to perform benchmark tests and output the value of any variables in the midst of data processing; (3) MATLAB has excellent graphical capabilities which enables mapping, display and storage of the color-coded optical property map with minimum coding necessary. Nevertheless, MATLAB has a major disadvantage as it suffers from long computational times and cannot be readily used for real-time applications. For example it generally takes about 100 – 200 seconds to obtain the attenuation map from a standard volumetric OCT dataset using the MATLAB platform,

but only about 1 – 2 seconds using the C++ platform. In addition, it will not be feasible to acquire, process, display and store all OCT data in real-time using the MATLAB platform, especially in conjunction with a graphical user interface (GUI) and other additional algorithms (e.g. Doppler and *en face* mapping). For this reason, any new algorithms are eventually translated onto the C++ platform, where a stable release of the OCT software is generated and updated periodically throughout the code development process.

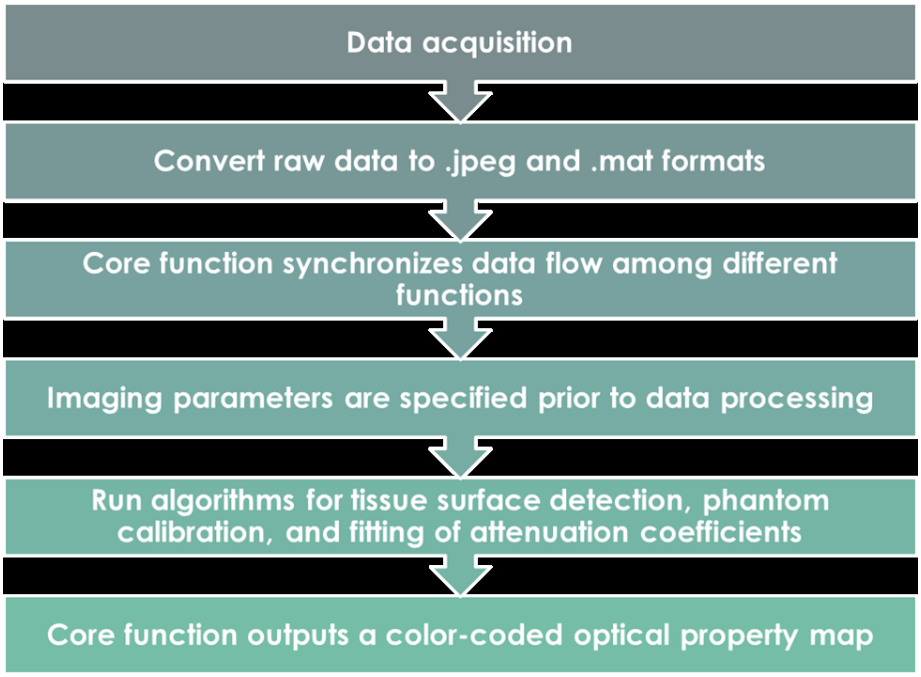

Figure 6. Workflow of the MATLAB software for optical property mapping.

SECTION 7: C++ CODE FOR OPTICAL PROPERTY MAPPING

The final section of this chapter discusses the C++ code for optical property mapping.

There are three major differences between the MATLAB and C++ versions. First of all, the C++ platform contains a considerably larger software architecture which also houses other OCT imaging modules including Doppler imaging and *en face* imaging. Secondly, the C++

platform is linked to the OCT hardware and acquires data in real-time (as opposed to the MATLAB platform where pre-recorded OCT datasets are fed into the software for post-processing); and thirdly, GPU-based CUDA programming must be implemented to maintain the computational speed of the C++ software. Currently, the OCT hardware is capable of acquiring, processing, displaying and storing data in real-time in approximately 1 to 2 seconds for each 8-16 mm^3 tissue block. As a result, the optical mapping algorithm must operate at an equal or faster speed to maintain the same level of computational efficiency.

Figure 7 describes the overall workflow for the home-built C++ code for optical property mapping. First, we take advantage of the existing OCT software architecture which already calibrates and performs fast Fourier transforms on the raw OCT dataset by default. If the user selects the attenuation module, the data will then be automatically transferred from the central processing unit (CPU, or "host") to the graphical processing unit (GPU, or "device") for CUDA programming. It should be noted that large chunks of data (e.g. 10,000 to 20,000 A-lines) should be transferred to the GPU at a time, as it takes a relatively long time to complete each CPU-GPU transfer. Once the transfer is complete, several CUDA functions are performed (e.g. averaging the OCT signal laterally for speckle suppression, tissue surface detection, phantom calibration, data fitting and finally, the extraction of the attenuation coefficient). For each of these CUDA function, the data is divided into hundreds and thousands of smaller sub-segments (e.g. 30 A-lines), which are then sent to different threads of the GPU for simultaneous computation of simple operations such as averaging, taking the natural log, or performing a linear fit. Then the results from these multiple threads are integrated once again to form the *en face* attenuation matrix (at 52 attenuation values per frame x the number of frames passed to the GPU at a time). Finally, the *en face*

attenuation matrix is transferred back to the CPU where the optical property map is computed and shown on a display device controlled by OpenGL on the graphical user interface (GUI).

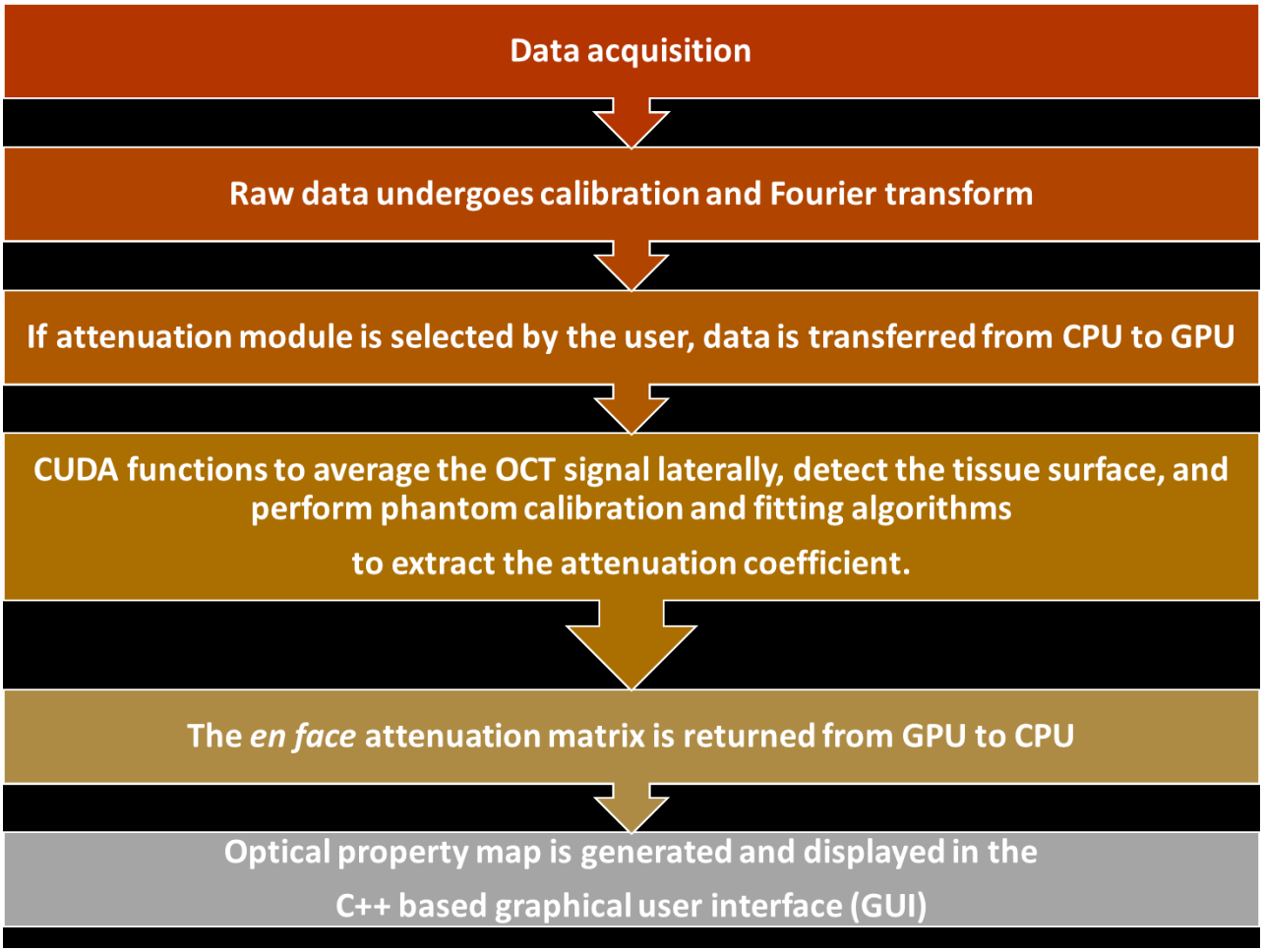

Figure 7. Workflow of the C++ based optical property mapping algorithm

SECTION 8: SUMMARY

In this chapter, we first described the overall software architecture designed for the OCT imaging system. Then, we focus on the theory and mathematics used to obtain the optical attenuation coefficients for brain cancer applications. Finally, we discussed the algorithms used to process and display the attenuation using both the MATLAB and C++ platforms.

CHAPTER 4: A SYSTEMATIC STUDY OF EX VIVO HUMAN BRAIN CANCER

SECTION 1: OVERVIEW

In this chapter, we investigated the potential of OCT for label-free imaging of human brain cancer in a systematic study with 32 patients and over 4,600 data points (*66, 72*). First, we established a set of optical attenuation parameters and statistically analyze a training dataset (with 16 patients) to establish a diagnostic threshold for pathologically confirmed cases of brain cancer. Then, we applied this diagnostic threshold in an independent double-blinded study (with another 16 patients) to identify the OCT detection sensitivity and specificity. Finally, we constructed a color-coded map from the *ex vivo* dataset in order to offer direct visual cues to the neurosurgeons for real-time detection of cancer versus non-cancer at high resolution.

SECTION 2: EXPERIMENTAL DESIGN

As demonstrated in **Figure 1**, the purpose of this systematics study is to evaluate the feasibility of OCT in distinguishing cancer from non-cancer for patients undergoing brain surgery (*66, 72*). As the first step, freshly resected *ex vivo* human brain tissues were identified and resected using MRI-guided surgical navigation for patients with low-grade (grade II glioma) and high-grade (grade IV glioma, or glioblastoma, GBM) brain cancers. Two-dimensional OCT cross-sectional images (in the x and z directions) were then acquired over the three-dimensional tissue sample *ex vivo* at a uniform interval of 0.5 mm (in the y-direction) using one of the two swept-source OCT (SS-OCT) imaging systems. Each cross-sectional image was then divided into 3 sub-sections to obtain 3

different attenuation data points. After imaging, the tissues were sent for histological processing and were reviewed by a pathologist for validation of the brain tissue type and cancer grade.

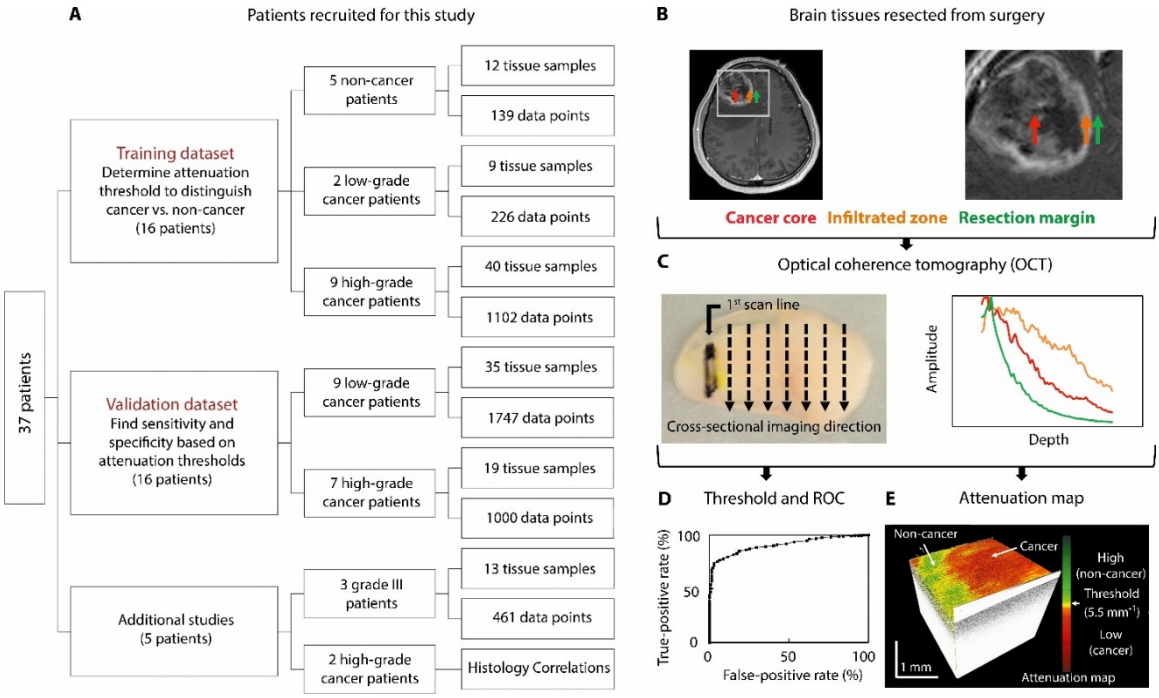

Figure 1. Study design to differentiate cancer versus non-cancer with OCT. We recruited 37 patients for this study, generating over 4670 data points. **(B)** Brain cancer samples were obtained from cancer core (red arrow), infiltrated zone (orange arrow), and resection margin (green arrow) during surgery. **(C)** Tissues were marked with yellow dye (at the 1st scan line) for imaging registration. Cross-sectional OCT imaging of the tissue was then performed along dotted lines. The depth-dependent OCT signal profiles were acquired over different, relatively homogenous regions and analyzed to obtain the optical attenuation values for differentiating cancer versus non-cancer samples. Results showed that OCT signal profiles (curves) and the tissue attenuation values (slope of the curve) differed among cancer core (red), infiltrated zone (orange) and non-cancer resection margin (green). After OCT imaging, tissues were prepared for histology and evaluated by a neuro-pathologist. **(D)** Based on the OCT data, optimal attenuation thresholds and receiver operating characteristics (ROC) curves were determined using brain tissues in the training dataset. Using these parameters, a validation dataset was recruited to establish the OCT sensitivity and specificity in identifying cancer versus non-cancer using a double-blinded procedure. **(E)** To facilitate potential intra-operative use, a 3D volumetric reconstruction of the OCT images was generated with an overlaid color-coded attenuation map of the *ex vivo* human brain tissue. **Figure and figure legends are originally from Kut *et al.*, Detection of human brain cancer infiltration**

ex vivo and in vivo using quantitative optical coherence tomography. Science translational medicine, 7(292), 292ra100-292ra100 (2015). Reprinted with permission from AAAS.

For the purposes of this study, more than 1450 data points were acquired from the training dataset with 16 patients (i.e., 9 high-grade, 2 low-grade, and 5 non-cancer) (*66, 72*). The data from this training set is used to establish an optimal diagnostic threshold which can differentiate brain cancer from non-cancer (white matter) based on the optical attenuation properties of imaged tissue.

Once the optimal diagnostic threshold is established, we perform a separate, double-blinded study in a validation dataset with another 16 patients (7 high-grade, 9 low-grade) and over 3200 data points to establish the OCT detection sensitivity and specificity (using the diagnostic threshold as determined by the training dataset).

In other words, we have acquired a total of 4675 data points from a total of 32 patients (16 high-grade, 11 low-grade, 5 non-cancer) for a systematic and quantitative analysis of human brain cancer tissues. Finally, 5 additional patients were imaged which included the attenuation analyses for 3 grade III glioma patient, and OCT-histology correlations for 2 additional grade IV glioma patients for OCT-histological correlations. In total, 37 patients were imaged and were assigned to the different datasets (e.g. training versus validation) serially based on the date of the surgery.

Table 1 summarizes the patient characteristics for all 37 patients recruited for this study (*66, 72*). These patient characteristics included age at surgery, sex, race, diagnosis, treatment, age at diagnosis, brain cancer location, and the recruited category. Notably, patients with grade I gliomas were excluded from this systematic study because of its distinct nature from other glioma grades; while grade II-IV gliomas are incurable brain cancers which are extremely aggressive and infiltrative in nature, grade I gliomas are typically non-infiltrative and is generally curable.

#	Age at surgery	Sex	Race	Diagnosis	Treatment	Age at diagnosis	Cancer location	Recruited category
1	60	M	C	Seizure	New	60	Temporal	T
2	21	M	C	Seizure	New	21	Temporal	T
3	23	M	C	Seizure	New	23	Temporal	T
4	23	F	AA	Seizure	New	23	Temporal	T
5	32	F	AA	Seizure	New	32	Temporal	T
6	41	M	W	Grade II	New	41	R temporal	T
7	23	M	W	Grade II	New	23	R frontal	T
8	54	M	W	Grade IV	New	54	R temporo-parietal	T
9	24	M	O	Grade IV	New	24	L occipital	T
10	27	F	W	Grade IV	New	27	L frontal	T
11	51	F	W	Grade IV	Recurrent	51	R temporal	T
12	41	F	W	Grade IV	Recurrent	41	L occipital	T
13	74	M	O	Grade IV	New	74	R frontal	T
14	47	M	H	Grade IV	New	47	R parieto-occipital	T
15	29	M	W	Grade IV	Recurrent	25	R frontal	T
16	75	M	W	Grade IV	New	75	L frontal	T
17	53	M	W	Grade II	New	53	R frontal	V
18	32	F	W	Grade II	New	32	L frontal	V
19	41	F	H	Grade II	New	41	L frontal	V
20	33	M	O	Grade II	New	33	L temporo-parietal	V
21	70	F	W	Grade II	New	70	R frontal	V
22	39	M	W	Grade II	Recurrent	20	R frontal	V
23	29	M	W	Grade II	New	29	R frontal	V
24	28	F	W	Grade II	New	28	L temporal	V
25	36	M	W	Grade II	New	36	R frontal	V
26	64	F	H	Grade II	New	64	L frontal	V
27	50	M	AA	Grade IV	Recurrent	49	R temporal	V
28	71	M	O	Grade IV	New	71	R temporal	V
29	63	M	AA	Grade IV	Recurrent	63	R frontal	V
30	70	M	W	Grade IV	New	70	L temporal	V
31	73	M	W	Grade IV	Recurrent	71	L temporo-frontal	V
32	56	F	O	Grade IV	New	56	R parieto-occipital	V
33	62	M	O	Grade IV	New	62	R fronto-parietal	OHC
34	80	M	W	Grade IV	New	80	R frontal	OHC
35	33	M	W	Grade III	New	33	R perirolandic	III
36	32	M	W	Grade III	New	32	L frontal	III
37	31	F	W	Grade III	New	31	R temporo-occipital	III

Table 1. Patient characteristics. Thirty-seven patients were recruited for this study. M: Male, F: Female, C: Caucasian, AA: African American, H: Hispanic, O: other, R: right, L: left, T: training dataset, V: validation dataset, OHC: OCT-histology correlation and III: attenuation analyses for

grade III glioma. **Table and table legends are originally from Kut *et al.*, Detection of human brain cancer infiltration ex vivo and in vivo using quantitative optical coherence tomography. Science translational medicine, 7(292), 292ra100-292ra100 (2015). Reprinted with permission from AAAS.**

SECTION 3: IMAGING OF EX VIVO HUMAN BRAIN CANCER

For the *ex vivo* study, fresh human brain tissues were surgically removed from 37 patients and scanned over a given volume to generate depth-dependent OCT signal profiles using the cabinet-sized FDML swept-source OCT (SS-OCT) imaging system and a 12-mm diameter handheld imaging probe (*66, 72*). Tissue attenuation values were estimated with the phantom calibration method (*39*), where the averaged OCT signal profile from the human brain tissue sample is normalized with the OCT signal from a silicon oxide phantom with known attenuation coefficients.

As demonstrated in the previous chapters, the cabinet-sized FDML SS-OCT imaging system is capable of scanning up to 220,000 A-lines per second, or 110 - 220 frames per second (assuming that 1000 – 2000 A-lines are captured for each cross-sectional frame). In other words, our OCT imaging system took approximately 1 to 2 seconds to acquire, process, display and store the raw OCT data and its associated attenuation results for an 8-16 mm^3 tissue block.

The default OCT field of view (FOV) is currently set to 8-16 mm^3. However, we can significantly increase the field of view using a robotic translational stage. For example, **Figure 2** demonstrates how a robotic translational stage can be used to increase the FOV by 4.5 times (from 8 mm^3 to 36 mm^3) (*66, 72*). In fact, the FOV can increase even more by employing the use of a high-performance and long-range robotic translational device. In our case, the FOV is actually restricted by the size of the raw OCT dataset (which is currently at 2GB for each 8 mm^3 tissue block, and can conceivably reach a data size at around 200 GB if the FOV is increased 100-fold).

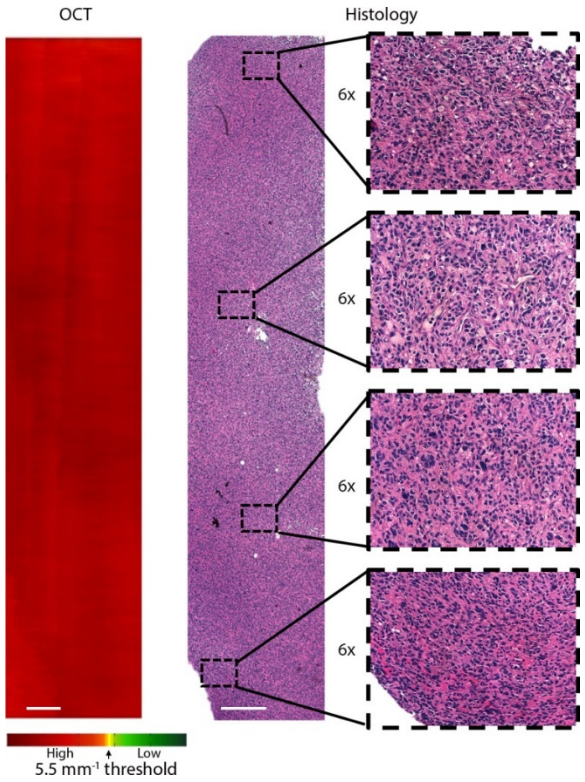

Figure 2. Improved OCT field of view with robotic positioning. Expanded field of view (at 10 mm × 2 mm × 1.8 mm = 36 mm^3) was conveniently demonstrated with the use of a robotic translational stage for *ex vivo* imaging of a high-grade human brain cancer tissue block. Corresponding histology is shown, with high cancer density. Scale bars, 0.5 mm. **Figure and figure legends are originally from Kut *et al.*, Detection of human brain cancer infiltration ex vivo and in vivo using quantitative optical coherence tomography. Science translational medicine, 7(292), 292ra100-292ra100 (2015). Reprinted with permission from AAAS.**

Finally, an optimal attenuation threshold is established based on the attenuation results and the corresponding histological validation of the imaged tissues. This threshold is established for the identification of high-grade (i.e., grade IV) and low-grade (i.e. grade II) human brain cancer with high detection sensitivity and specificity. Finally, OCT images were displayed in 3D and overlaid with an *en face,* color-coded optical property map which reflects the attenuation properties of the brain tissues. We will go over the methodology and results in detail in the following sections.

SECTION 4: ACQUIRING HUMAN BRAIN TISSUE SAMPLES

For all of the 37 patients in the study, brain tissues were freshly resected from the patient using standard neurosurgical techniques (which includes microsurgical dissection when necessary, and the use of routine intra-operative surgical navigation). Tissues necessary for clinical diagnosis of the patient were obtained and sent to the Pathology department. If there are any excess tissues (which will otherwise be discarded in the course of surgery), these tissues will be sent to the laboratory for research purposes.

Non-cancer tissue samples were obtained from control, non-cancer patients who underwent surgery (i.e. temporal lobectomy) as part of seizure treatment. Tissue samples from high-grade and low-grade brain cancer patients, on the other hand, were obtained from the cancer core and infiltrated zone, as categorized by the neurosurgeon and later validated by a neuro-pathologist. Finally tissues were also obtained from the resection margins of brain cancer patients which showed normal pathology (i.e., less than 5% cancer cells based on visual estimate by the neuropathologist). These resection margins from brain cancer patients were either obtained as part of the planned trajectory to the cancer core, or were resected along the surgically defined margins at the interface between infiltrated cancer and the normal brain.

SECTION 5: IMAGING PROTOCOL

As described in Chapter 2, a home-built cabinet-sized FDML SS-OCT system was used to image all the *ex vivo* brain tissue samples obtained from brain cancer and control patients.

The *ex vivo* OCT imaging protocol can be described as follows. First, each tissue sample was freshly obtained from the operating room and immediately sent to the laboratory for imaging. Then, each tissue was re-sectioned into flat, homogeneous samples at approximately 50 mm^3 per

sample. For histological registration and correlation purposes, the tissue surfaces were marked with a 3-mm line using a yellow margin marking dye (MasterTech). After the yellow dye is affixed onto the tissue surface, a cover glass was carefully placed on top of the tissue surface to prevent dehydration of the tissue and also to flatten the tissue surface. The tissues were then kept in a 4^{o}C refrigerator until it is time for imaging.

To begin the imaging procedure, the tissue sample is first transferred onto the imaging stage. Then, an infrared sensor card was used to align the OCT infrared imaging beam onto the 3 mm yellow line on the tissue. This marked our first OCT scan line and the first two-dimensional, cross-sectional (B-scan) OCT image was obtained in the x and z directions. Afterwards, the translational stage was moved manually such that cross sectional images can be acquired at 0.5 mm intervals along the horizontal plane in the y direction using the C++ based, home-built OCT imaging software. Finally, the OCT imaging data was stored digitally in a computer for image post-processing and attenuation analyses. Notably, the real-time optical mapping algorithm (which is developed in 2014) was not implemented for the purposes of this systematic study. This is because the systematic *ex vivo* study started in 2011, several years before the real-time optical mapping algorithm was developed. However, we will discuss the results of the real-time optical mapping algorithm in the later sections of this chapter.

At the end of the imaging session, the tissue samples were placed in 10% neutral buffered formalin overnight. After formalin fixation, the tissue samples were then transferred to a phosphate buffered saline (PBS) solution and re-sectioned at the first OCT scan line (yellow line) for histological processing and correlation.

Each of the resulting histological slides contained multiple 5-µm thick H&E-stained tissue samples sectioned at an interval of 0.5 mm per slide, and bears a close correspondence to the location and orientation of the OCT cross-sectional images. A neuropathologist reviewed the histological slides and allocated each tissue sample to one of three categories (cancer core, infiltrated zone, and non-cancer).

SECTION 6: TRAINING DATASET – OPTICAL ATTENUATION DIFFERENCES BETWEEN CANCER AND NON-CANCER

After imaging, the attenuation results are obtained using the following protocol. First, the depth-dependent OCT signal profiles are quantitatively analyzed. Each OCT image is divided into 1 to 3 sections depending on the tissue features and characteristics, such that each section roughly consists of a homogeneous tissue region. Then, the optical attenuation value was computed using the phantom calibration method (*68*) and other processing techniques as described in the previous section (*66, 72*). After processing, the attenuation coefficients for the brain tissues were divided into several categories for statistical analyses. These categories include cancer core, infiltrated zone and resection margin for tissue samples obtained from cancer patients, and non-cancer samples obtained from control patients. The results are described as follows:

First, let us study the attenuation results from the training dataset. Freshly resected *ex vivo* human brain tissue samples from 16 patients (i.e. 9 high-grade, 2-low-grade and 5 non-cancer) were characterized to establish the differences in optical attenuation between brain cancer and non-cancer white matter (*66, 72*). To ensure that the grouping of cancer and non-cancer tissues is accurate, the diagnosis of all cancer versus non-cancer tissues were first confirmed with histological validation by a neuro-pathologist.

As shown in **Figure 3A,** there was little to moderate overlap in the distribution of optical attenuation values between cancer and non-cancer white matter (*66, 72*). There is a 9% overlap between high-grade infiltrated zone and non-cancer white matter, versus a 33% overlap between high-grade cancer core and non-cancer white matter. Similarly, there is a 6% overlap between low-grade infiltrated zone and non-cancer white matter, versus a 37% overlap between low-grade cancer core and non-cancer white matter.

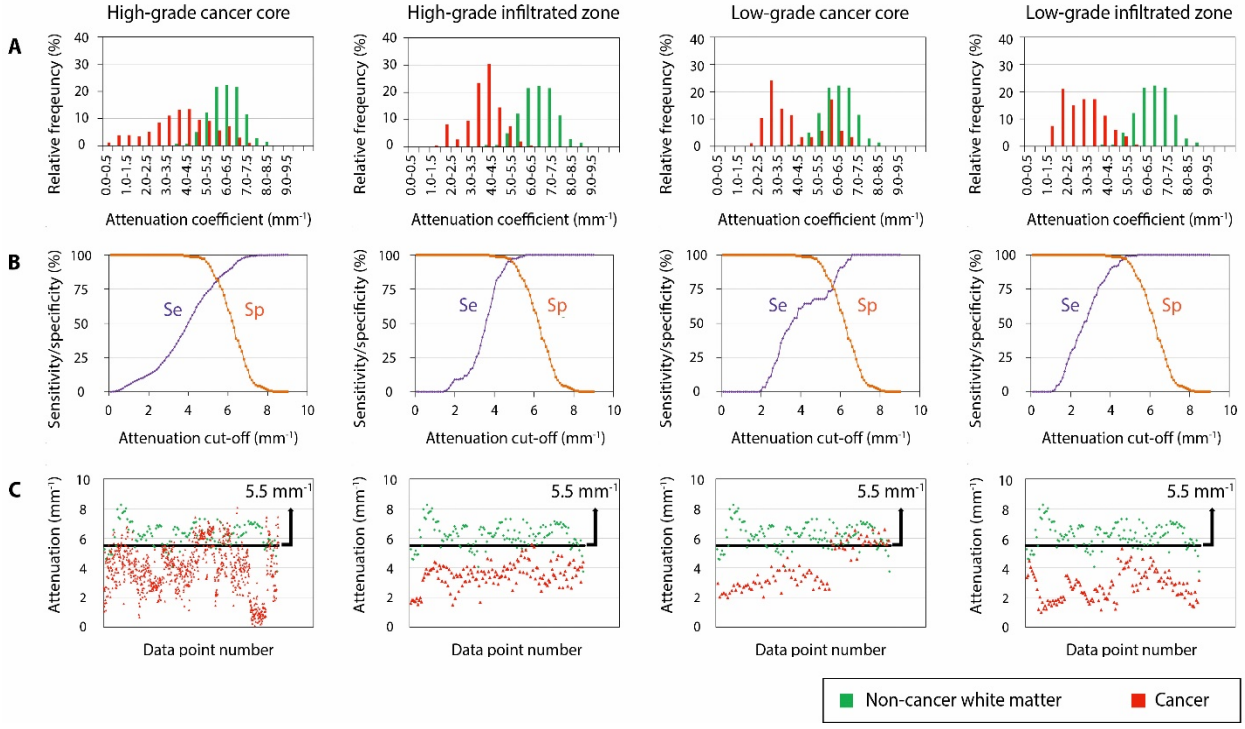

Figure 3. Establishing the optical attenuation threshold for high-grade and low-grade brain cancers in patients. The histogram distribution **(A)**, the diagnostic sensitivity/specificity **(B)**, and the optimal attenuation threshold **(C)** for both cancer core and infiltrated zone in tissue blocks freshly resected from 9 high-grade, 2 low-grade and 5 control patients within the training dataset. At the 5.5 mm^{-1} optical attenuation threshold, maximum sensitivity was achieved while maintaining at least 80% specificity for differentiating cancer versus non-cancer tissues in cancer core and infiltrated zone. **Figure and figure legends are originally from Kut *et al.*, Detection of human brain cancer infiltration ex vivo and in vivo using quantitative optical coherence tomography. Science translational medicine, 7(292), 292ra100-292ra100 (2015). Reprinted with permission from AAAS.**

On the overall, brain cancer tissues (including both cancer core and the infiltrated zone) were found to have lower attenuation values when compared with the surrounding non-cancer white matter. **Table 2** summarizes the attenuation data for the different tissue types and cancer grade (*66, 72*). For the comparison between high-grade brain cancer and non-cancer patients, the average optical attenuation value of non-cancer white matter (at 6.2 mm^{-1}) was significantly higher than the attenuation value of the infiltrated zone (at 3.5 mm^{-1}) and of the cancer core (3.9 mm^{-1}). Similarly, for the comparison between low-grade brain cancer and non-cancer patients, the average optical attenuation value of non-cancer white matter (at 6.2 mm^{-1}) was significantly higher than infiltrated zone (2.7 mm^{-1}), but not significantly higher than cancer core (4.0 mm^{1}).

However, no significant differences were found for the attenuation values in low-grade versus high-grade patients in both the infiltrated zone (i.e., at 2.7 ± 1.0 in low-grade versus 3.5 ± 0.8 in high-grade; $p = 0.45$) and in the cancer core (i.e., at 4.0 ± 1.4 in low-grade versus 3.9 ± 1.6 in high-grade; $p = 0.94$). The p-values are computed using Welch's t-test, which is an adaptation of the student t-test but assumes unequal variance between the 2 samples.

SECTION 7: TRAINING DATASET – SETTING AN OPTIMAL DIAGNOSTIC ATTENUATION THRESHOLD

Next, we perform a systematic, quantitative analysis on the data in the training dataset with 16 patients (i.e., $n = 16$) to establish an optimal diagnostic attenuation threshold which can be used to distinguish between brain cancer and non-cancer white matter.

As demonstrated in **Figure 3A**, the distribution of optical attenuation coefficients for non-cancer, cancer core and infiltrated zone tissue samples were grouped into binned histograms at 0.5 mm^{-1}/bin for high-grade and low-grade cancers (*66, 72*). To find the attenuation threshold, we

estimated and plotted the sensitivity and specificity for each of these categories which were published in **Figure 3B** for the detection of brain cancer versus non-cancer white matter (*66, 72*). Finally in **Figure 3C**, we obtained the estimation for the sensitivity/specificity values when the diagnostic threshold is set to different attenuation values (i.e., over an attenuation range of 0-10 mm^{-1} evaluated at step intervals of 0.1 mm^{-1}) for both high-grade and low-grade brain cancer tissues (*66, 72*).

Based on the results, we determine the optimal attenuation threshold to be the threshold value which yielded maximum sensitivity while maintaining at least 80%specificity.

Tissue	***n***	**Attenuation mean ± SD (mm^{-1})**	***P*-value (vs. non-cancer tissue)**
Control patients (seizure)			
Non-cancer white matter	5	6.2 ± 0.8	N/A
High-grade cancer patients			
Cancer core	9	3.9 ± 1.6	0.002
Infiltrated zone	3	3.5 ± 0.8	0.004
Non-cancer resection margin (white matter)	4	7.1 ± 1.0	0.902
Low-grade cancer patients			
Cancer core	2	4.0 ± 1.4	0.120
Infiltrated zone	2	2.7 ± 1.0	0.037

Table 2. Attenuation data in the training dataset for patients with high- and low-grade brain cancer. Quantitative attenuation values are provided for 16 patients in the training set (9 high-grade, 2 low-grade, 5 control). *P*-values were calculated using two-sample, one-tailed Welch's t-test based on the hypothesis that non-cancer white matter has higher attenuation. **Table and table legends are originally from Kut *et al.*, Detection of human brain cancer infiltration ex vivo**

and in vivo using quantitative optical coherence tomography. Science translational medicine, 7(292), 292ra100-292ra100 (2015). Reprinted with permission from AAAS.

Now, let us take a look at the results (*66, 72*). Based on the training set, we determined the optimal threshold attenuation value. There are different criteria we can use to determine the optimal threshold attenuation value. For example, one common criteria is to find the threshold value which yields the highest sum of sensitivity and specificity. For brain cancer applications, however, surgeons value specificity over sensitivity as inadvertent resection of the normal brain (especially in eloquent areas such as the speech and motor areas) will have tremendous negative consequences to the patient's prognosis and quality of life. As a result, here, we choose to adopt a criteria which ensures that the optimal diagnostic threshold will be able to achieve at least 80% specificity, while yielding the highest sensitivity. Consequently, we find this optimal attenuation threshold to be 5.5 mm^{-1}. Even though the optimal attenuation threshold was evaluated independently for high-grade versus low-grade brain cancer patients, we found that the optimal attenuation threshold happened to be identical at 5.5 mm^{-1} for both cancer grades. Using this specified optimal diagnostic attenuation threshold, we determined the receiver operating characteristics (ROC) for the detection of both high-grade and low-grade brain cancers. The results are demonstrated in **Figure 4A** (*66, 72*).

Furthermore, the attenuation results of the brain cancer sample can be displayed as a color-coded optical property map which is well correlated with histology (*66, 72*). **Figure 4B** shows one example of the OCT-histology correlation (*66, 72*). Notably, the *en face* color-coded optimal property map represents the attenuation characteristics of a three-dimensional brain tissue sample along the entire imaging depth (1.8 mm), while the corresponding histology images are denoting a two-dimensional horizontal sectioning of this tissue sample which is cut at a specific depth, or z –coordinate. During histo-pathological validation, the neuro-pathologist reviewed different

histological sections at different z-coordinates, and concluded that this particular brain cancer sample contained areas with high cancer density (which is shown in red in the optical property map), areas with medium cancer density (which is shown in yellow in the optical property map) and areas with low cancer density which is described by the pathologist as a diffusely infiltrated area with mostly non-cancer white matter with some neoplastic cell components (shown in green in the optical property map).

SECTION 8: VALIDATION DATASET – DETERMINING THE OCT DETECTION SENSITIVITY AND SPECIFICITY

Next, we conducted an independent and double-blinded study to determine the sensitivity and specificity associated with the optimal attenuation threshold. For this independent study, we recruited brain tissues from an additional 16 patients to form the validation dataset (*66, 72*).

In order to achieve a double-blinded study, the OCT researcher was blinded to the tissue type and grade when imaging the tissue and performing post-processing to obtain the attenuation coefficients. Similarly, the neuropathologist for this study was also blinded to the tissue type and grade when giving his histopathological evaluation of the tissue samples. For this dataset, a total of 59 tissue samples (i.e., 19 tissue samples from high-grade brain cancer patients, and 40 tissue samples from low-grade brain cancer patients) (*66, 72*).

To obtain the OCT detection sensitivity, we need to divide the tissue samples into four different categories (i.e., true condition positive, true condition negative, predicted condition positive and prediction condition negative). First of all, the high-grade and low-grade brain tissue samples were grouped separately and therefore evaluated separately (in other words, we are evaluating the OCT detection sensitivity and specificity for each of the two cancer grades).

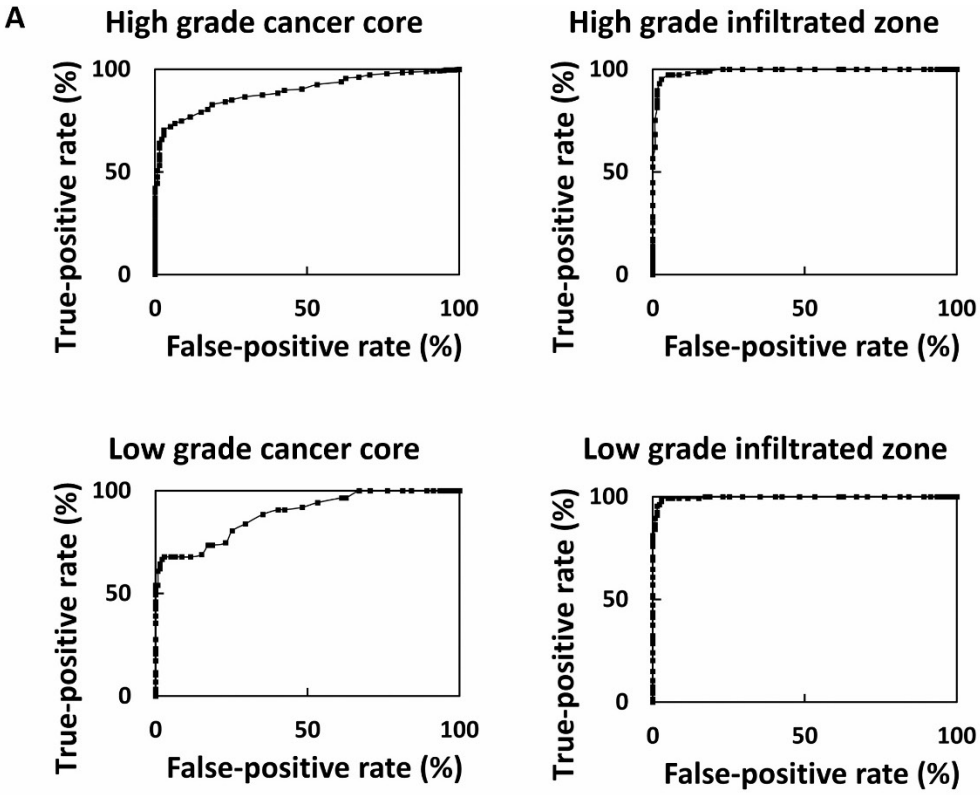
A
High grade cancer core
High grade infiltrated zone
Low grade cancer core
Low grade infiltrated zone
True-positive rate (%)
False-positive rate (%)
0
50
100

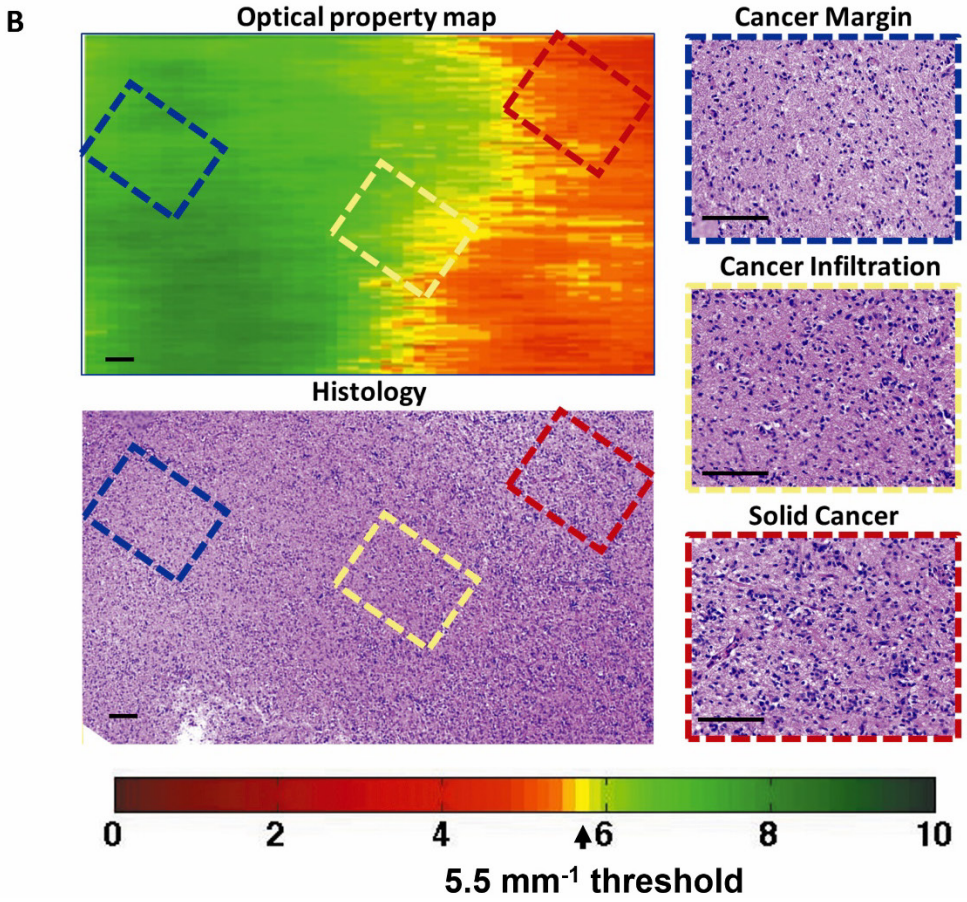
B
Optical property map
Histology
Cancer Margin
Cancer Infiltration
Solid Cancer
0
2
4
6
8
10
5.5 mm-1 threshold

Figure 4. Sensitivity and specificity in cancer core and infiltrated zones and histology correlating with OCT maps. (A) Receiver operating characteristic (ROC) curves with true-positive (sensitivity) and false-positive (1 - specificity) rates were computed for cancer core and infiltrated zone in tissues obtained from 16 patients within the training dataset. **(B)** *En face* attenuation results of a high-grade brain cancer tissue block (2 mm x 2 mm x 1.8 mm) are shown with corresponding histology**.** Areas of high cancer density have low optical attenuation (red). Areas of medium cancer density have medium optical attenuation (yellow). Areas with low cancer density (diffusely infiltrated area) have high optical attenuation (green). The corresponding histology, obtained *en face* (same orientation as the attenuation map), was provided for comparison. Scale bars, 100 μm. **Figure and figure legends are originally from Kut *et al.*, Detection of human brain cancer infiltration ex vivo and in vivo using quantitative optical coherence tomography. Science translational medicine, 7(292), 292ra100-292ra100 (2015). Reprinted with permission from AAAS.**

For the purposes of this study, a tissue sample (at about 50 mm^3 volume) was classified as prediction condition positive (i.e. predicted as cancer using OCT) if ≤50% of the attenuation data points were lower than the diagnostic threshold value at 5.5 mm^{-1}. On the other hand, a tissue sample was classified as prediction condition negative (i.e., predicted as non-cancer using OCT) if >50% of the attenuation data points were higher than the diagnostic threshold at 5.5 mm^{-1}.

Furthermore, the true conditions were determined based on histo-pathological analysis of the brain tissue samples by a neuro-pathologist who was blinded to the OCT results and to the true diagnosis of the patients. In other words, the tissue sample was classified as true condition positive (i.e. determined to be cancer using histology) if >5% of the tissue sample contained cancer cells. Similarly, the tissue sample was classified as true condition negative (i.e. determined to be non-cancer based on histology) if there is ≤5% cancer cells on the histological slides.

Based on the prediction outcomes (i.e., OCT attenuation data) and the true outcomes (i.e., the histological evaluation), we count the number of tissue samples in the following major categories: (1) true positive, or TP (which means the number of samples which are prediction condition positive and true condition positive); (2) true negative, or TN (which means the number of samples which are prediction condition negative and true condition negative); (3) false-positive,

or FP (which means the number of samples which are prediction condition positive but true condition negative); and (4) false-negative, or FN (which means the number of samples which are prediction condition negative but true condition positive). Notably, false-positive is known as Type I error while false-negative is known as Type II error in standard statistical analyses.

Finally, the OCT detection sensitivity (which is also known as the true positive rate and is defined by the proportion of true condition positive which are identified correctly as such) can be obtained with the following equation: $Sensitivity = \frac{TP}{TP+FN}$. The OCT detection specificity (which is also known as the true negative rate, and is defined by the proportion of true condition negative which are identified correctly as such) can be obtained with the following equation: $Specificity = \frac{TN}{TN+FP}$.

Finally, the OCT detection sensitivity and specificity results are summarized in **Table 3** (*66, 72*). Using a diagnostic optical attenuation threshold of 5.5 mm^{-1}, the specificity was found to be 100% and the sensitivity was found to be 92% for high-grade brain cancer patients (n = 7). Using the same diagnostic optical attenuation threshold, the specificity was found to be100% and the sensitivity was found to be 80% for low-grade brain cancer patients (n = 9).

Cancer	***n* patients**	**OCT**		**Surgeon**	
		Sensitivity (%)	**Specificity (%)**	**Sensitivity (%)**	**Specificity (%)**
High-grade	7	92	100	100	50
Low-grade	9	100	80	100	40

Table 3. Sensitivity/specificity analyses for brain cancer patients in the validation dataset. For the validation dataset, an independent subset of tissues from 16 patients with high- and low-grade brain cancers were obtained for blinded analyses at the chosen optical attenuation threshold (5.5 mm^{-1}). These data as well as the surgeon's independent assessment of the tissues were compared with the gold standard histopathology to obtain sensitivity and specificity. **Table and**

table legends are originally from Kut *et al.*, Detection of human brain cancer infiltration ex vivo and in vivo using quantitative optical coherence tomography. Science translational medicine, 7(292), 292ra100-292ra100 (2015). Reprinted with permission from AAAS.

SECTION 9: OCT VERSUS SURGEON IN DETECTION OF HUMAN BRAIN CANCER VERSUS NON-CANCER

Furthermore, the diagnostic sensitivity and specificity values for OCT were compared with the diagnostic sensitivity and specificity of the surgeon in the identification of brain cancer tissues.

Here, the surgeon detection sensitivity and specificity are defined by the following. Here, the prediction conditions are determined by the surgeon's impression of the tissue sample (i.e. whether the sample is cancer or non-cancer). In other words, the surgeon gave his perception of cancer and non-cancer tissue samples based on all pre-operative and intra-operative imaging information which are available (such as surgical microscope, surgical navigation data and intra-operative or pre-operative MRI scans). In addition, the surgeon is also added by his surgical experience in detecting cancer versus non-cancer based on the gross appearance of the tissue samples resected, as well as by the surgeon's knowledge of the patient's clinical history.

After the surgeon gave his impression, the results were recorded and the same tissue samples were sent to the laboratory for OCT imaging and attenuation computations. Finally, the OCT and surgeon detection sensitivity and specificity were evaluated using similar techniques as described in the previous section.

Here are the results (which are also shown in **Table 3**) (*66, 72*): after comparing the surgeon's impression of the tissue with the blinded histological diagnosis for 16 patients in the validation cohort, we find that the surgeon has a detection specificity of 50% and sensitivity of 100% for high-grade brain cancer. For low-grade brain cancer, the surgeon has a detection

specificity of 40% and a sensitivity of 100%. In contrast, OCT has a detection specificity of 80-100% and a detection specificity of 92-100% (as described in the previous section). These results are significant, since surgeons generally value specificity over sensitivity in the operating room in an attempt to preserve critical brain functions including motor, speech and sensory areas.

SECTION 10: ATTENUATION RESULTS FOR THE NEWLY DIAGNOSED VERSUS RECURRENT BRAIN CANCER

To evaluate whether previous brain cancer treatments have an effect on the attenuation results, we consolidated the training and evaluation datasets in an attempt to study the differences in optical attenuation values among different sub-groups of low- and high-grade cancer.

The results are summarized in **Table 4** (*66, 72*). On the overall, we find that regardless of whether the patient is newly diagnosed with brain cancer or if the patient is suffering from a recurrent brain cancer, brain cancer tissues have significantly lower attenuations when compared with the non-cancer white matter. In addition, there were no significant differences between the attenuation values for the newly diagnosed versus recurrent brain cancers.

SECTION 11: ATTENUATION RESULTS FOR CANCER CORE AND INFILTRATED ZONE

Furthermore, we conducted additional analyses to evaluate if there are any differences in the optical attenuation values for different cancer locations (*66, 72*). Our results showed that the cancer core had comparable attenuation values when compared with the infiltrated zones (with p-value at 0.51 for high-grade and p-value at 0.80 for low-grade using Welch's t-test). In addition, there were no significant differences in the attenuation values between low-grade and high-grade brain cancer.

Tissue	*n*	Attenuation (mm^{-1})	*P*-value (vs. non-cancer WM)	*P*-value (new vs. recurrent)
Control patients (seizure)				
Non-cancer white matter	5	6.2 ± 0.8	N/A	N/A
High-grade patients (newly diagnosed)				
Cancer core	9	3.6 ± 1.6	< 0.001	0.225
Infiltrated zone	3	3.7 ± 1.3	0.030	N/A
Non-cancer resection margin (white matter)	5	6.4 ± 1.0	0.368	0.835
High-grade patients (recurrent)				
Cancer core	6	4.6 ± 1.4	0.022	0.225
Infiltrated zone	1	3.7 ± 0.7	N/A	N/A
Non-cancer resection margin (white matter)	2	6.2 ± 1.0	0.500	0.835
Low-grade patients (newly diagnosed)				
Cancer core	10	3.8 ± 1.3	<0.001	N/A
Infiltrated zone	4	3.6 ± 1.3	0.005	N/A
Non-cancer resection margin (white matter)	3	5.9 ± 1.1	0.353	N/A
Low-grade patients (recurrent)				
• Cancer core	1	3.2 ± 0.5	N/A	N/A
• Infiltrated zone	1	3.6 ± 1.6	N/A	N/A

Table 4. Optical attenuation differences between treated and untreated brain tissues for patients in the combined training and validation datasets. Data are provided for 32 patients and are reported as averages ± SD. *P*-values were determined using a two-sample, one-tailed Welch's t-test based on the hypothesis that non-cancer white matter (WM) has higher attenuation than cancer and newly diagnosed and recurrent brain tissues have equal attenuation, respectively.

Table and table legends are originally from Kut *et al.*, Detection of human brain cancer infiltration ex vivo and in vivo using quantitative optical coherence tomography. Science translational medicine, 7(292), 292ra100-292ra100 (2015). Reprinted with permission from AAAS.

SECTION 12: ATTENUATION RESULTS FOR CANCER VERSUS NON-CANCER GRAY MATTER

In the previous sections, we primarily compared the attenuation results between cancer and non-cancer white matter. **Table 5** summarizes the attenuation results for superficial non-cancer gray matter which exists in the brain tissue surface in the cortical areas (*66, 72*).

According to the table, non-cancer gray matter had significantly lower attenuation when compared with high- and low-grade cancer cores, but not with high- or low-grade infiltrated zones. It should be noted that the non-cancer resection margin referred to tissue samples which consisted of primarily non-cancer gray matter (as opposed to the non-cancer resection margins in the previous tables which referred to tissue samples consisting primarily of non-cancer white matter).

SECTION 13: QUALITATIVE, STRUCTURAL DIFFERENCES BETWEEN CANCER AND NON-CANCER

In addition to optical property mapping, OCT is also capable of identifying microscopic structures from within the tissue sample. The qualitative structural characteristics of these brain tissues can therefore complement attenuation data and aid in the detection of cancer from non-cancer.

Figure 5 illustrated some of the characteristic, qualitative differences between brain cancer and non-cancer white matter (*66, 72*). Using OCT, we were able to identify the presence of necrosis and hypercellularity in high-grade brain cancer. On OCT images, these structural features appeared as heterogeneous regions of hypo-intense signals (representing necrosis) which were surrounded by hyper-intense signals (representing regions with hypercellularity) in high-grade cancer.

For low-grade brain cancer, we were able to identify the presence of hypercellularity and also microcysts in low-grade brain cancer. The presence of microcysts are specific to human brain cancer (especially in low-grade brain cancers); in other words, microcysts will only be present when there is brain cancer, and not when there is inflammation or other non-neoplastic pathologies in the brain (*73*). In comparison, the OCT images for non-cancer white matter were much more homogeneous and did not show the presence of any neoplastic changes.

Tissue	***n***	**Attenuation (mm^{-1})**	***P*-value (vs. non-cancer GM)**
Control patients (seizure)			
Non-cancer gray matter	5	2.8 ± 0.9	N/A
High-grade cancer patients			
Cancer core	15	4.2 ± 1.5	0.014
Infiltrated zone	4	3.7 ± 1.2	0.132
Non-cancer resection margin (gray matter)	6	3.4 ± 1.1	0.173
Low-grade cancer patients			
Cancer core	11	3.8 ± 1.2	0.047
Infiltrated zone	5	3.6 ± 1.4	0.160
Non-cancer resection margin (gray matter)	4	3.1 ± 1.5	0.370

Table 5. Optical attenuation differences between cancer and non-cancer gray matter for patients in the combined training and validation datasets. Data are averages ± SD. *P*-values were determined using a two-sample, one-tailed Welch's t-test, based on the hypotheses that non-cancer gray matter has lower attenuation than cancer. **Table and table legends are originally from Kut *et al.*, Detection of human brain cancer infiltration ex vivo and in vivo using quantitative optical coherence tomography. Science translational medicine, 7(292), 292ra100-292ra100 (2015). Reprinted with permission from AAAS.**

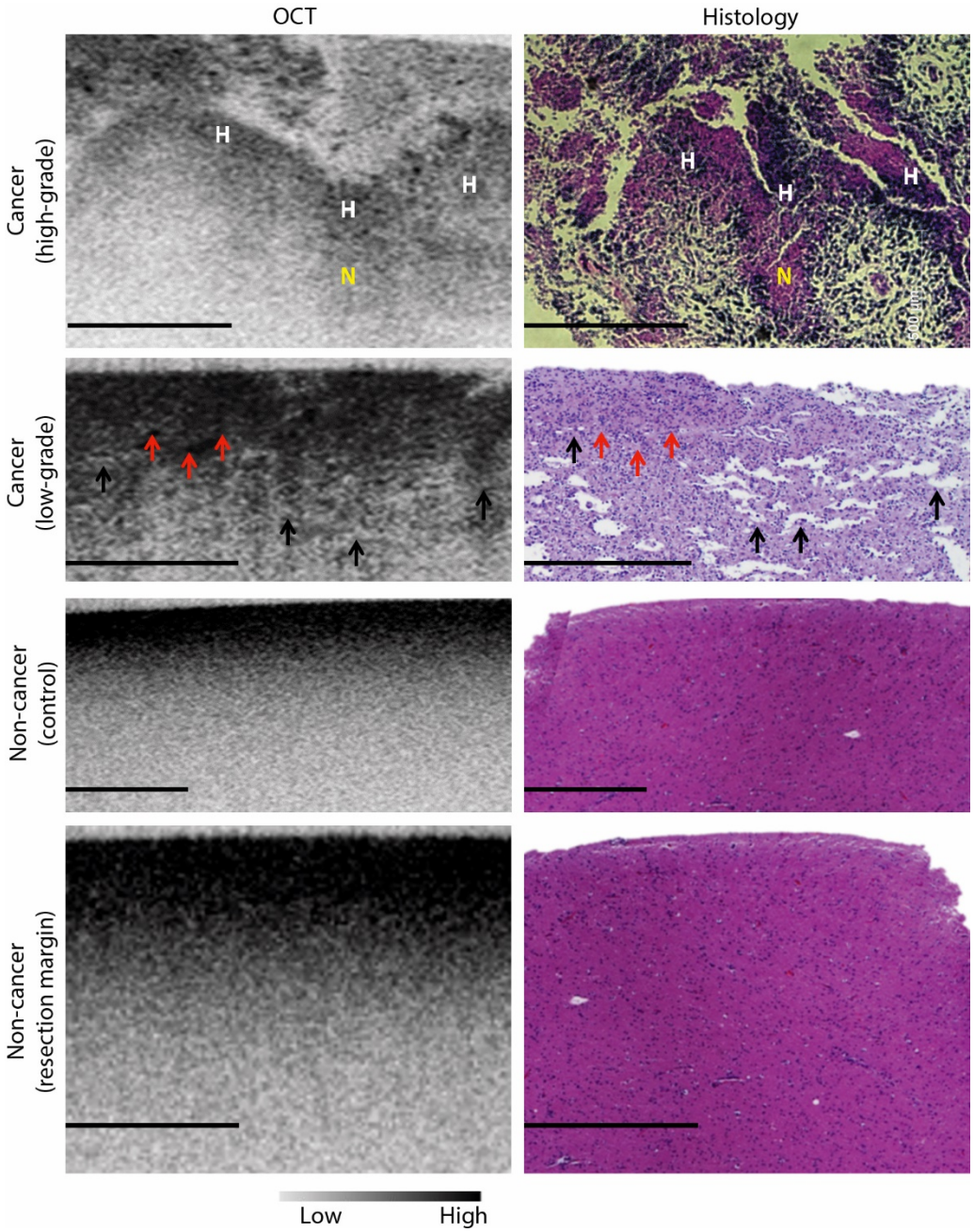

Figure 5. OCT revealed microscopic features that can help distinguish brain cancer versus non-cancer tissue in patients. Cross-sectional OCT images visualized tumor-specific characteristics, such as necrosis (N) and hypercellularity (H), in high-grade brain cancer. Similarly, OCT revealed microcyst formation (black arrows) and hypercellularity (red arrows) in low-grade brain cancer. In contrast, non-cancer white matter tissues—obtained from resected tissues from a seizure patient (control) and from the resection margin of a brain cancer patient—appeared homogeneous with high attenuation on OCT images. Scale bars, 500 μm. **Figure and figure legends are originally from Kut *et al.*, Detection of human brain cancer infiltration ex vivo and in vivo using quantitative optical coherence tomography. Science translational medicine, 7(292), 292ra100-292ra100 (2015). Reprinted with permission from AAAS.**

SECTION 14: ATTENUATION RESULTS FOR GRADE III GLIOMA

It should be noted that our study primarily focused on the attenuation results for high-grade (grade IV) and low-grade (grade II) brain cancer. This is because grade I gliomas were intentionally excluded from this study due to its non-infiltrative nature (which is unlike all other glioma grades) and due to the fact that grade I glioma patients rarely undergo surgery for tumor resection. As for grade III glioma, this is because the differentiation of grade III is traditionally difficult and often very controversial (*74*).

Nevertheless, we have studied the attenuation results for three patients with grade III brain cancer to complete our comprehensive evaluation of brain cancer tissue samples. **Figure 6** demonstrated the results of this analysis (*66, 72*).

On the overall, there was moderate to significant overlap in the distribution of optical attenuation values between non-cancer and grade III brain cancer tissues. There is a 24% overlap between grade III infiltrated zone and non-cancer white matter, and a 77% overlap between grade III cancer core and non-cancer white matter.

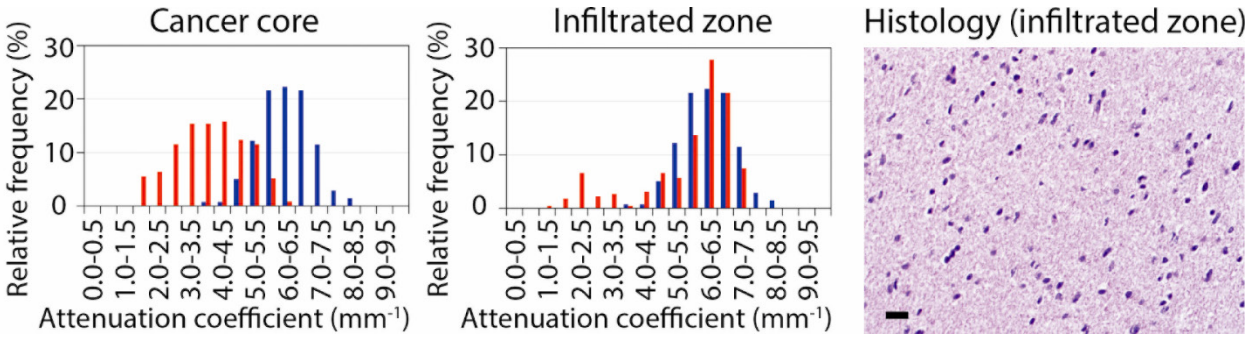

Figure 6. Dataset for grade III glioma. Histogram distributions were shown for both grade III cancer cores and infiltrated zones from three patients. The optimal attenuation threshold for grade III gliomas was determined to be at 5.5 mm^{-1}. Histological validation for the infiltrated zone samples revealed diffuse cancer infiltration (primarily white matter with some neoplastic cell components). Scale bar, 20 µm. **Figure and figure legends are originally from Kut *et al.*, Detection of human brain cancer infiltration ex vivo and in vivo using quantitative optical coherence tomography. Science translational medicine, 7(292), 292ra100-292ra100 (2015). Reprinted with permission from AAAS.**

Based on histo-pathological validation by the pathologists, the H&E slides for the grade III infiltrated zone revealed diffuse cancer infiltration which comprised of primarily non-cancer white matter with some neoplastic cell components. This (and the fact that only 3 grade III patients were recruited for this study) may account for the high percentage of overlap between grade III infiltrated zone and non-cancer white matter.

SECTION 15: SUMMARY OF STATISTICAL ANALYSES USED TO EVALUATE THE OPTICAL ATTENUATION OF HUMAN BRAIN

In this section, we summarized the statistical analyses used to determine whether there are significant differences in the optical attenuation values between two of the cancer or non-cancer sub-categories (*66, 72*). For example, to distinguish cancer from non-cancer white matter in the training dataset (i.e., **Table 2**), we performed a two-sample, one-tailed Student's t-test while assuming unequal variance (which is otherwise known as the Welch's t-test). The hypothesis here is that the optical attenuation values for non-cancer white matter is higher than the optical attenuation values for cancer core, infiltrated zone, and/or resection margins.

For intergroup analyses to evaluate whether there are any attenuation differences between newly diagnosed and recurrent brain cancer patients in the consolidated dataset containing both training and validation data (i.e., **Table 4**), we performed a two-sample, one-tailed Welch's t-test with the hypothesis that both groups have comparable attenuation values.

Similarly, for intergroup analyses to evaluate the optical attenuation values based on cancer density (i.e., cancer core versus infiltrated zone) and cancer grade (i.e. high-grade versus low-grade) using the consolidated dataset, we performed a two-sample, one-tailed Welch's t-test with the hypothesis that both groups have comparable attenuation values.

Finally, to evaluate the optical attenuation differences between cancer and non-cancer gray matter using the validation dataset, we performed a two-sample, one-tailed Welch's t-test with the hypothesis that gray matter has a lower attenuation compared to both cancer and non-cancer white matter tissues.

For all of the tests mentioned in this section, we have set the alpha value (also known as the significance level) to be 0.05. This means that in statistical hypothesis, we have attained statistical significance when the p-value is less than the significance level, or alpha (i.e., $p < 0.05$ for our study). Furthermore, we have also assumed a normal Gaussian distribution in the attenuation values for all of the brain tissue categories.

SECTION 16: BOOSTRAPPING

We have also performed bootstrapping for further validation of our statistics (*75*). In bootstrapping, we use the observed training dataset (n = 16) to generate 10,000 resampled datasets in an attempt to better estimate the true population distribution. First, we need to calculate the difference in mean (between cancer and non-cancer white matter). This difference in mean is calculated for both the observed data and the bootstrapped dataset. Then, we find the bias value for each tissue category (which is defined as the bootstrapped difference in mean minus the observed difference in mean). Finally, we estimate the true averaged attenuation value for each tissue category after accounting for the bias. Our results in **Table 6** revealed that there are no statistically significant differences between the original and bootstrapped distributions for all brain tissue categories (with p-values between 0.35 and 0.46). As a result, this suggests that our training and validation datasets can adequately reflect the true attenuation distribution of human brain tissues. For this study, n = 10,000 datasets were chosen since it is a sufficiently large number for estimation of the population

distribution; further increase in the resampling size does not exhibit changes in the obtained sampling means.

Tissue	Difference in Mean (WM – Tissue)	Bias	Corrected Mean	P-Value
LGG Tumor Core	**2.2**	**0.02**	**2.18**	**0.44**
LGG Infiltrated Zone	**3.5**	**-0.04**	**3.54**	**0.35**
HGG Tumor Core	**2.3**	**-0.03**	**2.33**	**0.35**
HGG Infiltrated Zone	**2.7**	**-0.01**	**2.71**	**0.46**

Table 6. Bootstrapping. Sixteen patients were recruited in the observed training dataset, while 10,000 resampled datasets were generated in an attempt to better estimate the true population distribution. Since p-values > 0.05, we cannot reject the null hypothesis that our observed dataset representative of the estimated true distribution of the population. LGG: low grade glioma; HGG: high-grade glioma; WM: white matter. **Table and table legends are originally published by Kut *et al.*, (2016). Detection of human brain cancer infiltration *in vivo* in murine and human brain using quantitative optical coherence tomography (to be submitted).**

SECTION 17: SUMMARY AND DISCUSSION

In summary, the goal of surgery in many cancers and especially in brain cancer is to achieve maximal safe cancer resection, while avoiding the damage of functional, non-cancer tissues. Studies have repeatedly and consistently shown that there is substantial survival benefit and delayed recurrence if a surgeon is able to achieve a clean cavity margin for the brain cancer patient (*1, 2, 8*). Furthermore, patients who underwent gross total resection (when compared with patients who only underwent subtotal resection) for both high-grade and low-grade brain cancers enjoyed

a 200% and 160% increase in median survival, respectively (*2, 8, 76, 77*). Furthermore, it is very important to preserve the surrounding non-cancer brain tissues. Studies have shown that patients who unfortunately incurred surgery-related deficits is associated with a 25% decrease in median survival, when compared with patients who underwent the surgery without deficits, regardless of the extent of cancer resection (*78*).

As discussed in a previous section, many imaging tools have been developed in an attempt to identify cancer tissues more readily in the operating room. These imaging tools include surgical navigation, ultrasound, fluorescence imaging, and intra-operative CT and MRI (*25, 28, 30, 79, 80*). However, while these modalities provide significant contributions to neurosurgery, each has its unique limitations in the identification and resection of infiltrative brain cancer margins. For example, pre-operative CT/MRI is currently the clinical standard of care and provides excellent anatomical details of the whole brain for surgical planning, but is very sensitive to brain shifts and position errors in the surgical environment (*22*). Intra-operative CT/MRI, on the other hand, is beneficial because it allows surgeons to assess the resection cavity of the patient mid-surgery, which can reduce the need for a second resection. However, intra-operative CT/MRI is also very expensive, time-consuming and does not provide real-time, continuous guidance.

Intra-operative ultrasound, on the other hand, is useful in the operating room because it can identify *in vivo* blood flow during the surgical resection, which can help to minimize excessive bleeding and stroke-related complications during surgery. However, its resolution and contrast is very limited for the detection of brain cancer and non-cancer, which is very difficult to tell apart using ultrasound alone (*24*).

5-ALA is a very promising technology which can provide intra-operative, fluorescence guided detection of human brain cancer. In addition, preliminary clinical studies have demonstrated that 5-ALA guided surgery can result in an increased extent of resection and improved overall survival for the brain cancer patient (*76, 77*). However, 5-ALA suffers from limited sensitivity in detecting the infiltrative cancer areas (and in detecting low-grade gliomas), since the uptake of 5-ALA uptake varies as a result of blood-brain barrier permeability, edema, cellular/vascular proliferation and cancer grade.

Finally, other emerging technology include stimulated Raman scattering microscopic which provided impressive identification of microscopic brain cancer structures with sub-cellular resolution (*30*); however, additional research is necessary to improve its imaging depth (~0.1 mm), field of view (~0.35 x 0.35 mm), and imaging speed (~1 fps) in order to translate this technology for surgical use in the operating room. On the other hand, visible and near-infrared spectroscopy provides precise estimation of multiple optical parameters which includes scattering, absorption coefficient and anisotropy factors (*81*); however, this imaging technique does not provide sufficiently high resolution for intra-operative brain cancer applications.

As discussed previously, OCT is an imaging modality which is complementary to the use of existing imaging tool. Most importantly, the results in this dissertation suggest that OCT and our developed optical property mapping is more effective than other surgical adjuncts for the specific application to reliably, quantitatively and volumetrically distinguish cancer from non-cancer tissues in real time and with continuous, intra-operative imaging guidance.

Compared with other imaging tools, OCT allows for a good imaging penetration (compared to visible light), label-free contrast, high-resolution imaging, and the ability to provide real-time

quantitative evaluation of optical properties e.g. the optical attenuation used in this study (*66, 72, 82*). In addition, OCT is attractive for intra-operative applications since it is easy to use and it provides non-contact imaging (i.e. imaging at several centimeters above the tissue surface) which minimizes the infection risks for the patients in the operating room.

As mentioned in previous chapters, several groups have made important contributions to the study of human brain cancer using OCT (*60-65, 83*). Our study builds upon these previous studies and moves OCT a critical step forward toward routine clinical use in patients. We accomplish this by performing a systematic and quantitative study which analyzes the optical characteristics of brain cancer and non-cancer in 32 patients (*66, 72*). In addition, we have developed a high-resolution, color-coded attenuation map which can enable real-time and intuitive differentiation of cancer versus non-cancer in large volumetric brain tissue samples. Furthermore, OCT is capable of providing real-time and continuous feedback to the surgeons as they resect the brain tumor core and as they clean up the resection cavity for residual cancer.

Very importantly, our data demonstrated that human brain cancer has a lower attenuation when compared with the surrounding non-cancer white matter (*66, 72*). Here, some readers may be initially perplexed by the outcomes, since it is well known that cancers in most systemic organs are associated with a higher optical attenuation than non-cancer, since cancer tissues generally have an increased cell density and a higher nuclear-to-cytoplasmic (NC) ratio.

To fully understand why brain cancer actually has a lower attenuation than non-cancer white matter, we need to first understand the biological and physical properties which determine the optical attenuation for a tissue sample. For most systemic organs, it is true that the optical

attenuation is governed by two key factors, which increases when there is an increase in cell density and in the NC ratio.

For brain cancers, however the optical attenuation is governed an additional key factor. In other words, the human brain is unique in that the degradation of myelin in white matter (which happens during brain cancer infiltration) will also result influence the attenuation values in the brain, and result in a significant drop in the optical attenuation value. As a result, this and other studies have demonstrated how non-cancer white matter has a higher optical attenuation owing to high myelin content, whereas gray matter has a lower attenuation owing to the absence of myelin (*60, 73, 84-87*).

Moreover, when brain cancer infiltrates into white matter, the optical attenuation is primarily determined by the percentage of myelin present (and only secondarily influenced by cancer density and NC ratio). In human brain cancer, it is known that the invading cancer cells will break down and decrease the expression of myelin in white matter in order to infiltrate the surrounding normal brain (*84-86*); as a result, this lowers the attenuation for both cancer core and infiltrated zone when compared with non-cancer white matter. Thus, our results in this dissertation are consistent with this physiological phenomenon, i.e., that non-cancer white matter had significantly higher attenuation when compared with brain cancer (regardless of grade) (*66, 72*).

On the other hand, when brain cancer infiltrates into gray matter (which lacks myelin), optical attenuation is primarily determined by an increased cell density and NC ratio; consequently, as shown in our study, both cancer core and infiltrated zone had higher attenuation when compared with non-cancer gray matter (*66, 72*). Furthermore, there is no significant difference between the cancer core and infiltrated zone, presumably because the cancer core has a

higher cell density (which increases attenuation) but more complete breakdown of myelin (which decreases attenuation). Finally, all of the attenuation comparisons (for non-cancer versus cancer, low-grade versus high-grade, and cancer core versus infiltrated zone) were largely consistent for both newly diagnosed and recurrent patients (*66, 72*). Thus, we are able to detect brain cancer from non-cancer tissues based on their optical attenuation properties. As a result, OCT is promising as a translational technique to guide the resection of primary brain cancer, especially when used in conjunction with other existing techniques such as cortical stimulation mapping to identify normal, eloquent cortex.

Furthermore, this systematic study reviewed over 4,6000 data points from 32 patients in order to establish an OCT diagnostic threshold in distinguishing cancer from non-cancer with excellent sensitivity (92-100%) and specificity (80-100%) (*66, 72*). Based on the attenuation data, we find that high-grade brain cancer had a higher OCT detection sensitivity but lower specificity when compared with low-grade brain cancer, even though the differences can be attributed to a limited number of tissue samples (and patients recruited) for each sub-category (*66, 72*). More importantly, OCT (at 92-100% sensitivity and 80-100% specificity) exhibited comparable sensitivity but enjoyed much improved specificity when compared with the clinical standard of care (100% sensitivity and 40-50% specificity) (*66, 72*). Here, the clinical standard of care is interpreted as the surgeon's perception of cancer versus non-cancer based on gross appearance of the tissue sample and aided with all imaging tools which are available to the surgeon during resection (which includes surgical navigation, surgical microscopic data, clinical history of the patient, as well as pre-operative and/or intra-operative MRI data). Finally, OCT on the overall also enjoyed better sensitivity (92-100%) and specificity (80-100%) when compared with studies on other imaging tools (which reported a sensitivity of 26-87% and specificity of 42-100% (*66, 72*).

In addition to attenuation analyses, OCT was also capable of detecting brain cancer based on its histological cancer features which include the presence of microcysts, hypercellularity and necrosis (*66, 72*). These histological cancer features are useful as their detection will aid the surgeon in his or her diagnostic of the brain cancer margin, and consequently assist him or her to achieve a cleaner resection margin. Notably, microcysts are generally found in lower-grade brain cancer, while heterogeneous patterns of necrosis/hypercellularity are generally found in higher-grade brain cancer. These cancerous features are helpful for tumor margin detection, since they are not characteristics of the normal brain.

As a result, OCT has great potential as an imaging tool for the localization and mapping of brain cancer margin. However, there are several existing limitations (*66, 72*). For example, OCT does not provide any provide molecular information (unlike Raman spectroscopy or fluorescence imaging). In addition, the current imaging system is also limited by a small imaging volume (at 8-16 mm^3). In order to scan the entire resection cavity to check for residual cancer, we will need to address two existing technical constraints: 1) we need to use a high-performance, high-range robotic device which can substantially increase the OCT imaging area (and volume) by 10- to 100-fold; 2) the computer hardware needs to increase its capacity to allow for storage of hundreds of GBs of data at a time (which will be necessary once we increase the OCT imaging area by 100-fold or higher). Alternatively, the imaging volume can also be addressed by co-registering the OCT images with surgical microscopes, which will allow seamless and continuous surgical guidance in the operating room (*61, 62*). Furthermore, OCT can be complemented by wide-field imaging technologies (e.g. MRI and fluorescence) to facilitate maximal safe cancer resections. In addition to optical property mapping, OCT can also yield other functional information such as Doppler to detect the presence of *in vivo* blood flow, and therefore preventing bleeding and stroke-related

complications during surgery. Finally, OCT can also benefit from future research and advances in the OCT light sources, which can in turn yield faster imaging speeds (e.g. >400 fps vs the current speed at up to 220 fps) (*88*) and axial resolution (e.g. <3 μm versus the current resolution at 6.4 μm in tissue) (*89*).

In conclusion, OCT could have immense translational potential in guiding primary brain cancer detection and resection in the operating room. In addition to primary brain cancer, OCT and the optical property mapping technique may also be useful for distinguishing cancer from non-cancer tissue for other brain cancers including metastatic (i.e. secondary) brain cancer. Building upon this study, we have already conducted the first *in vivo* clinical study on 3 high-grade brain cancer patients (which we will discuss at the next chapter). Overall, this dissertation sets the stage for future large-scale clinical trials and technological advancement that will eventually lead to an uniquely and valuable technology which is capable of detecting infiltrative brain cancer margins quickly and efficiently, resulting in cleaner resection margins for cancer patients and thus improved patient survival and quality of life.

CHAPTER 5: EVALUATION OF INTRA-OPERATIVE FEASIBILITY (IN VIVO MICE AND HUMAN STUDY)

SECTION 1: OVERVIEW

In this chapter, we investigate the intra-operative feasibility of using OCT to detect infiltrative brain cancer margins during surgical resection in the operating room. First, we evaluated the performance of OCT in detecting cancer *in vivo* in murine models implanted with high-grade human brain cancer (*66*). Then, we optimized a portable SS-OCT imaging system and traveled to Guadalajara, Mexico where we conducted a pilot feasibility study by imaging the human brain *in vivo* for 3 patients with high-grade brain cancer. Beyond this dissertation, we aim to continue the clinical studies and are currently in the midst of IRB review for a U.S. study at Johns Hopkins.

SECTION 2: EXPERIMENTAL DESIGN FOR IN VIVO MICE IMAGING

In the previous chapter, we discussed the results for our systematic study involving *ex vivo,* freshly resected human brain tissues obtained from the operating room.

In addition to human data, our study also evaluated the feasibility of OCT in detecting human brain cancer *in vivo* in murine models (*66*). Since the protocols for brain cancer implantation and resection protocols are already well-established for rodent models (*90-92*), only five mice were used for OCT imaging in an attempt to provide proof-of-concept data which evaluates the performance of OCT in the detecting of brain cancer.

SECTION 3: HIGH-GRADE BRAIN CANCER CELL LINES

In order to evaluate the intra-operative feasibility of OCT for the *in vivo* detection and resection of brain cancer margins in the operating, we settled on the use of 5 mice which are implanted with two different high-grade human brain cancer xenografts. These two brain cancer xenografts included 1) a U87 cell line which is a commercial, high-grade human brain cancer (i.e. glioblastoma) cell line; and 2) a NS272 cell line which is derived from a high-grade brain cancer (i.e. glioblastoma) patient-here at Johns Hopkins (*66*).

It is well known that human glioblastoma is extremely infiltrative in nature and forms fingerlike projections which extend from the tumor mass into different areas of the brain. In some cases, glioblastoma cancer cells can even result in the formation of "butterfly gliomas", which means that the glioblastoma cells have migrated via the corpus callosum into the opposite hemisphere of the brain. However, the U87 commercial cell line tends to form a very well-defined brain tumor and does not necessarily capture the highly infiltrative nature of glioblastoma cells.

In contrast, Dr. Alfredo Quinones-Hinojosa's research group (http://doctorqmd.com/the-team/basic-research-team/) has developed NS272, one of the brain tumor-initiating cell (BTIC) cell lines which accurately recapitulate features of the patient's glioblastoma histologically, molecularly and behaviorally (*93-100*). In other words, NS272 is a patient-derived cell line which forms highly aggressive and invasive brain tumors, and is a much more accurate representation of the true infiltrative nature of a human glioblastoma.

Figure 1 demonstrates the range of brain cancer behavior in mice, and the differences between the brain tumors formed by a commercial glioblastoma U87 cell line versus the patient-derived NS272 glioblastoma cell line (*66*). It should be noted that only glioblastoma (i.e. high-

grade brain cancer) cell lines were used in this study because there are no authoritative murine models with lower-grade gliomas at the time of this dissertation.

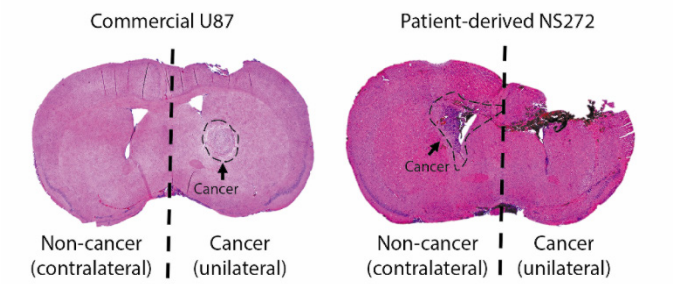

Figure 1. Human cell lines U87 and NS272 demonstrate the range of brain cancer behavior in mice. Mice were implanted with U87 (n = 3) or NS272 (n = 2) cancer cell lines in the right, unilateral hemisphere and underwent cancer resection. After surgery, the brains were extracted and processed for histology. Representative histological images demonstrate that U87 primarily produced spherical tumors with relatively clean margins, whereas NS272 produced remote brain cancer infiltration into the left, contralateral hemisphere via the white matter tracts. **Figure and figure legends are originally from Kut *et al.*, Detection of human brain cancer infiltration ex vivo and in vivo using quantitative optical coherence tomography. Science translational medicine, 7(292), 292ra100-292ra100 (2015). Reprinted with permission from AAAS.**

SECTION 4: IMPLANTATION OF BRAIN CANCER CELL LINES

In order to evaluate the OCT performance in distinguishing brain cancer from non-cancer *in* vivo, we stereotactically inoculated five NOD/SCID male mice (purchased from Charles River Laboratories) when they are 8 weeks old. The inoculation protocol has been previous described (*90*). For the purposes of this study, we used the bregma as a reference point and inoculated the brain cancer cell lines into the murine brain using the coordinates X : 3.5, Y : 1.4 and Z : 3.5 (*66*).

In three of the mice, we injected approximately 10^6 glioblastoma cells into the right hemisphere of each mouse brain *in vivo* using the commercial U87 cell line (purchased from ATCC), which produces mostly spherical and well-defined brain tumor masses (*66*) (**Figure 1**).

In the remaining two mice, we injected approximately 10^6 glioblastoma cells into the right hemispheres of each mouse brain *in vivo* using a patient-derived glioblastoma cell line (NS272) which is more infiltrative in nature and as a result, the NS272 cell is able to more accurately recapitulate the migratory and invasive behavior of cancer cells in high-grade brain cancer patients (**Figure 1**) (*66, 91, 92*).

Regardless of the cell line injected, all 5 mice underwent cancer resection (*90*) at approximately 4 weeks post implantation. The resection protocol is described as follows (*66*). First, we use a scalpel to make an incision on the scalp of each mouse. Then, we use a speed drill to expand the craniotomy window on the skull of each mouse. After surveying the brain tissue surface and making an initial estimate for the cancer location, we will then attempt a surgical resection of the brain cancer using a surgical microscope (Zeiss Pentero 800).

SECTION 5: IN VIVO IMAGING PROTOCOL FOR MICE

This section describes the *in vivo* imaging protocol used to image the mice brain during a brain cancer resection procedure (*66*). First, we acquired OCT images of the *in vivo* brain through the opening of the craniotomy window. Even though the OCT laser source is infrared and invisible to the eye, our imaging system is equipped with a green aiming beam which helps the researcher to direct the OCT beam onto the region of interest for imaging.

Before surgery, we image the tumor mass with OCT and generate the color-coded optical property map. Then, we begin the surgical resection procedure and attempt to remove as much cancer as possible with the help of a surgical microscope. Once surgery is completed, we image the resection cavity again using OCT and scan for the presence of any residual cancer. As control, we have acquire data on the contralateral (left) side of the brain which was not implanted with any

human brain tumor. To summarize, we collect a total of 3 OCT imaging datasets from each mouse at the following locations: 1) at a selected cancer site before surgery; 2) at the same cancer site after surgery, and 3) at a selected non-cancer site (which serves as the control) in the contralateral hemisphere of the brain which has not been inoculated with any cancer cells.

For each imaging dataset, 52 attenuation data points were acquired for each OCT cross-sectional frame. Generally speaking, we acquire 256 OCT cross-sectional frames over a 2-mm span in the y-direction. Using our SS-OCT imaging system and the handheld probe, we are thus able to acquire real-time, volumetric OCT datasets and to generate the corresponding optical property map in approximately 1-2 seconds for a tissue block which is 8 – 16 mm^3 in volume. For each of the OCT imaging datasets, an optical property map was generated by applying the same diagnostic attenuation threshold (at 5.5 mm^{-1}) obtained from the *ex vivo* human study.

After imaging, we sacrifice the mice and harvest their brains for pathological analysis. First, the mice brain was fixed in formalin overnight and then placed in a phosphate buffered saline (PBS) solution. Then, the mice brains were re-sectioned into coronal sections and submitted for histological processing. Once the histological slides are ready, the neuropathologist reviews the histological slides for validation of the OCT results.

SECTION 6: RESULTS FOR THE IN VIVO MICE STUDY

Figure 2 illustrates the results of the *in vivo* mice study (*66*). Based on this figure, we can observe that there is significant cancer present in the mouse brain prior to surgery. In the post-surgery and control images, however, we find residual traces of the brain cancer in the histological images. These residual brain cancer takes up approximately 5% to 10% of the imaged area.

To make sense of the data, histological data was also provided in **Figure 2**. Here, the histological slide was sectioned and displayed in the same orientation as OCT cross-sectional images (i.e., perpendicular to the tissue surface, or perpendicular to the OCT attenuation map and along the dotted lines in **Figure 2**) (*66*).

First of all, the optical property map in **Figure 2A** suggests that there is a significant amount of cancer (shown in red) present in the right hemispheric mouse brain. This suggests that the tumor implantation into the right hemisphere of the mouse brain was successful. Next, we observe in **Figure 2B** that there is still some residual cancer (shown in red) remaining in the right hemisphere of the mouse brain after surgery. This is confirmed by the corresponding histology in **Figure 2C,** which revealed the presence of cancer infiltration. Surprising, **Figure 2D** suggested that there is cancer in our control site, i.e., the left hemisphere of the brain which is not implanted with any brain cancer cells. While this may be puzzling at first, this phenomenon is caused by the presence of highly aggressive glioblastoma cells which has migrated from the right hemisphere into the left (or control) hemisphere of the mouse brain via the corpus callosum.

To conclude, we find good correlation between the optical property maps and the histological results. This suggests that while the attenuation threshold at 5.5 mm^{-1} was obtained from the *ex vivo* human study, the same threshold is also applicable in the *in vivo* mice model. Furthermore, we find that the optical property map is fairly accurate even in the presence of brain motions, uneven tissue surface and other surgical complications (e.g. bleeding). This result suggests that OCT is a feasible and attractive technology for use in the operating room.

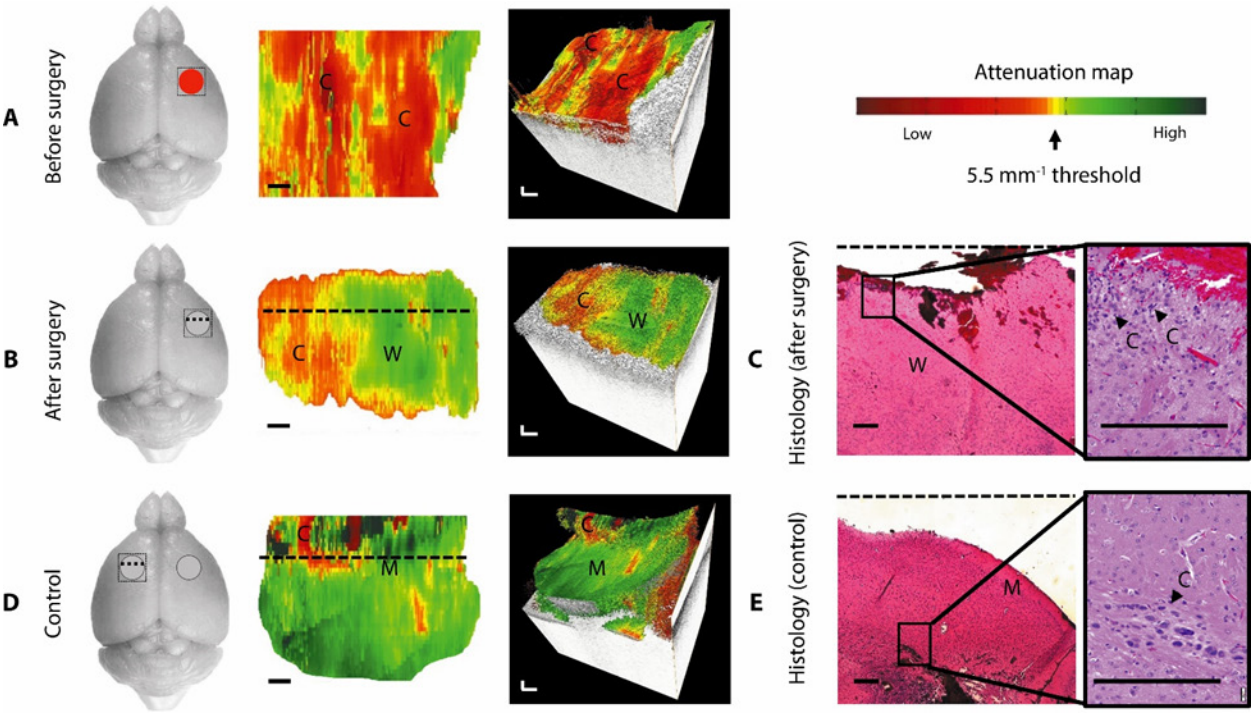

Figure 2. ***In vivo*** **brain cancer imaging in a mouse with patient-derived high-grade brain cancer (GBM272). (A** to **E)** Brain tissues were imaged *in vivo* at the cancer site before surgery (A) and at the resection cavity after surgery (B). After surgical imaging, mice (n = 5) were sacrificed and their brains were processed for histology**.** The corresponding histology for the resection cavity after surgery is shown (C). Using the same mouse, control images were imaged at a seemingly healthy area on the contralateral, left side of the brain (D), with its corresponding histology (E). The red circle indicates cancer, gray circle indicated resection cavity and square was the OCT field of view. 2D optical property maps were displayed using a 5.5 mm^{-1} attenuation threshold. C, cancer; W, non-cancer white matter; and M, non-cancer meninges. Aliasing artifacts at the image boundaries, which were produced when dorsal structures from outside the OCT depth were folded back into the image, were cropped out of image. 3D volumetric reconstructions were overlaid with optical property maps on the top surface. Optical attenuation properties were averaged for each sub-volume of 0.326 mm x 0.008 mm x 1.8 mm within the tissue block, with a step size of 0.033 mm in the x direction. Each histological image (C and E) represented a cross-sectional view of the tissue block: the image corresponds to a single perpendicular slice through the attenuation map, along the dotted lines in (B and D), respectively. Residual cancer cells were marked with black arrows and correspond to yellow/red regions on the attenuation maps (at the level of the dotted line). Scale bars, 0.2 mm. **Figure and figure legends are originally from Kut *et al.*, Detection of human brain cancer infiltration ex vivo and in vivo using quantitative optical coherence tomography. Science translational medicine, 7(292), 292ra100-292ra100 (2015). Reprinted with permission from AAAS.**

SECTION 7: REAL-TIME OCT BLOOD FLOW/VESSEL IMAGING

In addition to providing structural and attenuation data, OCT is also cable of detecting *in vivo* blood flow (due to the Doppler Effect). The detection of blood flow and blood vessel imaging, which is critical for *in vivo* studies to 1) avoid blood influence (false negatives) on OCT cancer detection using the quantitative optical property map); 2) minimize bleeding and stroke-related complications during surgery, especially for blood vessels with a diameter >= 0.5mm; and 3) enable characterization of tumor angiogenesis through blood vessel distribution and morphology, which provides additional parameters and increases sensitivity/specificity in identifying infiltrated brain cancer.

As proof-of-concept, we have implemented real time Doppler and/or speckle de-correlation methods to detect the presence of blood flow. Note that for brain cancer applications, it is important to detect the presence of blood vessels which are embedded beneath the brain tissues surface, and as a result, is not visible to the eye. If we can accomplish that, we will be able to reduce the probability for the surgeon to cut into a normal blood vessel, and therefore reduce the chances of bleeding and stroke complications during surgery.

After trying several different algorithms (such as Doppler OCT and Speckle Variance OCT) available in the existing literature (*101-106*) and by imaging the *in vivo* mice brain for the detection of blood flow, we conclude that the Intensity-Based Doppler Variance (IBDV) algorithm is the preferred method for brain cancer applications. While Doppler OCT and speckle variance OCT are generally excellent in the identification of microvasculature on the brain tissue surface, we are actually interested in the detection of embedded blood vessels which are invisible to the eye, and are relatively large in size (i.e., >0.5 mm which are the blood vessels at greater risks for bleeding and stroke complications during surgery). In short, the IBDV algorithm combines the

advantages of intensity-based methods and Doppler variance method. First, it retains more functional information of blood flow (e.g. transverse flow velocity); second, it is more specific in detecting flow signals especially for embedded blood vessels, and third, it is more robust against the bulk motion and phase instability within an *in vivo* setting.

Now, let us study the algorithm to obtain the IBDV signal. First of all, the algorithm to calculate Doppler variance is derived from autocorrelation techniques and is given by (*103, 105, 106*):

$$\sigma^2 = \frac{1}{T^2}\left[1 - \frac{\left|A_{i+1,z}A_{i,z}^*\right|}{A_{i+1,z}A_{i,z}^*}\right]$$

where σ^2 is the Doppler variance, $A_{i+1,z}$ is the (i+1)th frame at a depth of z and T is the time needed to capture two adjacent frames. Generally, this algorithm is used alongside with averaging in the lateral direction, or in both lateral and axial directions (*103, 105, 106*):

$$\sigma^2 = \frac{1}{T^2}\left[1 - \frac{\left|\sum_{i=1}^{Ni} A_{i+1,z}A_{i,z}^*\right|}{\sum_{i=1}^{Ni} A_{i+1,z}A_{i,z}^*}\right]$$

$$\sigma^2 = \frac{1}{T^2}\left[1 - \frac{\left|\sum_{i=1}^{Ni}\sum_{z=1}^{N_z} A_{i+1,z}A_{i,z}^*\right|}{\sum_{i=1}^{Ni} A_{i+1,z}A_{i,z}^*}\right]$$

where N_i is the total number of frames in the y (pitch) direction, and N_z is the total number of pixels in the axial direction. Notably, the last two equation involve both the amplitude and phase terms of the imaging data; as a result, they have good results only when the phase stability of the system is high. However, in an intra-operative environment where the subject is prone to brain shift and the pulsatile motions of the *in vivo* blood vessels, it is necessary to modify the algorithm such that it is more robust against *in vivo* brain motions.

This modified algorithm is described by

$$\sigma^2 = \frac{1}{T^2}\left[1 - \frac{\sum_{i=1}^{Ni}\sum_{z=1}^{Nz}\left|A_{i+1,z}A_{i,z}^{*}\right|}{\frac{1}{2}\sum_{i=1}^{Ni}\sum_{z=1}^{Nz}\left(\left|A_{i+1,z}\right|^2+\left|A_{i,z}\right|\right)^2}\right]$$

Where all of the phase terms are cancelled out, which leaves only intensity or amplitude terms in the equation (*103*)

A normal NOD/SCID mouse was used to evaluate the utility of IBDV algorithm in detecting *in vivo* blood flow in the brain. We used a scalpel to create an incision site on the scalp, and a speed drill to create the craniotomy window. The meningeal layer was also removed for easy access to and imaging of the cortical blood vessels.

Figure 3 presents a representative image of the intracranial blood vessels which are detected by the SS-OCT system. While the OCT imaging dataset was acquired, processed, displayed and stored in real-time, we currently use an off-line MATLAB implementation of the IBDV algorithm which took approximately 1 second per frame to process.

Using this imaging protocol, we were able to clearly identify blood vessels which are embedded underneath the brain surface. Using the IBDV algorithm, our OCT imaging system can detect blood vessels which are at least tens of microns in diameter. Naturally, larger vessels of more serious surgical concerns can be more readily visualized with OCT.

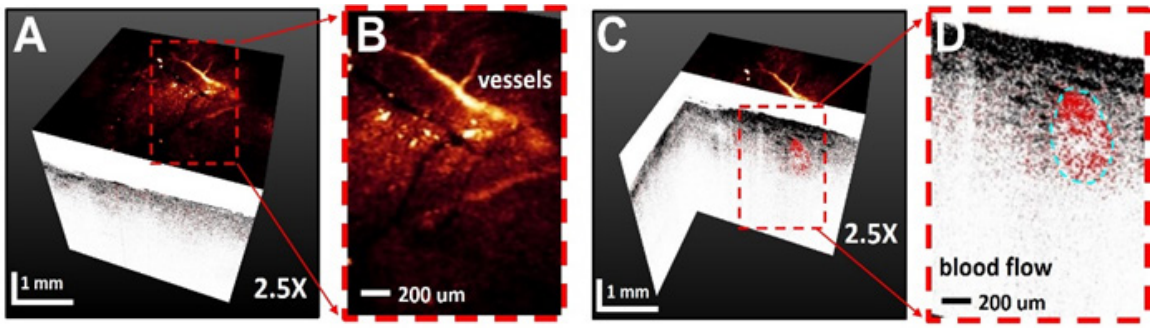

Figure 3. Real-time OCT imaging of blood vessels *in vivo in* normal mouse during brain surgery. (**A**) Volumetric OCT image (gray scale) overlaid with blood vessel *en face* projection map (brightness indicates blood flow). (**B**) 2.5X magnified view. (**C**) Cross-sectional OCT image superposed with blood flow profile. (**D**) 2.5X magnified view shows embedded blood vessel

beneath tissue surface. **Figure and figure legends are published by Kut *et al.* (2016), Detection of human brain cancer infiltration *in vivo* in murine and human brain using quantitative optical coherence tomography (to be submitted).**

SECTION 8: EFFECT OF TISSUE DEGRADATION

Finally, we have studied the effect of tissue degradation on the *ex vivo* mice brain once it is resected from the animal. 4 NOD/SCID mice were used to conduct this study. Overall, we find that there were no significant changes to the quality of the OCT image at 0 to 6 hours after harvesting the brain. In addition, the attenuation data did not change significantly at 0 to 6 hours after harvesting the brain. However, both the OCT image and the attenuation data deteriorated significant when imaged approximately one day after the brain had been harvested.

SECTION 9: OVERVIEW IN VIVO HUMAN STUDY

Since the ultimate goal of this project is to test the ability of OCT in detecting infiltrated brain cancer margins *in vivo* and in real time during surgery, our next step is to evaluate the OCT performance in the operating room without introducing risks to the patients.

Since November 2015, we have been actively recruiting brain cancer patients for our overseas clinical study in Hospital Civil de Guadalajara in Guadalajara, Mexico. To this date, we have collected OCT data from 3 adult primary brain cancer patients, which includes two adult patients with glioblastoma (i.e., high-grade brain cancer) and one adult patient with medulloblastoma (i.e., a cerebellar brain tumor which is more commonly found in pediatric patients). The OCT imaging protocol and *in vivo* results are described in the following sections.

SECTION 10: OCT IMAGING SYSTEM

For the *in vivo* human study, we are using a portable, suitcase-sized swept-source imaging system with a K-clock generator. As described in Chapter 2, this imaging system operates at a center wavelength of around 1310 nm with a spectral bandwidth of around 134 nm. The suitcase-sized system is above to scan at a rate of up to 100 kHz (i.e., up to 100,000 A-lines per second). In addition, we use a home-built, handheld imaging probe which is forward viewing and is capable of performing two-dimensional beam scanning (in the x and y direction) using two galvanometer optical scanners. Overall, the SS-OCT imaging system is capable of imaging at an axial resolution of around 9 µm and a lateral resolution of around 15 µm. Finally, a high-speed digitizer (ATS8351) and graphics processing unit (GeForce GTX 760) is used to enable real-time imaging of the brain tissue at several seconds per tissue sample.

Figure 4 illustrated the components of the complete OCT imaging system which included the suitcase-sized SS-OCT engine, a green aiming beam (for visualization of the infrared scanning beam on the brain tissue surface), galvanometer drivers and power supply, and a desktop computer system equipped with a high-performance digitizer and GPU video card.

Figure 4. Components of the complete OCT imaging system used for the *in vivo* clinical study in Hospital Civil de Guadalajara in Guadalajara, Mexico.

SECTION 11: IN VIVO HUMAN IMAGING PROTOCOL

The imaging protocol for imaging *in vivo* in patients is described as follows:

For each brain cancer patient, the surgery will go as usual as part of routine clinical care. Then, the neurosurgeon will select some suitable brain regions for *in vivo* OCT imaging. Notably, these imaged brain regions should be resected in the course of surgery anyways as part of standard of care; as a result, the site selection is not influenced by this study in any way.

Generally, it will take about 1-2 minutes to acquire *in vivo* OCT data for each selected brain region (at a volume of approximately 8 – 16 mm^3 per region). After the *in vivo* OCT dataset is acquired, the neurosurgeon will be free to resume his or her routine surgical duties. The research team will then receive the freshly resected tissues and place the tissues in formalin for the fixation process. Afterwards, the fixed tissues will be transferred to a phosphate buffered saline (PBS) medium, and stored in sealed containers.

Finally, the resected tissue samples are processed as H&E histological slides and reviewed by the neuro-pathologist for histological confirmation of the tissue type and cancer grade.

SECTION 12: SAFETY CONSIDERATIONS IN THE OR

Like any other clinical studies, it is of utmost importance to first ensure the safety of the patients. In this section, we demonstrate how previous literature have proven that OCT is a safe imaging tool for use in the clinical setting. We will also discuss what steps we have towards minimizing the risks for any patients who participate in this study.

First of all, the OCT imaging technology has been proven safe in multiple previous clinical studies. Multiple research groups have conducted clinical studies regarding the use of OCT

imaging on human patients (*41, 49, 58, 60, 107*), and no safety issues have occurred. Furthermore, OCT has is approved by the Food and Drug Administration (FDA) in the U.S. for retinal imaging, which has quickly become the standard of care for the diagnosis of many retinal diseases. In addition, OCT has also been approved by the FDA for other indications which include intravascular and esophageal imaging. For both intravascular and esophageal imaging, an FDA-approved OCT catheter is generally used to insert into the cavity (of the blood vessel or of the esophagus) for imaging. In contrast, our project uses a handheld OCT imaging probe which is expected to be safer (when compared to the OCT catheter) and is more robust against infection risks as the handheld probe will not contact the brain surface of the patient throughout the procedure.

In terms of sterilization, we will follow a standard sterilization protocol (which is routinely used for intra-operative ultrasounds in neurosurgical procedures here at Johns Hopkins). First, the OCT handheld probe is wiped down with a germicidal cleanser. Then, the OCT probe is encased in an FDA approved plastic sheath. **Figure 5** demonstrates the sterilization procedure for our OCT handheld imaging probe in the operating room, respectively. When compared to intra-operative ultrasound imaging, our handheld imaging probe has an inherent advantage as it is non-contact and will not directly contact the brain during imaging; instead, it will image at a working distance of 2.5 cm above the brain tissue surface. As a result, infection risks for OCT imaging should be comparable to the regular surgical procedure.

Most importantly, the imaging data collected in this study will only be used to evaluate the intra-operative feasibility of the technology. The data will not be used to influence the clinical decision in any way. In other words, the patient care remains unchanged.

Finally, patients will be monitored by the attending neurosurgeon for any potential side effects during the OCT imaging procedure. In addition, the patients will be monitored during follow-up visits (as part of their routine clinical care) by their primary neurosurgeon at 1, 3 and 6 months after the surgery. If any unanticipated problems occur, they will be reported promptly to the IRB. The aforementioned neurosurgeon(s) will be available to provide necessary care during the procedure and follow-ups, and to determine when and if the OCT imaging should stop.

Since we recruited our first patient for *in vivo* OCT imaging in November 2015, no complications have been reported for any of the recruited patients as a result of this clinical study.

Figure 5. Handheld OCT imaging probe in use in the operating room. In this clinical study, we follow the standard sterilization procedure in the operating room**. Figure and figure legends are published by Kut *et al.* (2016), Detection of human brain cancer infiltration *in vivo* in murine and human brain using quantitative optical coherence tomography (to be submitted).**

SECTION 14: IN VIVO HUMAN DATA

The following section summarizes the results from the *in vivo* clinical study.

At the time of this dissertation, 3 primary brain cancer patients (2 glioblastoma and 1 medulloblastoma patients) have already been recruited for this study. A total of 22 tissue samples were imaged in real-time using the suitcase-sized, swept-source OCT imaging system with the

built-in K-clock generator. **Figure 6** illustrates the use of the OCT handheld imaging probe on the human brain during the surgical resection procedure.

Figure 6. Imaging of the human brain during surgery. The OCT handheld imaging probe was used to image the brain tissue surface at working distance of 25 mm. At the time of this dissertation, we have collected data from 3 primary brain cancer patients for a total of 22 tissue samples. **Figure and figure legends are published by Kut *et al.* (2016), Detection of human brain cancer infiltration *in vivo* in murine and human brain using quantitative optical coherence tomography (to be submitted).**

Based on a careful review of the imaging datasets, we find that the optical attenuation values for the *in vivo* human brain is approximately 1 mm^{-1} lower than the optical attenuation values found in *ex vivo* human brain tissues. This suggests that we should also lower the optical attenuation threshold value accordingly, although we need to recruit more patients and tissue samples in order to make any statistically meaningful conclusions. **Figure 7** summarizes the attenuation results for the *in vivo* versus *ex vivo* datasets.

There could be several reasons behind the lower attenuation results found in *in vivo* datasets: 1) the OCT signal could be weaker due to the addition of the sterilized plastic sheath; 2) the presence of blood flow and brain motions may influence the OCT signal profile and consequently the attenuation results; 3) the suitcase-sized SS-OCT system (used for *in vivo* data collection) may have different imaging parameters which causes it behave slightly differently when compared with the cabinet-sized SS-OCT system (used for *ex vivo* data collection).

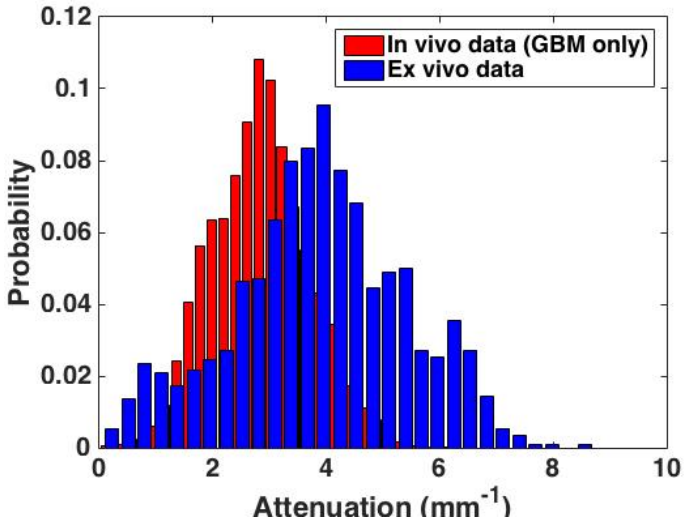

Figure 7. Comparison of attenuation results for the *in vivo* versus *ex vivo* dataset. The *in vivo* dataset (shown in red) was collected from 2 glioblastoma patients. The *ex vivo* dataset (shown in blue) was collected from the 9 glioblastoma patients in the *ex vivo* training dataset. Notably, *in vivo* data from the medulloblastoma patient was excluded for the purposes of this analysis. **Figure and figure legends are published by Kut *et al.* (2016), Detection of human brain cancer infiltration *in vivo* in murine and human brain using quantitative optical coherence tomography (to be submitted).**

To account for the drop in attenuation values (by 1 mm^{-1}), we have decided to display the optical property maps with a diagnostic attenuation threshold of 4.5 mm^{-1} (as opposed to the 5.5 mm^{-1} reported in the *ex* vivo human study). On the overall, the *in vivo* dataset behaves as expected; brain cancer tissues have a lower attenuation when compared with non-cancer white matter. **Figure 8** gives representative data of cancer versus non-cancer tissues detected in the *in vivo* study.

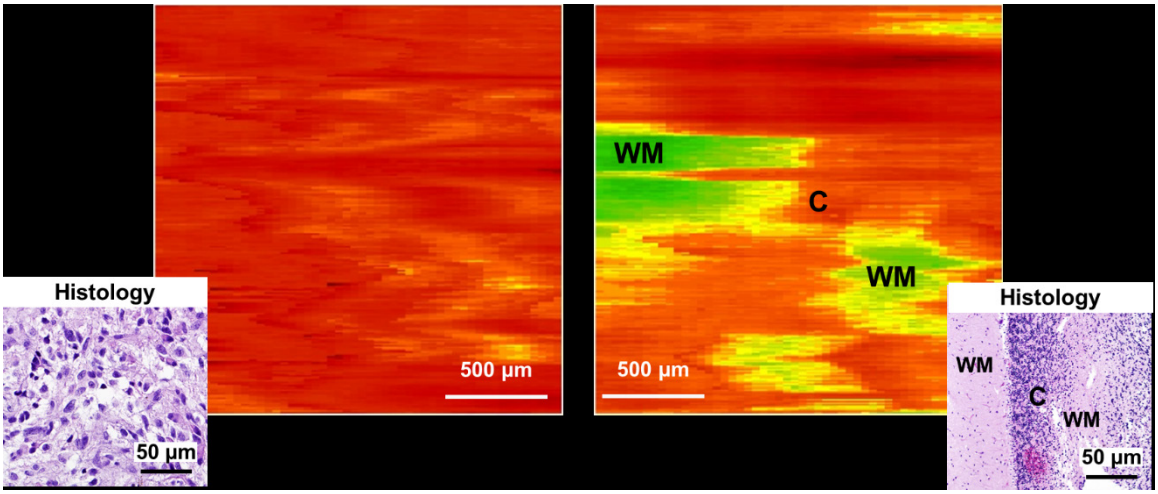

Figure 8. Optical property maps generated from the *in vivo* human data. On the left, we show the optical property map and the histological results for a brain tissue which exhibited high cancer density. On the right, we show the optical property map and histology for brain tissue which contained areas of concentrated cancer as well as areas of non-cancer white matter. On the overall, *in vivo* brain cancer has a lower attenuation the brain tissue when compared with *in vivo* non-cancer white matter. WM: White matter and C: Cancer. **Figure and figure legends are published by Kut *et al.* (2016), Detection of human brain cancer infiltration *in vivo* in murine and human brain using quantitative optical coherence tomography (to be submitted).**

CHAPTER 6: MULTI-PHOTON FLUORESCENCE

SECTION 1: OVERVIEW

In this chapter, we investigate the feasibility of using multi-photon fluorescence in detecting brain cancer margins, which will prove especially useful when used in conjunction with OCT. First, we evaluated the performance of MPF in detecting cancer *ex vivo* in murine models implanted with high-grade human brain cancer. Then, we obtained MPF images of *ex* vivo, freshly resected human brain cancer tissues from the operating room. Finally, we analyze the MPF data both qualitatively and quantitatively, and explore the potential of the OCT/MPF technique in clinical applications.

SECTION 2: COMPLEMENTARY TECHNIQUE TO OCT

As established in the previous chapters, OCT is a valuable technique which can be used to identify brain cancer margins with great sensitivity and specificity in the operating room. While OCT can be used as a standalone device, we believe that maximum clinical value will be achieved if OCT can be integrated into existing imaging technologies for eventual translation into the operating room. Macroscopically, OCT can be integrated with surgical image guidance systems such as surgical microscopes or marker-based tracking systems, which can be used to establish spatial coordinates for cancer versus non-cancer throughout the entire resection cavity. Microscopically, spot detection techniques such as Raman spectroscopy or multi-photon fluorescence are attractive because they can further improve the detection accuracy of OCT by providing complementary molecular information and by identifying subcellular structures at critical zones in the brain. In

this chapter, we focus on exploring the feasibility of identifying brain cancer margins with multi-photon fluorescence, and explore the future potential of an OCT-MPF integrated imaging system for brain cancer and other clinical applications.

SECTION 3: IMAGING PRINCIPLES

In traditional fluorescence imaging, a single photon is used to excite the electron of a fluorophore from the ground state to the excited state. Shortly after, the excited electron relaxes and return back to the ground state, releasing a lower-energy photon and thus generating a fluorescence signal in the process. In order for fluorescence to occur, the energy of the exciting photon must be equivalent to the energy difference between the excited and ground states of the electron (*108*).

In multi-photon fluorescence imaging, two or more photons are used to simultaneously excite the electron of a fluorophore. However, the combined energy of these photons must still match the energy difference between the excited and ground states of the electron (which is referred to as ΔE in this chapter). In order for the photon energies to combine, the photons must all arrive at the same location within a narrow time window (10^{-18}) to excite the same electron (*108*). Under normal daylight or white light conditions, it is virtually impossible to get two or more photons to arrive at the same location with such accuracy. As a result, a high photon flux at approximately 10^{20}-10^{30} photons per cm^2 per second is necessary for multi-photon excitation to occur (*108*). Nevertheless, we run into another problem: in order to achieve such a high photon flux, we will need to deposit approximately 10^{12} W per cm^2, which is equivalent to the power output of 5000 nuclear reactors converted to light and deposited on a single square centimeter (*109*). Clearly, biological tissues cannot remain viable when exposed to such a high power density for prolonged periods of time. How, then, can we achieve viable biological imaging without

vaporizing the tissue sample using multi-photon fluorescence? The answer lies in using pulsed lasers instead of using a continuous illumination source (*109*). For a pulsed laser, the laser emits pulses which are extremely high in power density but are only on for very short periods of time. As a result, even though the peak power during a pulse is extremely high, the averaged laser power is relatively low and roughly equivalent to the power output of a conventional confocal microscope (*109*). Generally speaking, the Ti:Sapphire lasers are preferred for multi-photon fluorescence imaging because they are capable of generating laser pulses for a duration of approximately 100 femtoseconds per pulse and with a low repetition rate at approximately 100 MHz (i.e. a time gap of 10 nanoseconds between 2 pulses) (*108, 109*). In addition to concentrating the photons temporally, we also concentrate the photons spatially by using a microscope objective lens with moderate to high numerical aperture (NA); since the numerical aperture is inversely proportional to the spot size in a Gaussian beam, a higher numerical aperture will focus the beam onto a small spot on the focal plane where the photon flux is extremely high. In summary, researchers are able to greatly increase the probability of multi-photon absorption by concentrating the photons both temporally and spatially. In additions, we are able to avoid depositing excessive power onto the tissue sample by the use of a pulsed laser.

In this chapter, we will focus on discussing the principles of two sub-categories of multiphoton fluorescence imaging: two-photon fluorescence (TPF) and second harmonic generation (SHG). In addition, we will detail the results made from our study of brain cancer tissues using these imaging modalities. Finally, we will discuss briefly regarding the future directions of the multi-photon imaging techniques and its implications in clinical applications.

SECTION 4: TWO-PHOTON FLUORESCENCE

Two-Photon Fluorescence (TPF) functions by exciting an electron in the fluorophore by the simultaneous arrival of two photons within a time window of 10^{-18} seconds (*108*). In order to generate a fluorescence signal, the combined energy of both photons must be roughly equal to the energy difference between the excited and ground sates of the electron. As a result, any combinations of two photons can be used to produce the required energy difference (ΔE). For convenience, however, two identical photons at half the energy level (i.e., 0.5 ΔE) are generally used to generate two-photon fluorescence images. Since the energy of a photon is inversely proportional to its wavelength, this means that we use photons at approximately double the wavelength for TPF when compared with traditional single-photon fluorescence imaging.

In addition, it is well known that the fluorescence emission by the fluorophore increases in proportion to the square of the excitation intensity (i.e. the number of photons per time and per square area). Furthermore, the excitation intensity is maximized at the focal point along the optical axis, but decreases in proportion to the square of the distance away from the focal point. This means that on the overall, the fluorescence emission reaches its peak at the focal point but decreases in proportion to the distance raised to the fourth power. As a result, we are able to confine the two photon fluorescence imaging volume to less than1 μm^3 at the focal point. This is a chief advantage of two-photon (and other types of nonlinear) fluorescence: since all fluorescence emissions can be pinpointed to the focal point, we are able to achieve superior image resolution when compared with confocal microscopy (which often suffers from poorer resolution due to out-of-focus fluorescence signals).

In fact, there are multiple advantages associated with TPF and other multi-photon fluorescence imaging methods (when compared with confocal microscopy) (*108*). First, multi-photon fluorescence has superior resolution since all fluorescence emissions can be pinpointed to the immediate vicinity of the focal point (*108, 110, 111*). Second, multi-photon fluorescence enjoys an improved depth penetration (*112, 113*). Readers may recall that multi-photon excitation uses longer wavelengths since two or more photons are required to reach the energy difference between the excited and ground states of the electron. As a result, MPF uses infrared light which penetrates deeper into the biological tissue with less absorption and scattering when compared with UV or visible light. Third, MPF has superior contrast when compared with confocal microscopy (*114*). Since a high photon flux is required for two or more photos to team up and excite an electron, any photons which are scattered are too diluted to produce an emission fluorescence signal. As a result, even though these scattered photons cannot contribute to the fluorescence signal, they also do not compromise the image contrast (unlike single-photon fluorescence in confocal microscopy) (*108*). Finally, photo-bleaching and photo-damage is localized to the focal point only MPF, but can occur throughout the tissue sample in confocal microscopy (*115*).

SECTION 5: SECOND HARMONIC GENERATION

Unlike other types of multi-photon fluorescence, higher order harmonic generation do not need to excite the electrons in a fluorophore to generate a fluorescence signal. Instead, higher order harmonic generation is a process where two or more photons are simultaneously scattered and combined to generate a new photon at higher energy (i.e. the sum of all original photons). While the process of higher order harmonic generations has long been recognized since the early days of

laser physics in the 1970s (*116, 117*), the method is not widely adopted for three-dimensional imaging of biological tissues until recently in the 21st century (*108, 118, 119*).

Generally, researchers adopt either second harmonic generation (SHG) or third harmonic generation (THG) for biological imaging. As suggested by their names, second harmonic generation uses the simultaneous scattering of two photons to generate a new photon at double the energy), whereas third harmonic generation uses the simultaneous scattering of three photons to generate a new photon at triple the energy. Since the photon energy is proportional to its frequency, SHG generates a new photon with twice the energy and therefore twice the frequency. Similarly, THG generates a new photon with triple the energy and triple the frequency. As a result, SHG and THG are often referred to as frequency doubling and tripling techniques, respectively. However, TGH is significantly more difficult to achieve than SHG; this is because there is very little third order non-linearity in biological tissues. As a result, this dissertation will focus on discussing the principles behind SHG, as well as the results generated with SHG imaging.

SECTION 6: AUTOFLUORESCENCE

Traditional confocal fluorescence imaging generally requires the injection of an exogenous contrast agent into the biological tissue/organism which is being studied. This is not ideal for clinical applications, as most exogenous fluorescence contrast agents are not FDA approved and therefore are difficult to translate into clinical use. Autofluorescence imaging, on the other hand, takes advantage of the natural emission of light produced directly from biological materials such as mitochondria or lysosomes when they have absorbed light. As a result, it is ideal for clinical applications as no exogenous contrast agents are necessary. Furthermore, the autofluorescence signals may reflect molecular and/or functional information regarding the biological tissue/organism, thus providing additional information to the clinical user.

Both two-photon fluorescence and second harmonic generation are excellent techniques to provide non-invasive and three-dimensional autofluorescence imaging of biological tissues. While confocal microscopy can be used with infrared light sources to produce an autofluorescence signal from the biological tissue, it is generally difficult for confocal techniques to separate other unwanted fluorescence signals from the true emission spectrum of the autofluorescence signals (which are very broad in spectrum). In addition, confocal microscopy can only image at very limited depths (at up to few of tens of micrometers). In contrast, two-photon fluorescence and second harmonic generation are capable of focusing the emission signal to the focal spot of the beam; as a result, it is capable of imaging at superior resolution while filtering unwanted signals from other locations of the tissue sample (*120*). Finally, TPF and SHG use light sources in the infrared range, with allows for imaging at up to 1-2 mm in depth.

In this study, we study the presence of nicotinamide adenine dinucleotide (NADH) and flavin adenine dinucleotide (FAD) signals in TPF imaging. NADH and FAD signals mostly originate from the cell mitochondria, as both are cofactors in the citric acid cycle for energy production. In addition, we also study SHG which requires the presence of non-centrosymmetric structures in order to produce a strong enough autofluorescence signal. Examples of non-centrosymmetric structures which are intrinsic to the biological tissue/organism include collagen, myosin and microtubules (*121*). In the next sections, we will discuss the study design and results associated with the NADH, FAD and SHG autofluorescence imaging of human brain cancer.

SECTION 7: MPF IMAGING SYSTEM

In this study, we use a home-built multiphoton fluorescence imaging platform which is modified from an Olympus confocal microscope. This platform is able to provide a lateral resolution of 0.34 μm and an imaging depth of 2 mm. **Figure 1** gives an overview of the imaging system.

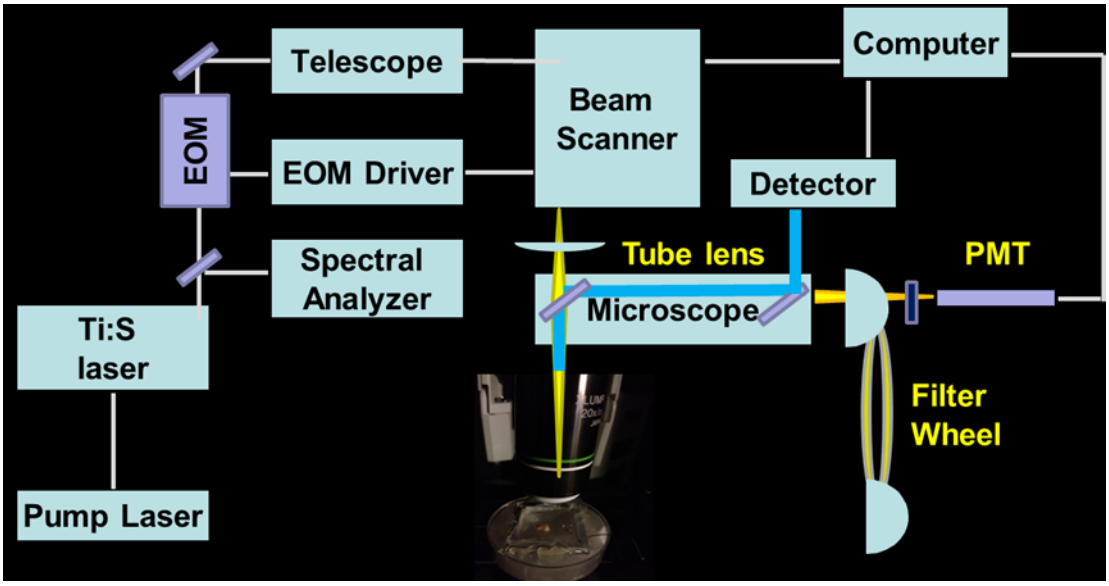

Figure 1. Design of the multi-photon fluorescence imaging system. Ti:S laser: Titanium-Sapphire laser; EOM: electro-optical modulator and PMT: photomultiplier tube. **Figure and figure legends are published by Kut *et al.* (2016), Detection of human brain cancer in *ex vivo* human using multi-photon fluorescence (to be submitted).**

An excitation wavelength between 750 nm and 780 nm was used to collect both two-photon fluorescence and second-harmonic generation signals, while different filters are used to separate the emission spectrums for NADH, FAD and SHG respectively. **Table 1** shows the two-photon and SHG emission spectra. When an excitation of 750 nm is used, the peak emissions for two-photon imaging are 450 nm and 525 nm, respectively; for SHG signals, the peak emission is 400 nm. As a result, we have selected an emission filter at 447 ± 30 nm to isolate the NADH signal; an emission filter at ≥ 496 nm to isolate the FAD signal; and finally, an emission filter at 390 ± 9 nm to select the SHG signal. For human brain cancer applications, we deposited a total of approximately 30-40 mW onto the brain tissue samples. Images were captured with a field of view of up to 0.75 X 0.75 mm^2 per two-dimensional frame at a particular depth in the image. If three

dimensional imaging is desired, we can also capture a series of two-dimensional images of the brain cancer tissue at a step size of approximately 1μm per frame in the z direction.

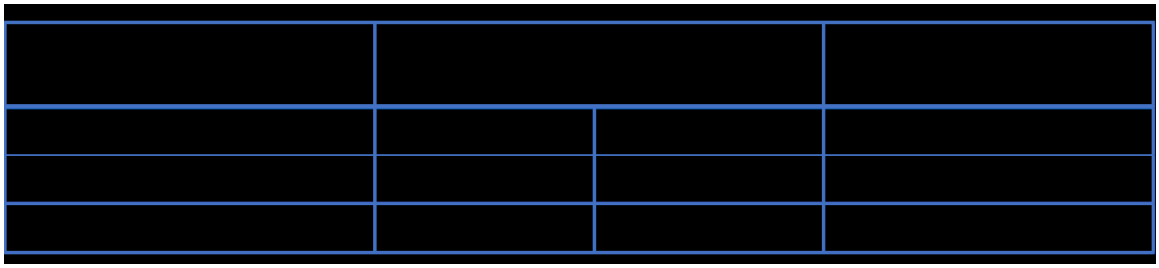

Table 1. Emission spectra of two-photon fluorescence and second harmonic generation imaging. The shaded areas represent the emission spectra captured by the NADH filter (in red), FAD filter (in blue) and SHG filter (in green), respectively.

In this study, we recruited a total of 32 patients who are undergoing brain lesion surgeries at Johns Hopkins. These patients include 19 patients with primary brain cancer in the cerebrum (i.e., 7 grade II, 6 grade III and 6 grade IV gliomas), 10 patients with secondary brain cancer (i.e., 9 lung metastasis and 1 gastrointestinal metastases) as well as 3 patients with miscellaneous brain lesions (i.e., 1 cerebellar brain tumor, 1 meningioma and 1 radionecrotic lesion).

For the purposes of this dissertation, we will only focus on the results from patients with primary brain cancer in the cerebrum (grade II-IV glioma) and with lung metastases to the brain. This is because we have very limited datasets for patients with other cancer types. In addition, it should be noted that patients with grade I gliomas were purposefully excluded from this systematic study because of its distinct nature from other glioma grades; while grade II-IV gliomas are incurable brain cancers which are extremely aggressive and infiltrative in nature, grade I gliomas are typically non-infiltrative and is generally curable.

SECTION 8: ACQUIRING HUMAN BRAIN TISSUE SAMPLES

For all of the 32 patients in the study, brain tissues were freshly resected from the patient using standard neurosurgical techniques (which includes microsurgical dissection when necessary, and the use of routine intra-operative surgical navigation). Tissues necessary for clinical diagnosis of the patient were obtained and sent to the Pathology department. If there are any excess tissues which will otherwise be discarded in the course of surgery), these tissues will be sent to the laboratory for research purposes.

Brain tissue samples from were obtained from patients and classified as cancer versus non-cancer, as categorized by the neurosurgeon and later validated by a neuro-pathologist. Notably, non-cancer tissues were also obtained from the resection margins which showed normal pathology (i.e., less than 5% cancer cells based on visual estimate by the neuropathologist). These resection margins from brain cancer patients were either obtained as part of the planned trajectory to the cancer core, or were resected along the surgically defined margins at the interface between infiltrated cancer and the normal brain.

SECTION 9: IMAGING PROTOCOL

As described in the earlier sections, a home-built MPF imaging system was used to image all the *ex vivo* brain tissue samples obtained from primary and secondary brain cancer patients.

The *ex vivo* MPF imaging protocol can be described as follows. First, each tissue sample was freshly obtained from the operating room and immediately sent to the laboratory for imaging. Then, each tissue was re-sectioned into flat tissue samples for optimal MPF imaging.

For histological registration and correlation purposes, the brain tissue samples were glued to a petri dish and then marked with India ink on the tissue surface. After the India ink is affixed onto the tissue surface, a cover glass was carefully placed on top of the tissue surface to prevent

dehydration of the tissue and also to flatten the tissue surface. The tissues were then kept in a 4°C refrigerator until it is time for imaging.

To begin the imaging procedure, the tissue sample is first transferred onto the imaging stage. Then, we add a drop of water to the cover glass and lower the objective lens onto the tissue surface. Next, we use the eyepiece to locate and center the India ink mark onto the center of the microscopic field of view (FOV). This marked our zero coordinates in the x and y direction. A translational stage was then used to record the spatial coordinates of the imaging beam as we move around the tissue sample. Once we have identified a region of interest, we will capture two-dimensional images with a 0.35 x 0.35 mm^2 field of view. Notably, we can direct the MPF imaging software to capture a three-dimensional volume at approximately 1-2 μm per frame in the z-direction. In addition, the x-y translational stage can be used to capture a mosaic image at a much larger field of view. Finally, the OCT imaging data was stored digitally in a computer for image post-processing and quantitative analysis using the ImageJ software or the MATLAB platform.

At the end of the imaging session, the tissue samples were placed in 10% neutral buffered formalin overnight. After formalin fixation, the tissue samples were then transferred to a phosphate buffered saline (PBS) solution and submitted for histological processing and correlation.

SECTION 10: STRUCTURAL CHARACTERISTICS FOR NON-CANCER BRAIN TISSUES

First, we study the structural characteristics of non-cancer white matter and gray matter in brain. Gray matter is a component of the central nervous system which contains numerous neuronal cell bodies as well as some supporting structures including neuropils, glial cells, synapses and capillaries; it is generally found in the cerebral cortex and in deep gray nuclei. White matter is also a component of the central nervous system which consists mostly of myelinated axons (which

transmit signals from one region in the brain to another) and the supporting glial cells; it is found in the deeper regions (i.e. sub-cortical layers) of the brain. The color difference between white matter and gray matter is mainly attributed to the presence of myelinated axons in white matter, which is highly scattering and therefore appears white to the human eye.

In this study, we study the qualitative brain characteristics of gray matter versus white matter, and validate with the corresponding histology. **Figure 2** shows the two-photon results (i.e., NADH and FAD images) as well as the corresponding histology for gray matter and white matter. Notably, we are able to detect the presence of neuronal cell bodies (marked by n) and the presence of supporting glial cells which include satellite oligodendrocytes (marked by so) and protoplasmic astrocytes (marked by pa). Notably, neuronal cell bodies (also known as soma) houses the cell nucleus of the neurons, as well as a myriad of different cell organelles including mitochondria, and Nissi granules. Satellite oligodendrocytes can be found adjacent to the neuronal cell bodies and are used to regulate the extracellular fluid and the micro-environment in gray matter (*122*). Protoplasmic astrocytes, on the other hand, are often found near the blood vessels to produce the perivascular effect, i.e., the interactions between the astrocytes and the endothelial cells of the blood vessels in an effort to regulate the blood-brain barrier; in addition, some protoplasmic astrocytes are also found adjacent to the pial surface. All of these structures can be found in the NADH, FAD and H&E images. Overall, gray matter is characterized by the presence of many neuronal cell bodies, which have a larger diameter when compared with the other supporting cells. Depending on the neuronal type, the cell body can appear ovoid, triangular, or star-shaped.

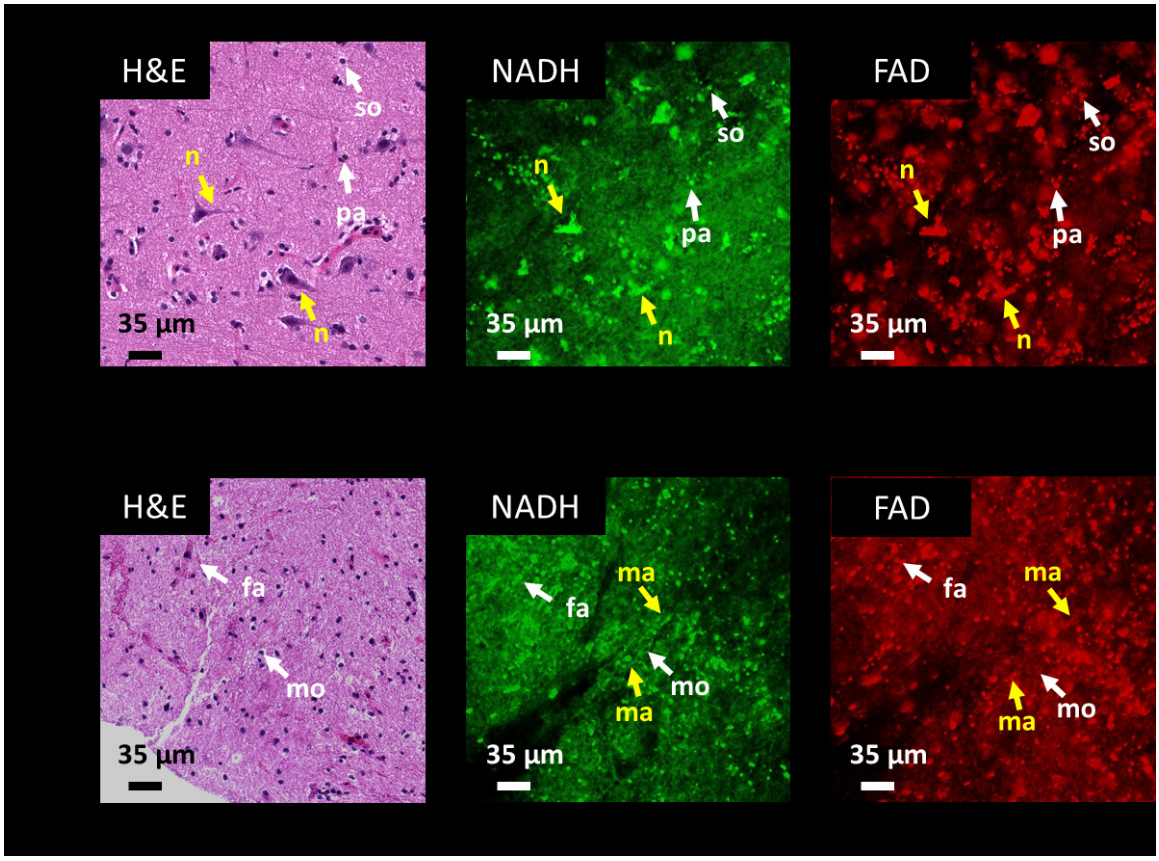

Figure 2. Structural characteristics of non-cancer gray matter versus white matter. Two-photon images (including NADH and FAD imaging) are presented along with its corresponding H&E histology. Overall, non-cancer gray matter can be characterized by the presence of neuronal cell bodies, and non-cancer white matter can be characterized by a dense population of supporting glial cells (e.g. oligodendrocytes and astrocytes) as well as the presence of myelinating axons. Notably, myelinating axons cannot be visualized on H&E histology alone without the addition of special stains e.g. Luxol blue stain. Abbreviations include n: neuronal cell body; so: satellite oligodendrocyte; pa: protoplasmic astrocyte; fa: fibrous astrocyte; mo: myelinating oligodendrocyte; and ma: myelinated axon. **Figure and figure legends are published by Kut *et al.* (2016), Detection of human brain cancer in *ex vivo* human using multi-photon fluorescence (to be submitted).**

White matter, on the other hand, is characterized by an absence of neuronal cell bodies, and the presence of numerous myelinated axons (marked by ma) and supporting glial cells which include the fibrous astrocytes and myelinating oligodendrocytes (marked by mo). Here, the fibrous astrocytes are generally used to form perivascular and subpial endfeet; addition, many fibrous astrocytes are also used to form perinodal processes at the nodes of Ranvier (i.e., the gaps in the

myelin sheath of a neuron). Myelinating oligodendrocytes, as the name suggests, are used to support and provide insulation to the neurons by forming the myelinated sheath (*122*). Overall, we can locate the presence of oligodendrocytes and astrocytes in NADH, FAD and H&E images. However, it should be noted that we can only observe the presence of myelinated axons in the NADH and FAD images, but not in the H&E image. This is because the presence of myelination cannot be easily observed using H&E stains alone, and will require special stains e.g. Luxol fast blue stain for visualization. Overall, white matter is characterized by a dense population of glial cells (e.g. oligodendrocytes, astrocytes) and also by the presence of myelinated axons in the image.

SECTION 11: STRUCTURAL CHANGES FOR GLIOMAS

Figure 3 and 4 demonstrates the typical cellular and vascular changes in primary brain cancer. In terms of cellular changes, grade II-IV gliomas are characterized by an increase in cellular density, increase in cellular heterogeneity, and a higher nuclei-to-cytoplasmic (NC) ratio when compared with non-cancer. In terms of vascular changes, grade II-IV gliomas are characterized by an increase in blood vessel density, the presence of dilated and irregularly shaped blood vessels, and the presence of invading cancer cells into the blood vessels.

Using two-photon fluorescence imaging, we study the brain characteristics for non-cancer, grade II glioma, grade III glioma and grade IV glioma. **Figure 5** demonstrates the cellular changes found in the different grades of primary brain cancer. First of all, let us look at the cellular changes for grade II glioma (when compared with the non-cancer white matter). While the cancer changes for grade II glioma is somewhat subtle, we can observe an increase in cellular density and an increase in cellular diameter on the overall. These cellular changes are especially evident in grade

III and IV glioma samples, which showed clearly enlarged and irregular-looking cancer cells which arise from the supporting glial cells of the brain. In addition, the cellular density is increased.

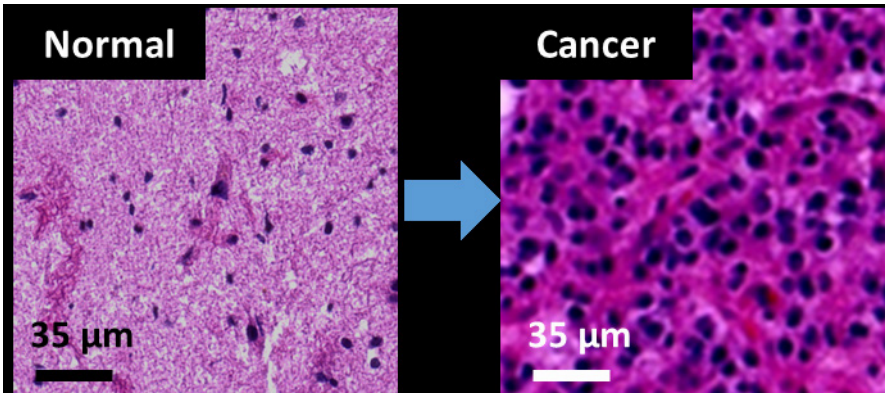

Figure 3. Typical cellular changes in primary brain cancer. Overall, primary brain cancer is characterized by a higher cell density, increased cell heterogeneity and a higher nuclei-to-cytoplasmic ratio. **Figure and figure legends are published by Kut *et al.* (2016), Detection of human brain cancer in *ex vivo* human using multi-photon fluorescence (to be submitted).**

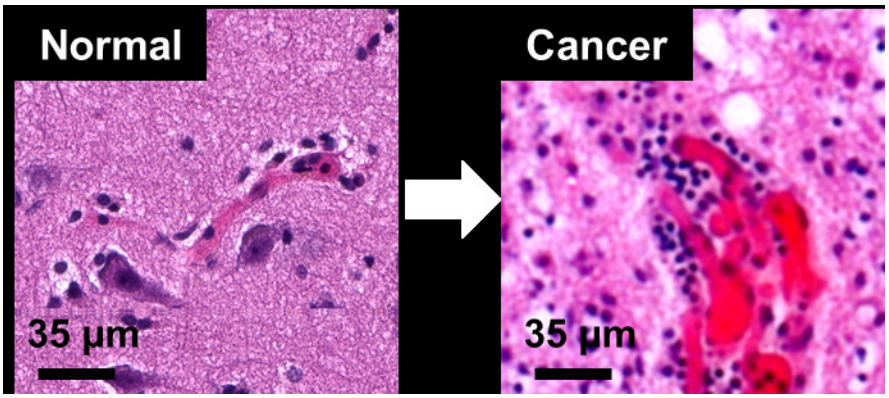

Figure 4. Typical vascular changes in primary brain cancer. Overall, primary brain cancer is characterized by a higher blood vessel density, the presence of dilated, irregularly shaped blood vessels, and the presence of infiltrating cancer cells into the surrounding blood vessels. **Figure and figure legends are published by Kut *et al.* (2016), Detection of human brain cancer in *ex vivo* human using multi-photon fluorescence (to be submitted).**

The vascular changes of primary brain cancer can be found in **Figure 6**. First of all, let us look at the vascular changes for grade II glioma (when compared with the non-cancer white matter). While the cancer changes for grade II glioma is somewhat subtle, we can observe a slight increase in blood vessel diameter. For grade III glioma, blood vessels are often dilated with

infiltration of cancer cells into the bloodstream. Finally, grade IV glioma shows the presence of necrosis and microvascular infiltration; it is common for blood vessels to appear distorted.

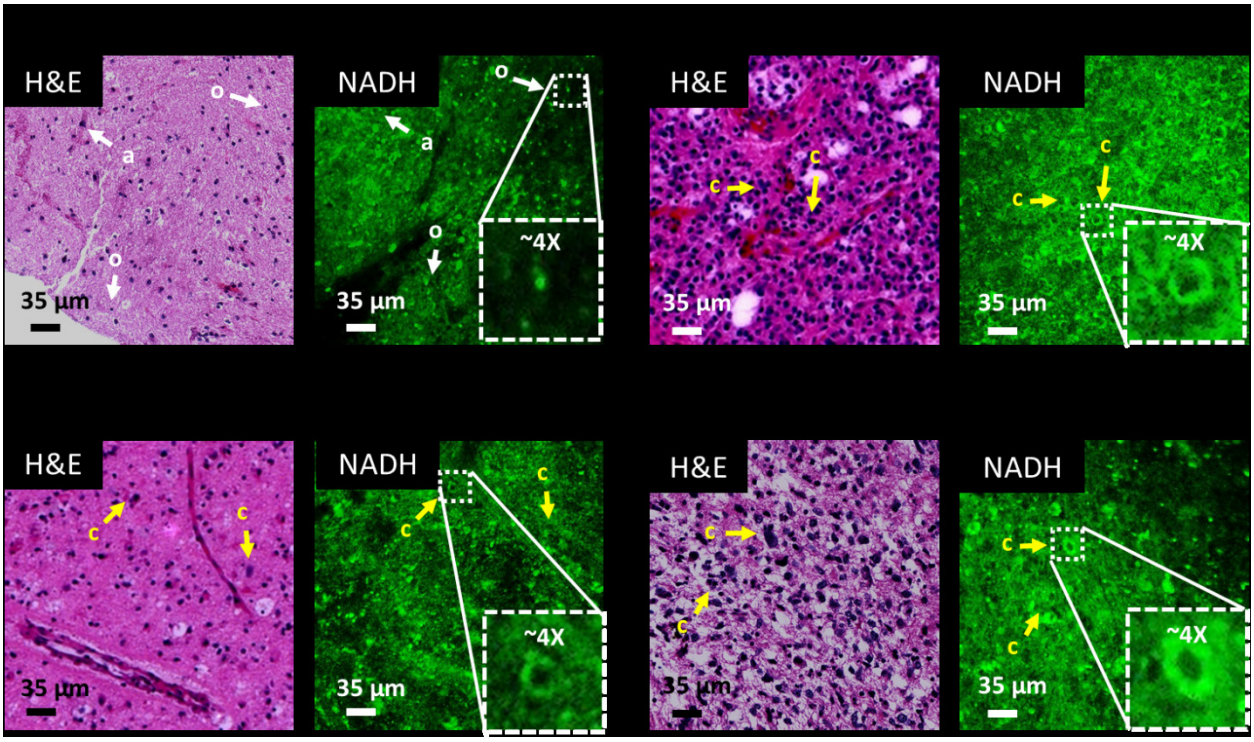

Figure 5. Cellular changes found in grade II-IV glioma when compared with non-cancer. On the overall, we observe and increase in cell density and an increase in cellular diameter as the cancer grade increases. Zoomed-in view of the cancer cell is at ~4X magnification. Abbreviations include a: astrocyte; o: oligodendrocyte, and c: cancer. **Figure and figure legends are published by Kut *et al.* (2016), Detection of human brain cancer in *ex vivo* human using multi-photon fluorescence (to be submitted).**

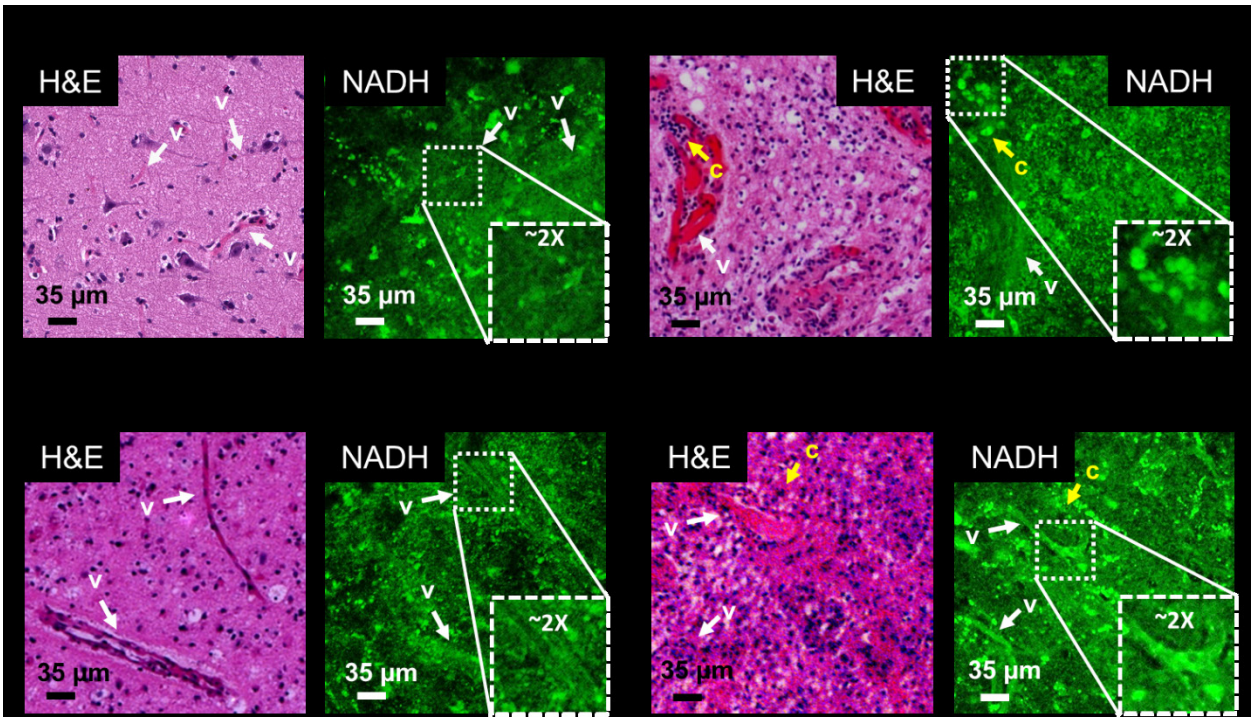

Figure 6. Vascular changes found in grade II-IV glioma when compared with non-cancer. On the overall, we observe and increase in cell density and an increase in cellular diameter as the cancer grade increases. Zoomed-in view of the cancer cell is at ~4X magnification. Abbreviations include a: astrocyte; o: oligodendrocyte, and c: cancer. **Figure and figure legends are published by Kut *et al.* (2016), Detection of human brain cancer in *ex vivo* human using multi-photon fluorescence (to be submitted).**

SECTION 12: VOLUMETRIC GLIOMA DATA

Notably, it is possible to reconstruct a three-dimensional volume of the multi-photon fluorescence data. To accomplish this, we obtain one 350 x 350 μm^2 frame (in the x-y direction) for every 1 µm step in the z direction. The three-dimensional volume can subsequently be generated using MATLAB or the Avizo software. **Figure 7** shows one such example, with the NADH volumetric reconstruction of different categories of freshly resected human brain tissues (which include non-cancer gray matter, non-cancer white matter, as well as grade IV infiltrated zone and cancer core).

SECTION 13: SECOND HARMONIC GENERATION IN GLIOMAS

As mentioned in the previous sections, second harmonic generation detects the presence of non-centrosymmetric fibers in biological tissues such as collagen, myosin and microtubules (*121*). In particular, the second harmonic generation (SHG) signal is strong when collagen is present in blood vessels, collagenous scars, or the growth of fibrous tissues surrounding a tumor mass.

In addition, the second harmonic generation is dependent on the collagen types. For example, collagen I exhibits a strong SHG signal while collagen IV has little to none SHG activity (*123*). Generally speaking, the SHG signal is weak in the normal brain. When glioma is present, however, the content of collagen I increases in pathological tumor vessels which will can exhibit a visible SHG signal (*124, 125*). **Figure 8** shows the example of a grade III brain cancer tissue sample with a pathological tumor blood vessel; in this example, the blood vessel has become hyperplastic as a result of the brain cancer. A hyperplasic blood vessel is characterized by a significant thickening of the vessel fall, the proliferation of pericytes and smooth muscle cells which support the blood vessels, and also the proliferation of endothelial cells.

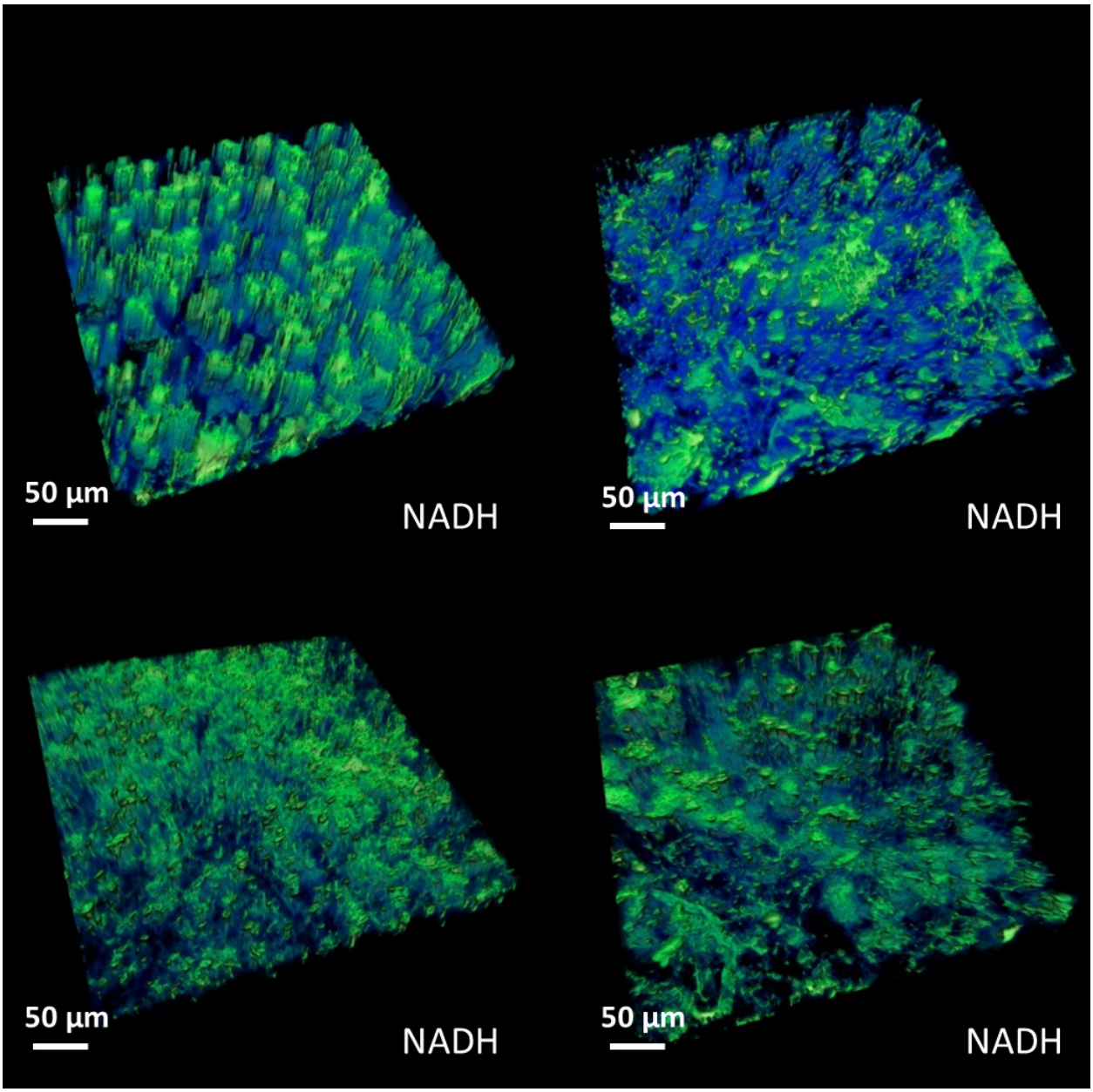

Figure 7. Volumetric reconstruction of two-photon fluorescence images. Here, we show the three-dimensional reconstruction for non-cancer gray matter, non-cancer white matter, grade IV infiltrated zone and grade IV cancer core using the NADH signal. **Figure and figure legends are published by Kut *et al.* (2016), Detection of human brain cancer in *ex vivo* human using multi-photon fluorescence (to be submitted).**

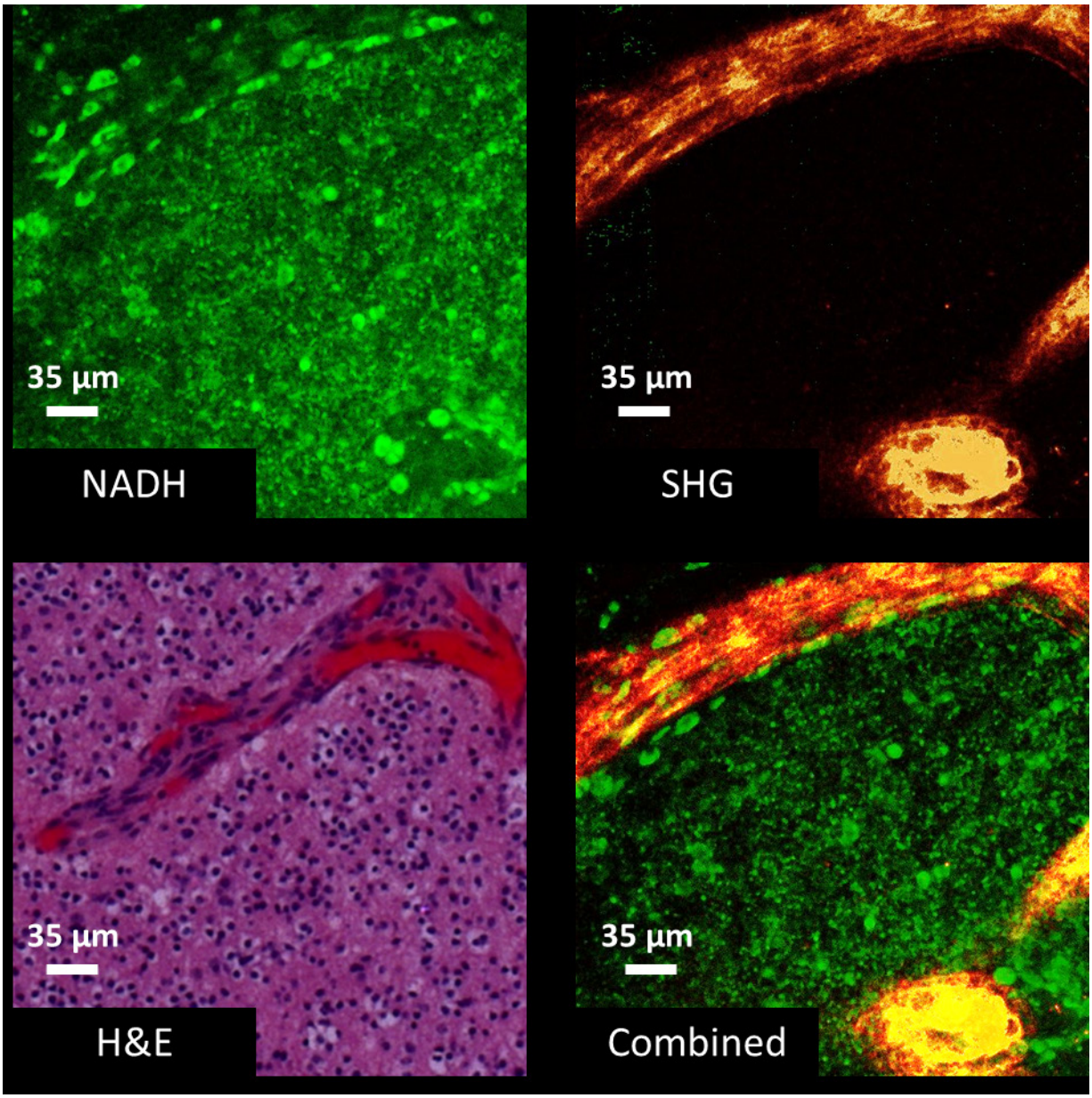

Figure 8. Example of pathological, hyperplastic blood vessel in glioma. Here, we show the NADH, SHG and H&E images for a grade III glioma with a hyperplastic blood vessel. Hyperplastic blood vessels are characterized by a marked thickening of the vessel wall, the proliferation of pericytes and smooth muscle cells surrounding the blood vessels, and in the proliferation of endothelial cells. Both collagen I and IV expressions will increase for a pathological tumor blood vessel in the brain, although collagen I is the collagen type which is responsible for the SHG signal. **Figure and figure legends are published by Kut *et al.* (2016), Detection of human brain cancer in *ex vivo* human using multi-photon fluorescence (to be submitted).**

SECTION 14: INTRODUCTION TO SECONDARY BRAIN CANCER

In addition to primary brain cancer, multi-photon fluorescence is also capable of differentiating among different secondary brain cancer types. Secondary brain cancer originates from cancer cells which have breached the blood-brain barrier and infiltrated into the brain from another part of the human body (i.e., from the primary cancer site). Overall, about 25-35% of all cancer patients eventually develop metastases to the brain, which often leads to severe neurologic symptoms and an overall worse prognosis; while the median survival for patients is less than 1 year with treatment, survival can decrease to 1-2 months without treatment (*126, 127*). Generally speaking, patients with only 1-2 isolated brain metastases are recommended for surgery, and maximal cancer resection is needed to prolong survival and delay recurrence. As a result, better image guidance techniques are necessary to identify the pathological characteristics of brain cancer in real-time during surgery and to maximize the extent of cancer resection.

Of all the cancers, lung cancer is the most common type to metastasize to the brain (35%); in addition, breast cancer, kidney cancer, gastrointestinal cancer and melanoma are also prove to metastasize to the brain (*127, 128*). In this study, we only focus on the differentiation of lung cancer subtypes which have metastasized into the brain with *ex vivo* brain tissues from 9 patients.

There are two major categories of lung cancer: small cell lung cancer (SCLC) and non-small cell lung cancer (NSCLC). Generally speaking, small cell lung cancer originates from small neuroendocrine cells, and is responsible for 10-15% of all lung cancers. The classification of small cell lung cancer is significant since this is the fastest growing and more aggressive lung cancer. SCLC is also known as oat cell carcinoma; as suggested by the name and as shown in **Figure 9**, SCLC cells are characterized by very small lung cancer cells which densely populate the tissue sample. In general, these SCLC cells have a much smaller cell diameter (with very little cytoplasm)

when compared to the normal lung. Due to their small and delicate nature, SCLC cells are easily crushed during brain tissue biopsies (i.e., a crush artefact) which will prevent pathologists from making an accurate and reliable diagnosis. As a result, imaging technologies such as multi-photon fluorescence can be useful as they can capture *in vivo* images of the brain non-invasively and without crushing the SCLC cells during the procedure.

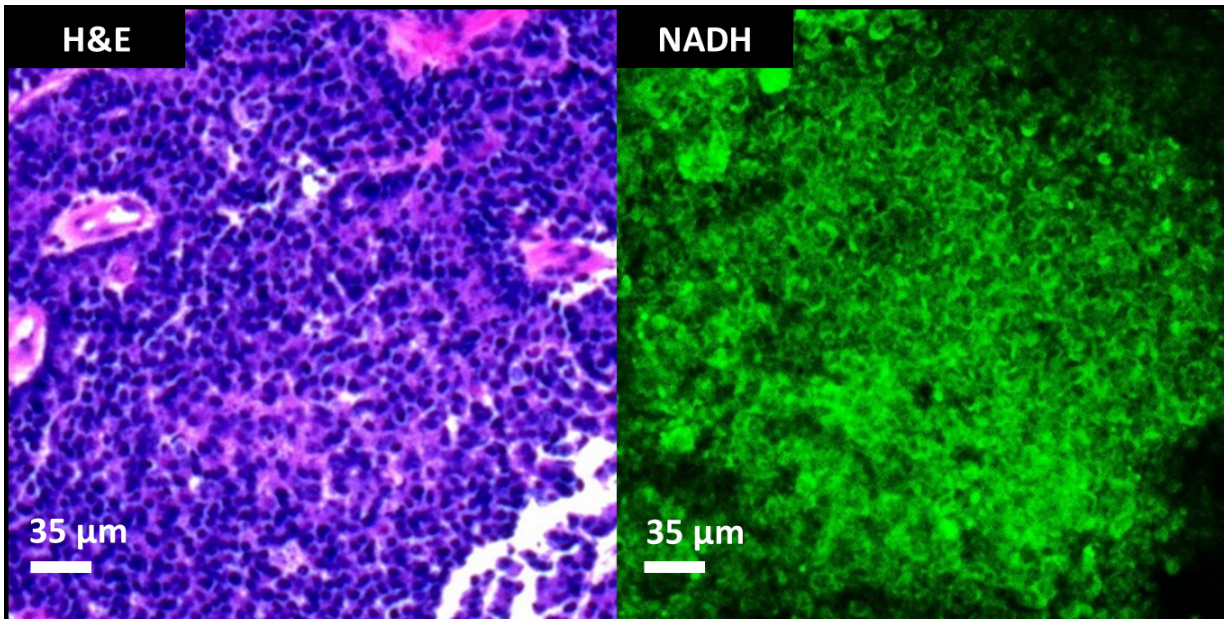

Figure 9. Structural characteristics of small cell lung cancer (SCLC) metastasized into the brain. Small cell lung cancer is also known as oat cell carcinoma, since the cancer is characterized by the presence of densely populated, small-diameter cancer cells. Generally speaking, these SCLC cells have a small cellular diameter but a high nuclei-to-cytoplasmic ratio since there is very little cytoplasm in each cell. Here, we show the NADH and the corresponding H&E images. **Figure and figure legends are published by Kut *et al.* (2016), Detection of human brain cancer in *ex vivo* human using multi-photon fluorescence (to be submitted).**

Non-small cell lung cancer, on the other hand, are responsible for 85-90% of all lung cancers. There are 3 major sub-types of NSLCs: large cell carcinoma, adenocarcinoma, and squamous cell carcinoma. Large cell carcinoma is an aggressive cancer type with poor prognosis; as demonstrated in **Figure 10**, it is characterized by the presence of pleomorphic giant cells (i.e., a tumor mass formed by the union of several cells and as a result, can be multi-nucleated).

Adenocarcinoma is the most common lung cancer subtype in females and in non-smokers; as demonstrated in **Figure 11**, it is characterized histologically by the presence of a fibrovascular core and by the presence of mucin in many cases. Squamous cell carcinoma, on the other hand, are often linked to smoking and are more common in men than in women; its pathology is characterized by the presence of large, flattened cells which originated from the squamous cells which line the inside of the lung's airways. In addition, key diagnostic features include the presence of intracellular bridges and squamous pearl formation as a result of intracytoplasmic keratin (figure not shown due to insufficient data).

To summarize, **Figures 9 to 11** highlights the histological differences amongst the different lung cancer subtypes. Overall, there are key structural and prognostic differences among the different lung cancer types; as a result, it is important to correctly differentiate the different lung cancer types from the normal brain during cancer resection.

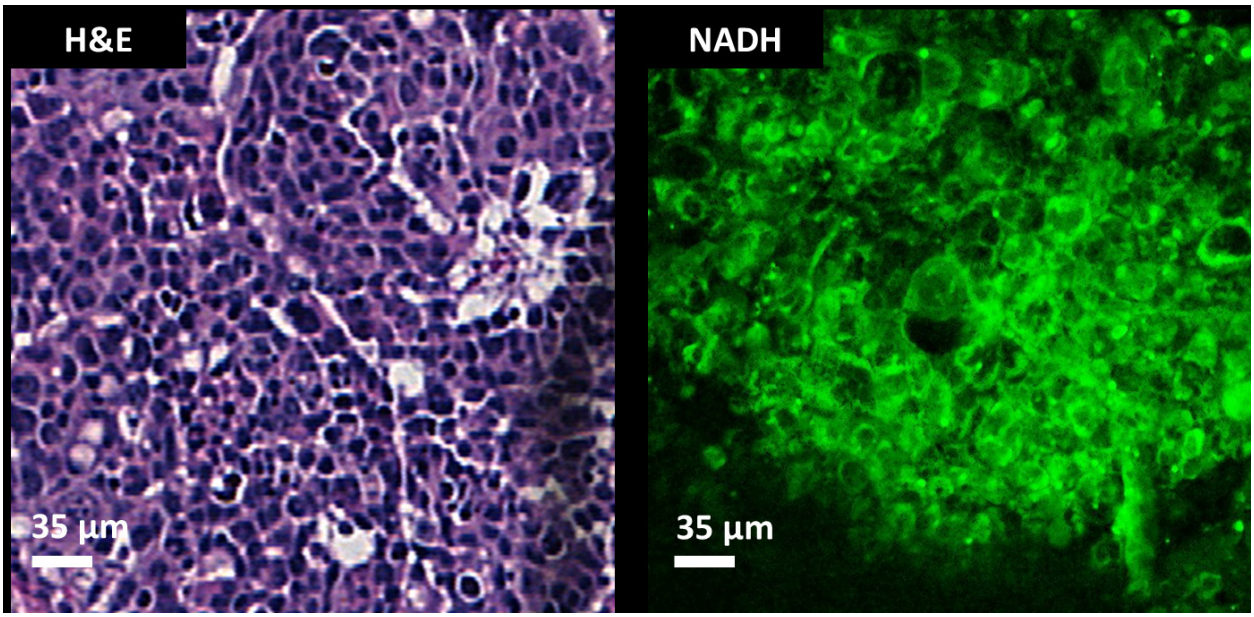

Figure 10. Structural characteristics of large cell lung carcinoma metastasized into the brain. Large cell carcinoma of the lung is a type of non-small cell lung cancer (NSCLC) and is characterized by the presence of pleomorphic giant cells which have large nuclei and abundant nuclei. Giant cells are formed by the joining of several cells, and can sometimes appear as multi-nucleated. Here, we show the NADH and the corresponding H&E images. **Figure and figure**

legends are published by Kut *et al.* (2016), Detection of human brain cancer in *ex vivo* human using multi-photon fluorescence (to be submitted).

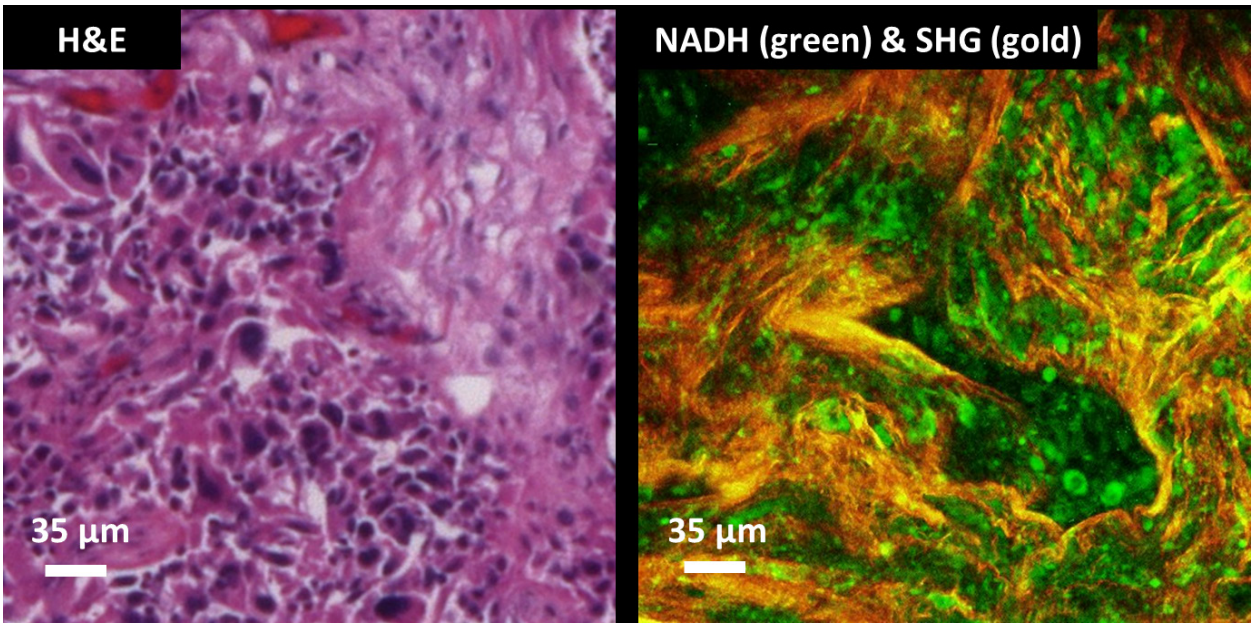

Figure 11. Structural characteristics of adenocarcinoma from the lung metastasized into the brain. Adenocarcinoma of the lung is a type of non-small cell lung cancer (NSCLC) and is characterized by the presence of fibrovascular cores and by the presence of mucin. Fibrovascular cores are abundant with collagen, which can be seen in the overlaid NADH (green) and SHG (gold) signals. For histological correlation, we also show the corresponding H&E images. **Figure and figure legends are published by Kut *et al.* (2016), Detection of human brain cancer in *ex vivo* human using multi-photon fluorescence (to be submitted).**

SECTION 15: SHG SIGNALS FOR SECONDARY BRAIN CANCER

In the previous section, we describe the pathological characteristics of lung adenocarcinoma (metastasized to the brain) which included the presence of collagen-rich fibrovascular cores. In fact, most metastases to the brain are enclosed by a fibrotic capsule which is responsible for the well-defined appearance of cancer metastases to the brain (as demonstrated in **Figure 12**). These fibrotic capsules are rich in collagen fibers, and as a result, exhibit strong second harmonic generation signal when imaged. As a result, the presence of abundant and strong SHG signals may aid surgeons in localizing the brain tumor and maximizing the extent of cancer resection.

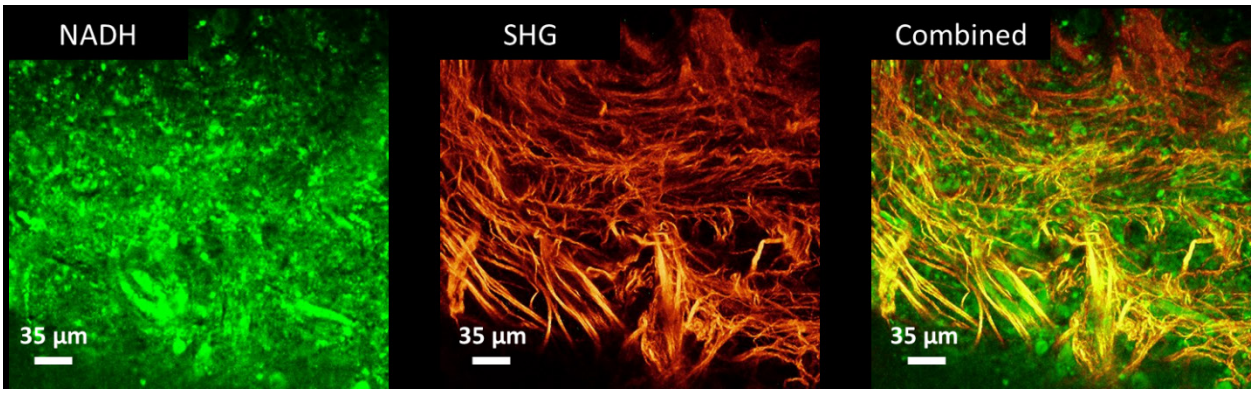

Figure 12. Fibrotic capsule surrounding the metastases to the brain is rich in collagen. Here, collagen-rich fibers are embedded within a brain cancer region close to the fibrotic outer capsule of the metastases. Here, we show the NADH, SHG, and the overlaid NADH/SHG images. **Figure and figure legends are published by Kut *et al.* (2016), Detection of human brain cancer in *ex vivo* human using multi-photon fluorescence (to be submitted).**

SECTION 16: QUANTITATIVE ANALYSIS

In addition to qualitative data, we can also post-process the MPF images and classify the images based on their cellular characteristics, vascular characteristics, and the degree of pleomorphism. For example, **Figure 13** shows the results of a maximally stabilizing extreme region (ESER) algorithm we have optimized for identification of cellular density and size in brain cancer. Using a similar algorithm, we can analyze the standard deviation of the cellular size (and other quantifiable features) to help us assess the degree of pleomorphism in the brain cancer tissue samples. Similarly, **Figure 14** shows the results of a line segmentation algorithm we have adapted for the identification of blood vessels in brain tissues.

To summarize, software algorithms can be optimized to identify the pathological features of brain cancer which cannot be identified by eye otherwise in the operating room.

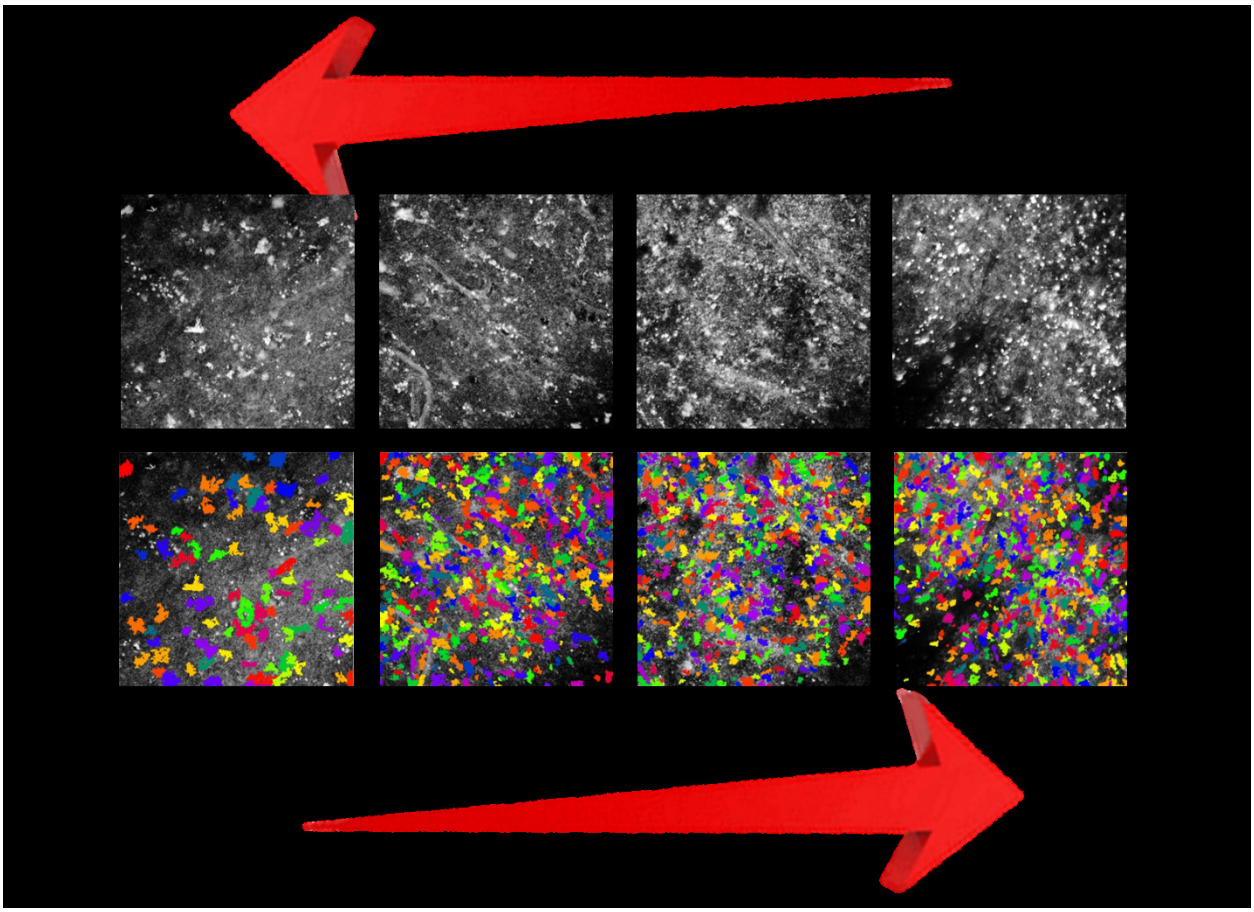

Figure 13. Evaluation of cellular size and density in human brain tissues using a maximally stabilizing extreme region (MSER) algorithm which we have optimized for brain cancer use. The top row shows the original NADH images (in black and white), while the second row shows the same image overlaid by cells identified using the MSER algorithm. Notably, the colors are used to distinguish one cells from another. **Figure and figure legends are published by Kut *et al.* (2016), Detection of human brain cancer in *ex vivo* human using multi-photon fluorescence (to be submitted).**

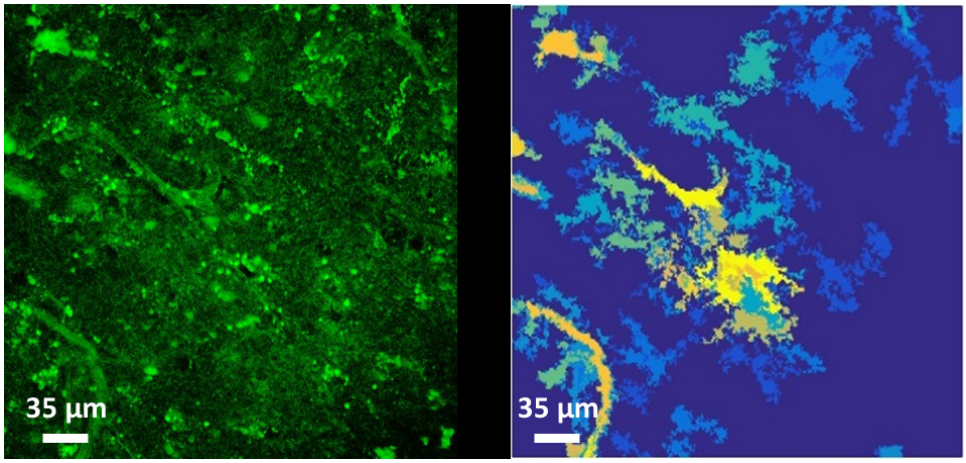

Figure 14. Segmentation of blood vessels in human brain tissues using a line segmentation algorithm which we have optimized for brain cancer use. In this example, we find the morphological line elements at different angles (between 0^o to 360^o). The image on the left is the original NADH image, while the image on the right is the segmented image. The segmented image is produced by summing the list of all morphological elements found between 0^o to 360^o. Bright yellow indicates high magnitude (i.e. morphological line elements identified at different angles), while dark blue indicates zero magnitude (i.e. no line elements found at any angle). **Figure and figure legends are published by Kut *et al.* (2016), Detection of human brain cancer in *ex vivo* human using multi-photon fluorescence (to be submitted).**

SECTION 17: MERGING OF OCT AND MPF

Multi-photon fluorescence is an excellent complementary imaging technique for OCT in the operating room for the resection of brain cancer. As demonstrated in previous sections, OCT is a volumetric imaging technique which can detect brain cancer from non-cancer with 92-100% sensitivity and 80-100% specificity based on its optical properties. However, OCT does not provide molecular or functional-specific information, and it is most useful in the differentiation of white matter and brain cancer. While OCT demonstrates lower attenuation properties in gray matter when compared with normal brain tissues, the difference is not statistically significant. MPF can help to provide complementary information by providing molecular signatures (e.g. NADH, FAD and the presence of non-centrosymmetric fibers). In addition, it is possible to analyze the ratio of NADH versus FAD to obtain the metabolic activity of the tissue sample. Importantly, MPF can help with the differentiation of gray matter and cancer with relative ease. However, MPF provides subcellular information at a narrow field of view (FOV) and as a result, it will be impractical to use MPF alone in the scanning of the entire resection cavity. However, it will be ideal to use OCT as a volumetric scanning tool for the entire resection cavity, and use MPF as a "zoom in" tool when OCT results at a specific spot in the brain is inconclusive. To summarize, the combination of OCT and MPF eliminates each other's disadvantages and together, they form a powerful tool in the identification and maximal cancer resection for human brain cancer. **Figure**

15 demonstrates the OCT and MPF results of the same brain tissue sample with a prominent blood vessel across the surface of the tissue sample. In addition, preliminary work has been performed by other members in Dr. Xingde Li's laboratory an integrated OCT/MPF system for multi-modal imaging of mice intestinal tissues (*129*).

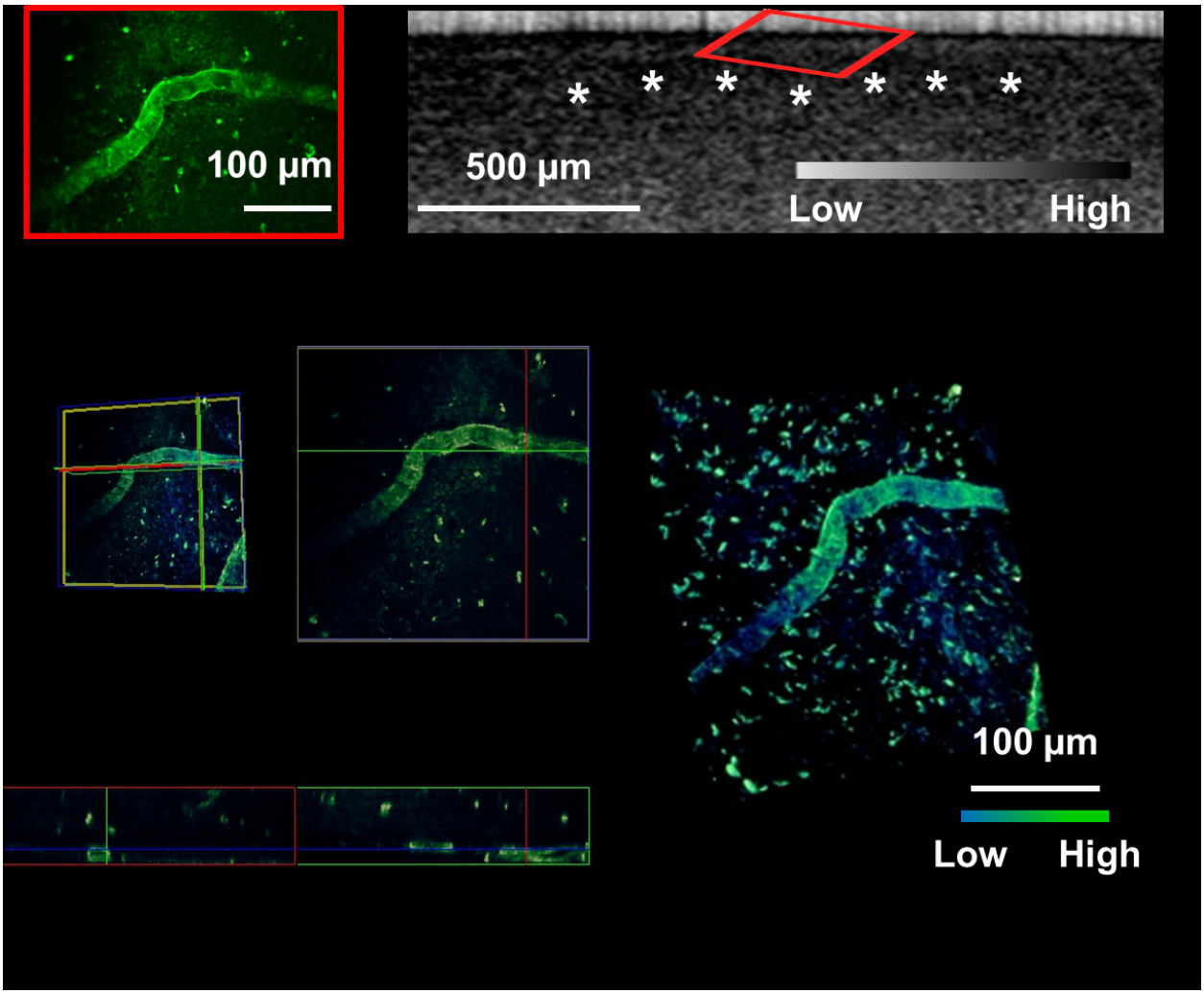

Figure 15. Registration of OCT and MPF images which shows the presence of a prominent blood surface spanning the surface of the tissue sample. Figure and figure legends are published by Kut *et al.* (2016), Detection of human brain cancer in *ex vivo* human using multi-photon fluorescence (to be submitted).

CHAPTER 7: CONCLUSIONS AND FUTURE DIRECTIONS

SECTION 1: OCT BRAIN CANCER STUDY

As demonstrated in Chapters 1 to 5 of this dissertation, complete brain cancer resection can prolong survival and delay recurrence. However, it is challenging to distinguish cancer from non-cancer tissues intra-operatively, especially at the transitional, infiltrative zones. This is especially critical in eloquent regions in the brain (for example, speech and motor areas). This study tested the feasibility of label-free, quantitative optical coherence tomography (OCT) for differentiating cancer from non-cancer in human brain tissues. Fresh *ex vivo* human brain tissues were obtained from 32 patients with grade II to IV brain cancer and 5 patients with non-cancer brain pathologies. On the basis of volumetric OCT imaging data, pathologically confirmed brain cancer tissues (both high- and low-grade) had significantly lower optical attenuation values at both cancer core and infiltrated zones when compared with non-cancer white matter, and OCT achieved high sensitivity (92-100%) and specificity (80-100%) at an attenuation threshold of 5.5 mm^{-1} for brain cancer patients. We also used this attenuation threshold to confirm the intra-operative feasibility of performing *in vivo* OCT-guided surgery using a murine model harboring human brain cancer. Our OCT system was capable of processing and displaying a color-coded optical property map in real time at a rate of 110 to 215 frames per second, or 1.2 to 2.4 s for an 8- to 16-mm^3 tissue volume, thus providing direct visual cues for cancer versus non-cancer areas. Our study demonstrates the translational and practical potential of OCT in differentiating cancer from non-cancer tissue. Its

intra-operative use may facilitate safe and extensive resection of infiltrative brain cancers and consequently lead to improved outcomes when compared with current clinical standards.

As a result, OCT has great potential as an imaging tool for the localization and mapping of brain cancer margin. However, there are several existing limitations (*66, 72*). For example, OCT does not provide any provide molecular information (which is unlike Raman spectroscopy, multi-photon fluorescence or confocal fluorescence imaging). In addition, the current imaging system is also limited by a small imaging volume (at 8-16 mm^3). In order to scan the entire resection cavity to check for residual cancer, we will need to address two existing technical constraints: 1) we need to use a high-performance, high-range robotic device which can substantially increase the OCT imaging area (and volume) by 10- to 100-fold (*66*); 2) the computer hardware needs to increase its capacity to allow for storage of hundreds of GBs of data at a time (which will be necessary once we increase the OCT imaging area by 100-fold or higher) (*66*). Alternatively, the imaging volume can also be addressed by co-registering the OCT images with surgical microscopes, which will allow seamless and continuous surgical guidance in the operating room (*61, 62*). Furthermore, OCT can be complemented by wide-field imaging technologies (e.g. MRI and fluorescence) to facilitate maximal safe cancer resections (*66*). In addition to optical property mapping, OCT can also yield other functional information such as Doppler to detect the presence of *in vivo* blood flow, and therefore preventing bleeding and stroke-related complications during surgery (*66*). Finally, OCT can also benefit from future research and advances in the OCT light sources (*66*), which can in turn yield faster imaging speeds (e.g. >400 fps vs the current speed at up to 220 fps) (*88*) and axial resolution (e.g. <3 μm versus the current resolution at 6.4 μm in tissue) (*89*).

In conclusion, OCT could have immense translational potential in guiding primary brain cancer detection and resection in the operating room. In addition to primary brain cancer, OCT

and the optical property mapping technique may also be useful for distinguishing cancer from non-cancer tissue for other brain cancers including metastatic (i.e. secondary) brain cancer. Building upon this study, we have already conducted the first *in vivo* clinical study on 3 high-grade brain cancer patients (which we discussed in Chapter 5). Additional future considerations include the construction of a miniature, turnkey imaging system which will facilitate the ease of transport and set up at different operating rooms throughout the day. Overall, this dissertation sets the stage for future large-scale clinical trials and technological advancement that will eventually lead to an uniquely and valuable technology which is capable of detecting infiltrative brain cancer margins quickly and efficiently, resulting in cleaner resection margins for cancer patients and thus improved patient survival and quality of life.

SECTION 2: MPF BRAIN CANCER STUDY

As demonstrated in Chapter 6 of this dissertation, multi-photon fluorescence is an excellent technique which can visualize subcellular structures of the brain in real-time and without the use of exogenous contrast agents. In order to assess the performance of MPF imaging to obtain real-time and clinically useful diagnostic information in the detection of human brain cancer versus non-cancer, *ex vivo* studies have been performed using freshly resected brain tissues obtained from patients who are undergoing neurosurgery as part of their standard of care. *Ex vivo* images of both primary and secondary brain cancer demonstrates the potential to allow a pathologist to study the pathological characteristics of the brain tumor non-invasively and in real-time at a resolution of 0.34 μm. In Chapter 6, we have demonstrated the structural differences among non-cancer white matter, non-cancer gray matter, grade II-IV glioma, as well as different subtypes of lung cancer which have metastasized to the brain (including small-cell lung cancer SCLC, and two subtypes of non-small cell lung cancer NSCLC including large cell carcinoma of the lung and

adenocarcinoma of the lung). In addition to qualitative data, post-processing of the MPF images can also help us to classify brain cancer versus non-cancer based on their cellular and vascular characteristics (as well as the degree of pleomorphism). In addition to structural data, MPF also provides molecular information e.g. the presence of NADH, FAD and functional information e.g. the redox ratio as defined by relative levels of NADH versus FAD. To summarize, these results suggest that MPF may become a useful complementary imaging technique alongside OCT to achieve maximal detection and resection of brain cancer in the operating room. Future directions of this project include the construction of a portable and inexpensive femtosecond laser source for intra-operative use; the development of a miniature handheld imaging probe which is optimized for brain cancer applications; and the development of a three detection channels in the MPF system which will allow simultaneous capture of NADH, FAD and SHG images.

SECTION 3: OTHER PROJECTS

In addition to the OCT and MPF brain cancer studies, we have also completed 10 miscellaneous projects throughout the course of my PhD. The results and conclusions from this study can be located in the Appendix Section of this dissertation.

SECTION 4: CONCLUSION

This dissertation has presented the use of optical coherence tomography (OCT) and multi-photon fluorescence in obtaining optical, structural, molecular and functional information of human brain cancer versus non-cancer tissues. A systematic *ex vivo* study has been performed using OCT to obtain the optimal diagnostic threshold for distinguishing brain cancer versus non-cancer tissues; in addition, an independent study using the optimal diagnostic threshold is able to achieve excellent sensitivity and specificity in the detection of brain cancer versus non-cancer. In addition, an *in vivo*

study has begun to evaluate the performance of OCT in detecting brain cancer in patients in the operating room, with excellent results. Finally, multi-photon fluorescence provides complementary information to OCT in the real-time detection of human brain cancer. While OCT is able to volumetrically scan the entire resection cavity in the brain, MPF can be used to zoom in and provide additional information to assist surgeons and pathologists with the diagnosis. To summarize, the results of this dissertation have motivated the development and optimization of the OCT and MPF software to enable *in vivo* imaging and analyses of brain cancer.

APPENDIX 0: OVERVIEW OF ADDITIONAL RESACH PROJECTS

In this dissertation, we have discussed the study design and results of OCT and MPF in the real-time detection of brain cancer margins in the operating room. In the appendix section, we will now give an overview of the other projects and/or publications completed in the course of the PhD.

These projects include: **(Appendix 1)** Study on the effect of intracranial albumin on extracellular fluid flow rates along white matter tracts in the brain; **(Appendix 2)** Viewpoint on the importance of the blood-brain barrier to the development of neurotherapeutics; **(Appendix 3)** Considerations on the planning of radiation treatment for brain tumors: Neural Progenitor Cell-Containing Niches; **(Appendix 4)** The study of inter- and intra-fraction patient positioning uncertainties for intracranial radiotherapies; **(Appendix 5)** A preliminary study of the injury sustained from heating systematically delivered, non-targeted dextran-supraparamagnetic iron oxide nanoparticles in mice; **(Appendix 6)** a study to evaluate the performance of MPF in detecting acute and chronic myocardial infarction in porcine hearts.

In addition, I have also performed several brief, exploratory studies which will not be included as part of this dissertation. These projects include an OCT study to detect the presence of atherosclerotic plaques in porcine coronary arteries; an OCT study to detect the presence of cancer implanted into the murine tibia; an OCT study to detecting structural characteristics of the bovine kidney; and finally a MPF study to detect the structural differences between normal versus cancer tissues for head and neck patients.

APPENDIX 1: THE EFFECT OF INTRA-CRANIAL ALBUMIN ON EXTRA-CELLULAR FLUID FLOW RATES ALONG WHITE MATTER TRACTS IN BRAIN

SECTION 1: OVERVIEW

Waste metabolites and tumor cells are typically drained from the local interstitium and carried by extracellular fluid flow to regional lymph nodes. Although the brain lacks lymphatics, extracellular fluid resulting from albumin extravasation through a disrupted blood brain barrier (BBB) could passively carry neurotoxic metabolites and glioma cells down adjacent white matter tracts (WMT).

This study sought to determine if increasing intracranial albumin concentrations affect extracellular fluid flow rates (ECFR) along WMT using both *in vivo* MRI imaging and *ex vivo* Evans blue validation. A total of 19 Sprague-Dawley rats were used for this study. First, increasing concentrations of bovine albumin labeled with Evans blue were injected stereotactically into the frontal lobe of rats for an initial baseline study. 7 hours later, rat brains were extracted, sectioned and imaged to measure ECFR. Following the baseline study, albumin labeled with Evans blue and/or gadolinium was similarly injected into rat brains and *in vivo* MRI was used to estimate ECFR. Rats were then sacrificed and their brains sectioned for Evans blue validation of ECFR.

On the overall, anterior-posterior ECFR (AP ECFR) for rats receiving 0.12 and 6.0 mg of albumin were 0.43 ± 0.15 and 1.02 ± 0.22mm/hour ($p=0.03$, $R=0.57$). *In vivo* MRI yielded an average AP ECFR of 1.3 and 1.7mm/hour after administering 3 and 6 mg of albumin, consistent

with our Evans blue measurements. MRI demonstrated markedly increased edema, as measured by T2-weighted images, adjacent to the albumin injection site, which extended further down the WMT than the albumin-gadolinium complex. To conclude, higher intracranial albumin concentrations result in local edema and higher ECFR along WMT. These results suggest that we could image albumin extravasation through the BBB using *in vivo* MRI, which have potential implications in monitoring waste, metabolite and tumor cell clearance in the brain.

SECTION 2: INTRODUCTION

Previous studies have long recognized two major pathways of interstitial clearance: 1) the glymphatic clearance whereby extracellular fluids drain through the astrocytic endfeet in the paravascular space and 2) the axonal clearance whereby extracellular fluids drain along the white matter tracts (*130-133*). Recently, much emphasis has been placed on the mechanisms of glymphatic clearance – namely, the study of aquaporin channels in the brain (AQP4) and how their insertion and activity at the astrocytic endfeet influence the bulk flow of extracellular fluids along the paravascular space (*131, 132*). However, it is also known that glymphatic clearance fails significantly during neuro-pathologic conditions, as diffuse gliosis results in the mislocation of aquaporin channels at the astrocytic endfeet (*131, 132*). In patients with brain tumors, the aggregation and passive transportation of glioma cells along the white matter tracts may additionally play a part in cancer dissemination, similar to how systemic cancer cells are carried to regional lymph nodes (*134, 135*) . Consequently, we would like to highlight the importance of the axonal clearance pathways along the white matter tracts, which could be targeted to maintain or even regulate ECF drainage and interstitium-CSF exchange, especially when glymphatic pathways fail. This study aims to achieve better understanding of extracellular fluid drainage along

the white matter tracts (in other words, the axonal clearance pathway) during blood-brain-barrier (BBB) disruption using both *in vivo* MRI and *ex vivo* Evans blue validation.

Extracellular fluid flow rate (ECFR) plays a significant role in fluid exchange and drainage within the brain (*130, 136-139*). Research on the dynamics and pathways of extracellular fluid (ECF) drainage from different regions of rat brain using radiolabeled tracers of different molecular weights reported similar clearance rates, suggesting that bulk ECF convective flow, and not diffusion, was primarily responsible for the transport (*138*). In pathologic conditions such as brain tumors, ischemia, HIV-1 encephalitis, Alzheimer's disease, Parkinson's disease and multiple sclerosis, ECF flow rates often increase as a result of brain swelling from blood-brain-barrier disruption and subsequent albumin extravasation into brain (*140*). While an intact BBB restricts the passage of large, water soluble compounds from blood to brain, a disrupted BBB allows albumin (67 kDa) to pass with ease (*133, 141-143*). As serum albumin moves into the brain, it osmotically brings water with it, creates peritumoral edema and leads to higher ECF flow rates along the brain's white matter tracts (WMT) which serve as the major fluid outflow pathways for extracellular fluid.

Since the bulk flow of extracellular fluid plays a significant role in neuropathology, monitoring and regulating the blood-brain-barrier permeability and ECFR could be a key target for therapeutic intervention. Recent studies in the glymphatic pathway suggests a significant and beneficial role in clearing neuro-toxic substances such as tau and beta-amyloids in Alzheimer's disease (*131, 132*) . On the other hand, the same high extracellular fluid flow rates may serve a different role in glioma patients and instead contribute to and accelerate the transport and deposition of tumor cells

to distant locations in the brain (*130, 144, 145*). Currently, glucocorticoids and agents targeting VEGF pathways have the potential to reduce BBB disruption and the extent of peritumoral edema. A better understanding and quantification of the degree of BBB disruption could enable us to one day quantify and monitor the rate of extracellular fluid clearance within the brain.

In this study, we simulate different degrees of BBB disruption by injecting various concentrations of albumin intracranially into rat brains, and evaluate the relationship between the concentration of albumin reaching the brain and the bulk ECFR along the draining white matter tracts. Our results illustrate quantifiable ECFR flow along the draining white matter tracts both with *in vivo* MRI and *ex vivo* Evans blue validation, and show comparable results with both methods. In summary, we intend to highlight the potential to monitor and measure extracellular fluid flow rates and BBB disruption patterns non-invasively using MRI, and provide a better understanding of interstitial clearance in the brain with important implications for neuro-therapeutic interventions. To our knowledge, there are no previous studies that explore the relationship between varying concentrations of BBB disruption and the ECFR along white matter tracts.

SECTION 3: EXPERIMENTAL DESIGN

SECTION 3.1 THE EFFECT OF LOCAL EVANS BLUE LABELED ALBUMIN CONCENTRATIONS ON EXTRACELULAR FLUID FLOW RATES ALONG ADJACENT WHITE MATTER TRACTS

Experimental Plan: 19 adult, female Sprague Dawley rats at age 57-90 days and approximately 200g were purchased from Charles River Laboratories (Wilmington, MA). In 15 rats (A1-15), specified amounts of bovine albumin tagged with Evans blue (EB-albumin) were injected intracranially to simulate passage of increasing amounts of albumin across the BBB. The EB-albumin draws water osmotically into the brain, which drains down adjacent WMT. The distance

that the labeled albumin was carried over a fixed period of time was used to estimate ECFR along WMT using histologic (EB-albumin complex) measurements. Flow rates along WMT were analyzed as a function of the amount of injected albumin.

Injection Coordinates: All animals were anesthetized by an intra-peritoneal injection from a ketamine/xylazine solution at doses of 75/7.5 mg/kg. Rats were placed in the prone position using a stereotactic frame. The scalp was shaved, prepped and draped in a sterile manner, with a mid-sagittal fronto-parietal scalp incision. The scalp was retracted and a burr hole drilled over the frontal lobe, using a 2mm drill bit and dental drill. Injection coordinates were determined at 1 mm anterior to the bregma, 4 mm lateral to the sagittal suture over the right hemisphere, at a depth of 3.3 mm into the frontal lobe. A needle attached to a 25 μL Hamilton syringe was positioned perpendicularly to the surface of the brain, and albumin labeled with Evans blue was injected into the right frontal lobe at the gray-white matter junction.

Stereotactic Frame for Injection: For the WMT flow rate studies, a manually operated stereotactic frame was used for the rats injected with EB- albumin complex.

Injection solution: Increasing doses of albumin ranging from 0.12-6.0 mg (or 6-300 mg/mL) of bovine albumin and 0.04 g (or 2 g/100 mL) of Evans blue (Fisher Scientific, Pittsburgh, PA) were mixed with 20 μL of 0.9% saline solution and injected stereotactically over 80 minutes into the right frontal lobe at the gray-white matter junction in rats. The zero-hour time point marked the beginning of injection.

Rat Brain Coronal Slices: At 7-9 hours post injection, the animals were euthanized by carbon dioxide. The brains were quickly extracted and placed on a coronal rat brain matrix. The brains were sectioned into approximately 0.75 mm coronal slices, which were placed onto positively

charged slides (Globe Scientific Inc.) and imaged to quantify both coronal and axial transport of the Evans-blue dye. The brains were then stored in a -80°C freezer**.**

Flow Rate Analysis: Anterior-Posterior (AP) ECFR were determined by counting the number of coronal slices with visible Evans blue dye, and assuming an average coronal slice thickness of 0.75 mm. Superior-Inferior (SI) ECFR were not quantified as EB-albumin had reached the end of the inferior dimension by the time of sacrifice, thus limiting the ability to measure flow rates in this direction. Flow rates along WMT were analyzed as a function of the amount of injected albumin.

SECTION 3.2 COMPARISON OF FLOW DOWN WHITE MATTER TRACTS AS MEASURED BY EVANS BLUE LABELED ALBUMIN (AUTOPSY) AND GADOLINIUM LABELLED ALBUMIN (MRI)

Experimental Design: 4 adult female Sprague Dawley rats (B1-4) were used. For B1, Evans blue was injected intracranially without albumin or gadolinium (Gd) to verify that the Evans blue dye alone did not affect MR image quality nor result in brain edema. In addition, this control animal (B1) was expected to provide information on the distribution of unbound Evans blue in the brain. In the other three animals, a Gd-albumin-Evans blue solution (Gd-albumin) was injected into brain parenchyma to simulate passage of known amounts of albumin across the BBB. Images were obtained to visualize the location and dispersion of Gd-albumin. The animals were subsequently autopsied so that the distributions of the EB-albumin and Gd-albumin could be compared. For experiments involving Gd-albumin in the injection solution: a digitally operated stereotactic frame was used for injections; early (2-4 hours following injection) and late (6-8 hours) MRI scans were performed and autopsies were conducted immediately after imaging.

Injection solution: For rat B1, we used a 20 µL solution of 0.02 g (or 1 g/100mL) Evans blue (Fisher Scientific, PA) with Gd-albumin (BioPal, Massachusetts) and bovine albumin. We used a

0.25mg/2.75mg/0.02g solution for rat B2, a 0.25mg/5.75mg/0.02g solution for rat B3 and a 0.5mg/5.5mg /0.04g solution of Gd-albumin/bovine albumin/Evans blue for rat B4.

Rat Brain Coronal Slices At 7-9 hours post injection, the animals B1, B2 and B4 were sacrificed and coronal sections were processed as described above. For Rat B3 in the MRI studies, the brain was placed in 10% formalin before coronal slices were obtained, imaged and documented.

MRI: MRI scans were obtained at approximately 2-4 hours and 6-8 hours post injection using a Bruker horizontal bore 9.4T animal system. The following imaging sequences were used: i) 2D fast low-angle shot (FLASH) sequence with echo time (TE)=2.3ms and repetition time (TR)=300ms, at a flip angle (α) of 30^o and slice thickness (z) = 0.5mm, field of view (FOV)=5.12 × 5.12mm and in-plane resolution at 200×200 μm^2; ii) 3D FLASH sequence with TE/TR=2.3/20ms and $\alpha=15^o$; iii) 2D rapid acquisition with relaxation enhancement (RARE) spin sequence at TE/TR=8-120/4000ms and z=0.5mm. 2D T1-weighted FLASH discriminates tissues with higher Gd concentrations and provides quantitative estimation of ECFR; 3D T1-weighted FLASH of select mice brains provide anatomic visualization of ECF flow patterns and its relationship with adjacent white mater tracts; T2-weighted RARE, on the other hand, distinguishes tissues with edema and provides a visual estimation of the degree of intracerebral edema.

Measurements of Gd-Albumin and EB-Albumin WMT flow rates: For Gd-Albumin, Anterior-Posterior (AP) ECFR were determined by counting the number of MRI coronal cross-sections (0.5 mm thick) with visible Gd-albumin contrast agent. ECFR in the AP direction measured by Evans blue vs. Gd-albumin were recorded and compared. For EB-albumin, AP ECFRs were calculated as described above.

SECTION 4: RESULTS

SECTION 4.1 THE EFFECT OF LOCAL EVANS BLUE LABELED ALBUMIN CONCENTRATIONS ON EXTRACELULAR FLUID FLOW RATES ALONG ADJACENT WHITE MATTER TRACTS

The site of intracranial injection was visually confirmed post-mortem in all 15 rats by the presence of Evans blue dye at the right frontal lobe injection site. In all animals, the entire brain was white except at the site of injection and along the ipsilateral draining WMT, especially at the external capsule. Coronal brain slices for rats A1-15 were obtained at the end of experiment or at 7 hours post injection. Examples of coronal slices from rats receiving 0.12 mg (A1) versus 6.0 mg albumin (A15) are shown in **Figure 1A-B**. Results for 15 rats receiving EB-albumin intracranial injections were demonstrated in **Figure 1C**. A correlation was observed between the intra-cerebrally administered dose of albumin and extracellular fluid flow rates (ECFR) ($R = 0.57$, $R^2 = 0.32$). Statistical significance of anterior-posterior (AP) flow rate of the labeled albumin within the WMT of rats were established for rats receiving lower doses (A1-7 and A10-11) vs. rats receiving the higher dose at 6mg (A12-15) **(Figure 1D)**. Average anterior-posterior (AP) flow rate of the labeled albumin within the WMT of rats receiving 0.12mg albumin (A1-2) was 0.43 mm/hour; and in those receiving 6mg albumin (A12-15), the average AP flow rate was 1.02 mm/hour ($p = 0.015$).

SECTION 4.2 COMPARISON OF FLOW DOWN WHITE MATTER TRACTS AS MEASURED BY EVANS BLUE LABELED ALBUMIN (AUTOPSY) AND GADOLINIUM LABELLED ALBUMIN (MRI)

Four adult female Sprague Dawley rats (B1-4) were used for this part of the study. Associated AP flow rates for each rat were recorded in **Table 1**. In rat B1, Evans blue was administered directly into brain parenchyma without albumin or gadolinium. This was done to ensure that the Evans blue would not affect the MRI and would not result in brain edema. In addition, it would provide information on the distribution of Evans blue that was not bound to albumin.

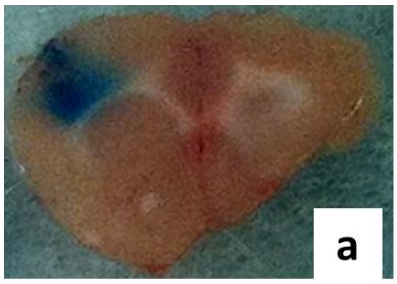

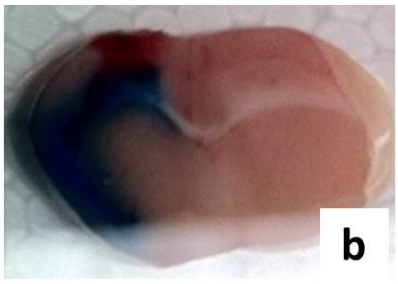

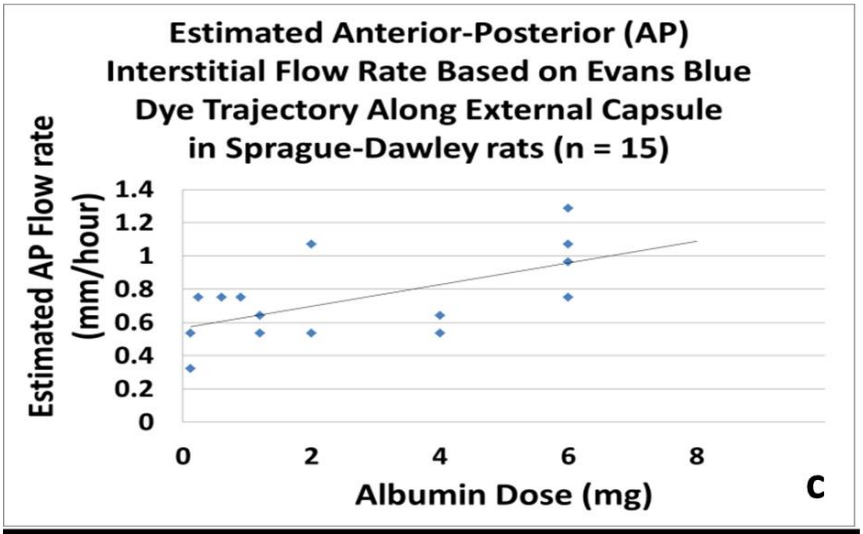

Rats	Albumin Dose (mg)	n	AP Flow Rate (mm/hour)	P-value (vs. 6mg albumin)
A1-2	0.12	2	0.43	0.015*
A3-5	0.24-0.9	3	0.75	0.048*
A6-7	1.2	2	0.59	0.013*
A8-9	2	2	0.80	0.28
A10-11	4	2	0.59	0.013*
A12-15	6	4	1.02	N/A

d

Figure 1. Systematic study of extracellular fluid flow rates along white matter tracts. (A-B) Coronal slices for rats receiving 0.12mg (left) versus 6mg (right) albumin injection, with same concentration of Evans blue (2g/100mL) in 0.9% saline solution. **(C)** Estimated anterior-posterior (AP) extracellular fluid flow based on Evans blue trajectory along external capsule in 15 female Sprague Dawley Rats (A1-15). Each data point represents the rate of EB-albumin flow along white matter tracts for each rat. **(D)** Averaged anterior-posterior (AP) extracellular fluid flow based on Evans blue trajectory along external capsule in 15 female Sprague Dawley Rats (A1-15). One-tailed t-test with unequal variances was used to calculate the p-value when compared with rats A12-15 which received the highest dose of albumin (6 mg). * indicates statistically significant difference with $p < 0.05$. **Figure and figure legends are published by Kut *et al.* (2016), Effect of extracellular fluid flow rates along white matter tracts in murine brain (to be submitted).**

Rat	Albumin Dose (mg)	AP Flow Rate (mm/hour)
B1	0	0.55
B2	3	1.3
B3[#]	6	2.2
B4	6	1.2

Table 1. Averaged Anterior-Posterior (AP) Extracellular Fluid Flow Based on Evans Blue Trajectory along External Capsule in 4 female Sprague Dawley Rats (B1-4) receiving Gd-albumin injections. [#]B3 rat brain was preserved in formalin before AP flow rates were estimated. **Figure and figure legends are published by Kut *et al.* (2016), Effect of extracellular fluid flow rates along white matter tracts in murine brain (to be submitted).**

Figure 2 shows the injection results for rat B1. No trajectories were observed along the external capsule at 2-4 hour and 6-8 hours post injection, validating the fact that Evans blue dye does not contribute to the lesions observed in MRI T1/T2 images. In addition, we found that when Evans blue alone (without albumin) was injected, the dye traveled 2-3 times slower and could be due to local protein binding or lack of edema contributed by the albumin. AP flow rate was estimated to be ~0.55mm/hour.

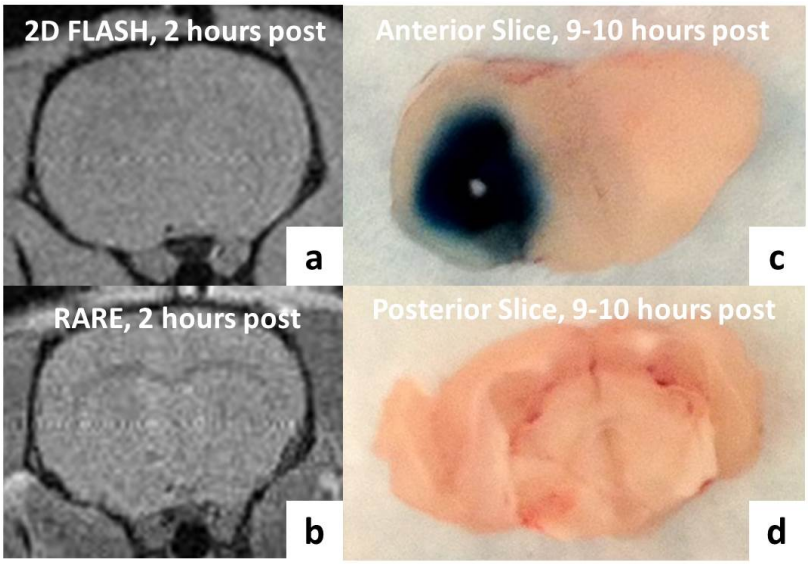

Figure 2. Gd-Albumin trajectory for control MRI rat B1 receiving 20 μ of 1g/100mL Evans blue, without any injections of albumin nor gadolinium. MR Images are only taken at 2 hours post injection and are acquired using a T1 2D FLASH (**Fig. S1a**) and T2 RARE (**Fig. S1b**) sequence, at resolution of 200 microns. T1 FLASH images do not demonstrate any gadolinium signal. T2 RARE Images does not demonstrate gadolinium signal and minimal edema. Corresponding anterior and posterior coronal slices (fresh sections, **Fig. S1c-d**) are taken at 9-10 hours post-injection. The Evans blue dye permeated 7 coronal slices, at an estimated anterior-posterior (AP) flow rate of ~0.55mm/hour. Flow pattern was observed to be different from albumin-injected rats, and demonstrated minimal flow/diffusion both along and peripheral to the external capsule. **Figure and figure legends are published by Kut *et al.* (2016), Effect of extracellular fluid flow rates along white matter tracts in murine brain (to be submitted).**

Our results also demonstrated that intracerebral albumin injections resulted in the development of local edema and increase flow down the WMT. **Figures 3-5** showed bright edema signal surrounding the external capsule at the right frontal lobe at 2 hours and 6 hours post injection. This was in contrast to the dark Gd-albumin signal along the external capsule (since gadolinium decreases both T1 and T2 values). At 2-4 hours post injection, edema signal permeated throughout the ipsilateral external capsule and the signal is especially strong at the lower end of the external capsule; signal enhancement from gadolinium, on the other hand, only traversed the upper half of the external capsule, suggesting that water at a comparable rate to albumin, leading to edema presence before enough water is drawn osmotically into the WMT to allow space for significant gadolinium/Evans blue entry. At 6-8 hours post injection, gadolinium had traversed the entire external capsule, with trace edema in the surrounding areas.

In rats B2-4, a Gd-albumin solution was stereotactically injected directly into brain parenchyma to simulate passage of known amounts of albumin across the BBB. Images were obtained to visualize the Gd-albumin signal. **Figures 3-5** showed the MRI documented trajectories of Gd-albumin dye traveling along the external capsule in the right frontal lobe at 2-4 hours and 6-8 hours per injection for rats B2-4. At 2-4 hours post injection, enhanced T1-weighted signal intensities reflecting the Gd-albumin were already apparent in many coronal slices and have an apparently

accelerated flow rate of 2.5-2.8mm/hour. At 6-8 hours post injection, the dye traversed 18 coronal slices on 2D FLASH images (0.5 mm/slice), which translates to 1.3mm/hour at 6mg albumin dose (B4). This is consistent with our results in the previous section for EB-albumin injections, which reports AP flow rates 0.8-1.3mm/hour at 6mg albumin dose (A12-15, n=4).

These animals were subsequently autopsied so the distribution of the EB-albumin and Gd-albumin could be compared. Fresh coronal slices for rats B1-4 were obtained at the end of the experiments (except rat B3 which was preserved in formalin before coronal slices were obtained). Examples of coronal slices form rats B1-4 are shown in **Figures 3-5**. Based on coronal sections obtained post-imaging (**Figures 3-5**), the Evans blue dye (injected within the same dose with Gd-albumin) traversed at an estimated AP flow rate of *1.3mm/hour* for rat B2 (*3mg total albumin*, fresh sections) and *1.2mm/hour* for rat B4 (*6mg total albumin***,** fresh sections) (**Table 1**). This is consistent with our Evans blue WMT flow rate results, which reports AP flow rate of 0.5-1.1mm/hour at 2-4mg albumin dose (A8-11, n = 4) and 0.8-1.3mm/hour at 6mg albumin dose (A12-15, n = 4). For rat B3, the Evans blue dye traversed at an estimated flow rate of 2.2mm/hour (6mg total albumin). However, since the brain of rat B3 was preserved in formalin before coronal sections, it is possible that the Evans blue dyed has diffused and spread to more sections during the formalin fixation process.

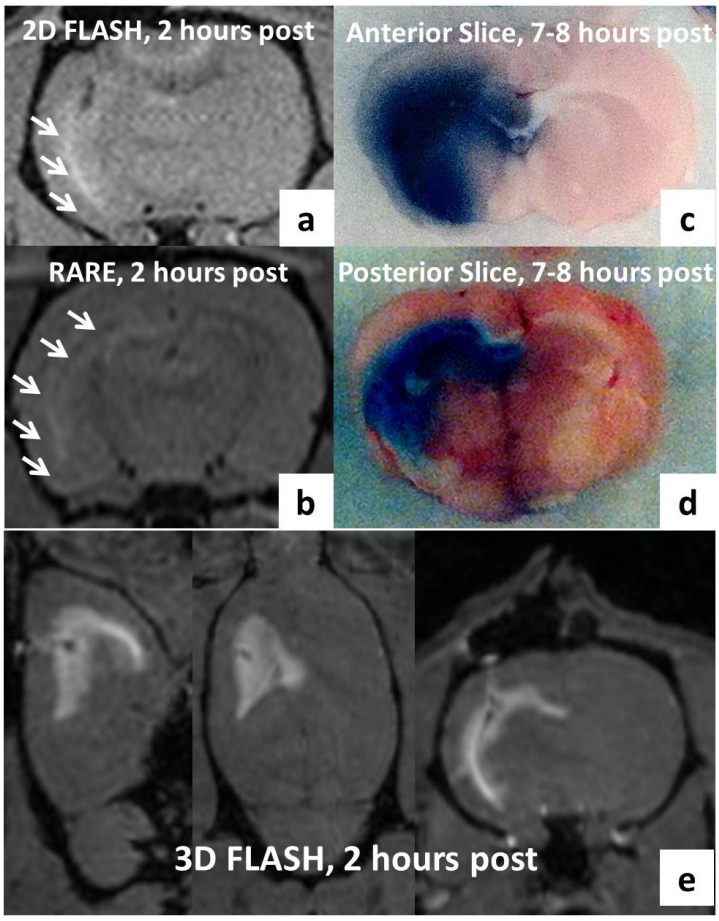

Figure 3. Gadolinium-Albumin trajectory for rat B2. (A-B) Gd-Albumin trajectory for MRI rat B2 receiving 20 microliters of 1g/100mL Evans blue, 0.25mg Gd-Albumin Complex and 2.75mg bovine albumin. Images are only taken at 2 hours post injection, as the animal died during the second imaging session at 6-hours post injection. MRI Images are acquired using a T1 2D FLASH (**A**) and T2 RARE (**B**) sequence, at resolution of 200 microns. T1 FLASH images demonstrate bright gadolinium signal (marked by arrows) along the external capsule ipsilateral to the injection site. T2 RARE Images demonstrate gadolinium signal (dark signal) along the upper half of the ipsilateral external capsule. This is accompanied by edema (bright signal marked by arrows) at the periphery and also towards end of the external capsule. Corresponding anterior and posterior coronal slices (fresh sections, **C-D)** are taken at 7-8 hours post-injection. The Evans blue dye permeated 13 coronal slices, at an estimated anterior-posterior (AP) flow rate of ~1.3mm/hour. Note that the AP flow rate was comparable to MRI rat B4, even though the Gd-albumin and Evans blue concentration has been cut down by 50%. This points to possible signal saturation with the lower doses given to the MRI rat B2**. (E)** 3D Gd-Albumin trajectory for MRI rat B2. Images are acquired using a T1 3D FLASH sequence, which demonstrate bright gadolinium signal along the external capsule in axial (left), sagittal (middle) and coronal views (right). Dark spot along trajectory indicates the injection track of the stereotactic needle. **Figure and figure legends are published by Kut *et al.* (2016), Effect of extracellular fluid flow rates along white matter tracts in murine brain (to be submitted).**

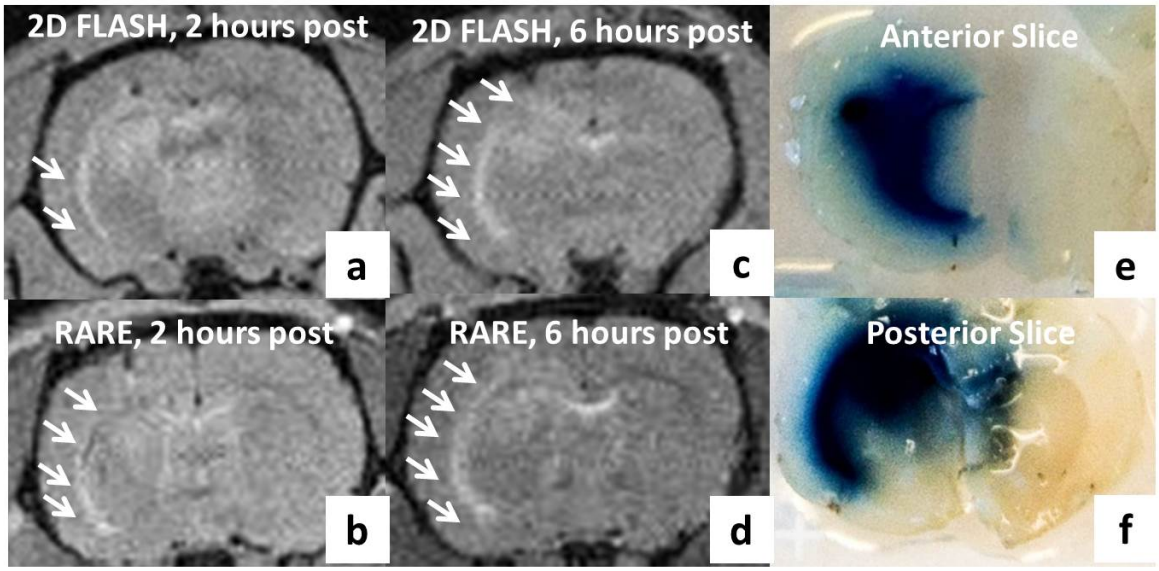

Fig. 4: Gd-Albumin trajectory for MRI rat B3 receiving 20 microliters of 1g/100mL. **(A-D)** Evans blue, 0.25mg Gd-Albumin Complex and 5.75mg bovine albumin. MR Images are acquired using a T1 2D FLASH and T2 RARE sequence, at resolution of 200 microns, and are taken at 2-4 hours (**A-B**) and 6-8 hours post injection (**C-D**). T1 FLASH images demonstrate bright gadolinium signal (marked by arrows) along the external capsule ipsilateral to the injection site. T2 RARE Images demonstrate gadolinium signal (dark signal) along the upper half of the ipsilateral external capsule. This is accompanied by edema (bright signal marked by arrows) at the periphery and also towards end of the external capsule 2 hours post injection, At 6 hours post-injection (right), gadolinium signal permeates throughout the external capsule, accompanied by peripheral edema (marked by arrows*)*.Corresponding anterior and posterior coronal slices (formalin-fixed sections, **E-F**) are taken at 7-8 hours post-injection. The Evans blue dye permeated 33 coronal slices (0.5mm thick), at an estimated anterior-posterior (AP) flow rate of ~2.2mm/hour. However, since the brain was preserved in formalin before coronal sections, it is possible that the Evans blue dyed has diffused and spread to more sections during the formalin fixation process. **Figure and figure legends are published by Kut *et al.* (2016), Effect of extracellular fluid flow rates along white matter tracts in murine brain (to be submitted).**

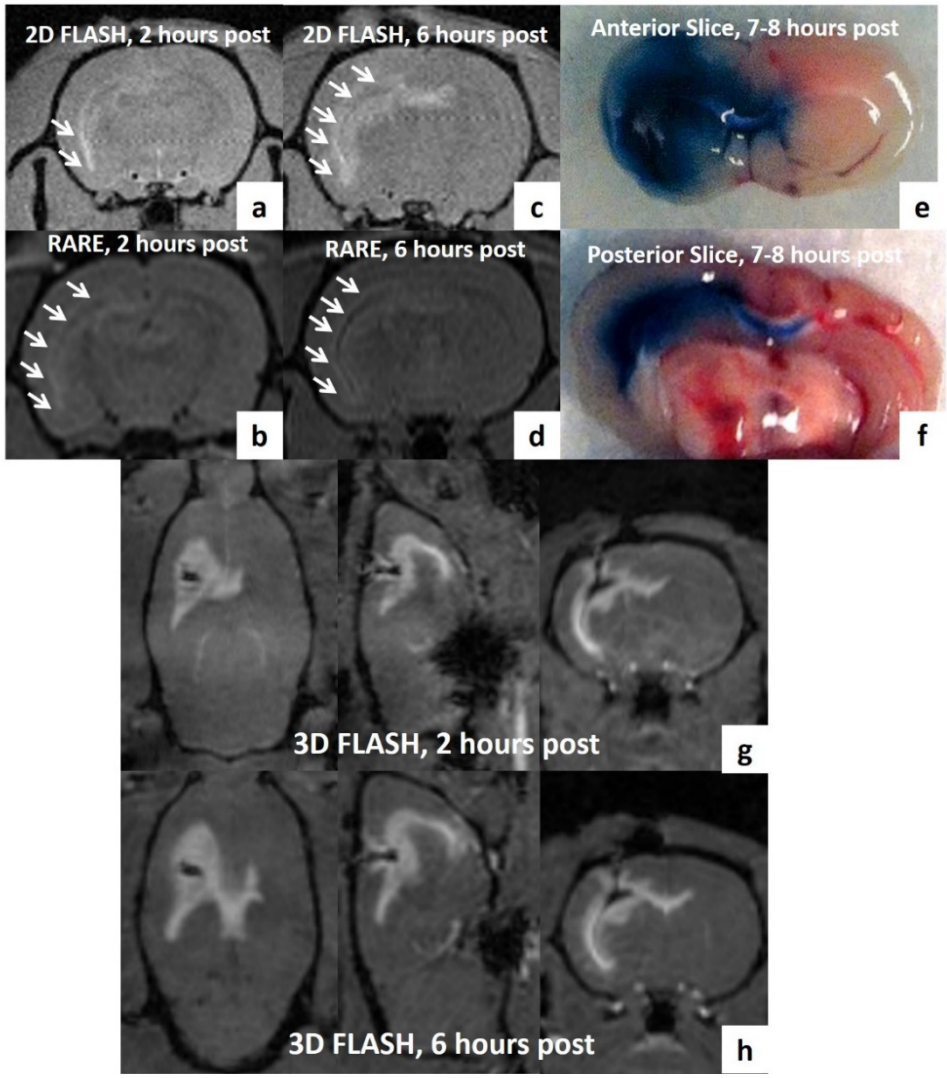

Figure 5. Gd-Albumin trajectory for MRI rat B4 receiving 20 microliters of 2g/100mL. **(A-D)** Evans blue, 0.5mg Gd-Albumin Complex and 5.5mg bovine albumin were injected into the rat brain. MRI Images are acquired using a T1 2D FLASH and T2 RARE sequence, at resolution of 200 microns, and are taken at 2-4 hours **(A-B)** and 6-8 hours **(C-D)** post injection. T1 FLASH images demonstrate bright gadolinium signal (marked by arrows) along the external capsule ipsilateral to the injection site. T2 RARE Images demonstrate gadolinium signal (dark signal) along the upper half of the ipsilateral external capsule. This is accompanied by edema (bright signal marked by arrows) at the periphery and also towards end of the external capsule 2 hours post injection, At 6 hours post-injection (right), gadolinium signal permeates throughout the external capsule, accompanied by peripheral edema (marked by arrows). Corresponding anterior and posterior coronal slices (fresh sections, **E-F**) are taken at 7-8 hours post-injection. The Evans blue dye permeated 12 coronal slices, at an estimated anterior-posterior (AP) flow rate of ~1.2mm/hour. **(G-H)** 3D Gd-Albumin trajectory for MRI rat B4. Images are acquired using a T1 3D FLASH sequence, which demonstrate bright gadolinium signal along the external capsule in axial (left), sagittal (middle) and coronal views (right). Dark spot along trajectory indicates the injection track of the stereotactic needle. **Figure and figure legends are published by Kut *et al.***

(2016), Effect of extracellular fluid flow rates along white matter tracts in murine brain (to be submitted).

SECTION 5: DISCUSSION AND CONCLUSION

Essentially all neurological diseases are associated with abnormal interstitial clearance from the brain. For neuro-degenerative diseases such as multiple sclerosis and Parkinson's disease, the failure of waste clearance leads to the aggregation of neurotoxic metabolites within the brain tissue and consequently brain injury (*146*). On the other hand, glioma cells in brain tumor patients may aggregate and drain along white matter with brain extracellular fluid, similar to how systemic cancer cells are carried to regional lymph nodes (*134, 135*).

Previous studies have recognized two major pathways of interstitial clearance: 1) the glymphatic pathway through the astrocytic endfeet and 2) the axonal pathway e along white matter tracts (*130-133*). Since glymphatic clearance fails significantly during neuro-pathologic conditions, our study aimed to better understand the axonal clearance pathways along the white matter tracts, which could be a target for enhanced ECF drainage. To accomplish this, we simulated different degrees of BBB disruption by injecting various concentrations of albumin intracranially into rat brains, and evaluated the relationship between the concentration of albumin reaching the brain and the resulting axonal clearance rates (ECFR) along the draining white matter tracts using both *in vivo* MRI and *ex vivo* Evans blue validation. More specifically, we aimed to elucidate how varying concentrations of BBB disruption affects ECFR along white matter tracts.

The BBB was first identified by Erlich in 1985 when he reported that intravenous injections of albumin bound dyes into rats stained all tissues except the brain (*131, 147*). Subsequent studies in both animals and humans demonstrated albumin extravasation into the brain when the BBB is disrupted by insults to the central nervous system e.g. tumor, infection, trauma, neurodegenerative diseases, and stroke (*133, 142, 143, 148*).

Furthermore, BBB disruption often results in intracranial edema and protein leakage that is specifically localized to the white matter tracts (WMT) (*149*). There is data showing a larger increase in extracellular fluid content in edematous white matter of dog brains, when compared with edematous cortical areas of the brain (*150*). Similarly in patients suffering from brain injury and associated edema, diffusion tensor imaging reveals the distortion, disruption and interruption of WMT that are displaced by the tumor and surrounding edema (*151*). ECF accumulation and drainage along WMT have additional implications for brain tumor patients and could reflect glioma dissemination patterns, as gliomas frequently occur along white matter tracts based on clinical, radiologic and pathologic observations (*142, 143, 152, 153*). These factors indicate a need to understand, visualize and measure ECFR and ECF drainage patterns along the white matter tract; this requires the utilization of an imaging method is safe, non-invasive and can be easily translated into clinical use; MRI is one such imaging method.

In this study, we used the direct administration of albumin into the rat brains as a controllable surrogate for a disrupted blood brain barrier. Instead of having albumin leak through a disrupted blood brain barrier, we injected a known concentration of albumin behind an intact blood brain barrier and were able to show that as we administered a larger amount of albumin into the brain, more water accumulated, and this translated into more water flow down the axonal pathways and along the white matter tracts. As expected, when EB-albumin was injected intracranially, it was carried by bulk flow of extracellular fluid along nearby WMT. Furthermore, as increasing concentrations of albumin were administered intracranially, the labeled albumin was carried to more distant locations along WMT. This suggested that the injected albumin osmotically

draws water into the brain from the capillaries, results in more edema around the injection site and increases bulk flow rates down the WMT.

Following the initial baseline study using EB-albumin, we proceed to establish non-invasive, imaging protocols for MRI using a 2D T1-weighted FLASH sequence for gadolinium visualization, 3D T1-weighted FLASH sequence for anatomic visualization of ECF flow patterns, and 2D T2-weighted RARE sequence for visual estimation of intracerebral edema at the 2-4 hour and 6-8 hour time points. A Gd-albumin solution was intracranially injected into brain parenchyma to simulate BBB disruption and resulting edema and protein leakage into brain. Based on the MRI results, we managed to draw similar conclusions from *in vivo* MRI studies in rats that intracerebral albumin injections resulted in the development of local edema and increased ECFR down the WMT. Our MRI T2 RARE images from rats B2-4 demonstrated markedly increased edema (bright signal) in the hemisphere where albumin was injected. This is in contrast to the dark Gd-albumin signal along the ipsilateral external capsule (since gadolinium decreases both T1 and T2 values). Since edema signal (bright) surrounded and extended beyond the Gd-albumin signal (dark) along the ipsilateral external capsule in T2 RARE images, our data suggests that water was able to travel down the white matter pathways at a comparable rate as the labeled albumin. It was worth noting that with diffusion, Gd-albumin reached low concentrations towards the end of the external capsule; since T2 reduction of Gd signal was much less pronounced than T1 reduction, this could account for the weak Gd-albumin signal (dark) on the T2 RARE images when compared with the strong edema signal (bright).

Furthermore, our 2D T1-weighted FLASH images result in bright gadolinium signal in 18 coronal slices (0.5 mm/slice), which translates into 1.3 mm/hour at 6 mg albumin dose (B4). This result is consistent with our results in the baseline study (0.8-1.3 mm/hour at 6 mg albumin dose,

A12-15, n = 4) as well as subsequent autopsy result of the same animal (B4) using EB-albumin validation (1.2 mm/hour).

As a result, we have demonstrated that non-invasive MRI scans can be used to non-invasively track the flow of labeled albumin down WMT, as the albumin drains from the intra-cerebral injection site. We also determined that the Evans blue dye alone did not enhance the MRI signal. In addition, when Evans blue was injected intracranially without albumin, the dye traveled 2-3 times slower and exhibited minimal flow along and peripheral to the external capsule.

It is also worth noting that the rat serum albumin concentration is about 30 mg/mL (*147*). As a result of the blood brain barrier, albumin concentration in the brain ranges between zero to serum albumin concentration, or 0 mg/mL to 30 mg/mL. Studies also demonstrate intracellular uptake of albumin by astrocytes and neurons, which suggest that the total albumin content in the brain could be higher than 30 mg/mL. In this study, we injected a total of 0 mg/mL to 300 mg/mL albumin into the brain in order to induce maximal edema and study anterior-posterior flow rates along the white matter tracts.

No direct comparisons between *ex vivo* Evans blue vs. *in vivo* MRI studies can be made due to inherent methodological differences. First, high concentrations of gadolinium (12.5-25mg/mL) resulted in higher sensitivity of detection when compared with Evans blue dye used in flow rate studies. In addition, MRI studies receive more accurate and complete dosing using the digital stereotactic injection frame (versus earlier WMT flow rate studies which used a manual stereotactic injection frame); such dose saturation may account for the similar flow rates observed for 3mg vs. 6mg albumin injections in the MRI study. Furthermore, the size and charge differences between EB-albumin (2 disulfonate groups, ~70kDa) and Gd-albumin (gadolinium (III) chelate, 74 kDa) may influence the rate of movement along white matter tracts. Finally, one rat brain was

preserved in formalin before coronal sections and AP ECFR measurements (as opposed to fresh sections and measurements) and exhibited twice the AP flow rate than other rats with 6mg total albumin injections (B4, A12-15). It is possible that the accelerated flow rates resulted from Evans blue diffusion in the anterior-posterior direction during the fixation process.

These observations have potentially important and practical implications. Glucocorticoids used to control peritumoral edema are associated with significant toxicities. As a result, clinicians work diligently to keep glucocorticoid doses to a minimum when starting these medications, and increasing the dose only when patients become symptomatic from brain edema. By then, there is sizable peritumoral edema and, by definition, fluids are entering brain parenchyma more rapidly than they are being cleared. Thus, the bulk flow velocity of extracellular fluid is maximal as it travels down the WMT. These rapid flow rates could facilitate the passive transport and clearance of neuro-toxic metabolites such as beta and tau amyloids in Alzheimer's disease. On the other hand, the same rapid flow rates could be detrimental to a cancer patient as it accelerates the passive dissemination of cancer cells to distant brain regions. In addition to the baseline disruption of the BBB frequently associated with neuro-pathological conditions, radiation therapy is known to further impair BBB integrity resulting in symptomatic and radiologic increases in brain edema and intracranial pressure. Our findings suggest that maintaining the BBB integrity with glucocorticoids or VEGF targeted agents may reduce the passive movement of tumor cells carried in the bulk flow of extracellular fluid to regions beyond the radiation field in newly diagnosed patients with high grade gliomas. In addition, we demonstrated the ability to track extracellular fluid flow rates along white matter pathways in the brain in a non-invasive manner using gadolinium contrast. Such identification of the WMT "draining" extracellular fluids could highlight the rate and drainage patterns of extracellular fluid down the white matter, when

glymphatic clearance pathways are clearly compromised due to mislocation of aquaporin channels. If this is true, we could take advantage of such information to modify therapeutic interventions, similar to the way physicians identify drainage of cancer cells and toxic metabolites to the lymph nodes in systemic disease. Consequently, further studies outlining the role of extracellular bulk flow in patients with neuro-pathological conditions are of great importance.

APPENDIX 2: VIEWPOINT ON THE IMPORTANCE OF BLOOD-BRAIN-BARRIER (BBB) TO THE DEVELOPMENT OF NEUROTHERAPEUTICS

In the course of my PhD, I reviewed the literature on the importance of blood-brain-barrier (BBB) to the development of neurotherapeutics to two clinical faculty, Professor Jaishri Blakeley and Professor Stuart Grossman. This viewpoint paper has been recently published in JAMA Neurology (*154*). Due to copyright permissions, this paper is not included in the dissertation.

APPENDIX 3: CONSIDERATIONS IN PLANNING THE RADIOTHERAPY OF BRAIN TUMORS: NEURAL PROGENITOR CELL-CONTAINING NICHES

SECTION 1: OVERVIEW

In the course of my PhD, I reviewed the literature regarding the considerations in planning radiation treatment for brain tumor patients with Professor Kristin Redmond at Radiation Oncology. This review paper has been published in Seminars in Radiation Oncology (*155*), and its purpose is to explore the controversy regarding the relationship between radiation dose to the neural progenitor cell (NPC) niches and patient outcome, both in terms of toxicity and tumor control. NPCs in the sub-ventricular zone (SVZ) and hippocampus are paradoxically associated with both the long term neuro-cognitive sequelae of brain irradiation and in resistance to therapy and tumor recurrence. The reconciliation of these somewhat opposing functions is challenging. Current literature suggests that irradiation and other treatments against the NPC in the hippocampus and the SVZ may influence patient outcome. As a result, both the SVZ and the hippocampus could have important implications on radiation treatment planning strategies, and future laboratory and clinical studies will be critical in designing future studies to optimize treatment outcome, effectiveness and safety. The full review paper is copied below for the completeness of this dissertation, with permission from Elsevier. **Reprinted from Seminars in Radiation Oncology, Kut, C., & Redmond, K. J., New Considerations in Radiation**

Treatment Planning for Brain Tumors: Neural Progenitor Cell–Containing Niches, Vol. 24, No. 4, pp. 265-272, Copyright (2015), with permission from Elsevier.

SECTION 2: INTRODUCTION

Radiation treatment is important in the management of many pediatric and adult brain tumors. However, radiation to the brain is associated with neuro-cognitive toxicity (*156-161*), and it is hypothesized that injury to these particularly radiosensitive regions of the brain during radiation may contribute to long term complications and reduced neuro-cognitive performances. Recently, controversy has developed regarding the relationship between radiation dose to the neural progenitor cell (NPCs) niches and patient outcome, both in terms of toxicity and tumor control (*162*).

A neural progenitor cell is a multi-potent stem cell with the capacity to differentiate into new neurons and glia (*163*). Within the mammalian brain, these NPCs are known to reside in two areas: the sub-ventricular zones and the sub-granular zones **(Figure 1)** (*164*). Both are considered the germinal regions of the adult human brain. The sub-ventricular zone (SVZ) is the largest germinal region in the adult mammalian brain and is located in the lining of the lateral ventricles, while the sub-granular zones (SGZ) is located within the dentate gyrus of the hippocampus (*165*).

While the functional role of NPCs in humans have not been fully defined, animal studies demonstrate that NPCs in the SVZ and the hippocampus are capable of self-renewal, injury repair, and tumor inhibition (*166-170*). It is hypothesized that injury to NPCs during radiation to the brain may contribute to the long term sequelae of radiation therapy, most notably in terms of neuro-psychological toxicity. Yet, paradoxically, emerging evidence suggests that NPCs may also contribute to cancer recurrence and glioma resistance to chemotherapy and radiation therapy (*171-*

174). The purpose of this critical review is to summarize the current literature and explore the controversy regarding radiation therapy to the SVZ and hippocampus.

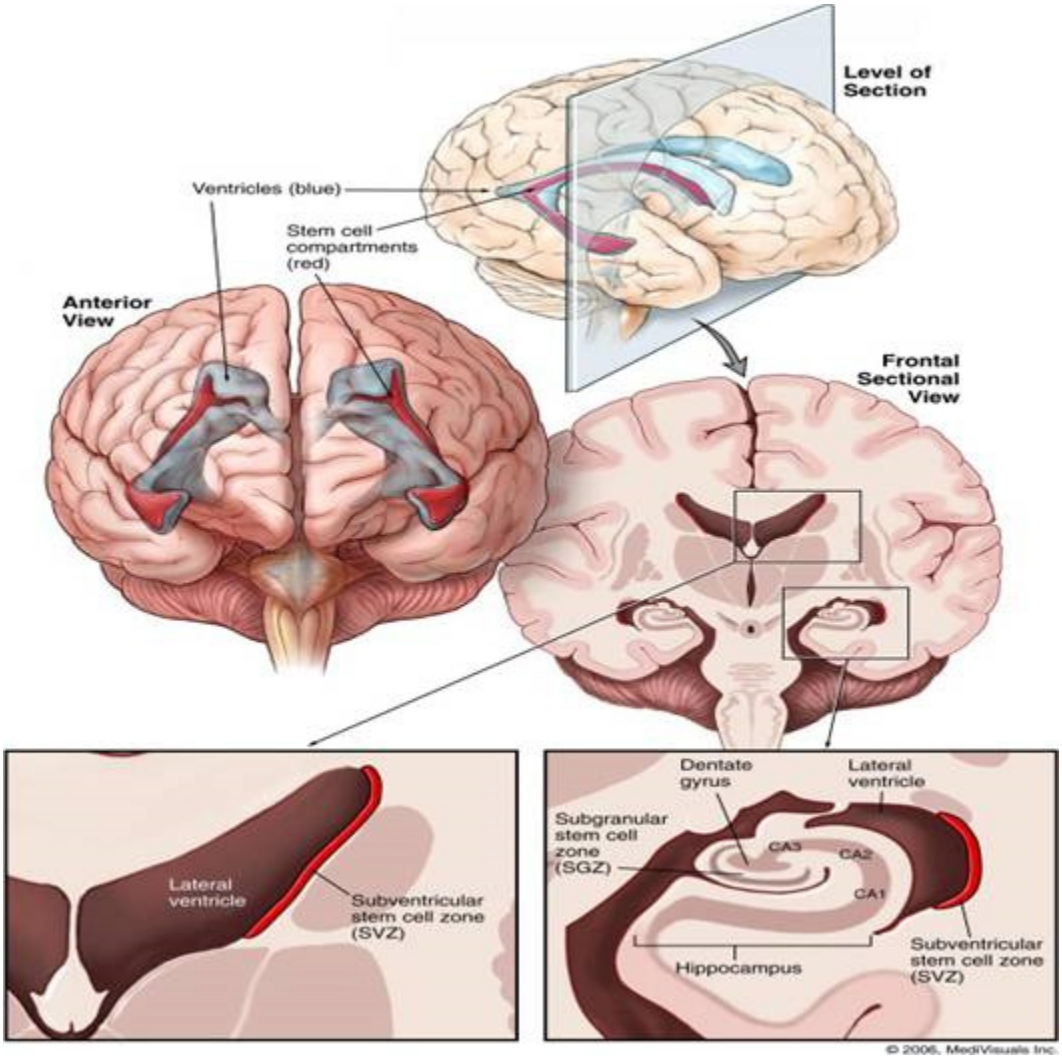

Figure 1. **Germinal regions of the adult human brain.** The sub-ventricular zone (SVZ) is the largest germinal region in the adult mammalian brain, located in the lateral wall of the lateral ventricle. The sub-granular zone (SGZ) is located within the dentate gyrus of the hippocampus. The CA1, CA2, and CA3 represent Cornu Annulis fields of hippocampus proper and, along with dentate gyrus, constitute the hippocampal formation, the primary memory center in the brain. Figure and figure legends are published in Kut& Redmond, (2014, October). New Considerations in Radiation Treatment Planning for Brain Tumors: Neural Progenitor Cell–Containing Niches. *In Seminars in radiation oncology* (Vol. 24, No. 4, pp. 265-272). **However, the copyright belonged to © 2006 MediVisuals Inc. and the figure was reprinted in our paper with permission from**

SECTION 3: RADIATION SPARING OF NEURAL PROGENITOR NICHES (NPC) MAY PRESERVE NEURO-COGNITIVE FUNCTION

Radiation to the brain is associated with neuro-cognitive toxicity and reduced performance on neuro-psychological testing, especially in children **(Figure 2)** (*156-161, 175, 176*). While the cause of radiation-induced damage to the brain is likely multi-factorial, there is a growing body of evidence which suggests that injury to the NPCs may play a role. In this section of the paper, we discuss the roles of NPCs and its impacts on neuro-cognitive performances. We will also summarize the current literature and discuss how NPC sparing radiation protocols in both the hippocampus and the SVZ may impact patient outcomes.

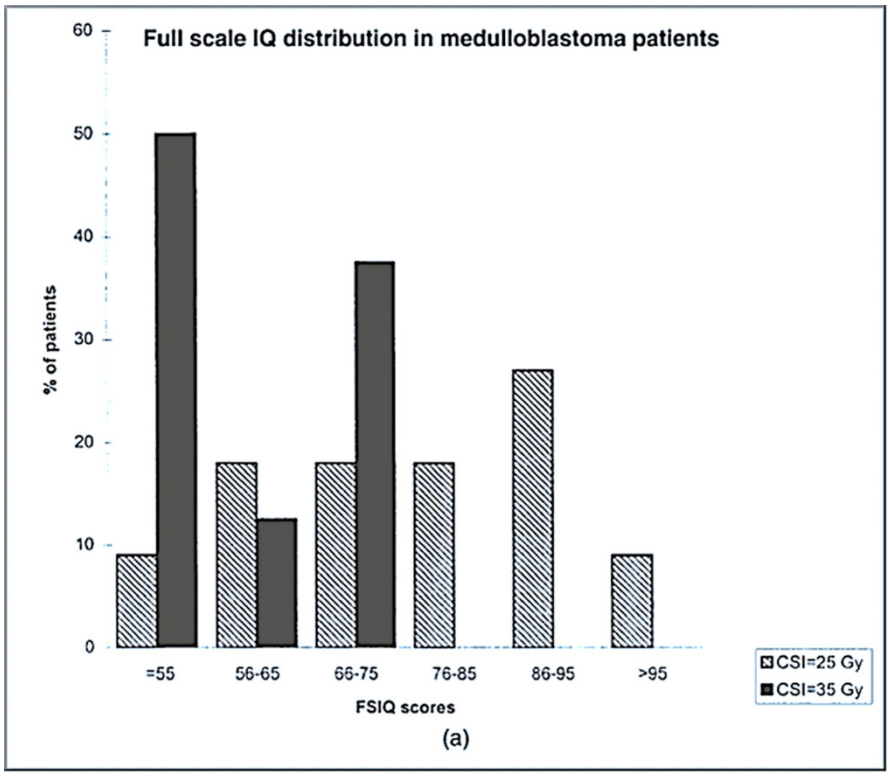

Figure 2. Full-scale IQ distribution in patients with medulloblastoma. Long-term neurocognitive deficits are observed with radiation therapies in a dose-dependent manner. In this study, patients treated with 35 Gy of craniospinal (CSI) radiation demonstrated significantly poorer performance on the full-scale IQ testing than patients treated with 25 Gy of CSI. Number of patients in group CSI = 25 Gy is 11. Number of patients in group CSI = 35 Gy is 8. FSIQ, full-scale IQ. Figure and figure legends are published in Kut& Redmond, (2014, October). New Considerations in Radiation Treatment Planning for Brain Tumors: Neural Progenitor Cell–Containing Niches. *In Seminars in radiation oncology* (Vol. 24, No. 4, pp. 265-272). **However, the original figure was reprinted with permission from Grill *et al.*, (1999). Long-term intellectual outcome in children with posterior fossa tumors according to radiation doses and volumes. *International Journal of Radiation Oncology* Biology* Physics*, *45*(1), 137-145.**

NPCs are capable of injury repair in both the SVZ of the lateral ventricles and the SGZ of the hippocampus. Previous studies have demonstrated how NPCs migrate to the site of inflammation and replace endogenous cells following cortical injury, stroke and epilepsy (*168, 169*). In other words, NPCs are capable of neuronal renewal and regeneration. Understandingly, radiation-induced damage to these progenitor cells could impact neuro-cognitive function (*177-183*). Moreover, radiation doses to the distinct NPC niches seem to have different levels of impact,

and previous studies have reported an especially strong association between radiation to the hippocampus and neuro-cognitive toxicity. For example, animal studies have shown that radiation to the brain significantly reduces the formation of new cells in the hippocampus and is associated with decreased performance of hippocampal-related tasks (*178, 179, 184, 185*).

Similarly, clinical studies have demonstrated that radiation to the hippocampus is associated with neuro-cognitive deficits (*186-192*). NPCs are also found in humans, and these germinal areas including the SVZ and the hippocampus have also been associated with the formation of new neurons (*163, 193*). Several studies linked radiation dose to brain regions such as the hippocampus to the development of neuro-cognitive deficits in children (*186, 191, 192*). Furthermore, prospective data from a pediatric study suggests a significant association between the mean radiation dose to the hippocampus and temporal lobe, and decline in neuro-cognitive performance **(Figure 3)** (*186*).

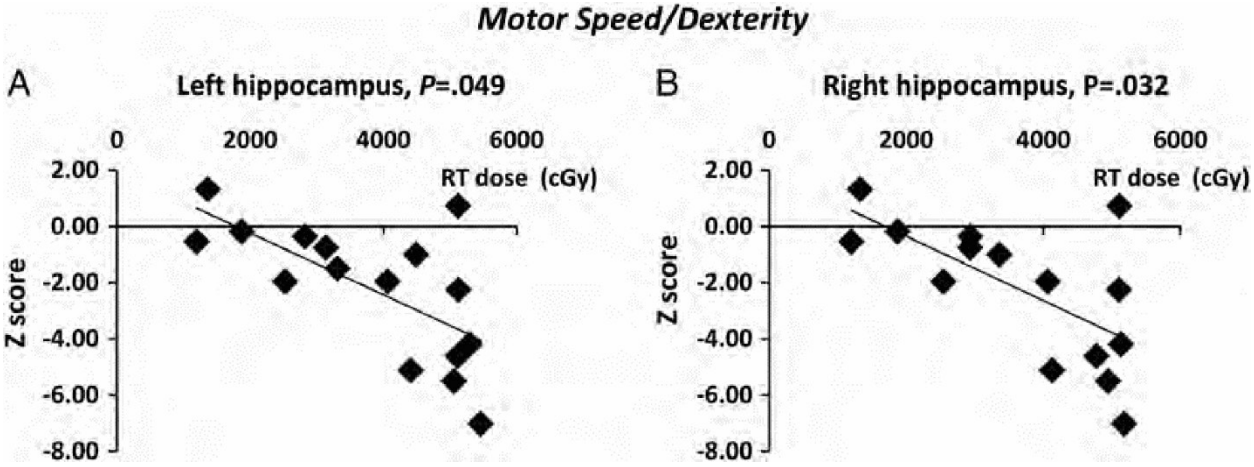

Figure 3. Performance on neuropsychological testing is worse with increasing radiation dose to the hippocampus. The performance on the Purdue Pegboard both hands test (*Z*-scores), a measure of motor dexterity and speed, at 6 months following completion of RT relative to (A) mean left

hippocampal radiation dose, $P = 0.049$, and (B) mean right hippocampal radiation dose, $P = 0.032$ is shown. Standardized scores were used in this analysis to account for the effect of age on test performance. Figure and figure legends are published in Kut& Redmond, (2014, October). New Considerations in Radiation Treatment Planning for Brain Tumors: Neural Progenitor Cell–Containing Niches. *In Seminars in radiation oncology* (Vol. 24, No. 4, pp. 265-272). **However, the original figure was reprinted with permission from Redmond *et al.* (2013). Association between radiation dose to neuronal progenitor cell niches and temporal lobes and performance on neuropsychological testing in children: a prospective study. *Neuro-oncology*, nos303.**

While studies have shown an association between the radiation therapy (RT) dose to the hippocampus and neuro-cognitive function, the relationship between RT dose to the SVZ and neuro-cognitive function is more controversial (*186, 194, 195*). Reductions in neuro-cognitive performance have been documented following administration of intra-thecal chemotherapy in children with leukemia (*187*). Given that the drug penetrates only a thin layer adjacent to the ventricular system, this suggests that periventricular cells may play an important role in neuro-cognitive function. However, improved neuro-cognitive performance in patients with CNS germ cell tumors who were treated with whole-ventricle radiation when compared with craniospinal radiation has been reported (*195*) suggesting that perhaps the cells lining the ventricle may not be as vital as other areas in the brain in neuro-cognitive sequelae of RT. In addition, only one animal study to date has documented a relationship between RT dose to the SVZ and performance on neuro-psychological testing (*196*), and no human studies have confirmed this relationship.

Given the potential relationship between radiation injury to the NPC and neuro-cognitive deficits, ongoing efforts are evaluating the possibility of hippocampal-sparing radiation therapy techniques. Several studies have suggested that sparing of the NPC in the hippocampus and SVZ is possible using modern treatment planning techniques **(Figure 4)** (*165, 197-200*). In addition, an animal study suggested that these techniques effectively spare the NPCs **(Figure 5)** (*198*).

Preliminary results from RTOG 0933 suggest that hippocampal-sparing may be associated with reduced short term memory deficits in patients with brain metastases compared with a historical control treated with conventional whole brain radiation therapy on an earlier RTOG study (*197*). Specifically, patients treated hippocampal sparing whole brain radiation therapy demonstrated a 7% memory loss, compared to 30% in the historical control. Quality-of-life assessments from the same study also demonstrated more favorable results for patients treated with hippocampal-sparing RT when compared with the historical control (*197*).

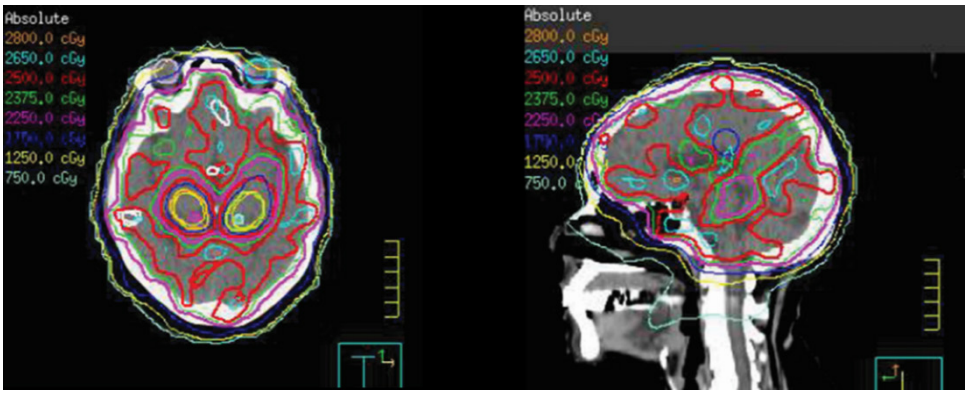

Figure 4. An example hippocampal-sparing prophylactic cranial irradiation (PCI) treatment plan. The prescription dose is 25 Gy in 10 fractions. The mean dose to the hippocampal avoidance region is <8 Gy with >90% of prescription dose covering >90% of whole brain. **Figure and figure legends are published in Kut& Redmond, (2014, October). New Considerations in Radiation Treatment Planning for Brain Tumors: Neural Progenitor Cell–Containing Niches. *In Seminars in radiation oncology* (Vol. 24, No. 4, pp. 265-272).**

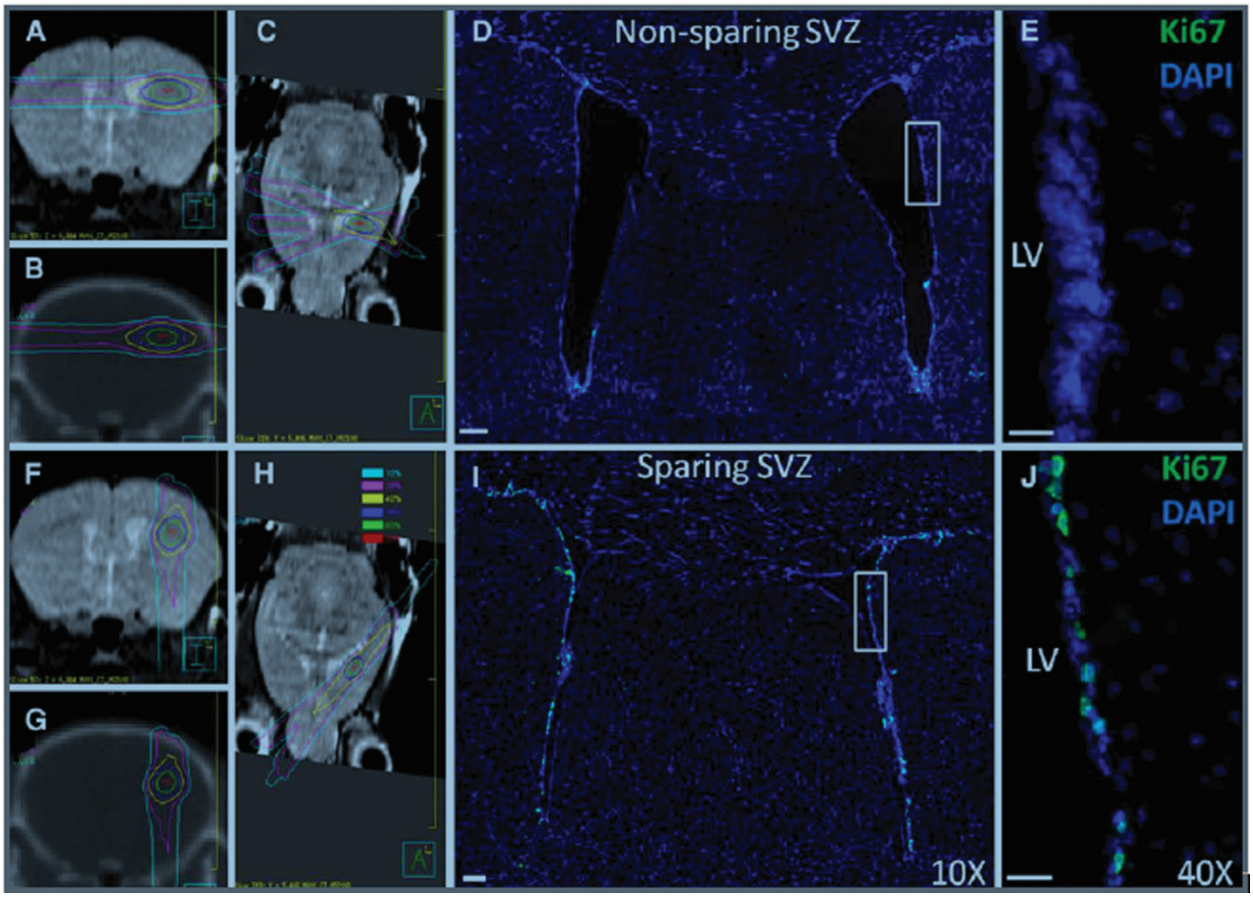

Figure 5. Mouse radiation treatment plans (left) and microscopy images (right) for the non–NPC-sparing (top) and NPC-sparing (bottom) radiotherapy plans. Left side MR and CT images from the mouse radiation treatment plans showing the radiation dose distribution for the non–NPC-sparing (A-C) and NPC-sparing radiation treatment plans (F-H). It can be noted that for the non–NPC-sparing plan, the region of the SVZ of the ipsilateral lateral ventricle receives a high radiation dose, whereas this region is effectively spared in the NPC-sparing plan. Scans taken are as follows: coronal MRI (A and F), coronal CT (B and G), and axial MRI (C and H). Dose values are shown in the legend. Right side coronal sections showing Ki-67 stains (green) in the SVZ of the lateral ventricles following non–NPC-sparing RT (D and E) and NPC-sparing RT (I and J). Ki-67 is a marker of cellular proliferation and is used in this model as a potential indicator of NPCs. Costaining is performed using DAPI (blue). Images (D and I) were taken with a 109 objective lens and the images (E and J) with 409 objective lens. CT, computed tomography; DAPI, 4′,6-diamidino-2-phenylindole; MRI, magnetic resonance imaging; LV, left ventricle. Figure and figure legends are published in Kut& Redmond, (2014, October). New Considerations in Radiation Treatment Planning for Brain Tumors: Neural Progenitor Cell–Containing Niches. *In Seminars in radiation oncology* (Vol. 24, No. 4, pp. 265-272). **However, the original figure was reprinted with permission from Redmond *et al.* (2011). A radiotherapy technique to limit dose to neural progenitor cell niches without compromising tumor coverage. *Journal of neuro-oncology*, *104*(2), 579-587.**

Given the optimistic phase II data, the concept of hippocampal sparing radiation therapy merits further investigation. An ideal population to further evaluate this hypothesis is in patients with small cell lung cancer (SCLC) who receive prophylactic cranial irradiation (PCI), since these patients do have an intra-parenchymal mass to confound the results, and the chemotherapy that they receive is relatively homogeneous. There is an ongoing single arm phase II study in patients with limited stage SCLC which is currently enrolling patients at our institution. The eligibility criteria are based on RTOG 0212 which will be used as a historical control. An intergroup study is currently under development to more definitively evaluate the concept in patients with limited and extensive stage SCLC in which patients will be randomized to either hippocampal-sparing PCI or conventional whole brain radiation.

SECTION 4: THE COMPLICATION: RADIATION TO NPC NICHES MAY IMPACT OUTCOMES IN CERTAIN TUMOR TYPES

Although the data outlined above suggests that limiting RT dose to the NPC regions might be beneficial in reducing neuro-cognitive sequelae of brain RT, the issue may not be as straightforward as it initially appears. While NPCs are associated with injury repair, there is also evidence that they may be involved with tumor control as well as tumor recurrence and cancer radio-resistant behaviors in certain tumor types. Interestingly, there is data to support both a positive and negative relationship in this setting.

For example, in vitro data from brain tumors suggest that NPCs may transform into cancer stem cells through a series of mutations in the oncogenes and tumor suppressor genes and that this ultimately may allow them to have pro-tumor behavior (*171-173*). Oncogenes in NPCs of the sub-ventricular zone can be activated to induce proliferation, survival and migration in mice, leading to the formation of gliomas (*177, 178*). Furthermore, NPCs share many properties with cancer

stem cells, including their ability to migrate in brain [40]. Glioma cells are shown to release factors that actively recruit nearby NPCs and induce their malignant transformation into cancer stem cells (*201*).

Previous studies have also suggested that radiation might encourage the induction of NPCs into cancer stem cells and that the consequent malignant transformation of NPCs may potentially contribute to the glioblastoma resistance to chemotherapy and radiation therapy. Radiated cancer cells showed an enrichment of CD-133 expressing cells, a marker which is specific for both NPCs and cancer stem cells. These CD-133+ cells survive radiation much more effectively by activating DNA damage repair mechanisms (*202*). It is postulated that CD133+ cancer stem cells become radio-resistant by promoting the translocation of L1CAM intracellular domains (L1-ICD) from the cytoplasm into the nucleus, which activates checkpoint responses and subsequent DNA damage repair (*202, 203*). Overall, these studies provide evidence that the CD133 positive cancer cells survive radiation more effectively and contribute to tumor growth through preferential activation of the DNA repair mechanisms. We can hypothesize from these studies that it is possible for CD133+ NPCs to transform into CD133+ cancer stem cells, especially since radiation specifically to the murine SVZ and the hippocampus has been linked to the formation of tumor satellites as well as an increased migration of NPCs to the tumor core and to the satellite sites (*204*).

Clinical data also supports the hypothesis that NPCs contributes to local recurrences and/or treatment resistance. Retrospective human studies have suggested worse patient outcomes with glioblastoma located immediately adjacent to lateral ventricles (*174, 202, 205-208*). The explanation for this finding is unclear, but emerging data suggests a potential relationship between radiation dose to the SVZ and patient outcome (*164, 207-209*). In a recent study, Chen *et al.* retrospectively examined adult GBM patients and reported improved progression free survival

(PFS) and overall survival (OS) in the subgroup of patients who underwent gross total resection, when they received an ipsilateral SVZ dose of ≥40 Gy compared to the same subgroup who received an ipsilateral SVZ dose <40 Gy **(Figure 6)** (*164*). Similarly, Lee *et al.* retrospectively studied adult GBM patients and reported improvements in both PFS and OS (*209*) among the patients who received high ipsilateral SVZ dose above 59.4 Gy. These results are important and suggest that higher radiation dose to the SVZ may be beneficial to patient outcomes. Furthermore, these studies suggest that acute toxicity of delivery of a high radiation dose to the SVZ may be acceptable as there was no statistically significant difference in the Karnofsky Performance Status (KPS) for patients receiving low dose to SVZ (<40 Gy) versus high dose (>60 Gy) to the SVZ (*164, 209*).

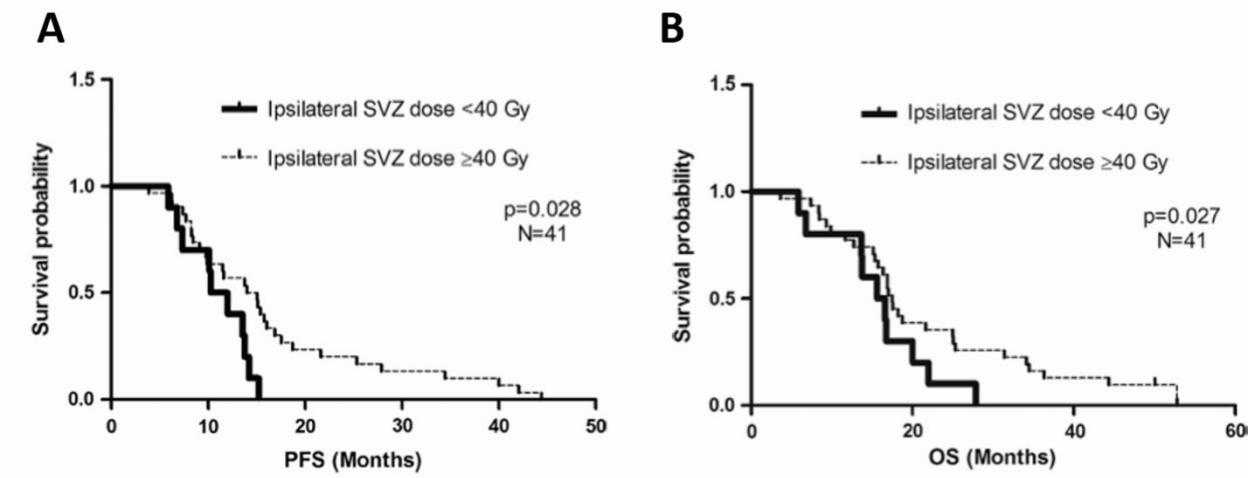

Figure 6. Progression-free survival (PFS) and overall survival (OS) improve in the subgroup of patients that underwent gross total resection and received increased dose to SVZ. (A) PFS by ipsilateral subventricular dose in gross total resection patients (n = 41). PFS in patients whose ipsilateral subventricular zone (SVZ) received less than 40 Gy was significantly different from that in those who received a dose of 40 Gy or greater as measured by median PFS of 10.3 vs 15.1 months (95% CI: 7.4-13.2 months) and log-rank test (PZ.023), as well as adjusted hazard ratio for PFS (2.60) (PZ.028). **(B)** Overall survival (OS) by ipsilateral subventricular dose in gross total resection patients (n = 41). OS in patients whose ipsilateral subventricular zone (SVZ) received less than 40 Gy was significantly different from those who received a dose of 40 Gy or greater as measured by median overall survival of 15.6 vs 17.5 months (95% CI: 11.3-19.9 months) and adjusted hazard ratio for progression-free survival (2.60) (PZ.027). Figure and figure legends are published in Kut& Redmond, (2014, October). New Considerations in Radiation Treatment Planning for Brain Tumors: Neural Progenitor Cell–Containing Niches. *In Seminars in radiation*

oncology (Vol. 24, No. 4, pp. 265-272). **However, the original figure was reprinted with permission from Chen *et al.* (2013). Increased subventricular zone radiation dose correlates with survival in glioblastoma patients after gross total resection. *International Journal of Radiation Oncology* Biology* Physics*, *86*(4), 616-622.**

Nevertheless, although the aforementioned retrospective series are thought provoking and hypothesis generating, they could be confounded. For example, outcomes could be impacted by differences in upfront bevacizumab administration or the salvage therapies used at the time of progression. Similarly, in these retrospective series, the dose received by the SVZ was likely directly impacted by tumor location and geometry since tumors that reside close to the SVZ likely received higher SVZ radiation dose. Furthermore, methylation status of the O6-methylguanine-methyltransferease (MGMT) promoter was not accounted for in these retrospective series, but could impact results (*164, 209*). As a result, prospective evaluation of the relationship between radiation dose to the SVZ and brain cancer patient outcomes will be critical to better understanding the relationship.

To address this question, a prospective single-arm phase II study in patients undergoing radiation therapy plus temozolomide chemotherapy for newly diagnosed GBM at our institution limited the radiation dose to the NPC niches as much as possible without compromising coverage of the tumor. The primary endpoint is local recurrence in the spared NPC niches. This study recently closed to accrual with results forthcoming (*209*). Another study under development at our institution in the same patient population will examine for a potential benefit in tumor outcomes with the delivery of higher doses of radiation therapy to the SVZ. Other interesting possibilities for future investigation might include therapeutic agents that target the SVZ. For example, recent findings have attributed dopamine signaling mechanisms of the D3 subtype receptor to the migratory behavior of NPCs towards the tumor site and suggested that D3 blocking drugs to the SVZ could also prolong patient survival (*210*).

SECTION 5: HOW TO RECONCILE OPPOSING VIEWPOINTS?

This review has explored the potential role of NPCs in the SVZ and hippocampus in both the long term neuro-cognitive sequelae of brain irradiation and in resistance to therapy and tumor recurrence. The reconciliation of these somewhat opposing functions is challenging and is a critical avenue for future laboratory studies and prospective clinical trials. One possibility is that the role of the NPCs varies with both tumor pathology and location in the brain. For example, given the vast heterogeneity of cancers, it is likely that the role of the NPCs varies dramatically between different pathologies as well as within the same tumor type and even the same tumor. In addition, it is possible that NPCs in the SVZ may play a different role than NPCs in the hippocampus, and perhaps they should be given different considerations during radiation treatment planning.

An improved understanding of this complex relationship will be critical to allowing us to apply it effectively in the clinic. Importantly, to date we remain uncertain of the precise radiation tolerance of NPC and cancer stem cells to fractionated radiation therapy. This detail is critical both in designing future studies to spare the NPC and in designing trials to intentionally deliver radiation dose to these areas in certain types of tumors.

Similarly, while we hypothesize that NPCs may transform into cancer stem cells and are associated with tumor recurrence and cancer radio-resistant behaviors, there are directly contradictory animal studies as well. For example, NPCs have been shown to migrate to the site of tumors with greater NPC attraction being associated with decreased tumor size and improved

overall survival (*166, 167, 170, 211*). This paradox once again highlights the need for additional studies, both in the lab and in the clinic, to more fully address this fascinating and seemingly vital question.

In summary, the relationship between NPC in the hippocampus and SVZ remains an interesting academic question and one which likely will have important implications on radiation treatment planning strategies in the future. However, additional laboratory and clinical studies will be critical in allowing us to explore this topic further and ultimately apply it to our patients with maximum effectiveness and safety.

APPENDIX 4: STUDY OF PATIENT POSITIONING UNCERTAINTIES FOR INTRACRANIAL RADIOTHERAPIES

SECTION 1: OVERVIEW

In the course of my MD and PhD, I assisted as a co-author in studying uncertainties of patient positioning for intracranial radiotherapies with Professor Tryggestad and other co-authors at Radiation Oncology. This paper has been published in the International Journal of Radiation Oncology, Biology and Physics with the purpose to determine whether frameless thermoplastic mask-based immobilization is adequate for image-guided cranial radiosurgery (*212*). Since this is not a first-authored paper (unlike others quoted in the appendix), only the abstract of the paper is copied below for the completeness of this dissertation. **Reprinted from International Journal of Radiation Oncology*Biology*Physics, Tryggestad, E., Christian, M., Ford, E., Kut, C., Le, Y., Sanguineti, G., Song, D.Y. & Kleinberg, L., Inter-and intrafraction patient positioning uncertainties for intracranial radiotherapy: a study of four frameless, thermoplastic mask-based immobilization strategies using daily cone-beam CT, Vol. 80, No. 1, pp. 281-290, Copyright (2011), with permission from Elsevier.**

SECTION 2: ABSTRACT

PURPOSE

The purpose of this study is to determine whether frameless thermoplastic mask-based immobilization is adequate for image-guided cranial radiosurgery.

METHODS AND MATERIALS

Cone-beam CT localization data from patients with intracranial tumors were studied using daily pre- and posttreatment scans. The systems studied were (1) Type-S IMRT (head only) mask (Civco) with head cushion; (2) Uni-Frame mask (Civco) with head cushion, coupled with a BlueBag body immobilizer (Medical Intelligence); (3) Type-S head and shoulder mask with head and shoulder cushion (Civco); (4) same as previous, coupled with a mouthpiece. The comparative metrics were translational shift magnitude and average rotation angle; systematic inter-, random inter-, and random intrafraction positioning error was computed. For strategies 1–4, respectively, the analysis for interfraction variability included data from 20, 9, 81, and 11 patients, whereas that for intrafraction variability included a subset of 7, 9, 16, and 8 patients. The results were compared for statistical significance using an analysis of variance test.

RESULTS

Results: Immobilization system 4 provided the best overall accuracy and stability. The mean interfraction translational shifts (± SD) were 2.3 (± 1.4), 2.2 (± 1.1), 2.7 (± 1.5), and 2.1 (± 1.0) mm whereas intrafraction motion was 1.1 (± 1.2), 1.1 (± 1.1), 0.7 (± 0.9), and 0.7 (± 0.8) mm for devices 1–4, respectively. No significant correlation between intrafraction motion and treatment time was evident, although intra-fraction motion was not purely random. Conclusions: We find that all frameless thermoplastic mask systems studied are viable solutions for image-guided intracranial radiosurgery. With daily pretreatment corrections, symmetric PTV margins of 1 mm would likely be adequate if ideal radiation planning and targeting systems were available.

APPENDIX 5: INJURY FROM HEATING SYSTEMATICALLY DELIVERED DEXTRAN-SUPRAPARAMAGNETIC IRON OXIDE NANOPARTICLE IN MICE

In the course of my MD and PhD, I studied the injury sustained from heating systematically delivered dextran-superparamagnetic iron oxide nanoparticles in mice in the Radiation Oncology Department. This viewpoint paper has been published in Nanomedicine (*213*) and is copied below for completeness of this dissertation. Due to copyright permissions, the full paper is not cited in this dissertation.

APPENDIX 6: PERFORMANCE OF MPF IN DETECTING MYOCARDIAL INFARCTION IN PORCINE HEARTS

SECTION 1: INTRODUCTION

There are 1.5 million cases of myocardial infarctions (MI) per year in the United States. Myocardial infarction (commonly known as a heart attack) occurs when the cardiac muscles are damaged due to insufficient blood flow.

Following a myocardial infarction, the damaged areas in the heart undergo a remodeling process with gradual changes in the structure and fiber orientation of the cardiomyocytes (i.e. cardiac muscle cells) over time. In addition, collagen deposition increases significantly in the heart for cases of chronic myocardial infarctions (i.e., hearts which have sustained a myocardial infarction event over 100 days ago). These structural and fiber orientation changes play a central role in the functional adaptation of the heart (*214*). However, the understanding of the remodeling process is limited by the lack of a three-dimensional visualization of the cardiomyocyte architecture. While permanent histological sections are the current gold standard to visualize subcellular pathological changes in the heart, these sections are two-dimensional in nature and require the physical sectioning of cardiac tissues. As a result, the cardiac tissue will not remain intact after sectioning, and as a result, histological sections are not ideal for the visualization of the cardiomyocyte fiber orientations, nor for the detection of the three-dimensional perimysial collagen network in the heart.

This study aims to determine if multi-photon fluorescence (including two-photon fluorescence and second harmonic generation) and optical coherence tomography techniques can be used to identify changes in the myocardial structures for normal, acute infarct (defined here as 8 days post infarction), and chronic infarct (defined here as more than 100 days post infarction) in five post-mortem, formalin-preserved swine hearts.

SECTION 2: MATERIALS AND METHODS

Formalin-preserved, post-mortem hearts were obtained from 5 swines (which include 1 normal, 1 with acute myocardial infarction, and 3 with chronic myocardial infarction). Each of the swine hearts and subsequently sectioned into thick cross-sections (along the short axis of the heart) and imaged with a homebuilt 3 frames per second (fps) multi-photon microscope with ~0.53 x 2.4μm lateral x axial resolution and at 780nm excitation wavelength. NADH, FAD and SHG images were obtained for the purposes of this study. Approximately 35 mW from the multi-photon fluorescence imaging system was deposited onto the porcine cardiac tissue sample.

In addition to multi-photon fluorescence the cardiac sections were also imaged with a homebuilt swept-source OCT system with a Fourier Domain Mode Locking (FDML) swept source fiber at a central wavelength of 1310nm and a bandwidth of approximately 110 nm. The SS-OCT system is able to capture images at ~16.0 x 9.0 μm lateral and axial resolution (in tissues), respectively. On average, the output power delivered to the tissue sample was about 15 mW. After image acquisition, Images were post-processed for 3D visualization and fiber angle calculations.

Notably, myocardial structures were imaged using multi-photon fluorescence and optical coherence tomography without the need of extraneous contrast agents. In other words, both MPF

and OCT imaging techniques are label-free; in addition, they provide real-time and non-invasive imaging of the cardiac tissues without disrupting its intact, three-dimensional fiber and collagen structures. For the purposes of this study, all images were acquired in real-time and post-processed later for contrast enhancements and volumetric reconstruction.

SECTION 3: RESULTS IN THE NORMAL HEART

In normal porcine heart, we are able to image the cardiomyocytes (i.e. cardiac muscle cells) and the perimysial collagen (i.e. collagen in the perimysial sheath which groups muscle fibers into bundles or fascicles) at high resolution. **Figure 1** shows the NADH and SHG results of the normal swine heart. While NADH and FAD provides the overall structural architecture of the cardiomyocytes, SHG signals helped us to clearly identify the presence of myosin filaments and perimysial collagen structures in the swine hearts. Recall that SHG is an imaging technique which identifies the presence of non-centrosymmetric fibers in biological tissues; in muscle, a bright SHG signal generally corresponds to the presence of myosin filaments (or more specifically, to the helix pitch of the myosin rods in the myosin/actin assembly) (*215*). In addition, SHG is also very sensitive to the presence of collagen I, which manifests itself in the perimysium of a normal swine heart.

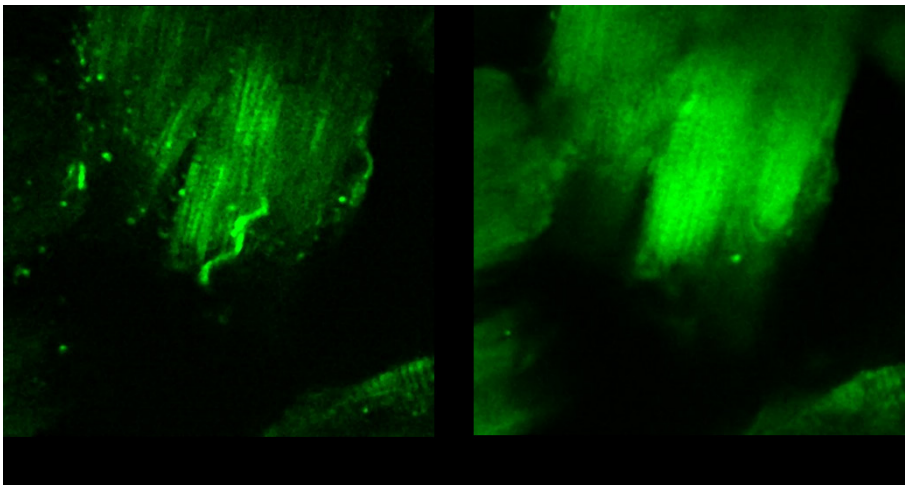

Figure 1. Multi-photon fluorescence images of normal swine heart. NADH and SHG images of normal cardiomyocytes in a control swine heart. Tissue architecture is shown in the NADH image, while the SHG image enables us to visualize the presence of myosin filaments in the cardiomyocytes, and also the presence of perimysial collagen which are used to form muscle bundles. Scale is at 87.5 µm x 87.5 µm per image. **Figure and figure legends are published by Kut *et al.* (2016), "MPF and OCT Findings of Myocardial Infarction in the Porcine heart", (to be submitted).**

In addition to two-dimensional images, we have also established that MPF is capable of imaging three-dimensional structures of the cardiomyocytes as well as the presence of the perimysial collagen network. As shown in **Figure 2**, we are able to detect perimysial collagen at approximately 4 cardiomyocytes apart (or approximately 60µm apart).

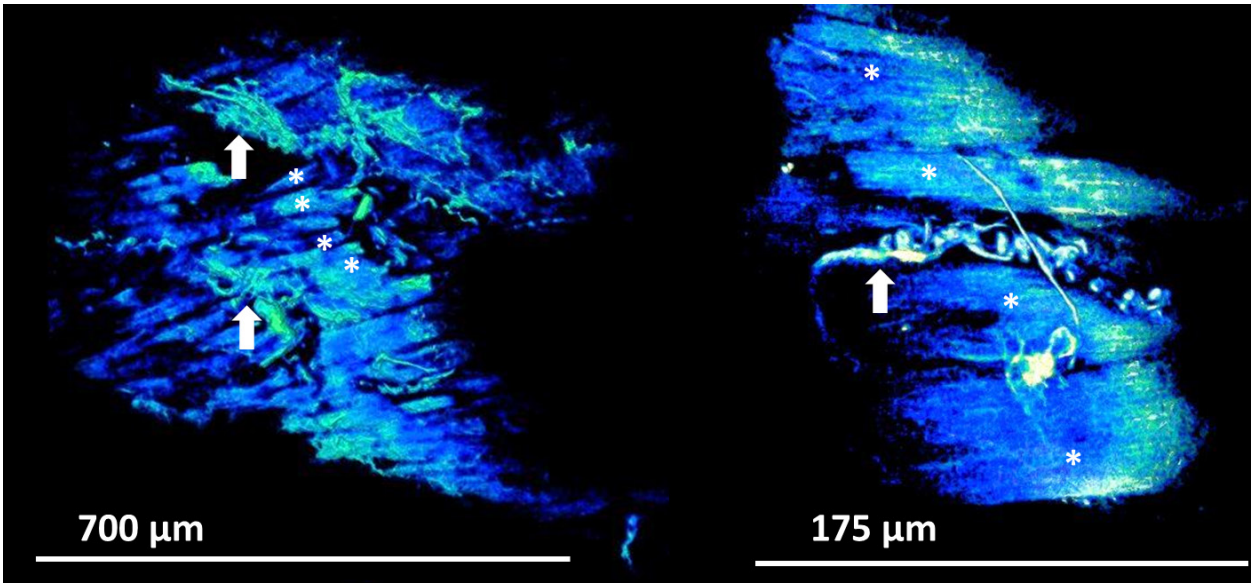

Figure 2. Volumetric visualization of normal porcine heart with heart muscle cells (*) and perimysial collagen (arrows). Figure and figure legends are published by Kut *et al.* (2016), "MPF and OCT Findings of Myocardial Infarction in the Porcine heart", (to be submitted).

In the normal heart, it is well known that cardiac muscles undergo a 120^{o} to 180^{o} change in fiber angles as we move from the epicardium (i.e. outermost layer) to the endocardium (i.e., innermost layer) of the heart (*214*). This is equivalent to approximately 5^{o} -30^{o} degree change in the fiber angle as we travel for one millimeter (mm) into the porcine heart. **Figure 3** shows the NADH results of the normal swine heart, which is consistent with the MRI findings as determined by Hsu *et al. (214)*.

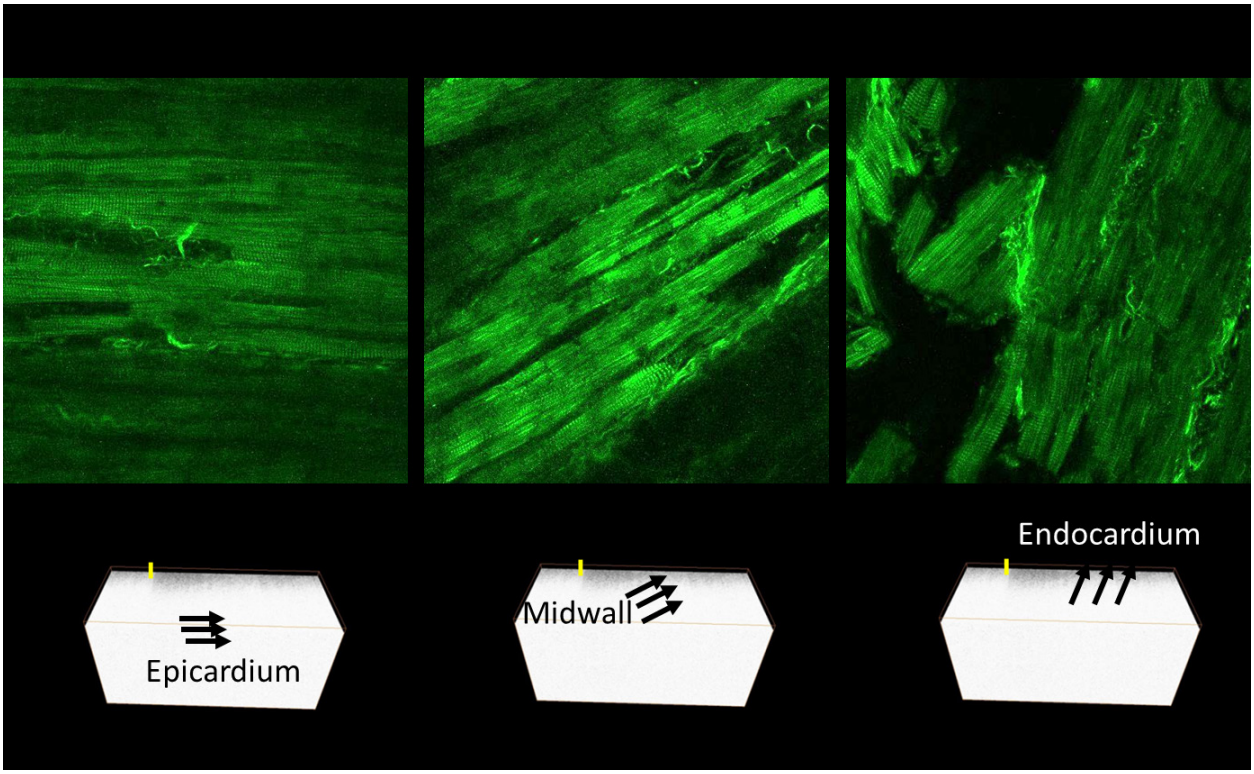

Figure 3. Fiber orientation changes from the epicardium to the endocardium of the heart. Epicardium is the outmost layer of the heart, midwall is the middle layer of the heart, and endocardium is the innermost layer of the heart. Here, we took 3 representative images at the different layers of the heart. Notably, previous literature indicates that there should be a 5-30^{o} change for each mm traveled into the heart (i.e. towards the endocardium). Here, the heart section is approximately 10 mm in thickness. As a result, there should be around a 3mm thickness of each layer, or a change of 15-90^{o} per layer. Overall, our NADH results are consistent with previous literature which roughly indicated a 45^{o} change for each layer in terms of fiber orientation.

Volumetric visualization of normal porcine heart with heart muscle cells (*) and perimysial collagen (arrows). **Figure and figure legends are published by Kut *et al.* (2016), "MPF and OCT Findings of Myocardial Infarction in the Porcine heart", (to be submitted).**

SECTION 4: RESULTS IN THE ACUTE INFARCT HEART

In the porcine hearts with sub-acute myocardial infarcts (i.e., at 8 days post-infarction), necrosis and disintegration of cardiac fibers were observed in both multi-photon fluorescence and optical coherence tomography images **(Figure 4**). Three-dimensional fiber orientations were visually assessed and calculated. For acute infarct, the fiber orientations at the epicardium, midwall and endocardium were largely preserved **(~10-11°/mm)**, despite significant necrosis and disintegration of cardiac fibers.

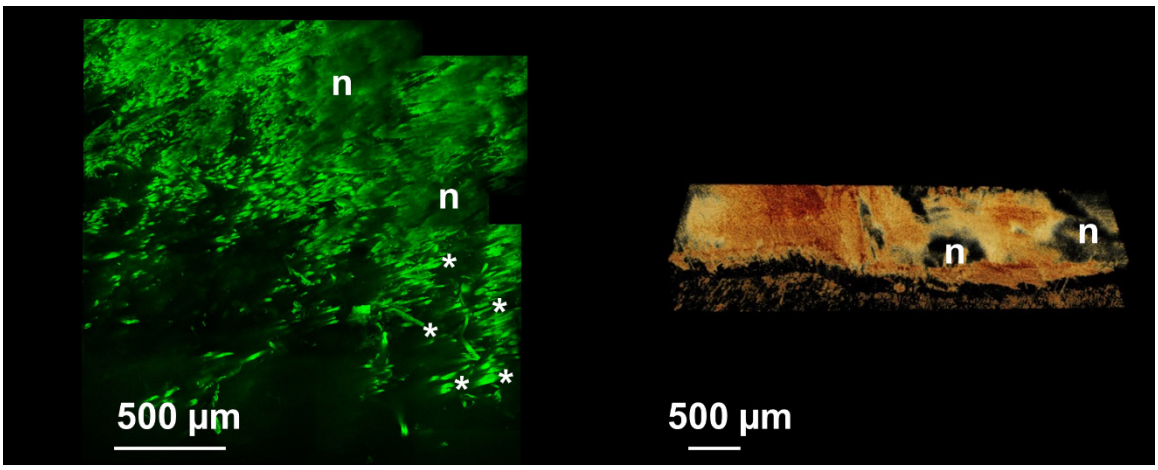

Figure 4. Cardiac changes in the acute infarct heart (i.e. at 8 days post infarction). (A) NADH and **(B)** OCT images shown significant necrosis (marked by n) and disintegration of cardiac fibers the acute infarct heart of a swine. In contrast to the necrotic regions, we have marked normal cardiomyocytes with an asterisk (*) sign. **Figure and figure legends are published by Kut *et al.* (2016), "MPF and OCT Findings of Myocardial Infarction in the Porcine heart", (to be submitted).**

SECTION 5: RESULTS IN THE CHRONIC INFARCT HEART

In chronic infarcts (>100 days post-infarction), significant cardiac remodeling was observed with.

Figure 5 demonstrates the three-dimensional multi-photon images of a normal swine heart versus

a chronic infarct heart. As you can observe in the image, there is significant collagen deposition and a complete disruption of cardiac fibers in the chronic infarct heart. As you can appreciate in this image, multi-photon provides ideal volumetric visualization of the infarct cardiac tissues, which cannot be otherwise observed on a two-dimensional histological slide.

SECTION 6: FIBER ORIENTATIONS

As described in the previous sections, a normal heart undergoes a 5 to 30^{o} change in the fiber orientation for each millimeter as we travel from the epicardium towards the endocardium of the heart (*214*). As demonstrated in **Figure 5**, we find in that the normal swine heart has approximately 11^{o}/mm change in fiber orientation. In the acute infarct heart, we find that the fiber orientation is largely preserved at approximately 10-11^{o}/mm change. In chronic infarct heart, however, the fiber organization is completely disrupted, making it impossible to assess the cardiac fiber orientations.

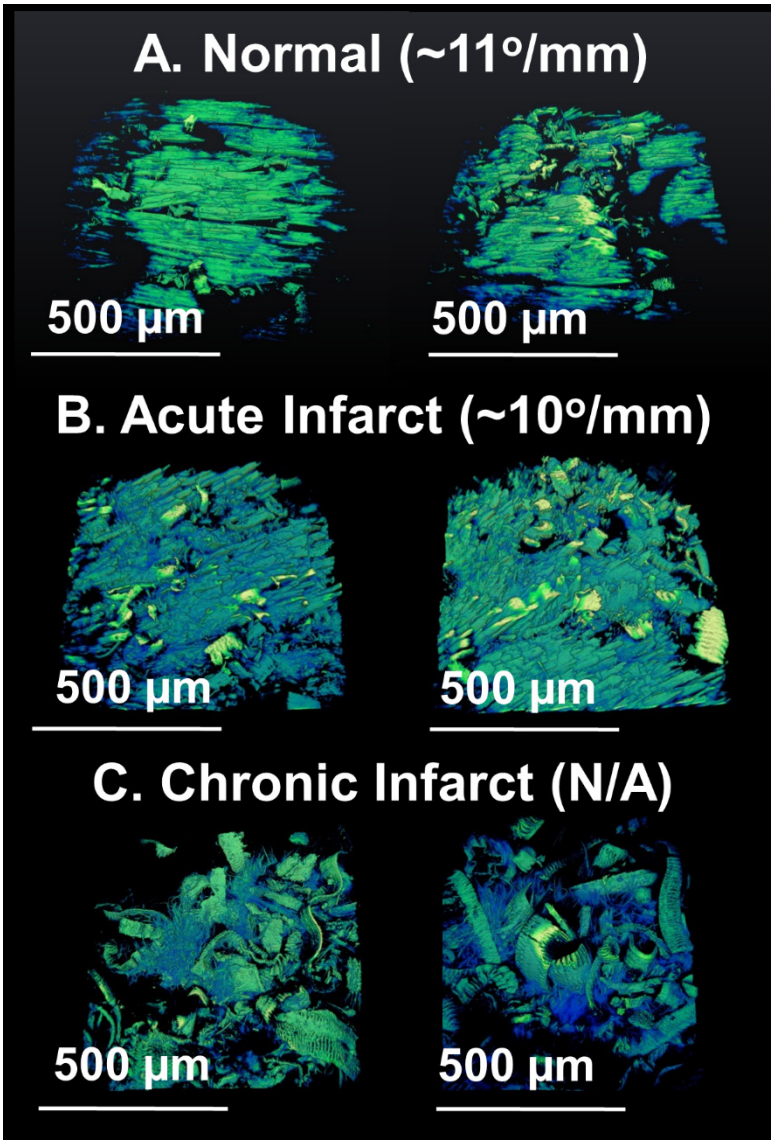

Figure 5. Fiber orientations in normal, acute infarct and chronic infarct swine hearts. Multi-photon fluorescence shows the myocardial changes in acute and chronic myocardial infarctions. In acute myocardial infarction, necrosis and disintegration of fibers occurs. However, the remaining, healthy cardiomyocytes remain a normal fiber orientation change between the endocardial and epicardial layers. In chronic myocardial infarct, however, the cardiac fibers are completely disrupted by a significant deposition of collagen. As a result, it is impossible to evaluate the fiber orientation changes in the chronic infarct swine hearts. **Figure and figure legends are published by Kut *et al.* (2016), "MPF and OCT Findings of Myocardial Infarction in the Porcine heart", (to be submitted).**

SECTION 7: MPF VERSUS HISTOLOGY

As demonstrated in the previous sections, multi-photon imaging demonstrated superior 2D visualization of myosin and collagen structures when compared with standard histological imaging e.g. H&E. Our results demonstrated excellent 2D and 3D visualization of cardiac muscle orientation and structures without histological slicing of the heart and without the need of contrast agents. **Figures 6 to 8** provides a direct comparison of the H&E versus MPF images in the detection of cardiac structures. Overall, MPF is able to provide label-free, non-invasive and three-dimensional imaging of the infarct heart tissue. Future investigation of bio-photonic imaging evaluation post-MI remodeling and myocardial disease affect collagen structure including additional targeted histological stains is warranted.

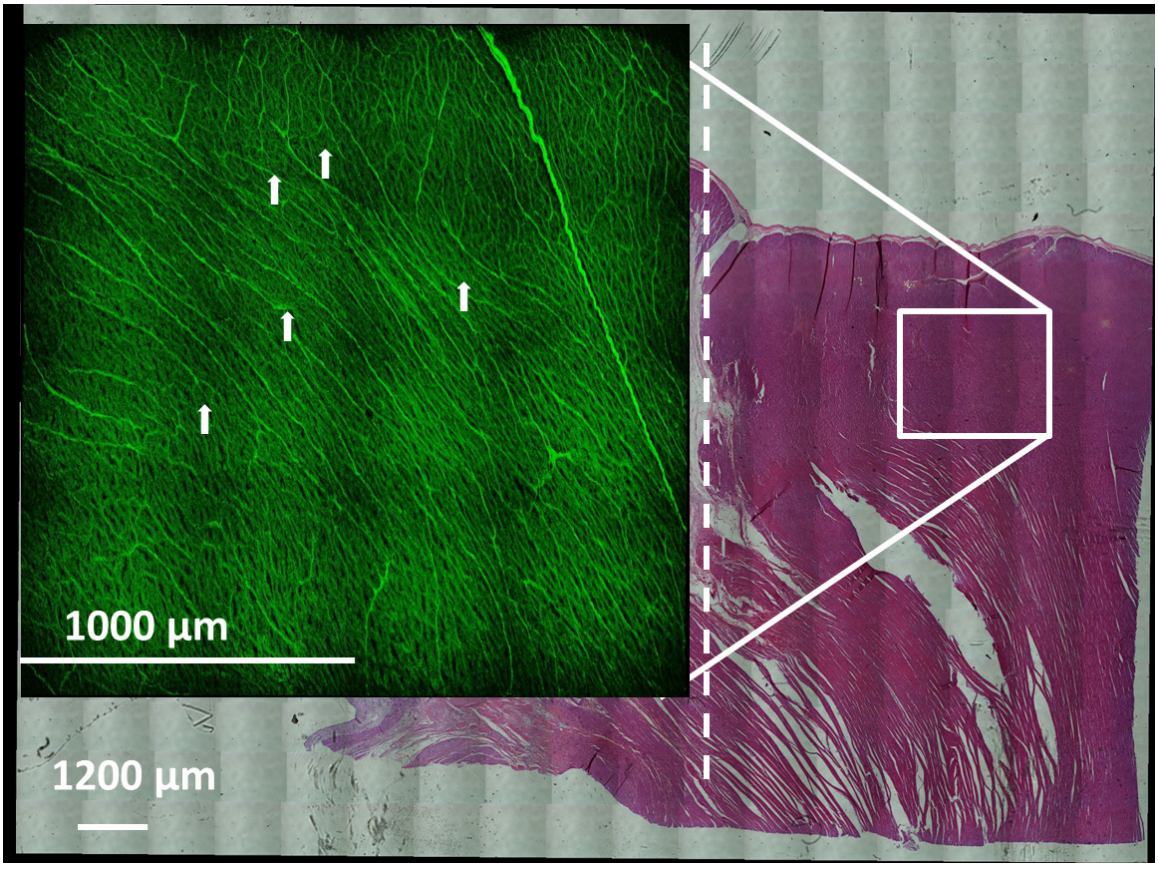

Figure 6. Histology versus multi-photon imaging of normal cardiomyocytes. Here, we show the H&E image of a swine heart tissue with regions of chronic infarction as well as region of

normal, healthy cardiomyocytes. In this image, we only highlight the white boxed region (which showed areas of healthy cardiomyocytes). As shown in the NADH image, MPF is able to clearly identify the presence of perimysial collagen (marked by arrows) which is responsible for organizing cardiomyocytes into different muscle bundles (at approximately 4 cardiomyocytes per perimysial bundle). **Figure and figure legends are published by Kut *et al.* (2016), "MPF and OCT Findings of Myocardial Infarction in the Porcine heart", (to be submitted).**

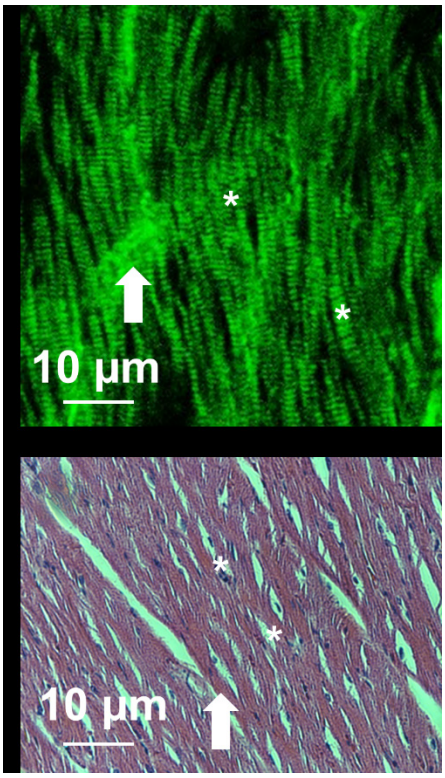

Figure 7. Zoomed in H&E and MPF images of normal cardiomyocytes. Here, we can appreciate the superior resolution of MPF in identifying the presence of myosin filaments (marked by small arrows) and the presence of perimysial collagen (marked by big arrow) surrounding the cardiac muscle cells. **Figure and figure legends are published by Kut *et al.* (2016), "MPF and OCT Findings of Myocardial Infarction in the Porcine heart", (to be submitted).**

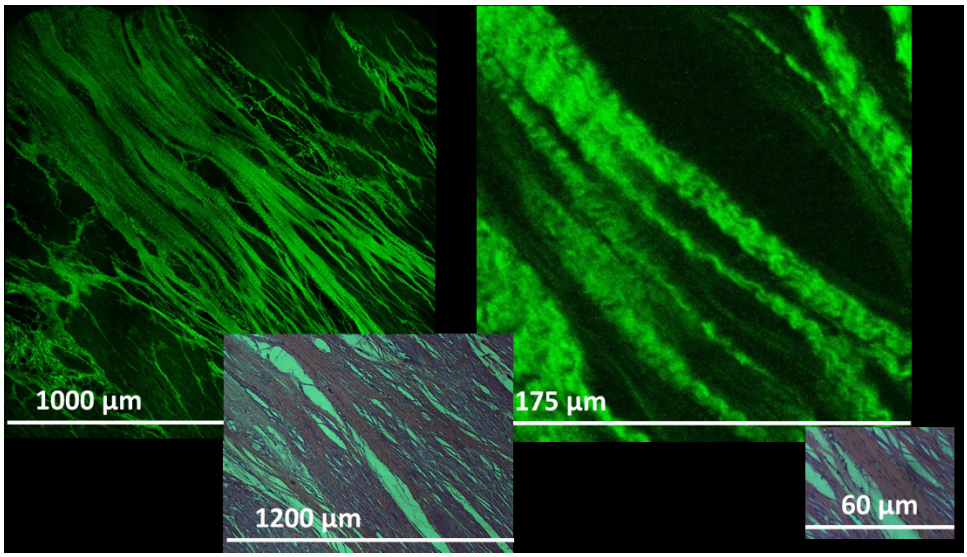

Figure 8. H&E and MPF images of chronic myocardial infarcts. Here, we can appreciate the superior resolution of MPF in identifying the presence of collagen I fibers deposited throughout the chronic myocardial infarction site, when compared with H&E imaging. Notably, no healthy cardiomyocytes can be observed from this figure from both MPF and H&E images. **Figure and figure legends are published by Kut *et al.* (2016), "MPF and OCT Findings of Myocardial Infarction in the Porcine heart", (to be submitted).**

APPENDIX 7: BIBLIOGRAPHY

1. G. E. Keles, K. R. Lamborn, M. S. Berger, Low-grade hemispheric gliomas in adults: a critical review of extent of resection as a factor influencing outcome. *J Neurosurg* **95**, 735-745 (2001).
2. K. L. Chaichana, I. Jusue-Torres, R. Navarro-Ramirez, S. M. Raza, M. Pascual-Gallego, A. Ibrahim, M. Hernandez-Hermann, L. Gomez, X. Ye, J. D. Weingart, A. Olivi, J. Blakeley, G. L. Gallia, M. Lim, H. Brem, A. Quinones-Hinojosa, Establishing percent resection and residual volume thresholds affecting survival and recurrence for patients with newly diagnosed intracranial glioblastoma. *Neuro-oncology*, (2013).
3. N. Sanai, M. Y. Polley, M. W. McDermott, A. T. Parsa, M. S. Berger, An extent of resection threshold for newly diagnosed glioblastomas. *J Neurosurg* **115**, 3-8 (2011).
4. W. Stummer, U. Pichlmeier, T. Meinel, O. D. Wiestler, F. Zanella, H. J. Reulen, Fluorescence-guided surgery with 5-aminolevulinic acid for resection of malignant glioma: a randomised controlled multicentre phase III trial. *The lancet oncology* **7**, 392-401 (2006).
5. K. L. Chaichana, C. Pendleton, L. Chambless, J. Camara-Quintana, J. K. Nathan, L. Hassam-Malani, G. Li, G. R. Harsh, R. C. Thompson, M. Lim, Multi-institutional validation of a preoperative scoring system which predicts survival for patients with glioblastoma. *Journal of Clinical Neuroscience* **20**, 1422-1426 (2013).
6. K. L. Chaichana, E. E. Cabrera-Aldana, I. Jusue-Torres, O. Wijesekera, A. Olivi, M. Rahman, A. Quinones-Hinojosa, When Gross Total Resection of a Glioblastoma Is Possible, How Much Resection Should Be Achieved? *World neurosurgery*, (2014).
7. E. Laws, M. E. Shaffrey, A. Morris, F. A. Anderson Jr, *Surgical management of intracranial gliomas—does radical resection improve outcome?* , (Springer, 2003).
8. M. J. McGirt, K. L. Chaichana, M. Gathinji, F. J. Attenello, K. Than, A. Olivi, J. D. Weingart, H. Brem, A. R. Quinones-Hinojosa, Independent association of extent of resection with survival in patients with malignant brain astrocytoma. *J Neurosurg* **110**, 156-162 (2009).
9. J. P. Almeida, K. L. Chaichana, J. Rincon-Torroella, A. Quinones-Hinojosa, The Value of Extent of Resection of Glioblastomas: Clinical Evidence and Current Approach. *Current neurology and neuroscience reports* **15**, 1-13 (2015).
10. K. L. Chaichana, K. K. Chaichana, A. Olivi, J. D. Weingart, R. Bennett, H. Brem, A. Quinones-Hinojosa, Surgical outcomes for older patients with glioblastoma multiforme: preoperative factors associated with decreased survival. Clinical article. *J Neurosurg* **114**, 587-594 (2011).
11. K. L. Chaichana, P. Zadnik, J. D. Weingart, A. Olivi, G. L. Gallia, J. Blakeley, M. Lim, H. Brem, A. Quinones-Hinojosa, Multiple resections for patients with glioblastoma: prolonging survival. *J Neurosurg*, (2012).
12. K. L. Chaichana, A. Quinones-Hinojosa, Neuro-oncology: Paediatric brain tumours—when to operate? *Nature Reviews Neurology* **9**, 362-364 (2013).

13. K. L. Chaichana, A. Quinones-Hinojosa, The need to continually redefine the goals of surgery for glioblastoma. *Neuro-oncology* **16**, 611-612 (2014).

14. A. B. Karim, B. Maat, R. Hatlevoll, J. Menten, E. H. Rutten, D. G. Thomas, F. Mascarenhas, J. C. Horiot, L. M. Parvinen, M. van Reijn, A randomized trial on dose-response in radiation therapy of low-grade cerebral glioma: European Organization for Research and Treatment of Cancer (EORTC) Study 22844. *International Journal of Radiation Oncology* Biology* Physics* **36**, 549-556 (1996).

15. A. Sanford, L. Kun, R. Sposto, E. Holmes, J. Wisoff, L. Heier, P. McGuire-Cullen, Low-grade gliomas of childhood: Impact of surgical resection. A report from the Children's Oncology Group. *J Neurosurg* **96**, 427-428 (2002).

16. J. S. Smith, E. F. Chang, K. R. Lamborn, S. M. Chang, M. D. Prados, S. Cha, T. Tihan, S. Vandenberg, M. W. McDermott, M. S. Berger, Role of extent of resection in the long-term outcome of low-grade hemispheric gliomas. *J Clin Oncol* **26**, 1338-1345 (2008).

17. M. J. McGirt, K. L. Chaichana, F. J. Attenello, J. D. Weingart, K. Than, P. C. Burger, A. Olivi, H. Brem, A. Quinones-Hinojosa, Extent of surgical resection is independently associated with survival in patients with hemispheric infiltrating low-grade gliomas. *Neurosurgery* **63**, 700-707; author reply 707-708 (2008).

18. J. M. Markert, THe role of early resection vs biopsy in the management of low-grade gliomas. *JAMA* **308**, 1918-1919 (2012).

19. A. S. Jakola, K. S. Myrmel, R. Kloster, S. H. Torp, S. Lindal, G. Unsgård, O. Solheim, Comparison of a strategy favoring early surgical resection vs a strategy favoring watchful waiting in low-grade gliomas. *JAMA* **308**, 1881-1888 (2012).

20. M. S. Berger, A. V. Deliganis, J. Dobbins, G. E. Keles, The effect of extent of resection on recurrence in patients with low grade cerebral hemisphere gliomas. *Cancer* **74**, 1784-1791 (1994).

21. N. Upadhyay, A. Waldman, Conventional MRI evaluation of gliomas. *The British journal of radiology*, (2014).

22. C. J. Spivak, F. Pirouzmand, Comparison of the reliability of brain lesion localization when using traditional and stereotactic image-guided techniques: a prospective study. *J Neurosurg* **103**, 424-427 (2005).

23. Z. Z. Zhang, L. B. Shields, D. Sun, Y. P. Zhang, M. A. Hunt, C. B. Shields, The Art of Intraoperative Glioma Identification. *Frontiers in Oncology* **5**, 175 (2015).

24. T. Selbekk, A. S. Jakola, O. Solheim, T. F. Johansen, F. Lindseth, I. Reinertsen, G. Unsgard, Ultrasound imaging in neurosurgery: approaches to minimize surgically induced image artefacts for improved resection control. *Acta neurochirurgica* **155**, 973-980 (2013).

25. O. M. Rygh, T. Selbekk, S. H. Torp, S. Lydersen, T. A. N. Hernes, G. Unsgaard, Comparison of navigated 3D ultrasound findings with histopathology in subsequent phases of glioblastoma resection. *Acta neurochirurgica* **150**, 1033-1042 (2008).

26. I. Jusué-Torres, R. Navarro-Ramírez, M. P. Gallego, K. L. Chaichana, A. Quiñones-Hinojosa, Indocyanine green for vessel identification and preservation before dural opening for parasagittal lesions. *Neurosurgery* **73**, ons145 (2013).

27. A. Quinones-Hinojosa, Aminolevulinic Acid Hydrochloride in Identifying Brain Tumor Stem Cells in Patients Undergoing Surgery for Anaplastic Astrocytoma or Glioblastoma. *In: ClinicalTrials.gov [Internet]. Bethesda (MD): National Library of Medicine (US)* **Available from: http://www.cancer.gov/about-cancer/treatment/clinical-trials/search/view?cdrid=721825&version=HealthProfessional of the record NLM Identifier: NCT01502605.**, (2012-Present).

28. W. Stummer, J.-C. Tonn, C. Goetz, W. Ullrich, H. Stepp, A. Bink, T. Pietsch, U. Pichlmeier, 5-ALA-Derived Tumor Fluorescence: The Diagnostic Accuracy of Visible Fluorescence Qualities as Corroborated by Spectrometry and Histology and Post-Operative Imaging. *Neurosurgery*, (2013).

29. M. Jermyn, K. Mok, J. Mercier, J. Desroches, J. Pichette, K. Saint-Arnaud, L. Bernstein, M.-C. Guiot, K. Petrecca, F. Leblond, Intraoperative brain cancer detection with Raman spectroscopy in humans. *Science translational medicine* **7**, 274ra219-274ra219 (2015).

30. M. Ji, D. A. Orringer, C. W. Freudiger, S. Ramkissoon, X. Liu, D. Lau, A. J. Golby, I. Norton, M. Hayashi, N. Y. Agar, Rapid, Label-Free Detection of Brain Tumors with Stimulated Raman Scattering Microscopy. *Science translational medicine* **5**, 201ra119-201ra119 (2013).

31. C. Pitris, C. Jesser, S. A. Boppart, D. Stamper, M. E. Brezinski, J. G. Fujimoto, Feasibility of optical coherence tomography for high-resolution imaging of human gastrointestinal tract malignancies. *J Gastroenterol* **35**, 87-92 (2000).

32. C. L. Shields, M. A. Materin, J. A. Shields, Review of optical coherence tomography for intraocular tumors. *Curr Opin Ophthalmol* **16**, 141-154 (2005).

33. A. M. Zysk, S. A. Boppart, Computational methods for analysis of human breast tumor tissue in optical coherence tomography images. *J Biomed Opt* **11**, 054015 (2006).

34. M. J. Cobb, J. H. Hwang, M. P. Upton, Y. Chen, B. K. Oelschlager, D. E. Wood, M. B. Kimmey, X. D. Li, Imaging of subsquamous Barrett's epithelium with ultrahigh-resolution optical coherence tomography: a histologic correlation study. *Gastrointest Endosc* **71**, 223-230 (2010).

35. L. Huo, J. Xi, Y. Wu, X. D. Li, Forward-viewing resonant fiber-optic scanning endoscope of appropriate scanning speed for 3D OCT imaging. *Opt Express* **18**, 14375-14384 (2010).

36. J. Xi, L. Huo, J. Li, X. D. Li, Generic real-time uniform K-space sampling method for high-speed swept-source optical coherence tomography. *Opt Express* **18**, 9511-9517 (2010).

37. K. Murari, J. Mavadia, J. Xi, X. D. Li, Self-starting, self-regulating Fourier domain mode locked fiber laser for OCT imaging. *Biomedical optics express* **2**, 2005-2011 (2011).

38. J. Mavadia, J. Xi, Y. Chen, X. D. Li, An all-fiber-optic endoscopy platform for simultaneous OCT and fluorescence imaging. *Biomedical optics express* **3**, 2851-2859 (2012).

39. J. Xi, Y. Chen, X. D. Li, Characterizing optical properties of nano contrast agents by using cross-referencing OCT imaging. *Biomedical optics express* **4**, 842-851 (2013).

40. W. Liang, J. Mavadia, X. Li, 9 Optical Coherence Tomography. *Diagnostic Endoscopy*, 135 (2013).

41. J. G. Fujimoto, Optical coherence tomography for ultrahigh resolution in vivo imaging. *Nat Biotechnol* **21**, 1361-1367 (2003).

42. J. S. Schuman, M. R. Hee, C. A. Puliafito, C. Wong, T. Pedut-Kloizman, C. P. Lin, E. Hertzmark, J. A. Izatt, E. A. Swanson, J. G. Fujimoto, Quantification of nerve fiber layer thickness in normal and glaucomatous eyes using optical coherence tomography: a pilot study. *Archives of ophthalmology* **113**, 586-596 (1995).

43. M. R. Hee, C. A. Puliafito, C. Wong, J. S. Duker, E. Reichel, B. Rutledge, J. S. Schuman, E. A. Swanson, J. G. Fujimoto, Quantitative assessment of macular edema with optical coherence tomography. *Archives of ophthalmology* **113**, 1019-1029 (1995).

44. M. R. Hee, C. A. Puliafito, C. Wong, E. Reichel, J. S. Duker, J. S. Schuman, E. A. Swanson, J. G. Fujimoto, Optical coherence tomography of central serous chorioretinopathy. *American journal of ophthalmology* **120**, 65-74 (1995).

45. M. R. Hee, C. R. Baumal, C. A. Puliafito, J. S. Duker, E. Reichel, J. R. Wilkins, J. G. Coker, J. S. Schuman, E. A. Swanson, J. G. Fujimoto, Optical coherence tomography of age-related macular degeneration and choroidal neovascularization. *Ophthalmology* **103**, 1260-1270 (1996).

46. J. Zahlava, I. Karel, J. Lestak, OPTICAL COHERENCE TOMOGRAPHY OF AGE-RELATED MACULAR DEGENERATION. *Focus on Macular Degeneration Research*, 179 (2004).

47. G. J. Tearney, H. Yabushita, S. L. Houser, H. T. Aretz, I.-K. Jang, K. H. Schlendorf, C. R. Kauffman, M. Shishkov, E. F. Halpern, B. E. Bouma, Quantification of macrophage content in atherosclerotic plaques by optical coherence tomography. *Circulation* **107**, 113-119 (2003).

48. I.-K. Jang, G. J. Tearney, B. MacNeill, M. Takano, F. Moselewski, N. Iftima, M. Shishkov, S. Houser, H. T. Aretz, E. F. Halpern, In vivo characterization of coronary atherosclerotic plaque by use of optical coherence tomography. *Circulation* **111**, 1551-1555 (2005).

49. X. Li, S. Boppart, J. Van Dam, H. Mashimo, M. Mutinga, W. Drexler, M. Klein, C. Pitris, M. Krinsky, M. Brezinski, Optical coherence tomography: advanced technology for the endoscopic imaging of Barrett's esophagus. *Endoscopy* **32**, 921-930 (2000).

50. M. J. Cobb, J. H. Hwang, M. P. Upton, Y. Chen, B. K. Oelschlager, D. E. Wood, M. B. Kimmey, X. Li, Imaging of subsquamous Barrett's epithelium with ultrahigh-resolution optical coherence tomography: a histologic correlation study. *Gastrointestinal endoscopy* **71**, 223-230 (2010).

51. G. Tearney, M. Brezinski, J. Southern, B. Bouma, S. Boppart, J. Fujimoto, Optical biopsy in human urologic tissue using optical coherence tomography. *The Journal of urology* **157**, 1915-1919 (1997).

52. C. Jesser, S. Boppart, C. Pitris, D. Stamper, G. P. Nielsen, M. Brezinski, J. Fujimoto, High resolution imaging of transitional cell carcinoma with optical coherence tomography: feasibility for the evaluation of bladder pathology. *The British journal of radiology* **72**, 1170-1176 (1999).

53. A. V. D'Amico, M. Weinstein, X. Li, J. P. Richie, J. Fujimoto, Optical coherence tomography as a method for identifying benign and malignant microscopic structures in the prostate gland. *Urology* **55**, 783-787 (2000).

54. C. Pitris, M. E. Brezinski, B. E. Bouma, G. J. Tearney, J. F. Southern, J. G. Fujimoto, High resolution imaging of the upper respiratory tract with optical coherence tomography: a feasibility study. *American journal of respiratory and critical care medicine* **157**, 1640-1644 (1998).

55. C. Pitris, A. Goodman, S. A. Boppart, J. J. Libus, J. G. Fujimoto, M. E. Brezinski, High-resolution imaging of gynecologic neoplasms using optical coherence tomography. *Obstetrics & Gynecology* **93**, 135-139 (1999).

56. S. Boppart, A. Goodman, J. Libus, C. Pitris, C. Jesser, M. Brezinski, J. Fujimoto, High resolution imaging of endometriosis and ovarian carcinoma with optical coherence tomography: feasibility for laparoscopic-based imaging. *BJOG: An International Journal of Obstetrics & Gynaecology* **106**, 1071-1077 (1999).

57. S. A. Boppart, W. Luo, D. L. Marks, K. W. Singletary, Optical coherence tomography: feasibility for basic research and image-guided surgery of breast cancer. *Breast cancer research and treatment* **84**, 85-97 (2004).

58. S. A. Boppart, M. E. Brezinski, C. Pitris, J. G. Fujimoto, Optical coherence tomography for neurosurgical imaging of human intracortical melanoma. *Neurosurgery* **43**, 834-841 (1998).

59. H. J. Bohringer, E. Lankenau, V. Rohde, G. Huttmann, A. Giese, Optical coherence tomography for experimental neuroendoscopy. *Minim Invasive Neurosurg* **49**, 269-275 (2006).

60. H. J. Bohringer, E. Lankenau, F. Stellmacher, E. Reusche, G. Huttmann, A. Giese, Imaging of human brain tumor tissue by near-infrared laser coherence tomography. *Acta Neurochir (Wien)* **151**, 507-517; discussion 517 (2009).

61. S. Kantelhardt, M. Finke, A. Schweikard, A. Giese, Evaluation of a Completely Robotized Neurosurgical Operating Microscope. *Neurosurgery* **72**, A19-A26 (2013).

62. M. Finke, S. Kantelhardt, A. Schlaefer, R. Bruder, E. Lankenau, A. Giese, A. Schweikard, Automatic scanning of large tissue areas in neurosurgery using optical coherence tomography. *The International Journal of Medical Robotics and Computer Assisted Surgery* **8**, 327-336 (2012).

63. K. Bizheva, W. Drexler, M. Preusser, A. Stingl, T. Le, H. Budka, A. Unterhuber, B. Hermann, B. PovazË, H. Sattmann, Imaging ex vivo healthy and pathological human brain tissue with ultra-high-resolution optical coherence tomography. *Journal of biomedical optics* **10**, 011006-0110067 (2005).

64. O. Assayag, K. Grieve, B. Devaux, F. Harms, J. Pallud, F. Chretien, C. Boccara, P. Varlet, Imaging of non tumorous and tumorous human brain tissue with full-field optical coherence tomography. *NeuroImage: Clinical*, (2013).

65. H. Böhringer, D. Boller, J. Leppert, U. Knopp, E. Lankenau, E. Reusche, G. Hüttmann, A. Giese, Time-domain and spectral-domain optical coherence tomography in the analysis of brain tumor tissue. *Lasers in surgery and medicine* **38**, 588-597 (2006).

66. C. Kut, K. L. Chaichana, J. Xi, S. M. Raza, X. Ye, E. R. McVeigh, F. J. Rodriguez, A. Quiñones-Hinojosa, X. Li, Detection of human brain cancer infiltration ex vivo and in vivo using quantitative optical coherence tomography. *Science translational medicine* **7**, 292ra100-292ra100 (2015).

67. G. E. Keles, D. A. Lundin, K. R. Lamborn, E. F. Chang, G. Ojemann, M. S. Berger, Intraoperative subcortical stimulation mapping for hemispheric perirolandic gliomas located within or adjacent to the descending motor pathways: evaluation of morbidity and assessment of functional outcome in 294 patients. *J Neurosurg* **100**, 369-375 (2004).

68. J. Xi, Y. Chen, X. Li, Characterizing optical properties of nano contrast agents by using cross-referencing OCT imaging. *Biomedical optics express* **4**, 842-851 (2013).

69. L. V. Wang, H.-i. Wu, *Biomedical optics: principles and imaging*. (John Wiley & Sons, 2012).

70. W. Yuan, C. Kut, W. Liang, X. D. Li, Ultrafast and robust characterization of OCT-based optical attenuations using a novel frequency-domain algorithm. *Biomedical Optics Express (To be submitted)*, (2016).

71. J. R. Lakowicz, *Principles of Fluorescence Spectroscopy*. (Springer, New York, ed. 3rd, 2011), pp. 954.

72. C. Kut, J. Xi, K. L. Chaichana, X. Ye, F. J. Rodriguez, E. R. McVeigh, A. Quinones-Hinojosa, X. D. Li, SS-OCT Imaging and Optical Property Mapping for Intro-operative Guidance of Brain Tumor Surgery. *Biomedical Optics 2014*, BT3A.63 (2014).

73. F. J. van der Meer, D. J. Faber, M. C. Aalders, A. A. Poot, I. Vermes, T. G. van Leeuwen, Apoptosis- and necrosis-induced changes in light attenuation measured by optical coherence tomography. *Lasers Med Sci* **25**, 259-267 (2010).

74. D. N. Louis, H. Ohgaki, O. D. Wiestler, W. K. Cavenee, P. C. Burger, A. Jouvet, B. W. Scheithauer, P. Kleihues, The 2007 WHO classification of tumours of the central nervous system. *Acta neuropathologica* **114**, 97-109 (2007).

75. R. G. Brereton, *Applied chemometrics for scientists*. (John Wiley & Sons, 2007).

76. P. A. Valdes, A. Kim, M. Brantsch, C. Niu, Z. B. Moses, T. D. Tosteson, B. C. Wilson, K. D. Paulsen, D. W. Roberts, B. T. Harris, delta-aminolevulinic acid-induced protoporphyrin IX concentration correlates with histopathologic markers of malignancy in human gliomas: the need for quantitative fluorescence-guided resection to identify regions of increasing malignancy. *Neuro-oncology* **13**, 846-856 (2011).

77. D. W. Roberts, P. A. Valdes, B. T. Harris, A. Hartov, X. Fan, S. Ji, B. W. Pogue, F. Leblond, T. D. Tosteson, B. C. Wilson, K. D. Paulsen, Adjuncts for maximizing resection: 5-aminolevuinic acid. *Clin Neurosurg* **59**, 75-78 (2012).

78. M. J. McGirt, D. Mukherjee, K. L. Chaichana, K. D. Than, J. D. Weingart, A. Quinones-Hinojosa, Association of surgically acquired motor and language deficits on overall survival after resection of glioblastoma multiforme. *Neurosurgery* **65**, 463-469; discussion 469-470 (2009).

79. K. Özduman, E. Yıldız, A. Dinçer, A. Sav, M. N. Pamir, Using intraoperative dynamic contrast-enhanced T1-weighted MRI to identify residual tumor in glioblastoma surgery: Technical note. *J Neurosurg* **120**, 60-66 (2014).

80. E. Uhl, S. Zausinger, D. Morhard, T. Heigl, B. Scheder, W. Rachinger, C. Schichor, J.-C. Tonn, Intraoperative computed tomography with integrated navigation system in a multidisciplinary operating suite. *Neurosurgery* **64**, ons231-ons240 (2009).

81. Y. Zhang, Y. Chen, Y. Yu, X. Xue, V. V. Tuchin, D. Zhu, Visible and near-infrared spectroscopy for distinguishing malignant tumor tissue from benign tumor and normal breast tissues in vitro. *Journal of biomedical optics* **18**, 077003-077003 (2013).

82. M. J. Cobb, Y. Chen, S. L. Bailey, C. J. Kemp, X. D. Li, Non-invasive imaging of carcinogen-induced early neoplasia using ultrahigh-resolution optical coherence tomography. *Cancer Biomark* **2**, 163-173 (2006).

83. D. Levitz, L. Thrane, M. Frosz, P. Andersen, C. Andersen, S. Andersson-Engels, J. Valanciunaite, J. Swartling, P. Hansen, Determination of optical scattering properties of highly-scattering media in optical coherence tomography images. *Optics express* **12**, 249-259 (2004).

84. M. Alaminos, V. Dávalos, S. Ropero, F. Setién, M. F. Paz, M. Herranz, M. F. Fraga, J. Mora, N.-K. V. Cheung, W. L. Gerald, EMP3, a myelin-related gene located in the critical 19q13. 3 region, is epigenetically silenced and exhibits features of a candidate tumor suppressor in glioma and neuroblastoma. *Cancer Research* **65**, 2565-2571 (2005).

85. V. R. Amberger, T. Hensel, N. Ogata, M. E. Schwab, Spreading and migration of human glioma and rat C6 cells on central nervous system myelin in vitro is correlated with tumor malignancy and involves a metalloproteolytic activity. *Cancer Research* **58**, 149-158 (1998).

86. D. K. Binder, M. S. Berger, Proteases and the biology of glioma invasion. *Journal of neuro-oncology* **56**, 149-158 (2002).

87. F. Bevilacqua, D. Piguet, P. Marquet, J. D. Gross, B. J. Tromberg, C. Depeursinge, In Vivo Local Determination of Tissue Optical Properties: Applications to Human Brain. *Applied optics* **38**, 4939-4950 (1999).

88. L. Reznicek, T. Klein, W. Wieser, M. Kernt, A. Wolf, C. Haritoglou, A. Kampik, R. Huber, A. S. Neubauer, Megahertz ultra-wide-field swept-source retina optical coherence

tomography compared to current existing imaging devices. *Graefe's Archive for Clinical and Experimental Ophthalmology*, 1-8 (2014).

89. J. Xi, A. Zhang, Z. Liu, W. Liang, L. Y. Lin, S. Yu, X. D. Li, Diffractive catheter for ultrahigh-resolution spectral-domain volumetric OCT imaging. *Optics letters* **39**, 2016-2019 (2014).

90. T. M. Kauer, J.-L. Figueiredo, S. Hingtgen, K. Shah, Encapsulated therapeutic stem cells implanted in the tumor resection cavity induce cell death in gliomas. *Nature neuroscience* **15**, 197-204 (2011).

91. S.-c. Yu, Y.-f. Ping, L. Yi, Z.-h. Zhou, J.-h. Chen, X.-h. Yao, L. Gao, J. M. Wang, X.-w. Bian, Isolation and characterization of cancer stem cells from a human glioblastoma cell line U87. *Cancer letters* **265**, 124-134 (2008).

92. K. L. Chaichana, H. Guerrero-Cazares, V. Capilla-Gonzalez, G. Zamora-Berridi, P. Achanta, O. Gonzalez-Perez, G. I. Jallo, J. M. Garcia-Verdugo, A. Quiñones-Hinojosa, Intra-operatively obtained human tissue: protocols and techniques for the study of neural stem cells. *Journal of neuroscience methods* **180**, 116-125 (2009).

93. K. L. Chaichana, H. Guerrero-Cazares, V. Capilla-Gonzalez, G. Zamora-Berridi, P. Achanta, O. Gonzalez-Perez, G. I. Jallo, J. M. Garcia-Verdugo, A. Quinones-Hinojosa, Intra-operatively obtained human tissue: protocols and techniques for the study of neural stem cells. *J Neurosci Methods* **180**, 116-125 (2009).

94. P. Sun, S. Xia, B. Lal, C. G. Eberhart, A. Quinones-Hinojosa, J. Maciaczyk, W. Matsui, F. DiMeco, S. M. Piccirillo, A. L. Vescovi, J. Laterra, DNER, an Epigenetically Modulated Gene, Regulates Glioblastoma-Derived Neurosphere Cell Differentiation and Tumor Propagation. *STEM CELLS* **27**, 1473-1486 (2009).

95. M. Ying, S. Wang, Y. Sang, P. Sun, B. Lal, C. R. Goodwin, H. Guerrero-Cazares, A. Quinones-Hinojosa, J. Laterra, S. Xia, Regulation of glioblastoma stem cells by retinoic acid: role for Notch pathway inhibition. *Oncogene* **30**, 3454-3467 (2011).

96. S. Abbadi, J. J. Rodarte, A. Abutaleb, E. Lavell, C. L. Smith, W. Ruff, J. Schiller, A. Olivi, A. Levchenko, H. Guerrero-Cazares, A. Quinones-Hinojosa, Glucose-6-phosphatase is a Key Metabolic Regulator of Glioblastoma Invasion. *Molecular Cancer Research*, (2014).

97. J. Tilghman, H. Wu, Y. Sang, X. Shi, H. Guerrero-Cazares, A. Quinones-Hinojosa, C. G. Eberhart, J. Laterra, M. Ying, HMMR Maintains the Stemness and Tumorigenicity of Glioblastoma Stem-like Cells. *Cancer Research* **74**, 3168-3179 (2014).

98. Y. Feng, M. Zhu, S. Dangelmajer, Y. M. Lee, O. Wijesekera, C. Castellanos, A. Denduluri, K. L. Chaichana, Q. Li, H. Zhang, A. Levchenko, H. Guerrero-Cazares, A. Quinones-Hinojosa, Hypoxia-cultured Human Adipose-Derived Mesenchymal Stem Cells are Nononcogenic and have Enhanced Viability, Motility, and Tropism to Brain Cancer. (Submitted).

99. C. L. Smith, K. L. Chaichana, B. Lin, T. O'Donnell, S. Gupta, S. Shah, J. Wang, O. Wijesekera, M. Delannoy, A. Levchenko, A. Quinones-Hinojosa, Pre-exposure of Human Adipose Mesenchymal Stem Cells to Soluble Factors Enhances their Homing to Brain Cancer. (Submitted).

100. C. L. Smith, D.-H. Kim, N. Sedora-Roman, H. Guerrero-Cazares, S. Gupta, T. O'Donnell, K. L. Chaichana, H. N. Kim, F. Rodriguez, S. Abbadi, M. Delannoy, K.-Y. Suh, A. Quinones-Hinojosa, A. Levchenko, A Novel Nanotopographic Platform for Screening Glioma Cell Migratory Behavior and Predicting Patient Outcomes. (Submitted).

101. Y. Zhao, Z. Chen, C. Saxer, S. Xiang, J. F. de Boer, J. S. Nelson, Phase-resolved optical coherence tomography and optical Doppler tomography for imaging blood flow in human skin with fast scanning speed and high velocity sensitivity. *Optics letters* **25**, 114-116 (2000).

102. A. Mariampillai, M. K. Leung, M. Jarvi, B. A. Standish, K. Lee, B. C. Wilson, A. Vitkin, V. X. Yang, Optimized speckle variance OCT imaging of microvasculature. *Optics letters* **35**, 1257-1259 (2010).

103. G. Liu, L. Chou, W. Jia, W. Qi, B. Choi, Z. Chen, Intensity-based modified Doppler variance algorithm: application to phase instable and phase stable optical coherence tomography systems. *Optics express* **19**, 11429-11440 (2011).

104. H. Li, B. A. Standish, A. Mariampillai, N. R. Munce, Y. Mao, S. Chiu, N. E. Marcon, B. C. Wilson, A. Vitkin, V. X. Yang, Feasibility of interstitial Doppler optical coherence tomography for in vivo detection of microvascular changes during photodynamic therapy. *Lasers in surgery and medicine* **38**, 754-761 (2006).

105. Y. Zhao, Z. Chen, C. Saxer, Q. Shen, S. Xiang, J. F. de Boer, J. S. Nelson, Doppler standard deviation imaging for clinical monitoring of in vivo human skin blood flow. *Optics letters* **25**, 1358-1360 (2000).

106. G. Liu, W. Qi, L. Yu, Z. Chen, Real-time bulk-motion-correction free Doppler variance optical coherence tomography for choroidal capillary vasculature imaging. *Optics express* **19**, 3657-3666 (2011).

107. X. D. Li, S. Martin, C. Pitris, R. Ghanta, D. L. Stamper, M. Harman, J. G. Fujimoto, M. E. Brezinski, High-resolution optical coherence tomographic imaging of osteoarthritic cartilage during open knee surgery. *Arthritis research & therapy* **7**, R318 (2005).

108. M. Oheim, D. J. Michael, M. Geisbauer, D. Madsen, R. H. Chow, Principles of two-photon excitation fluorescence microscopy and other nonlinear imaging approaches. *Advanced drug delivery reviews* **58**, 788-808 (2006).

109. M. D. Cahalan, I. Parker, S. H. Wei, M. J. Miller, Two-photon tissue imaging: seeing the immune system in a fresh light. *Nature Reviews Immunology* **2**, 872-880 (2002).

110. W. Denk, K. Svoboda, Photon upmanship: why multiphoton imaging is more than a gimmick. *Neuron* **18**, 351-357 (1997).

111. E. Beaurepaire, M. Oheim, J. Mertz, Ultra-deep two-photon fluorescence excitation in turbid media. *Optics Communications* **188**, 25-29 (2001).

112. P. Theer, M. T. Hasan, W. Denk, Two-photon imaging to a depth of 1000 μm in living brains by use of a Ti: Al 2 O 3 regenerative amplifier. *Optics letters* **28**, 1022-1024 (2003).

113. M. Oheim, E. Beaurepaire, E. Chaigneau, J. Mertz, S. Charpak, Two-photon microscopy in brain tissue: parameters influencing the imaging depth. *Journal of neuroscience methods* **111**, 29-37 (2001).

114. W. Denk, J. H. Strickler, W. W. Webb, Two-photon laser scanning fluorescence microscopy. *Science* **248**, 73-76 (1990).

115. A. Hopt, E. Neher, Highly nonlinear photodamage in two-photon fluorescence microscopy. *Biophysical journal* **80**, 2029-2036 (2001).

116. R. Hellwarth, P. Christensen, Nonlinear optical microscopic examination of structure in polycrystalline ZnSe. *Optics Communications* **12**, 318-322 (1974).

117. C. Sheppard, J. Gannaway, R. Kompfner, D. Walsh, The scanning harmonic optical microscope. *Quantum Electronics, IEEE Journal of* **13**, 912-912 (1977).

118. P. J. Campagnola, L. M. Loew, Second-harmonic imaging microscopy for visualizing biomolecular arrays in cells, tissues and organisms. *Nature biotechnology* **21**, 1356-1360 (2003).

119. C.-K. Sun, in *Microscopy Techniques*. (Springer, 2005), pp. 17-56.

120. N. J. Durr, C. T. Weisspfennig, B. A. Holfeld, A. Ben-Yakar, Maximum imaging depth of two-photon autofluorescence microscopy in epithelial tissues. *Journal of Biomedical Optics* **16**, 026008-026008-026013 (2011).

121. R. M. Williams, W. R. Zipfel, W. W. Webb, Interpreting second-harmonic generation images of collagen I fibrils. *Biophysical journal* **88**, 1377-1386 (2005).

122. N. Baumann, D. Pham-Dinh, Biology of oligodendrocyte and myelin in the mammalian central nervous system. *Physiological reviews* **81**, 871-927 (2001).

123. A.-M. Pena, T. Boulesteix, T. Dartigalongue, M.-C. Schanne-Klein, Chiroptical effects in the second harmonic signal of collagens I and IV. *Journal of the American Chemical Society* **127**, 10314-10322 (2005).

124. D. Mustafa, M. Van Der Weiden, P. Zheng, A. Nigg, T. M. Luider, J. M. Kros, Expression sites of colligin 2 in glioma blood vessels. *Brain pathology* **20**, 50-65 (2010).

125. W. Paulus, W. Roggendorf, D. Schuppan, Immunohistochemical investigation of collagen subtypes in human glioblastomas. *Virchows Archiv A* **413**, 325-332 (1988).

126. J. B. Posner, in *Brain metastasis*. (Springer, 1980), pp. 2-29.

127. S. Garber, R. Jensen, Image guidance for brain metastases resection. *Surgical neurology international* **3**, 111 (2012).

128. G. Schackert, A. Steinmetz, U. Meier, S. B. Sobottka, Surgical management of single and multiple brain metastases: results of a retrospective study. *Oncology Research and Treatment* **24**, 246-255 (2001).

129. J. Xi, Y. Chen, Y. Zhang, K. Murari, M.-J. Li, X. Li, Integrated multimodal endomicroscopy platform for simultaneous en face optical coherence and two-photon fluorescence imaging. *Optics letters* **37**, 362-364 (2012).

130. N. J. Abbott, Evidence for bulk flow of brain interstitial fluid: significance for physiology and pathology. *Neurochem Int* **45**, 545-552 (2004).

131. J. J. Iliff, M. Nedergaard, Is there a cerebral lymphatic system? *Stroke* **44**, S93-S95 (2013).

132. M. Nedergaard, Garbage Truck of the Brain. *Science* **340**, 1529-1530 (2013).

133. M. Proescholdt, B. Hutto, L. Brady, M. Herkenham, Studies of cerebrospinal fluid flow and penetration into brain following lateral ventricle and cisterna magna injections of the tracer [< sup> 14</sup> C] inulin in rat. *Neuroscience* **95**, 577-592 (1999).

134. J. Sleeman, The lymph node as a bridgehead in the metastatic dissemination of tumors. *Recent Results in Cancer Research*, 55-81 (2000).

135. G. H. Lyman, A. E. Giuliano, M. R. Somerfield, A. B. Benson III, D. C. Bodurka, H. J. Burstein, A. J. Cochran, H. S. Cody III, S. B. Edge, S. Galper, American Society of Clinical Oncology guideline recommendations for sentinel lymph node biopsy in early-stage breast cancer. *Journal of clinical oncology* **23**, 7703-7720 (2005).

136. C. P. Geer, S. A. Grossman, Interstitial fluid flow along white matter tracts: a potentially important mechanism for the dissemination of primary brain tumors. *J Neurooncol* **32**, 193-201 (1997).

137. H. F. Cserr, Physiology of the choroid plexus. *Physiol Rev* **51**, 273-311 (1971).

138. H. F. Cserr, D. N. Cooper, P. K. Suri, C. S. Patlak, Efflux of radiolabeled polyethylene glycols and albumin from rat brain. *Am J Physiol* **240**, F319-328 (1981).

139. G. A. Rosenberg, W. T. Kyner, E. Estrada, Bulk flow of brain interstitial fluid under normal and hyperosmolar conditions. *Am J Physiol* **238**, F42-49 (1980).

140. Y. Persidsky, S. H. Ramirez, J. Haorah, G. D. Kanmogne, Blood–brain barrier: structural components and function under physiologic and pathologic conditions. *Journal of Neuroimmune Pharmacology* **1**, 223-236 (2006).

141. T. Kuroiwa, M. Shibutani, R. Okeda, Blood-brain barrier disruption and exacerbation of ischemic brain edema after restoration of blood flow in experimental focal cerebral ischemia. *Acta neuropathologica* **76**, 62-70 (1988).

142. E. Mandonnet, L. Capelle, H. Duffau, Extension of paralimbic low grade gliomas: toward an anatomical classification based on white matter invasion patterns. *Journal of neuro-oncology* **78**, 179-185 (2006).

143. A. Giese, L. Kluwe, B. Laube, H. Meissner, M. E. Berens, M. Westphal, Migration of human glioma cells on myelin. *Neurosurgery* **38**, 755-764 (1996).

144. C. J. Endres, B. S. Kolachana, R. C. Saunders, T. Su, D. Weinberger, A. Breier, W. C. Eckelman, R. E. Carson, Kinetic modeling of [11C]raclopride: combined PET-microdialysis studies. *J Cereb Blood Flow Metab* **17**, 932-942 (1997).

145. O. R. Blaumanis, M. L. Rennels, P. A. Grady, Focal cerebral edema impedes convective fluid/tracer movement through paravascular pathways in cat brain. *Adv Neurol* **52**, 385-389 (1990).

146. , (!!! INVALID CITATION !!!).

147. B. J. Barber, V. L. Stanhope, Bromcresol green assay is nonspecific for rat plasma albumin. *American Journal of Physiology - Heart and Circulatory Physiology* **262**, H299-H302 (1992).

148. Y. Ji, S. Powers, J. T. Brown, R. Miner, Characterization of the tumor invasion area in the rat intracerebral glioma. *J Neuro-Oncol* **30**, 189-197 (1996).

149. H. B. Stolp, K. M. Dziegielewska, C. J. Ek, M. D. Habgood, M. A. Lane, A. M. Potter, N. R. Saunders, Breakdown of the blood–brain barrier to proteins in white matter of the developing brain following systemic inflammation. *Cell and Tissue Research* **320**, 369-378 (2005).

150. A. Fenske, M. Samii, H. J. Reulen, O. Hey, Extracellular space and electrolyte distribution in cortex and white matter of dog brain in cold induced oedema. *Acta Neurochirurgica* **28**, 81-94 (1973).

151. K. I. Olsen, P. Schroeder, R. Corby, I. Vucic, D. M. E. Bardo, Advanced magnetic resonance imaging techniques to evaluate CNS glioma. *Expert Review of Neurotherapeutics* **5**, 3-11 (2005).

152. M. Rosenblum, A. Eisenberg, D. Norman, Brain tumor invasion: clinical patterns of malignant astrocytoma spread. *J Neurosurg* **76**, 383A (1992).

153. P. C. Burger, P. J. Dubois, S. C. Schold Jr, K. R. Smith Jr, G. L. Odom, D. C. Crafts, F. Giangaspero, Computerized tomographic and pathologic studies of the untreated, quiescent, and recurrent glioblastoma multiforme. *Journal of neurosurgery* **58**, 159-169 (1983).

154. C. Kut, S. A. Grossman, J. Blakeley, How critical is the blood-brain barrier to the development of neurotherapeutics? *JAMA neurology* **72**, 381-382 (2015).

155. C. Kut, K. J. Redmond, in *Seminars in radiation oncology*. (Elsevier, 2014), vol. 24, pp. 265-272.

156. A. Horská, A. LaClair, M. Mohamed, C. Wells, T. McNutt, K. Cohen, M. Wharam, E. Mahone, W. Kates, Low cerebellar vermis volumes and impaired neuropsychologic performance in children treated for brain tumors and leukemia. *American Journal of Neuroradiology* **31**, 1430-1437 (2010).

157. E. L. Chang, J. S. Wefel, K. R. Hess, P. K. Allen, F. F. Lang, D. G. Kornguth, R. B. Arbuckle, J. M. Swint, A. S. Shiu, M. H. Maor, Neurocognition in patients with brain metastases treated with radiosurgery or radiosurgery plus whole-brain irradiation: a randomised controlled trial. *The lancet oncology* **10**, 1037-1044 (2009).

158. L. M. DeAngelis, J.-Y. Delattre, J. B. Posner, Radiation-induced dementia in patients cured of brain metastases. *Neurology* **39**, 789-789 (1989).

159. G. Welzel, K. Fleckenstein, J. Schaefer, B. Hermann, U. Kraus-Tiefenbacher, S. K. Mai, F. Wenz, Memory function before and after whole brain radiotherapy in patients with and without brain metastases. *International Journal of Radiation Oncology* Biology* Physics* **72**, 1311-1318 (2008).

160. B. Fisher, W. Seiferheld, C. Schultz, L. DeAngelis, D. Nelson, S. Schold, W. Curran, M. Mehta, Secondary analysis of Radiation Therapy Oncology Group study (RTOG) 9310: an intergroup phase II combined modality treatment of primary central nervous system lymphoma. *Journal of neuro-oncology* **74**, 201-205 (2005).

161. I. T. Gavrilovic, A. Hormigo, J. Yahalom, L. M. DeAngelis, L. E. Abrey, Long-term follow-up of high-dose methotrexate-based therapy with and without whole brain irradiation for newly diagnosed primary CNS lymphoma. *Journal of Clinical Oncology* **24**, 4570-4574 (2006).

162. I. C. Gibbs, D. Haas-Kogan, S. Terezakis, B. D. Kavanagh, The Subventricular Zone Neural Progenitor Cell Hypothesis in Glioblastoma: Epiphany, Trojan Horse, or Cheshire Fact? *International Journal of Radiation Oncology* Biology* Physics* **86**, 606-608 (2013).

163. P. S. Eriksson, E. Perfilieva, T. Björk-Eriksson, A.-M. Alborn, C. Nordborg, D. A. Peterson, F. H. Gage, Neurogenesis in the adult human hippocampus. *Nature medicine* **4**, 1313-1317 (1998).

164. L. Chen, H. Guerrero-Cazares, X. Ye, E. Ford, T. McNutt, L. Kleinberg, M. Lim, K. Chaichana, A. Quinones-Hinojosa, K. Redmond, Increased Subventricular Zone Radiation Dose Correlates With Survival in Glioblastoma Patients After Gross Total Resection. *International Journal of Radiation Oncology* Biology* Physics*, (2013).

165. I. J. Barani, L. W. Cuttino, S. H. Benedict, D. Todor, E. A. Bump, Y. Wu, T. D. Chung, W. C. Broaddus, P.-S. Lin, Neural stem cell-preserving external-beam radiotherapy of central nervous system malignancies. *International Journal of Radiation Oncology* Biology* Physics* **68**, 978-985 (2007).

166. K. S. Aboody, A. Brown, N. G. Rainov, K. A. Bower, S. Liu, W. Yang, J. E. Small, U. Herrlinger, V. Ourednik, P. M. Black, Neural stem cells display extensive tropism for pathology in adult brain: evidence from intracranial gliomas. *Proceedings of the National Academy of Sciences* **97**, 12846-12851 (2000).

167. K. Staflin, M. Lindvall, T. Zuchner, C. Lundberg, Instructive cross-talk between neural progenitor cells and gliomas. *Journal of neuroscience research* **85**, 2147-2159 (2007).

168. A. Arvidsson, T. Collin, D. Kirik, Z. Kokaia, O. Lindvall, Neuronal replacement from endogenous precursors in the adult brain after stroke. *Nature medicine* **8**, 963-970 (2002).

169. G. E. Goings, V. Sahni, F. G. Szele, Migration patterns of subventricular zone cells in adult mice change after cerebral cortex injury. *Brain research* **996**, 213-226 (2004).

170. J. Y. Jeon, J. H. An, S. U. Kim, H. G. Park, M. A. Lee, Migration of human neural stem cells toward an intracranial glioma. *Experimental & molecular medicine* **40**, 84-91 (2008).

171. P. Lantos, D. Cox, The origin of experimental brain tumours: a sequential study. *Experientia* **32**, 1467-1468 (1976).

172. P. Lantos, G. Pilkington, The development of experimental brain tumours a sequential light and electron microscope study of the subependymal plate. *Acta neuropathologica* **45**, 167-175 (1979).

173. C. Calabrese, H. Poppleton, M. Kocak, T. L. Hogg, C. Fuller, B. Hamner, E. Y. Oh, M. W. Gaber, D. Finklestein, M. Allen, A perivascular niche for brain tumor stem cells. *Cancer cell* **11**, 69-82 (2007).

174. A. Ayuso-Sacido, J. A. Moliterno, S. Kratovac, G. S. Kapoor, D. M. O'Rourke, E. C. Holland, J. M. García-Verdugo, N. S. Roy, J. A. Boockvar, Activated EGFR signaling increases proliferation, survival, and migration and blocks neuronal differentiation in post-natal neural stem cells. *Journal of neuro-oncology* **97**, 323-337 (2010).

175. R. K. Mulhern, T. E. Merchant, A. Gajjar, W. E. Reddick, L. E. Kun, Late neurocognitive sequelae in survivors of brain tumours in childhood. *The lancet oncology* **5**, 399-408 (2004).

176. T. E. Merchant, R. K. Mulhern, M. J. Krasin, L. E. Kun, T. Williams, C. Li, X. Xiong, R. B. Khan, R. H. Lustig, F. A. Boop, Preliminary results from a phase II trial of conformal radiation therapy and evaluation of radiation-related CNS effects for pediatric patients with localized ependymoma. *Journal of Clinical Oncology* **22**, 3156-3162 (2004).

177. J. R. Fike, R. Rola, C. L. Limoli, Radiation response of neural precursor cells. *Neurosurgery clinics of North America* **18**, 115-127 (2007).

178. R. Rola, J. Raber, A. Rizk, S. Otsuka, S. R. VandenBerg, D. R. Morhardt, J. R. Fike, Radiation-induced impairment of hippocampal neurogenesis is associated with cognitive deficits in young mice. *Experimental neurology* **188**, 316-330 (2004).

179. G. Winocur, J. M. Wojtowicz, M. Sekeres, J. S. Snyder, S. Wang, Inhibition of neurogenesis interferes with hippocampus-dependent memory function. *Hippocampus* **16**, 296-304 (2006).

180. E. Tada, J. Parent, D. Lowenstein, J. Fike, X-irradiation causes a prolonged reduction in cell proliferation in the dentate gyrus of adult rats. *Neuroscience* **99**, 33-41 (2000).

181. E. Tada, C. Yang, G. T. Gobbel, K. R. Lamborn, J. R. Fike, Long-term impairment of subependymal repopulation following damage by ionizing irradiation. *Experimental neurology* **160**, 66-77 (1999).

182. S. Mizumatsu, M. L. Monje, D. R. Morhardt, R. Rola, T. D. Palmer, J. R. Fike, Extreme sensitivity of adult neurogenesis to low doses of X-irradiation. *Cancer research* **63**, 4021-4027 (2003).

183. M. L. Monje, S. Mizumatsu, J. R. Fike, T. D. Palmer, Irradiation induces neural precursor-cell dysfunction. *Nature medicine* **8**, 955-962 (2002).

184. T. M. Madsen, P. Kristjansen, T. G. Bolwig, G. Wörtwein, Arrested neuronal proliferation and impaired hippocampal function following fractionated brain irradiation in the adult rat. *Neuroscience* **119**, 635-642 (2003).

185. M. D. Saxe, F. Battaglia, J.-W. Wang, G. Malleret, D. J. David, J. E. Monckton, A. D. R. Garcia, M. V. Sofroniew, E. R. Kandel, L. Santarelli, Ablation of hippocampal neurogenesis impairs contextual fear conditioning and synaptic plasticity in the dentate gyrus. *Proceedings of the National Academy of Sciences* **103**, 17501-17506 (2006).

186. K. J. Redmond, E. M. Mahone, S. Terezakis, O. Ishaq, E. Ford, T. McNutt, L. Kleinberg, K. J. Cohen, M. Wharam, A. Horska, Association between radiation dose to neuronal progenitor cell niches and temporal lobes and performance on neuropsychological testing in children: a prospective study. *Neuro-oncology* **15**, 360-369 (2013).

187. L. Iuvone, P. Mariotti, C. Colosimo, F. Guzzetta, A. Ruggiero, R. Riccardi, Long-term cognitive outcome, brain computed tomography scan, and magnetic resonance imaging in children cured for acute lymphoblastic leukemia. *Cancer* **95**, 2562-2570 (2002).

188. P. G. Lesnik, K. T. Ciesielski, B. L. Hart, E. C. Benzel, J. A. Sanders, Evidence for cerebellar-frontal subsystem changes in children treated with intrathecal chemotherapy for leukemia: enhanced data analysis using an effect size model. *Archives of Neurology* **55**, 1561 (1998).

189. D. P. Waber, N. J. Tarbell, C. M. Kahn, R. D. Gelber, S. E. Sallan, The relationship of sex and treatment modality to neuropsychologic outcome in childhood acute lymphoblastic leukemia. *Journal of Clinical Oncology* **10**, 810-817 (1992).

190. S. J. Bakke, A. Fossen, I. Storm-Mathiesen, S. O. Lie, Long-term cerebral effects of CNS chemotherapy in children with acute lymphoblastic leukemia. *Pediatric Hematology-Oncology* **10**, 267-270 (1993).

191. G. T. Armstrong, N. Jain, W. Liu, T. E. Merchant, M. Stovall, D. K. Srivastava, J. G. Gurney, R. J. Packer, L. L. Robison, K. R. Krull, Region-specific radiotherapy and neuropsychological outcomes in adult survivors of childhood CNS malignancies. *Neuro-oncology* **12**, 1173-1186 (2010).

192. R. Jalali, I. Mallick, D. Dutta, S. Goswami, T. Gupta, A. Munshi, D. Deshpande, R. Sarin, Factors influencing neurocognitive outcomes in young patients with benign and low-grade brain tumors treated with stereotactic conformal radiotherapy. *International Journal of Radiation Oncology* Biology* Physics* **77**, 974-979 (2010).

193. N. Sanai, A. D. Tramontin, A. Quiñones-Hinojosa, N. M. Barbaro, N. Gupta, S. Kunwar, M. T. Lawton, M. W. McDermott, A. T. Parsa, J. M.-G. Verdugo, Unique astrocyte ribbon in adult human brain contains neural stem cells but lacks chain migration. *Nature* **427**, 740-744 (2004).

194. S. Khatua, G. Dhall, S. O'Neil, R. Jubran, J. G. Villablanca, A. Marachelian, A. Nastia, R. Lavey, A. J. Olch, I. Gonzalez, Treatment of primary CNS germinomatous germ cell tumors with chemotherapy prior to reduced dose whole ventricular and local boost irradiation. *Pediatric blood & cancer* **55**, 42-46 (2010).

195. D. J. Mabbott, E. Monsalves, B. J. Spiegler, U. Bartels, L. Janzen, S. Guger, N. Laperriere, N. Andrews, E. Bouffet, Longitudinal evaluation of neurocognitive function after treatment for central nervous system germ cell tumors in childhood. *Cancer* **117**, 5402-5411 (2011).

196. F. Lazarini, M.-A. Mouthon, G. Gheusi, F. De Chaumont, J.-C. Olivo-Marin, S. Lamarque, D. N. Abrous, F. D. Boussin, P.-M. Lledo, Cellular and behavioral effects of cranial irradiation of the subventricular zone in adult mice. *PLoS One* **4**, e7017 (2009).

197. V. Gondi, in *ASTRO*. (2013), vol. Abstract LBA 1.

198. K. J. Redmond, P. Achanta, S. A. Grossman, M. Armour, J. Reyes, L. Kleinberg, E. Tryggestad, A. Quinones-Hinojosa, E. C. Ford, A radiotherapy technique to limit dose to neural progenitor cell niches without compromising tumor coverage. *Journal of neuro-oncology* **104**, 579-587 (2011).

199. V. Gondi, R. Tolakanahalli, M. P. Mehta, D. Tewatia, H. Rowley, J. S. Kuo, D. Khuntia, W. A. Tomé, Hippocampal-Sparing Whole-Brain Radiotherapy: A "How-To" Technique Using Helical Tomotherapy and Linear Accelerator–Based Intensity-Modulated Radiotherapy. *International Journal of Radiation Oncology* Biology* Physics* **78**, 1244-1252 (2010).

200. A. N. Gutiérrez, D. C. Westerly, W. A. Tomé, H. A. Jaradat, T. R. Mackie, S. M. Bentzen, D. Khuntia, M. P. Mehta, Whole brain radiotherapy with hippocampal avoidance and

simultaneously integrated brain metastases boost: a planning study. *International Journal of Radiation Oncology* Biology* Physics* **69**, 589-597 (2007).

201. E. I. Fomchenko, E. C. Holland, Platelet-Derived Growth Factor–Mediated Gliomagenesis and Brain Tumor Recruitment. *Neurosurgery clinics of North America* **18**, 39-58 (2007).

202. S. Bao, Q. Wu, R. E. McLendon, Y. Hao, Q. Shi, A. B. Hjelmeland, M. W. Dewhirst, D. D. Bigner, J. N. Rich, Glioma stem cells promote radioresistance by preferential activation of the DNA damage response. *Nature* **444**, 756-760 (2006).

203. L. Cheng, Q. Wu, Z. Huang, O. A. Guryanova, Q. Huang, W. Shou, J. N. Rich, S. Bao, L1CAM regulates DNA damage checkpoint response of glioblastoma stem cells through NBS1. *The EMBO journal* **30**, 800-813 (2011).

204. G. Tabatabai, B. Frank, R. Möhle, M. Weller, W. Wick, Irradiation and hypoxia promote homing of haematopoietic progenitor cells towards gliomas by TGF-β-dependent HIF-1α-mediated induction of CXCL12. *Brain* **129**, 2426-2435 (2006).

205. K. L. Chaichana, M. J. McGirt, J. Frazier, F. Attenello, H. Guerrero-Cazares, A. Quinones-Hinojosa, Relationship of glioblastoma multiforme to the lateral ventricles predicts survival following tumor resection. *Journal of neuro-oncology* **89**, 219-224 (2008).

206. N. F. Jafri, J. L. Clarke, V. Weinberg, I. J. Barani, S. Cha, Relationship of glioblastoma multiforme to the subventricular zone is associated with survival. *Neuro-oncology* **15**, 91-96 (2013).

207. P. Evers, P. Lee, J. DeMarco, N. Agazaryan, J. Sayre, M. Selch, F. Pajonk, Irradiation of the potential cancer stem cell niches in the adult brain improves progression-free survival of patients with malignant glioma. *BMC cancer* **10**, 384 (2010).

208. T. Gupta, V. Nair, S. N. Paul, S. Kannan, A. Moiyadi, S. Epari, R. Jalali, Can irradiation of potential cancer stem-cell niche in the subventricular zone influence survival in patients with newly diagnosed glioblastoma? *Journal of neuro-oncology* **109**, 195-203 (2012).

209. P. Lee, W. Eppinga, F. Lagerwaard, T. Cloughesy, B. Slotman, P. L. Nghiemphu, P.-C. Wang, P. Kupelian, N. Agazaryan, J. Demarco, Evaluation of high ipsilateral subventricular zone radiation therapy dose in glioblastoma: a pooled analysis. *International Journal of Radiation Oncology* Biology* Physics*, (2013).

210. R. Kast, B. Ellingson, C. Marosi, M.-E. Halatsch, Glioblastoma treatment using perphenazine to block the subventricular zone's tumor trophic functions. *Journal of neuro-oncology*, 1-6 (2013).

211. R. Glass, M. Synowitz, G. Kronenberg, J.-H. Walzlein, D. S. Markovic, L.-P. Wang, D. Gast, J. Kiwit, G. Kempermann, H. Kettenmann, Glioblastoma-induced attraction of endogenous neural precursor cells is associated with improved survival. *The Journal of neuroscience* **25**, 2637-2646 (2005).

212. E. Tryggestad, M. Christian, E. Ford, C. Kut, Y. Le, G. Sanguineti, D. Y. Song, L. Kleinberg, Inter-and intrafraction patient positioning uncertainties for intracranial radiotherapy: a study of four frameless, thermoplastic mask-based immobilization strategies using daily cone-beam CT. *International Journal of Radiation Oncology* Biology* Physics* **80**, 281-290 (2011).

213. C. Kut, Y. Zhang, M. Hedayati, H. Zhou, C. Cornejo, D. Bordelon, J. Mihalic, M. Wabler, E. Burghardt, C. Gruettner, Preliminary study of injury from heating systemically delivered, nontargeted dextran-superparamagnetic iron oxide nanoparticles in mice. *Nanomedicine* **7**, 1697-1711 (2012).

214. E. W. Hsu, A. Muzikant, S. Matulevicius, R. Penland, C. Henriquez, Magnetic resonance myocardial fiber-orientation mapping with direct histological correlation. *American Journal of Physiology-Heart and Circulatory Physiology* **274**, H1627-H1634 (1998).

215. S. V. Plotnikov, A. C. Millard, P. J. Campagnola, W. A. Mohler, Characterization of the myosin-based source for second-harmonic generation from muscle sarcomeres. *Biophysical journal* **90**, 693-703 (2006).

APPENDIX 8: CURRICULUM VITAE

CURRICULUM VITAE FOR Ph.D. CANDIDATES

The Johns Hopkins University School of Medicine

Name: Carmen Kut **Date of this version:** 03/17/2016

Educational History:

Ph.D.	2016	Program in Biomedical Engineering. Mentors: Xingde Li PhD and Elliot McVeigh PhD	Johns Hopkins School of Medicine
M.D.	2018	To be completed	Johns Hopkins School of Medicine
B.S.	2008	Biomedical Engineering	Johns Hopkins University

Other Professional Experience (in reverse chronological order, latest first). Summer research positions, specialty courses, etc. If desired, list research rotations at Johns Hopkins here.

Undergraduate Johns Hopkins	2004-2008	Lab of Aleksander Popel, PhD,
Undergraduate Hopkins	2006-2008	Lab of Russell Taylor PhD, Johns
Undergraduate Hopkins	2007-2008	Lab of Joel Bader PhD, Johns
MD Rotation	2009-2011	Lab of Robert Ivkov PhD and Lab of Theodere DeWeese MD, Johns Hopkins
PhD Rotation Hopkins	2011-2016	Lab of Xingde Li, PhD, Johns
PhD Rotation Hopkins	2011-2016	Lab of Elliot McVeigh, MD, Johns

(Lab experience prior to PhD not included here)

Scholarships, fellowships, or other external funding

Pre-doctoral Grants (3 total):

- NIH F30 Pre-doctoral Fellowship for MD/PhDs – Impact Score 13, Top 3 Percentile, July 2014-**Present**
- NIH/NCI PS-OC EOC Pilot Project Graduate Student Support Jan 2012 – July 2012
- NIH TPTRI Imaging Grant Trainee, FY Jan 2011 – Jan 2012

Research Grants (5 total; 4 received, 1 pending award):

- Initiated, wrote and received $25,000 pilot grant from NIH NCI via Hopkins PS-OC EOC Pilot Project FY July 2011 – July 2012 (in name of PIs), for project entitled Measuring Interstitial bulk flow kinetics as a potential method to elucidate glioma cell migration along white matter tracts.
- Helped to prepare a Coulter Foundation proposal FY July 2014-2015 (in name of PIs) for my thesis project entitled Optical Mapping for Intra-operative Guidance during Brain Cancer Surgery, which resulted in a $70,000 award for the laboratory.
- Helped to prepare a Coulter Foundation proposal FY July 2015-2016 (in name of PIs) for my thesis project entitled Further Development of OCT Imaging Technology for Real-Time, Label Free Technology, which resulted in a $96,366 award for the laboratory.
- Helped to prepare an NIH R01 proposal in (in name of PIs) for my thesis project entitled Intra-Operative, Label-Free Detection of Brain Cancer Infiltration with Quantitative Optical Imaging which is ranked in the top 1st percentile and results in a ~$2,000,000 award.
- Helped to prepare a TEDCO MII Phase I grant (in the name of PIs) for my thesis project entitled Color-coded Quantitative Brain Cancer Mapping for Real-time Intraoperative Guidance which resulted in a $100,000 award for the laboratory.

Academic and other honors at Hopkins and elsewhere (graduation with honor, service awards, Hopkins student awards, etc,)

Academic Awards and Honors

2014-Present	NIH F30 Pre-doctoral Fellowship Award with Impact score of 13, in the top 3 percentile
2014-Present	Siebel Scholar, Class of 2015 awarded annually for academic excellence and demonstrated leadership to 85 top students from the world's leading graduate schools.
2014-2015	JHU Award for Graduate Teaching Assistants (given to one graduate student per year within the entire Johns Hopkins WSE)

2014-2015	OSA Biomedical Optics International Topical Meetings Best Poster Award
2008-2009	USA Today All-stars Academic First Team USA Today
	Selected as one of 20 only (nation-wide) college students based on academics and leadership to All-stars Academic First Team (http://www.jhu.edu/~gazette/2008/18feb08/18usat.html)
2008-2009	JHU Michael J. Muuss Research Award
	(granted to one senior each year giving significant contribution to research in the Computer Science Department at Johns Hopkins)
2008-2009	JHU Richard J. Johns Outstanding Academic Achievement Award
	(granted to BME seniors with outstanding cumulative GPA), 2008
2008-2009	ACMP Young Investigator's Award, 4th place
2008-2009	JHU #1 rank in Graduation (Year of 2008)
	Class rank amongst all students in class of 2008, School of Engineering, Hopkins
2008-2009	Member of Omicon Delta Kappa (national leadership honor society)
2007-2008	Member of Tau Beta Pi
	(recognizes engineering students of distinguished scholarship and exemplary character)
2007-2008	Member of BME Honor Society
2005-2008	Dean's List (inclusive, every semester during undergraduate studies)

Other Research Accomplishments

- First-Authored publication in Science Translational Medicine, 2015
- Transitioned my PhD work from the laboratory to the clinic by initiating, organizing and conducting the first in vivo, intraoperative human study of the optical mapping technology using OCT in November, 2015.
- NIH F30 Pre-doctoral Fellowship Award with Impact score of 13, in the top 3 percentile, 2014

Publications, peer reviewed, candidate's name in bold, reverse chronological order. Include reviews

Pending Publications

- **Kut C.** *et al*, Translating from the laboratory to the OR: Detection of brain cancer infiltration *in vivo* in patients using quantitative optical coherence tomography. (We have collected data from 3 patients in Nov 2016 and aim to submit in summer 2016 after collecting additional patient datasets)

- **Kut C.,** Rincon-Torroella J., Liang W.X., Hall G., Rodriguez F.J., Quinones-Hinojosa A., Li X.D., Detection of human brain cancer infiltration *ex vivo* using multi-photon fluorescence (to be submitted in April, 2016).
- Yuan W., **Kut C.**, Liang W.X., Li X.D., Ultrafast and robust characterization of OCT-based optical attenuations using a novel frequency-domain algorithm. *Biomedical Optics Express* (To be submitted in late March, 2016).

Publications

- **Kut C.**, Chaichana K.L., Xi J.F., Raza S.M., Ye X.B., McVeigh E.R., Rodriguez F.J., Quinones-Hinojosa A., Li X.D., " Detection of Human Brain Cancer Infiltration ex vivo and in vivo Using Quantitative Optical Coherence Tomography", *Science Translational Medicine* 7.292 (2015): 292ra100.
- **Kut C.**, Grossman S., Blakeley J."How critical is the blood brain barrier to the development of neurotherapeutics?" *JAMA Neurology* 72.4 (2015): 381-382.
- **Kut C.**, Redmond R. "New Considerations in Radiation Treatment Planning for Brain Tumors: Neural Progenitor Cell Containing Niches", *Seminars in Radiation Oncology*, High Grade Glioma Edition 24.4 (2014): 265-272.
- Fleming I., **Kut C.**, Macura K., Su L.M., Rivaz H., Schneider C., Hamper U., Lotan T., Taylor R., Hager G., Boctor E. "Ultrasound elastography as a tool for imaging guidance during prostatectomy: Initial experience." *Medical Science Monitor: International Medical Journal of Experimental and Clinical Research* 18.11 (2012): CR635.
- **Kut C.**, Zhang Y.G., Hedayati M., Zhou H.M., Cornejo C., Bordelon D., Mihalic J., Gruettner C., Geyh A., Brayton C., DeWeese T.L., Ivkov R. "Preliminary study of injury from heating systemically delivered, nontargeted dextran-superparamagnetic iron oxide nanoparticles in mice." *Nanomedicine* 7.11 (2012): 1697-1711.
- Tryggestad E., Christian M., Ford E., **Kut C.**, Le Y., Sanguineti G., Tryggestad E., Christian M., Ford E., **Kut C.**, Le Y., Sanguineti G., Song D., Kleinberg L. Tryggestad, Erik, et al.

  "Inter-and intrafraction patient positioning uncertainties for intracranial radiotherapy: a study of four frameless, thermoplastic mask-based immobilization strategies using daily cone-beam CT." *International Journal of Radiation Oncology* Biology* Physics* 80.1 (2011): 281-290.
- **Kut, C.,** Golkhou V., and Bade J.S. "Analytical approximations for the amplitude and period of a relaxation oscillator." *BMC Systems Biology* 3.1 (2009): 6.
- **Kut, C.**, F. Mac Gabhann, and A. S. Popel. "Where is VEGF in the body? A meta-analysis of VEGF distribution in cancer." *British Journal of Cancer* 97.7 (2007): 978-985.

Publications, chapters and other nonwpeer reviewed, candidate's name bold, reverse chron. Order

Book Chapters

- **Kut C.,** Rincon-Torroella J., Quinones-Hinojosa A. and Li X.D. **Optical Coherence Tomography and Quantitative Optical Imaging of Brain Cancer,** *The Textbook of Advanced Neurophotonics and Brain Mapping, Taylor and Francis Book, pending publication in 2016.*
- **Kut C.** and Redmond K. **The Role of Adjuvant Therapy in Subtotal Resection and High Grade Ependymomas,** *Best Evidence Medicine for Brain Tumor Surgery, Thieme Medical Publishers Inc. 2012*
- **Kut C.** and Redmond K. **Spinal Radiosurgery – Current and Future Applications,** *Handbook of Radiosurgery in CNS Disease, Demos Medical Publishing, 2011*

Posters, abstracts, etc. Candidate's name in bold, reverse chronological order

Conference Abstracts, Talks and Proceedings

- **Kut C.,** Xi J.F., Chaichana K.L., Rinco-Torroella J., Rodriguez F., McVeigh E.R., Quinones-Hinojosa A., Li X.D. **Real-time, Label-Free Detection of Human Brain Cancer Infiltration,** oral presentation at 2015 SNO Neuro-Tumor Dinner Club Meeting
- **Kut C.**, Xi J.F., Chaichana K.L., Rinco-Torroella J., Rodriguez F., McVeigh E.R., Quinones-Hinojosa A., Li X.D. **Real-time, Label-Free Optical Property Mapping for Detecting Glioma Invasion with SS-OCT for Potential Guidance of Surgical Intervention,** oral presentation at 2015 SPIE Meeting.
- **Kut C.,** Liang W.X., Hall G., Chaichana K.L., Quinones-Hinojosa A., Li X.D. **Label-Free and Real-time Histologic Imaging of Brain Cancer with Multiphoton Microscopy for Potential Guidance of Surgical Intervention,** oral presentation at 2015 SPIE Meeting.
- Yuan W., **Kut C.**, Liang W.X., Li X.D., **Generic frequency-domain method for ultrafast and robust characterization of optical attenuation from OCT Images,** poster presentation at 2015 SPIE Meeting.
- **Kut C.**, Xi J.F., Chaichana K.L. Ye X.B., McVeigh E.R., Rodriguez F.J., McVeigh E.M., Quinones-Hinojosa A., Li X.D. **In Vivo and Ex Vivo Imaging of Human Brain Tumors Using Swept-Source Optical Coherence Tomography,** poster award winner at 2014 BIOMED OSA Meeting.
- **Kut C.**, Pashakhanloo F., Liang W.X., Schuleri K.H., McVeigh E.R., Herzka D.A., Li X.D. **Multi-photon microscopy of ventricular changes in porcine acute and chronic myocardial infarction models,** *poster presentation at 2014 SPIE Biophotonics West Annual Meeting*
- **Kut C.**, Chacko V., Tyler B., Pathak A.P., Bhujwalla Z., McVeigh E., Li X.D., Herzka D., Grossman S. **The effect of increasing concentrations of intracranial albumin on fluid flow rates within adjacent white matter tracts in rats**, *poster presentation at 2013 ISMRM Annual Meeting.*
- **Kut C.**, Chacko V., Tyler B., Pathak A.P., Bhujwalla Z., McVeigh E., Li X.D., Herzka D., Grossman S. **Determining extracellular fluid velocity along white matter tracts with**

injections of increasing concentrations of intracranial albumin using both histological and radiological techniques, *poster presentation at 2013 AACR Annual Meeting.*

- **Kut C.**, Xi J.F., Raza S., Mavadia J., Liang W.X., Guerrero-Cazares H., McVeigh E., Quinones-Hinojosa A., Li X.D. **Application of optical coherence tomography in brain cancer: detecting glioma invasion from non-neoplastic white matter in human ex vivo samples,** ***oral presentation at 2013 SPIE Annual Meeting***
- **Kut C.**, Raza S., Liang W.X., Abutaleb A., Xi J.F., Mavadia J., Ye X.B., Guerrero-Cazares H., McVeigh E., Li X.D., Quinones-Hinojosa A. **High resolution optical guidance of glioma margin identification – optimizing extent of resection,** *poster presentation at 2012 SNO Annual Meeting*
- **Kut C.**, Chacko V., Tyler B., Bhujwalla Z.M., Pathak A.P., Li, X.D., McVeigh, E, Herzka D., Grossman S.A.. **The effect of increasing concentrations of intracranial albumin on fluid flow rates within adjacent white matter tracts in rats ,** *poster presentation at 2012 SNO Annual Meeting*
- **Kut C.**, Zhang Y.G., Hedayati M., Zhou H.M., Cornejo C., Bordelon D., Mihalic J., Gruettner C., Geyh A., Brayton C., DeWeese T.L., Ivkov R. **Assessing Murine Hepatic and Splenic Injury from Inadvertent Heating of Systematically Delivered Non-targeted Magnetic Nanoparticles,** *oral presentation at 9th international conference on the scientific and clinical applications of magnetic carriers, Minneapolis, MN, May 22 2012.*
- **Kut C.**, Zhang Y.G., Hedayati M., Zhou H.M., Cornejo C., Bordelon D., Mihalic J., Gruettner C., Geyh A., Brayton C., DeWeese T.L., Ivkov R. **Preliminary Assessment of Potential Murine Hepatic and Splenic Injury Resulting from Inadvertent Heating of Systematically Delivered Non-targeted Magnetic Nanoparticles,** *poster presentation at 2012 STM Annual Meeting*
- **Kut C.**, Xi J.F., Raza R., Mavadia J., Guerrero-Cazares H., McVeigh E.M., Quinones-Hinojosa A., Li X.D. **Detecting Glioma Tumor Features in Human Ex Vivo Samples Using Swept-Source OCT,** poster presentation at Biomedical Optics Conference, Optical Society (OSA) 2012.
- **Kut C.**, Zhang Y.G., Hedayati M., Zhou H.M., Cornejo C., Bordelon D., Mihalic J., Gruettner C., Geyh A., Brayton C., DeWeese T.L., Ivkov R. **Preliminary Assessment of Potential Murine Hepatic and Splenic Injury Resulting from Inadvertent Heating of Systematically Delivered Non-targeted Magnetic Nanoparticles,** *poster presentation at Scientific Retreat 2011 for Department of Radiation Oncology and Molecular Radiation Sciences*

Inventions, Patents, Copyrights (pending, awarded)

Patents

- Filed PCT Patent **PCT/US15/22432** (Hopkins filing number: **C12934**) entitled **Quantitative Tissue Property Mapping for Real-Time Tumor Detection and Interventional Guidance (2014).**

Service and leadership

Here list activities at Hopkins or in the community during your time in the graduate program,

Leadership and Community Service:

- **Founder and President of Medical And Educational Perspectives (MEP, a.k.a EP) http://www.mepjhu.com/mep/ (2004-Present)**

  MEP is started in 2004 with the mission of advancing global public health education to at-need communities around the globe. We have taught HIV prevention, sex education and other public health programs to high school students, orphans, and teachers from the Zijin County in China, Chennai in India, and also from Kawagwe and Pemba Island in Tanzania. In order to continue the health education programs at various international locations after the Hopkins team has left, we have partnered with multiple volunteers from the local communities and succeeded in establishing 9 chapters in 5 countries and over 3 continents between 2004 and 2008. In addition, MEP worked with US embassies and consulates during these educational programs, and have been recognized at several occasions. For example, Mr. Michael Retzer, the US Ambassador in Tanzania, held a press conference exclusively for EP (currently known as MEP) http://tanzania.usembassy.gov/sp_08092007.html.

  In 2008, MEP is transformed from a student group into a nonprofit organization formally registered in Baltimore, Maryland, USA. Since then, we have grown to support the development of affordable medical solutions which can benefit at-need communities both in the US and worldwide. To support this goal, we have launched two Johns Hopkins-recognized courses. In the first course, an interdisciplinary team (composing of MD, PhD, MPH and MBA students) complete evaluations of medical devices through interviews and observations at 10-15 different hospitals, nonprofits, industries and government representatives throughout Bangalore, Hyerderabad, Mumbai, Pune, Valsad and Dervan India. In the fall course, students spend several weeks working in interdisciplinary teams at Johns Hopkins to understand what it takes to bring a medical device into the market, and to develop a sustainable financial plan (whether as a startup or as a nonprofit). In these two courses students learn about the scientific foundation, global health context, and business ecosystem for these devices. Through this work, MEP facilitates and fosters interdisciplinary education, entrepreneurship and medical innovation.

  Recently, MEP redirects its focus to Baltimore City Health, and is currently hosting a "Campaign for Progress" event where it solicits over 50 health-related idea submissions from the Baltimore community and from the JHU community. Currently, MEP is working with representatives from the Baltimore City Health Department, Johns Hopkins School of Public Health, and from the Baltimore community to select the top 5 health related ideas which are specific to Baltimore (which ranges from helmet safety for children to the difficulty in reading drug labels due to illiteracy). Once the top 5 ideas are selected, MEP

will work with the selected teams to develop a campaign and to brainstorm on feasible solutions for these Baltimore-specific health issues.

To This date, MEP has obtained over $165,000 funding and has supported 6 inventor teams and over 50 students (MD, PhD and MPH) in the development and evaluation of affordable medical devices. With these funding, MEP hosts an annual "Call for Innovation" event which attracted JHU inventor teams to present their work to CEOs, investors and professors (http://mepjhu.tumblr.com). To date, MEP has ~300 members and closely supported 26 teams; in addition, MEP has solicited entries from ~50 teams.

- **Founding Member and President of JHU SPIE Chapter 2013-2014**
- **Lectures Committee Chair, Hopkins Imaging Initiative 2011-2012**
- **Founder and President of Johns Hopkins Student Research Group (JHSRG) 2006-2008**

Miscellaneous:

- Reviewer for Hopkins Imaging Initiative Conference, October 2011 and 2013
- Reviewer for Biomedical Optics Express, 2011-Present
- Reviewer for Annals of Biomedical Engineering (ABME), 2014-2015